Substituted Na-based Layered Tellurates: Synthesis, Local Structure and Na-Dynamics

Frida Sveen Hempel

November 1, 2023

Series of dissertations submitted to the
Faculty of Mathematics and Natural Sciences, University of Oslo
No. 2688

ISSN 1501-7710

Cover: UiO.
Print production: Graphic center, University of Oslo.

Preface

This dissertation has been submitted to the University of Oslo (UiO) in partial fulfilment of the academic degree of Philosophiae Doctor.

The work presented in this thesis was divided between the groups Process Technology and Functional Materials at SINTEF and the Nanostructures and Functional Materials (NAFUMA) at the Department of Chemistry, University of Oslo. The supervision of this work was done by Bjørnar Arstad from SINTEF and Helmer Fjellvåg at UiO.

The work builds on the results from Xinyu Li's thesis "Solid Electrolytes for Li and Na-ion Batteries". This thesis was a part of the SELiNaB-project, which also included the work of temporary researchers Julia Wind and Federico Bianchini.

The project was funded by the Research Council of Norway with project number P#272402 and P#25544.

Acknowledgements

I have to start by thanking both of my supervisors. Bjørnar, you have been so generous with your time, and I must honestly say that I would never have finished without you. Especially during the long lockdown, you called in to check how I was doing and having an hour-long discussion of details in the NMR spectra was invaluable. I am very grateful for all of the time you have spent on me. Helmer, you have such great insights and I always appreciate getting to discuss my results with you. You are definitely an in high demand, but luckily your input is always valuable and certainly worth waiting for.

A special thank you to the three members of the SELiNaB-project, all of whom helped me tremendously at the beginning of the project and gave me support during many early crises and unfamiliar lab procedures. Xinyu Li for your support with synthesis and Julia Wind for your general guidance and life lessons about academic work. But a special thank you have to be given to Federico Bianchini, as you have been my closest collaborator even after moving on to new positions elsewhere. I'm so grateful for your patience, all of your thourough feedback on articles, and high confidence in my understanding of DFT modelling. I am so grateful I got to work with you.

I must also thank David Wragg for all of your help with XRD, both general support in the lab and identifying mysterious peaks in the diffractogram. But also all support and guidance when our planned PDF analysis kept on expanding, so that the planned very simple analysis ended up as its own track. And on that note I am so grateful for Wojtek, which joined our PDF project and did most of the fittings of both the modulated structure and the RMC modelling. You have been endlessly helpful and are such a great teacher, this work has been extremely valuable to me. I also need to thank Charlotte Martineau-Corcos for her collaboration on the variable temperature NMR and dynamics. It was really interesting for me to get in contact with the wider world of NMR, although through Corona appropriate means.

Then of course I would like to thank my other colleagues at the battery group and the rest of NAFUMA. I am sad so much of my time with you was spent through screens, you are a great group of people that has made the at times frustrating experience of a lock down based PhD much more bearable. I'm very happy I currently get to work on with so many of you, and that the battery world in Norway is small enough so that we'll surely meet and collaborate again.

Finally, I would like to thank my family for their never-ending support. My parents Tore and Runi, my sister Johanne and her boyfriend Pål. Thanks to all of my friends who have listened patiently while I try to explain my research, although most of you understand it better than you think. And finally, thanks to my amazing wife Tora, I would not have gotten through this without you. You are the best support and partner anyone could ever wish for.

List of abbreviations

AIMD	*Ab-Initio* Molecular Dynamics
BPP	Bloembergen, Purcell, Pound (relaxation behaviour)
CEI	Cathode Electorlyte Interphase
DEC	Diethyl Carbonate
DFT	Density Functional Theory
DMC	Dimethyl Carbonate
DOR	DOuble Rotation
EC	Ethylene Carbonate
EFG	Electric Field Gradient
EMC	Ethyl Methyl Carbonate
EV	Electric Vehicle
ICE	Internal Combustion Engine
LDH	Layered Double Hydroxides
LE	Liquid Electrolytes
LGPS	$Li_{10}GeP_2S_{12}$
LIB	Lithium Ion Battery
MAS	Magic Angle Spinning

MQMAS	Multi-Quantum Magic Angle Spinning
NASICON	NA-Super Ionic CONductor
NIB	Sodium Ion Battery
Ni-MH	Nickel Metal-Hydride Batteries
NMC	Nickel Manganese Cobalt oxide
NMR	Nuclear Magnetic Resonance (spectroscopy)
NMTO	$Na_2Mg_2TeO_6$
NNTO	$Na_2Ni_2TeO_6$
NZSO	$Na_3Zn_2SbO_6$
NZTO	$Na_2Zn_2TeO_6$
PC	Propylene Carbonate
PDF	(Atomic) Pair Distribution Function
r.f.	Radio Frequency
RMC	Reverse Monte Carlo
SEI	Solid Electorlyte Interphase
SLR	Spin Lattice Relaxation
SOC	State Of Charge
SSE	Solid State Electrolyte
SSR	Spin-Spin Relaxtion
TMD	Transition Metal Dichalcogenides
XRD	X-Ray Diffraction

Summary

In order to reduce the emission of greenhouse gasses the world has to transition to renewable energy systems. Electric vehicles have been at the forefront of battery development in the later years. These types of batteries need high capacity, and Li-ion batteries emerged as the superior battery technology. Li-ion batteries have thus dominated battery research and development in recent times.

As renewable energy generation systems expand, batteries will likely become important as secondary storage systems. Prioritization for stationary, secondary storage is markedly different from primary, transportable storage. Losses in volumetric and gravimetric energy density are easily compensated by adding more batteries. The most important parameters are price and use of materials with global availability and abundance. Na-ion batteries are one of the next-generation battery technologies. Na is globally well distributed, and in addition, non-critical elements like Fe are used in the cathode materials. A major concern with today's technology is safety, for example, replacing flammable liquid electrolytes. Solid-state electrolytes (SSEs) replace the liquid with a thermally stable solid material. SSEs reduce both the probability and the consequences of battery fires. This thesis focuses on solid-state electrolytes for Na-ion batteries.

Solid-state batteries are currently limited by low ionic conductivity compared to the liquid analogue. Improving ionic conductivity is a major concern for commercialization. Ionic conductivity is a long-range mechanism, but any improvements will also change the behaviour of the conduction ions at a local scale. This thesis will therefore focus on the very local behaviour and structure of a solid-state electrolyte candidate. The material investigated is the layered oxide $Na_2Zn_2TeO_6$. The Na content of layered materials is well known to influence conductivity and phase stability. The Na content is changed by substituting the framework cations Zn and Te with Ga and Sb. Behaviour and structure are characterized by measurement techniques like nuclear magnetic resonance and total scattering X-ray diffraction.

The first work of this thesis establishes a reliable synthesis route for the substituted materials. They are well known to have phases similar in energy. Previous substitution efforts report high concentrations of secondary phases. We synthesize the materials using a sol-gel synthesis method, ensuring a homogeneous distribution of precursors. The synthesis was characterized by ^{125}Te and ^{23}Na MAS NMR, which confirms nominal substitution and no unchanged regions. Comparing ^{125}Te NMR and DFT simulations of the chemical shift, demonstrates the influence of different Na-environments on the ^{125}Te spectra.

The second work focuses on the influence of Ga-substitution on Na-dynamics. Ga-substitution reduces Na-content and is thus assumed to increase Na-conductivity by decreasing Na-Na repulsion. We use variable temperature MAS and static ^{23}Na NMR, relaxometry and *ab-inito* molecular dynamics to find that the Na-dynamics is increasing with Ga-substitution. We show a decrease in activation energy, larger than previous measurements for ionic transport.

Our third work characterizes a superstructure in $Na_2Zn_2TeO_6$. The simplest fitting using the symmetrical unit cell leaves a series of unfitted, small peaks. We identify that these correspond to a $2\times2\times3$ supercell, described by a commensurate modulation of the original symmetry. The commensurate superstructure can be described by modulation vectors, found by randomizing the starting points to ensure a global minimum is found. The resulting superstructure has a positional exchange between Te and Zn in two of the eight columns. We define the Na-structure as the positional and occupational distribution of Na-atoms in the material, and we find it to be very complex. One of the three symmetric positions was found to be completely empty. A new ”hybrid” position was identified, which was offset halfway between the empty site and the adjacent site.

The last work investigates the influence on the Na-structure of increasing Na-content by Sb-substitution. The substitution is characterized by ^{125}Te MAS NMR. We show that the Na placement is completely determined by the electrostatic interactions with the framework cations. Any Na or Na-vacancy compensating for Sb or Te is placed in the position that optimizes charge compensation. The Na-placement is described by conditional probability. We also identify additional structural deformations in the Na-environments by ^{23}Na MQMAS. All substituted samples have significant Na-dynamics at room temperature.

Sammendrag

Dersom verden skal nå målene satt av Parisavtalen og redusere global oppvarming, trenger vi en overgang til fornybare energisystemer. Batteriutviklingen har i de siste årene vært drevet av utviklingen av elbiler, der Li-ionebatterier har vært den dominerende teknologien. Dette kommer til å forandre seg når man bygger ut fornybare energikjeder, der batterier kommer til å bli viktige som sekundære lagringssystemer. Kravene som stilles til stasjonære batterier er veldig ulik fra transportable batterier. Kravene til både volumetrisk og gravimetrisk energitetthet er lavere, siden man kan kompensere gjennom å legge til batterier. Pris vil være en viktigere parameter, som bestemmes av tilgjengelighet av råvarene. Na er jevnt fordelt globalt, og i tillegg brukes ikke-kritiske elementer som Fe i katoden. Na-ionebatterier har derfor blitt pekt ut som en av neste generasjons batteriteknologier En stor bekymring med dagens teknologi er sikkerhet. Flytende eletrolytter er brennbare, og kan både starte og akselerere batteribranner. Faststoffelektrolytter vil derfor forbedre sikkerheten gjennom å erstatte væsken med et termisk stabilt fast materiale, som reduserer sannsynligheten for og konsekvensene av batteribranner.

Denne oppgaven fokuserer på faststoffelektrolytter for Na-ion batterier. Den største begrensningen for faststoffelektrolytter er ioneledningsevne, som er lavere enn hos løsemiddelbaserte elektrolytter. Forbedring av ioneledningsevne må dermed forbedres om faststoffelektrolytter skal kommersialiseres. Ioneledningsevne er en langdistansemekanisme, men eventuelle forbedringer vil også endre oppførselen til ledningsionene på lokal skala. Denne oppgaven vil derfor fokusere på den lokale oppførselen og strukturen til det lagdelte oksidet $Na_2Zn_2TeO_6$, som er en lovende faststoffelektrolyttkandidat. Konduktivitet og fasestabilitet i lagdelte materialer er kjent for å påvirkes av Na-innholdet, som vi endrer ved å erstatte rammeverkkationene Zn og Te med Ga og Sb. Vi karakteriserer Na-dynamikk og struktur ved hjelp av kjernemagnetisk resonans og totalspredningsrøntgendiffraksjon. Det første arbeidet i denne oppgaven etablerer en robust syntesemetode for de substituerte materia-

lene. Denne typen lagdelte materialer er kjent for å ha faser som ligger veldig nær i energi, som gjør sekundærfaser vanskeligere å unngå. Tidligere synteser på lignende materialer rapporterer høye konsentrasjoner av sekundærfaser. Vi syntetiserer materialene ved hjelp av en sol-gel syntesemetode, noe som sikrer en homogen fordeling av forløpere. Syntesen ble karakterisert av ^{125}Te og ^{23}Na MAS NMR, som bekrefter nominell substitusjon og kan validere at man ikke har uendrede regioner. Sammenligning av ^{125}Te NMR- og DFT-simuleringer av det kjemiske skiftet, demonstrerer påvirkningen av forskjellige Na-miljøer på ^{125}Te-spektrene.

Det andre arbeidet fokuserer på hvordan Ga-substitusjon påvirker Na-dynamikken i materialene. Na-innholdet reduseres for å kompensere for Ga-substitutsjonen, noe som antas å øke Na-ledningsevnen ved å redusere Na-Na-frastøtning. Dette karakteriserer vi gjennom MAS og statisk ^{23}Na NMR fra lav til høytemperatur, relaksasjonsmålinger og *ab-inito* molekylær dynamikk simulering. Vi finner at Na-dynamikken øker med Ga-substitusjon, og rapporterer en større reduksjon i aktiveringsenergi enn tidligere målinger for ionetransport.

Vårt tredje arbeid karakteriserer en superstruktur i $Na_2Zn_2TeO_6$. Tilpasning av diffraktogrammet med den symmetriske enhetscellen etterlater en rekke små, utilpassede topper. Vi identifiserer at disse tilsvarer en $2\times2\times3$ supercelle, som vi beskriver gjennom en modulert struktur basert på den opprinnelige symmetrien. Denne superstrukturen beskrives ved hjelp av modulasjonsvektorer, som vi finner ved å randomisere startpunktene. Dette sikrer at vi finner det et globale minimumet. Vi finner at superstrukturen har en posisjonsutveksling mellom Te og Zn i to av de åtte kolonnene i supercellen. Na-strukturen på sin side er kompleks, med stor variasjon både i posisjon og okkupans. En av de tre symmetriske posisjonene ble funnet å være helt tom. En ny posisjon ble identifisert, posisjonert halvveis mellom den tomme og naboposisjonen.

I det siste arbeidet undersøker vi påvirkningen på Na-strukturen som kommer av å øke Na-innholdet ved Sb-substitusjon. Substitusjonen er karakterisert ved hjelp av ^{125}Te MAS NMR. Vi viser at Na-plasseringen bestemmes av elektrostatiske interaksjoner med kationene i mellomlagene. Eventuelle Na eller vakanser plasseres i posisjonen som gir best ladningskompensasjon for Sb/Te. Na-plasseringen er beskrevet ved betinget sannsynlighet. Vi identifiserer også ytterligere strukturelle deformasjoner i Na-miljøene ved hjelp av ^{23}Na MQMAS. Alle substituerte prøver har betydelig Na-dynamikk ved romtemperatur.

List of Figures

1.1 Overview of cathode and anode materials for Na-ion batteries 25

2.1 Common stacking types for layered oxides 33
2.2 Na sites in layered oxides 34
2.3 Phase diagram for Na_xCoO_2 35
2.4 Di- and trivacancy model, compared with proposed Na-structures 38
2.5 Superstructure of O3-$Na_{5/8}MnO_2$ 42
2.6 Pathway migration in $Na_{0.56}CoO_2$ 45
2.7 Comparison between Na diffusion mechanisms 46
2.8 Phonon modes for NZTO and NMTO. 48
2.9 Summary of temperature dependent ionic conductivity of a few Na-based electrolytes. 50
2.10 Definition of electrolyte stability window 51
2.11 Structure of β-alumina 53
2.12 Structure of rhomohedral and monoclinic NASICON 54

3.1 Bragg's law 60
3.2 Gyromagnetic ratio and frequency of different iosotopes 63
3.3 NMR pulse sequences 66
3.4 Motional timescales and effect on nuclear spin dynamics 67

4.1 Diffractogram and lattice parameters of NZTO and all Ga-substituted samples. 75
4.2 ^{125}Te MAS NMR spectra in 11.75 T field for all Ga-substituted samples 76
4.3 Structure and calculated chamical shift from different Te-environments from combinations of Na-neighbours 78
4.4 Te-environments from 50ps MD at 750K 81

4.5 Static and MAS ^{23}Na NMR of NZTO at 100K 83
4.6 Na-sites with closest neighboring Na-site and decomposition of 100K MAS ^{23}Na NMR 85
4.7 Static and MAS ^{23}Na spectra of x = 0.20, and static and MAS ^{23} Na NMR spectra at 100 K 87
4.8 ^{23}Na MAS NMR of NZTO at temperatures (293-208) 88
4.9 Temperature dependence for diffusion induced ^{23}Na SLR rates T_1 for all Ga-substituted samples 89
4.10 Measured and calculated diffractogram of NZTO, compared in linear and logarithmic to highlight unfitted supercell peaks 94
4.11 Powder diffraction pattern of $Na_2Zn_2TeO_6$ fitted with commensurate modulation model 98
4.12 Te/Zn superstructure 100
4.13 Overview of the Na-substructure 101
4.14 Detailed overview of Na-substructure, separated into the two *6g* and *4f* . . . 102
4.15 Comparison of the measured PDF with the calculated for the average, the modulated and the RMC calucalted structure 104
4.16 RMC simulated structure 106
4.17 DFT calculated energy/volume curves for NZSO and NZTO 108
4.18 Diffractogram and lattice parameters for Sb-substituted samples 109
4.19 Symmetrical Na-sites and Te-Te distances 111
4.20 Decomposed ^{125}Te NMR MAS spectra 112
4.21 Sb/Te series with the corresponding Na-environments 114
4.22 ^{23}Na NMR of the Sb-substituted samples 118
4.23 ^{23}Na MQMAS of the Sb-substituted samples 119

5.1 ^{23}Na MAS NMR spectra of Ga-substituted samples at 100K. 128
5.2 Comparison of Na-jumps in filled and underfilled layer. 131

List of Tables

2.1 Ordering patterns of Na in Na_xCoO_2 39
2.1 Cont. ordering patterns of Na in Na_xCoO_2. 40

4.1 Integration of ^{125}Te-spectra for Ga-substituted materials 77
4.2 Activation energy for all ga-substituted samples 90
4.3 AIMD calculation of Na diffusion in an average lattice 91
4.4 Average crystal structure description of of $Na_2Zn_2TeO_6$ 96
4.5 Occupancy modulation amplitudes in $Na_2Zn_2TeO_6$ 96
4.6 Atomic position modulation amplitudes in $Na_2Zn_2TeO_6$ 97
4.7 Calculated probabilities for different Te-configurations 115

5.1 Comparison of Na-distributions reported in literature between different measurement techniques 126
5.2 Activation energy and ionic conductivity for NZTO and different SSE-candidates 134

Contents

1 Introduction **21**

1.1 Motivation 21

1.1.1 Batteries in an energy perspective 21

1.1.2 Na-ion batteries and solid state electrolytes 24

1.2 Scope of work 26

2 Background **31**

2.1 Layered oxides 31

2.2 Na-ordering and coordination 37

2.3 Na-dynamics and disorder 44

2.4 Solid-state electrolytes and its competitors 49

2.4.1 Liquid electrolytes 50

2.4.2 Polymer-based and composite solid state electrolytes 52

2.4.3 Layered oxides 52

2.4.4 Aluminates 53

2.4.5 NaSICON-type conductors 54

2.4.6 Sulfides 55

3 Methods **57**

3.1 Synthesis 57

3.2 X-ray diffraction 59

3.2.1 Rietveld refinement 60

3.2.2 Total scattering XRD and pair distribution function 61

3.3 Nuclear magnetic resconance spectroscopy 62

3.3.1 The NMR experiment 64

3.3.2 Characterization of motion 66

3.4 Modeling and simulations . . . 70
3.4.1 Density functional theory . . . 70
3.4.2 Reverse Monte Carlo . . . 71
3.4.3 NMR spectral fitting . . . 71

4 Summary of articles 73
4.1 The effect of Ga-susbtitution on the local structure of NZTO . . . 74
4.1.1 Structure and phase purity from the sol-gel synthesis method . . . 74
4.1.2 ^{23}Na and ^{125}Te NMR spectra . . . 76
4.1.3 DFT calculations of Na-influence on ^{125}Te-spectra . . . 77
4.1.4 *Ab Initio* MD simulations on structural changes from Ga-substitution on NZTO . . . 79
4.2 Na-dynamics and structure in Ga-substituted NZTO . . . 82
4.2.1 Low temperature ^{23}Na NMR . . . 83
4.2.2 High temperature ^{23}Na NMR . . . 86
4.2.3 Relaxation measurements . . . 88
4.2.4 *Ab-initio* MD simulations for ionic conductivity . . . 90
4.3 Superstructure of locally disordered $Na_2Zn_2TeO_6$ . . . 93
4.3.1 X-ray diffraction and superstructure . . . 93
4.3.2 Modulated structure of Zn and Te . . . 99
4.3.3 Modulated structure of Na . . . 100
4.3.4 Total scattering XRD and RMC modeling . . . 103
4.4 Substitution mechanism in Na-deficient O3-phases . . . 107
4.4.1 Phase stability . . . 107
4.4.2 Crystal structure and substitution . . . 109
4.4.3 Sb-substitution on NZTO . . . 110
4.4.4 ^{23}NMR MAS NMR . . . 116
4.4.5 ^{23}NMR MQMAS . . . 117

5 Discussion 121
5.1 Sol-gel synthesis . . . 121
5.2 Characterization of solid solution derivates . . . 122
5.3 The validity of Wyckoff sites as approximation for Na-sites . . . 124
5.4 Na-disorder in Sb- and Ga-substituted variants . . . 127
5.5 Interlayer interactions . . . 129

5.6 Investigating changes in Na-dynamics from Ga-sub- stitution 130
5.7 Comparison of Ga-substituted NZTO with other Na-ion conductors 133

6 Concluding remarks and outlook 137

Chapter 1

Introduction

1.1 Motivation

1.1.1 Batteries in an energy perspective

As stated by the IPCC in their report in the autumn of 2021, reaching the 1.5℃ goal set by the Paris Agreement in 2016, or even the 2℃ goal is becoming highly unlikely. It will take unprecedented efforts by all countries on Earth.[1] One of the major polluters is the energy sector, which is responsible for a large amount of emissions.[1] To have any hope for mitigating the catastrophic consequences of climate change, a green revolution is of vital importance.

Fossil fuels are the current dominant technology in the energy sector. The industrial revolution was powered by the steam engine, which burns organic matter like coal to evaporate water, which is transformed into mechanical power by pushing a piston. Similar techniques are used in newer energy production methods, where turbines convert the kinetic energy to electricity. One important feature of these processes is that they can be started as a response to demand. On the other hand, most renewable processes must be harvested when available and stored for future use. Hydro-power and geothermal heat have built-in long-term storage, but wind and solar power will have to rely on secondary storage systems. Energy storage is therefore as important as production in the energy systems. A good energy storage system should combine storage on multiple time scales. Long-term storage offsets fluctuating energy availability, and short-term storage offsets fluctuating power demand, and can thus reduce the total energy demand. Natural gas is the most widespread

backup for renewable energy sources today,[2] which increases the emissions of otherwise green energy mixes. To help ease the transition to fully renewable systems, carbon capture and storage can decrease the emissions from these plants.[3] Hydropower is one of the better and more widespread long-term storage methods, but implementation must be limited to countries where water is not a strained resource.[4] Another possible option is production and storage of hydrogen. Some energy-scarce countries like Japan and Korea are increasing national development to combat their energy insecurity.[5] The main technology for short-term storage is batteries. A combination of all these technologies, carefully selected to exploit the available resources of a given area (and not put a too high load on specific natural resources) should ensure a robust energy production and storage system.

Fossil fuels are the current dominant technology in the energy sector. The industrial revolution was powered by the steam engine, which burns organic matter like coal to evaporate water, which is transformed into mechanical power by pushing a piston. Similar techniques are used in newer energy production methods, where turbines convert the kinetic energy to electricity. One important feature of these processes is that they can be started as a response to demand. On the other hand, most renewable processes must be harvested when available and stored for future use. Hydro-power and geothermal heat have built-in long-term storage, but wind and solar power will have to rely on secondary storage systems. Energy storage is therefore as important as production in the energy systems. A good energy storage system should combine storage on multiple time scales. Long-term storage offsets fluctuating energy availability, and short-term storage offsets fluctuating power demand, and can thus reduce the total energy demand. Natural gas is the most widespread backup for renewable energy sources today,[2] which increases the emissions of otherwise green energy mixes. To help ease the transition to fully renewable systems, carbon capture and storage can decrease the emissions from these plants.[3] Hydropower is one of the better and more widespread long-term storage methods, but implementation must be limited to countries where water is not a strained resource.[4] Another possible option is production and storage of hydrogen. Some energy-scarce countries like Japan and Korea are increasing national development to combat their energy insecurity.[5] The main technology for short-term storage is batteries. A combination of all these technologies, carefully selected to exploit the available resources of a given area (and not put a too high load on specific natural resources) should ensure a robust energy production and storage system.

Batteries are built on converting chemical to electric energy, with commercial use dating back to the 1800s.[6] However, these were primary batteries and the reaction irreversibly

dissolves one of the electrodes and the battery cannot be reused. A secondary battery has a reversible chemical reaction, allowing the battery to be reused over a long period. The dominating battery technology today is the Li-ion battery (LIB). The potential technology is best demonstrated by the Nobel Prize in Chemistry 2019. This was awarded M. Stanley Whittingham, John B. Goodenough[7] and Akira Yoshino[8] for "laying the foundation for a fossil fuel-free society".

The LIB is a versatile technology which can be tailored for different use depending on different needs: high power, high energy density or low price. The start of the LIB growth enabled the growth of portable electronics such as cell phones and laptops. With the steady improvements in LIB technology, the electric vehicle sector has exploded in the later years.[9] However, as battery use increases and diversifies, there are discussions about the necessity of diversifying battery technologies. While Li is still abundant, there are concerns about whether the supply can meet the growing need. In addition, the Li sources are geographically quite limited, with only five countries accounting for 97% of the production in 2018.[10] Other materials in use in LIB are even more problematic. Many batteries use nickel manganese cobalt oxides (NMC) as the cathode, with the Co used in cathode being controversial due to concerns about human rights violations.[11,12] This is best addressed by diversifying battery technology and energy storage. Hydrogen fuel cells are likely a very good alternative for certain transportation applications like aviation or long-haul transport, where the requirements for energy density are extremely high.[13] The critical issue facing hydrogen is addressing storage problems, but there have been advances in cryogenic and compressed storage which have matured as storage systems over the last decades.[14]

The possible changes to diversify batteries include developing new cathode material for LIBs or switching to other battery technologies. In the second category, we find nickel metal-hydride batteries (Ni-MH). They were commercially used in the 1990s,[15] even in some early EVs.[16] They have long cycle life and are non-toxic and non-hazardous. They do however rely on rare earth elements, which also have issues with distribution, scarcity and mining. Therefore, they have seen an increase in research interest in recent years despite their lower energy density.[17] Another promising battery technology is the Na-ion battery (NIB), which changes the Li-ion to the larger Na-ion.

1.1.2 Na-ion batteries and solid state electrolytes

The Na-ion battery (NIB) is conceptually very similar to the LIB but substitutes Li with the heavier and larger Na-ion as the charge carrier. The active materials are only a fraction of the full battery pack, and the decrease in weight-specific capacity should be negligible. Areas like grid storage are not limited with regard to weight-specific capacity and are expected to expand massively with the societal transition to greener energy. This favours batteries which are cheap, safe, and preferably environmentally friendly. Stationary storage puts less pressure on commonly emphasized parameters such as weight, fast charging speeds and high voltage, where the latter is easily compensated by the addition of more cells.

The main advantage of NIBs is the global availability of Na, which is an important aspect of energy security. Na is the 4th most available element in the earth's crust, with global availability and the resources include low-cost salts such as Na_2CO_3, Na_2SO_4 and NaCl.[18] A deliberate choice of cathode, can avoid several other expensive, toxic and geographically limited materials such as Co. NIBs are structurally similar to LIBs, which puts them at an advantage compared to other battery technologies, like metal hydrides. This allows us to build on knowledge from LIB production and possibly use the same production facilities. NIBs are often also said to be a cheaper alternative to LIB, but this usually overlooks that there is always some cost associated with transferring from one technology to another. The main price difference of NIBs is the use of an Al-current collector at both electrodes, which is cheaper and lighter. Li forms a binary alloy with Al and therefore needs a more expensive, heavier Cu-current collector at the anode.[18] This is also an important political point as Cu is one of the EUs strategic raw materials, and much of Co-mining in Congo is from Cu-ores, and thus the extraction is often connected to similar ethical concerns.[10] The price is also likely reduced as the better cathode materials for NIBs can avoid expensive elements like Co and Ni.

While NIBs were researched in the 1970s and 80's alongside LIBs, interest dipped in the 90s with the commercialization of the latter. The radius of the Na-ion is around 1.16 Å, while the Li-ion is much smaller at 0.9 Å. This size difference makes finding appropriate electrode materials harder, which has been one of the limiting factors for the use of NIB. Current research has identified a few material classes as the main electrode candidates for NIBs (shown in figure 1.1). Possible cathode materials are layered oxides, NASICONs, phosphate polyanions, sodium fluorophosphates and Prussian blue analogues. Fe-based materials seem to be one of the better cathode candidates, like α-$NaFeO_2$ which would be

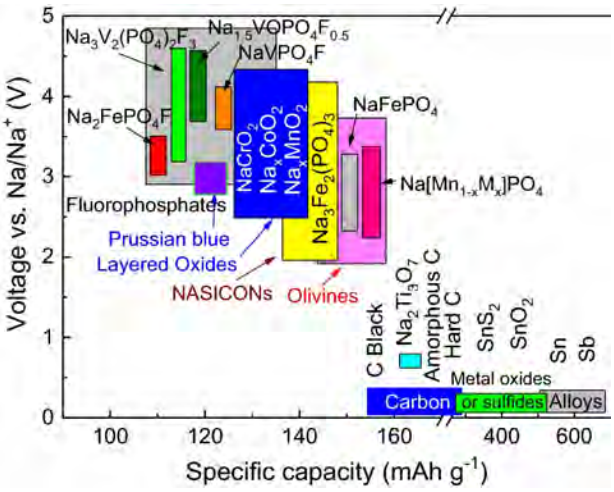

Figure 1.1: Selection of often studied cathode and anode materials for Na-ion batteries, represented by specific capacity and operating voltage vs Na/Na^+. Figure reproduced from Wang et al with permission.[19]

the first cathode with $Fe^{3+/4+}$ redox reaction.[20] Fe is abundant, cheap and has many advantages in the refinement process, compared to the problems for LIBs described above.[20] On the anode side, we have the option to use either intercalation or conversion reactions. The suggested materials are carbon-based materials hard and soft carbon, graphene and carbon nanotubes, transition metal oxides, sulphides or alloys (with e.g. Sn, Sb, Ge or Bi).[19]

The size of the battery packs for grid applications is becoming massive, and therefore, the safety aspect is vital. NIBs use double Al-current collectors, and can thus both be transported and stored in the fully discharged state. The Cu-current collector used in LIB would oxidize, dissolve and internally short circuit the cell if stored at 0% state of charge (SOC), and is thus best preserved at 30% SOC.[21] The additional stored energy poses an additional risk in terms of accidents and will thus have more energy for thermal runaway. The Al-collector is very resistant to oxidation and can easily be stored at 0% SOC.[22]

One of the more limiting points for commercial use of NIB is the lack of a suitable electrolyte. The commercial standard in LIB is using liquid electrolytes (LE) made up of Li-salts, like $LiPF_6$, dissolved in organic solvents like ethylene carbonate (EC), diethyl carbonate (DEC), dimethyl carbonate (DMC), and ethyl methyl carbonate (EMC). These solvents are generally flammable, presenting large security hazards.[23] As previously stated, the large facilities of batteries for grid storage should prioritize security, and therefore replace the LE. One possibility is a solid-state electrolyte (SSE). Depending on the choice of material,

these are less flammable and with the higher heat tolerance also allow denser cell packing. The LE also needs a full casing for the liquid and a separator which keeps the battery from short-circuiting. The SSE can act as the separator, as it is placed between the anode and cathode and no casing needs to keep the liquid in.

1.2 Scope of work

This PhD thesis reports work identifying new synthesis routes and advanced characterization on the layered oxide $Na_2Zn_2TeO_6$ and Ga^{3+}- and Sb^{5+}-substituted derivatives. This material is of interest as a potential candidate for SSE, and the substitutions tune material properties by changing the Na content.

The work extends the findings in the thesis work "Solid Electrolytes for Li and Na-ion Batteries" by Xinyu Li in the NAFUMA group, in turn, part of the SELiNaB-project with temporary researchers Julia Wind and Federico Bianchini. They explored the material $Na_2Zn_2TeO_6$ (NZTO) as a possible solid-state electrolyte, which has a relatively high ionic conductivity of 10^{-4} S/cm and low electronic conductivity.[24,25] It is structurally similar to the layered redox-active oxides commonly used as cathode materials. However, the transition metal *M* is exchanged for the red-ox inactive cations Zn^{2+} and Te^{6+}. The structural similarity means that the type of material is already well known which gives a good foundation for further development.

Na-content is an important influencing factor for both structure type and Na-dynamics in layered oxides.[26,27] The previous work used a Li^+ substitution on the Zn-site, increasing Na content and producing two-phase materials for lower substitution levels. In this thesis work, we expand on this by both decreasing and increasing Na content. This is achieved by Ga^{3+} substitution on the $Zn2\widehat{+}$-site or by Sb^{5+} on the Te^{6+} site. The former substitution is often discussed as a strategy for improving the ionic conductivity of the material.[28,29] The Na^+ ion is much larger than the Li^+ ion in the dominating battery technology, which means these materials will have different limitations. Na-ion conductors are dominated by Na-Na repulsion which decreases Na-conductivity, compared to the Li-analogues which typically get anti-site disorder with framework cations *M* due to similar size, making secondary phases and decreasing cycle life.[30] Decreasing Na-content decrease Na-Na repulsion and eases Na-movement, increasing the conductivity.[29] However, previous attempts of Ga-substitution demonstrates limited increases in conductivity,[29] which is why we want to investigate Na-movement on the local scale. This will give us a fundamental understanding of the move-

ment of the Na-ions, instead of the aggregate property of total conductivity, and how these are influenced by the Na-content. This fundamental understanding will enable us to create better strategies for further improvements in Na-conductivity.

The inclusion of only red-ox inactive cations in the framework restricts the degree of freedom of the Na distribution. Red-ox active cations can change oxidation state and allow inhomogeneous Na-distribution while keeping the electroneutrality. The influence of Na-ratio on phase stability and ionic conductivity can therefore be studied using this fixed Na-ratio with homogeneous distribution. This could give a more fundamental insight into the Na structure and dynamics in the whole class of layered oxides (also the ones with red-ox active cations) as the Na is given one less degree of freedom. This work expands this investigation to the Na-richer materials, where Te^{6+} is substituted by Sb^{5+}. These materials are O3-type phase, a similar structure with half the available Na-positions. This Na structure is used to investigate the balance between Na-Na repulsions and charge compensation with the surrounding framework layer. Figures of different stacking types are shown in figure 2.1, with a detailed view of the relevant structures in figure 2.2.

We also investigate the interlayer Na-substructure. The layered oxides are usually described as being built up by independent, rigid 2D sheets of the $[MO_2]_n$ with the Na-layer only restricted by the in-layer Na-substructure. But as with most materials, the rigid average structure rarely represents the true atomic arrangement on the local scale. The previous work in the SELiNa project identified deviations from the average structure in the form of stacking faults of the structurally similar $Na_2Ni_2TeO_6$-type.[31] We expand on this work by investigating the superstructure of both the $[MO_2]_n$ layer and the Na-structure. We also investigate if the Na-layers are independent, as deformations in the framework layer can allow one Na-layer to influence the next. If we want to improve ionic conductivity, we need to understand all possible Na interactions.

Small substitutions of one element in the framework are a common tactic for tailoring materials to specific properties. Mixing framework cations to combine their advantages has been a standard in the development of layered oxides for battery technology. However, substitution requires rigid control of synthesis conditions and verification of a successful synthesis as quality control. The layered oxides have multiple phases very close in energy,[32] meaning small differences in Na-ratio could give materials with multiple phases.[27] The previous Li^+-substitution produced two phase systems at small substitution concentration. This work, therefore, focuses on identifying a robust synthesis route. We use sol-gel-synthesis which dissolves all precursors and then disperses them in a carbon matrix before firing, to

ensure that the starting point is a homogeneous distribution of all precursors.

Verification of element substitutions can be difficult with smaller concentrations, as standard techniques XRD lacks contrast for elements close in weight. Techniques like ICP-MS can confirm the nominal amount and has low detection limits for elements, but one cannot verify that the substitution is homogeneous and not segregated into islands with higher substitution or secondary elements. NMR is often used for such purposes with great success, as it gives local information on just the immediate chemical environment, as the measured signal is only affected by the elements in the closest coordination sphere.

As a characterization of the substitution mechanism, it is useful to use one of the framework cations as the ”observer” nucleus. ^{125}Te NMR is known to be very sensitive to small variations in the local environment, due to the high number of electrons.[33] This makes it a well-suited candidate to characterize the degree of substitution in the framework layer and has currently been explored in detail. The other good options are not used, ^{67}Zn has a low frequency in the 11.75 T field (defined by the instrument used), and loose information of the substituted positions in the Ga-substituted series. $^{121/123}$Sb NMR has large quadropolar coupling constants and fast relaxation, which gives broad unobservable peaks due to the rapid relaxation.[34] Finally, the $^{69/71}$Ga both have high enough frequency, but are not present in the unsubstituted sample, which is why ^{125}Te is the better option.

^{23}Na NMR is able to characterize both the structure of the Na-layer and the dynamics. The highly dynamic nature of the layer averages out the signal, making it difficult to gain insight into the Na distribution and local environments. In order to gain detailed insight, the properties are instead investigated with low temperature ^{23}Na NMR and ^{125}Te NMR. Combining these studies with DFT simulations clarifies the influence of the different Na-configurations on the ^{125}Te-spectra.

The local feature of NMR is also its greatest limitation. Depending on the sensitivity of the observed nuclei, the chemical environment observed by NMR spectra is usually only influenced by the very closest neighbouring atoms, maybe in the 2nd or 3rd coordination spheres. Long-range structural variables are not observable by NMR, which is why NMR is often used in combination with a long-ranging technique like XRD. However, to bridge the gap between the two, we employ total scattering XRD. This is the Fourier transform of the diffractogram which gives us the atomic pair distribution function (PDF) of all of the interatomic bond lengths in the material. PDF is often used to describe materials that are aperiodic in their disorder, where the deviations are difficult to solve in the averaged diffractogram.[35] In this work, we describe the long-range structural disorder in NZTO by a

reverse Monte Carlo (RMC) fitting to the PDF. This is combined with modulated structure which is fitted to the supercell peaks of the standard diffractogram. As a combination, these two are able to describe a commensurate $2\times2\times3$ superstructure in NZTO.

The motivation to study NZTO and its derivatives is the possible use as an SSE. Previous studies have used average techniques like impedance spectroscopy[29] or simulations using macroscopic potentials.[36] These can give a quantification of changes in parameters, but not the fundamental mechanics behind these changes. We instead want to look at the fundamental material properties like structure and Na-dynamics and see how these are influenced by reducing and increasing the Na content. This is done by a combination of characterization on three different length scales. At this point, the work can be related back to battery research. A better understanding of the bottlenecks of Na-movement enables us to make better strategies for improving the Na-mobility and thus make a better SSE.

Chapter 2

Background

2.1 Layered oxides

Layered materials encompass a wide variety of structural types. They are some of the newest, most groundbreaking materials, but are also important historical technological breakthroughs. Chinese porcelain has been admired throughout history for its delicacy, thin enough ”view the sparkle of water” and often compared to egg shells.[37] The secret is a layered kaolin clay treated with urea, which created the required plasticity through weakening H-bonds between the layers. 7000 years later, the early petrochemical industry uses acid-treated layered clay as a catalyst for the hydrocracking process.[38] This type of material might even have played a part in one of life's most fundamental processes. The clay montmorillonite is a catalyst for the polymerization of RNA and increases the conversion of fatty acid micelles into vesicles in which the clay and RNA can be encapsulated.[39] This creates an encapsulation of the catalytically active surface within a membrane vesicle, which can grow and divide without losing the encapsulated contents. Clay in hot springs could therefore have played a vital part in the formation of life on Earth.

A common classification of layered materials is the charge of the layers. The examples described above are cationic clays, with one negatively charged layer of covalently linked Si-tetrahedra. Charge compensating is achieved by a cation layer, typically Mg or Al in octahedral coordination.[40] Examples of positively charged layers with charge-compensating anions would be layered double hydroxides (LDH). These are typically lab created, in contrast to the naturally occurring cationic clays.[38] The last type is the neutral layers, which includes many hydroxides, phosphites and chalcogenides.

Newer types of layered materials have size effects from their anisotropic nature. This gives rise to so-called 2D materials which can have different optical, electronic and structural properties compared to their bulk counterpart. Of the most famous materials is graphene, which can be thought of as a one-layer version of graphite. When separating one graphene layer from graphite, the different electronic properties along the layer direction can be exploited. The most important is that there is no electric resistance in the *xy*-direction, which is altered by both layer stacking or edge termination and thus gives wide tuning abilities.[41] The special properties of graphene increased the focus on other 2D materials, especially if other electric properties could be identified. One such example is the transition metal dichalcogenides MX_2 (TMDs). This is an indirect-gap semiconductor in bulk, but the monolayer is a direct-gap semiconductor.[42] Later research has expanded these materials into insulators, topological insulators, semi-metals and superconductors.[43,44]

Some materials can be described as layered when looking at their atomic structure, but lack common layered aspects like intercalation. These are materials where bond strengths are of similar strength. They are therefore also not easily delaminated, another common feature of layered materials. Some of these have a high degree of anisotropy, like for example the perovskite-type phases like Ruddlesden-Popper[45] or Aurivillus ceramics.[46,47]

Most of the layered materials have the possibility of intercalating other species within their layers. This alters structural features such as bond length, angle and possibly stacking order, but leaves the framework of the layered structure intact. Intercalation compounds have been especially important in the development of the current high-energy battery technology. The previously mentioned Nobel prize of Li-ion battery is (in truth) the combination of three different intercalation materials: Whittingham demonstrating the principle of the battery with the cathode Li_xTiS_2, Goodenough increasing the voltage by changing the cathode for Li_xCoO_2 and finally Yoshino commercializing the battery with petroleum coke as the anode. Further development has further cemented these materials as a vital part of all possible materials for battery technology.

The oxides used for battery technology are usually on the form A_xMO_2. These have one or more cations *M* located within $(MO_2)_n$, which are layers of edge-sharing octahedra. The *A* is an alkali ion, positioned in between the $(MO_2)_n$ layers with a filling $x \leq 1$ giving either full or partially filled layers. Both different species of *M* or a partially filled *A*-layer can be ordered so that very similar materials are described using different space groups. This makes comparison using general trends of the material difficult.

Delmas et al. suggested a classification to allow for a simple comparison between sim-

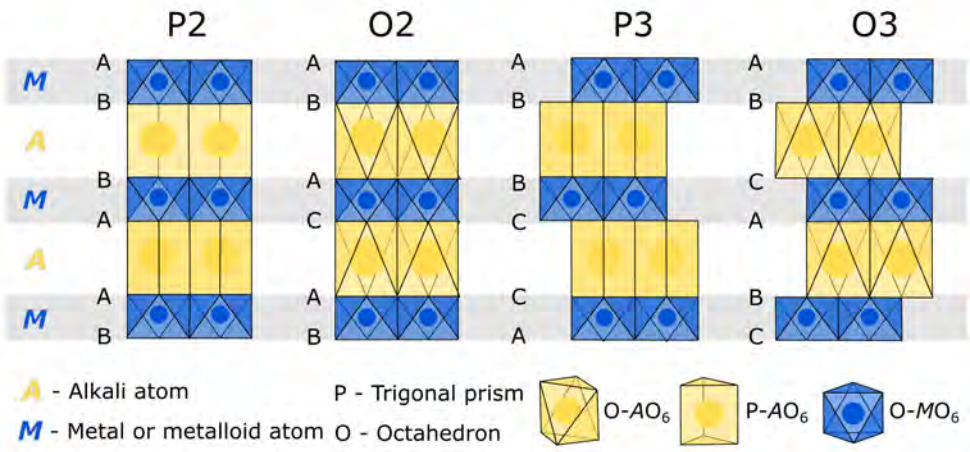

Figure 2.1: Common stacking types for layered oxides, adopted from Bianchini et al.[48]

ilar layered phases. This only uses the coordination of the *A* cation and the number of distinct O-layers.[49] A few examples is shown in figure 2.1. The stacking of the O-layers gives the alkali ion either a prismatic (P) or an octahedral (O) coordination. The number of O-layers with different *x, y*-coordinates along *z* give the number of the phase. The common P2 type has an ABBA stacking of oxygen layers. The A^+ is placed between the AA or BB, giving prismatic coordination. The similar phase P3 has the stacking sequence ABBCCA. Na is placed in AA, giving prismatic *A*-coordination, but the third O-placement is different in *x, y*. If the O-layer is shifted over the Na-layer, the Na-coordination is octahedral, giving the common O3-type with ABCABC-stacking or the less common O2-type with ABACA-stacking. In addition one can get mixed stackings like the OP4, which has a more complicated stacking sequence of ABBACBBCA, giving alternating layers of prismatic and octahedrally coordinated *A*.[50] Sometimes people want to denote distortions of these set phases, denoted with a ', like the common O'3 (or O3'). These could be due to symmetry breaking by secondary phenomena like Na-ordering and Jahn-Teller distortions.[32] To limit the scope of the following discussion, only the Na-based oxides will be considered.

The following section will focus on the P2-type and O3-type phases and requires an in-depth understanding of the Na-sites, shown in figure 2.2. The O3-structure is simple, with all Na-sites in edge-sharing octahedra with the framework octahedra. If only one cation specie is present in the framework, there is only one type of Na-site. However, if we have multiple framework cations, the Na-site can be further differentiated. The simplest P2-

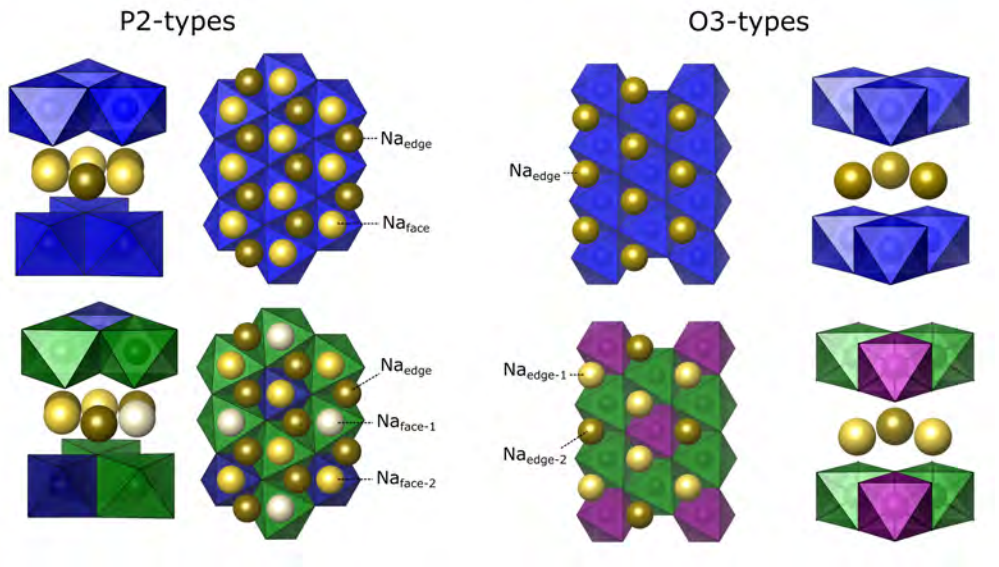

Figure 2.2: Na sites in different types of layered oxides, demonstrating the differentiation from the different *M* in the framework. With only one *M*, the O3 has one Na site (Na_{edge}), while P2 has two types of Na-sites: Na_{edge} and Na_{face}. With more than one type of cation *M*, the ordering of these cations will determine the number of Na-sites. NZTO and NZSO is depicted as examples of materials with further differentiation. The former differentiates the Na_{face} into two types, depending on whether they are coordinated to two Zn-octahedra or one Zn and one Te. In the NZSO, the Na_{edge} is differentiated into two types, two out of the three Na-sites have the Sb-octahedra on the same side and one on the diagonal.

structure has all Na in prismatic coordination, which can either be edge- or face-sharing with the framework octahedra. These can also be further differentiated if there are multiple cation species in the framework, in an ordered fashion. There is no agreed way to refer to these different Na sites between materials, with some using a numbered system,[51] some using the Wyckoff site[25] and some only referring to the type of coordination.[52]

These different phases have been shown to be highly dependent on synthesis conditions, which suggests how similar they are in stability.[27] A phase diagram of Na_xCoO_2 is shown in figure 2.3 and displays regions of different phases depending on Na-content and synthesis temperature. This demonstrates that only certain combinations of Na-ratio and synthesis temperature yield single phases, outside these regions two phases coexist. Of the different phases, the P2-type phase is shown to be stable in high synthesis temperatures and intermediate Na-ratios. Lower synthesis temperatures give either a P'3 or an O'3

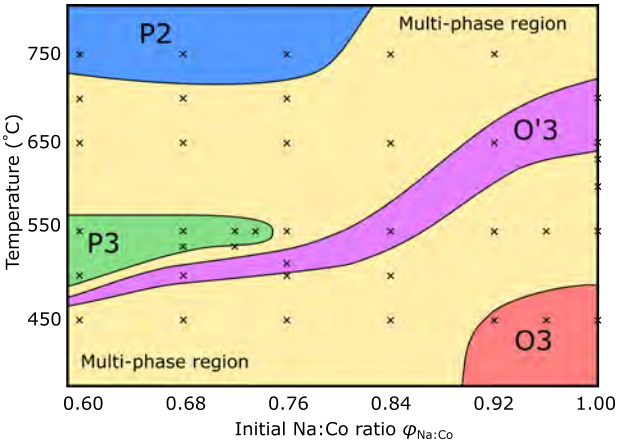

Figure 2.3: Phase diagram for Na_xCoO_2. The multi-phase region has multiple different phases have combinations of the surrouning single phases. Measuring points marked by x. Figure adopted from Lei et al. with permission.[27]

type structure.

This phase diagram was further complicated by Bianchini et al.[32] The synthesis of $Na_{2/3}MO_2$ with M = Mn, Co was shown to be governed by a combination of thermodynamically stable and kinetically limited phases. The synthesis follows a series of fast reactions to metastable phases O3, O'3 and P3, before a slow nucleation and growth of the thermodynamically stable P2-phase. This is understood as the first formation is not limited by composition, and will therefore form the stable O3 $NaCoO_2$ with CoO as an impurity. The formation continues to two Na-poor O'3 and P3 with either CoO, Co_2O_3 or Na_2O as impurities before the slow nucleation and growth of $Na_{2/3}CoO_2$. The first reaction is notably fast for how solid-state reactions are usually conceptualized, with a reaction time of only a few minutes. The mentioned time frame of this nucleation and growth is about one hour, which should be longer than the 16 hours used by Lei et al. for the synthesis used to produce the phase diagram.[27] This theory was validated with the Mn-system.

Phase stability can also be studied by the evolution during electrochemical cycling, as it can be used to relate Na-content to phase stability. Behaviour during cycling is a broad topic, and discussions here will here be limited to the understanding it gives on phases and their relation to the Na-content. The Na-based layered oxides have a tendency for phase transformation through layer glides, especially at low Na concentrations.[30] The phase transformations between the stacking types P2 to O2, OP4 or from P3 to O3 are low energy transitions, which can occur without breaking the strong M-O bonds. Transitions from P2 to

P3 or O3 require a rotation for all MO_6 octahedra, and will therefore require high temperatures to break the M-O bonds. The phase transformations are also effectively driven by the Na-concentration, especially at the lower concentration. When Na^+ is extracted from a phase with prismatic Na-coordination, the O^{2-}/O^{2-} repulsion increases as the prismatic is a very high energy configuration. A layer glide to the lower energy octahedral Na coordination will compensate for the high repulsion. This means v_{Na} is less stable in prismatic sites than octahedral sites, which could explain the existence of the OP4-phase. In this OP4 phase, the Na-ions go into the prismatic layer and the vacancies go to the octahedral layer.

The phase stability is studied by Katcho et al., which suggests the P2 is stabilized over O3 due to the larger interlayer spacing.[53] Another study by Radin suggests the Na-Na repulsion is better balanced in the P2-structure at intermediate concentrations.[54] This is different from the Li-analogue, where the similar Li^+/M^{n+} ionic radius allows for anti-site disorder, leading to a spinel transformation. The large ionic radius of the Na^+ ions prevents this type of defect. Instead, the increased ionic repulsion from the larger atoms gives an increased tendency to Na-ordering for certain fractions, which will be discussed in detail in section 2.2.

A more in-depth discussion on deformations of the Na-layer will be discussed in detail in the following passages, but some discussion of the deformations in the framework layer should also be considered. Roger et al. demonstrate a layer deformation Na_xCoO_2.[55] When Na is placed into the prism's face sharing with the Co-octahedra, this creates a layer distortion in the *z*-direction as a response. The O3-type $NaFe_{1/2}Mn_{1/2}O_2$ characterized by Lu et al showed large variations in the layer distance between adjacent layers, forming a wave-like deformation.[56] This is notable as the Na-layer is full and has only prisms that are edge-sharing with the Fe/Mn octahedra. There must then be other mechanisms for layer deformations than face-sharing Na-prisms or Na-vacancies, but this mechanism was not identified.

When there is more than one specie of framework cations *M*, an additional structural ordering is introduced through their in-layer distribution. One example of this is the tertiary tellurates described by Evstigneeva et al: $Na_2M_2TeO_6$ with M = Ni, Co, Mg.[24] They all demonstrate ordering in the framework layer, where one Te is surrounded by six M^{2+}. There is very little mixing between the sites due to the large difference in oxidation number between Te^{6+} and M^{2+}.[33] However, the stacking of the layers differ depending on the cation *M*. The Ni-type have a layer stacking which gives pure Te-columns and pure Ni-columns, giving a $P6_3/mcm$ space group. The Zn, Co and Mg have a stacking that gives one pure

M-column, and two that are alternating *M*/Te, which is a $P6_322$ symmetry. Later characterization on the Zn-type demonstrates a quite high degree of stacking faults, with 5% following the Ni-stacking.[31]

2.2 Na-ordering and coordination

The Li-based layered materials are generally limited by the small size of the Li-ion allowing for anti-site disorder. Much of the literature on these materials thus deals with problems related to secondary phases.[30] On the other hand, the Na-based materials are mainly limited by the Na-Na interactions of the much larger Na-ion. Na-ordering limits ionic conduction and should therefore be avoided. However, studying Na-ordering in the materials where it is present can be used to understand the influences on the Na, both interactions with itself and the framework. This section will therefore focus on some of the materials in which Na-ordering have been observed, before moving on to Na-dynamics in the following section.

Toumar et al. simulate all ordered states for all oxides with a single transition metal *M* in O3-Na_xMO_2.[57] They find orderings that are a ground state for at least one *M* for eight different Na-fractions *x*, with x = 1/3 and 1/2 being the only ground states for all systems. Some ground states have homogenous Na/v_{Na} distribution, but other exhibit clear vacancy clustering in lines. It is therefore argued that electrostatic Na-Na interactions cannot be the only influencing factor on the Na-order. They also investigate translations of the Na-orderings between layers, and find a small, but non-negligeable influence from the stacking sequence.[58]

The P2-phase is slightly more complicated. There are now Na-coordination polyhedra that are either edge- or face-sharing with the framework octahedra, Na_e and Na_f. Toumar et al. demonstrate no ordered states but found that the calculated difference between the two Na-sites in the P2-Na_xMO_2 varies considerably along the different transition metals. The difference between the Na-sites in Co and Ni was the lowest, so these materials should have the Na-lattice with the largest influence from configurational entropy.[57]

The following section will mainly discuss Na ordering in the three transition metal versions with the three *M* with the most reported ordered states: Na_xCoO_2, Na_xMnO_2 and Na_xVO_2, with some focus on their partially substituted derivatives. Some discussion on other oxides, with an emphasis on the tellurates, is then provided later.

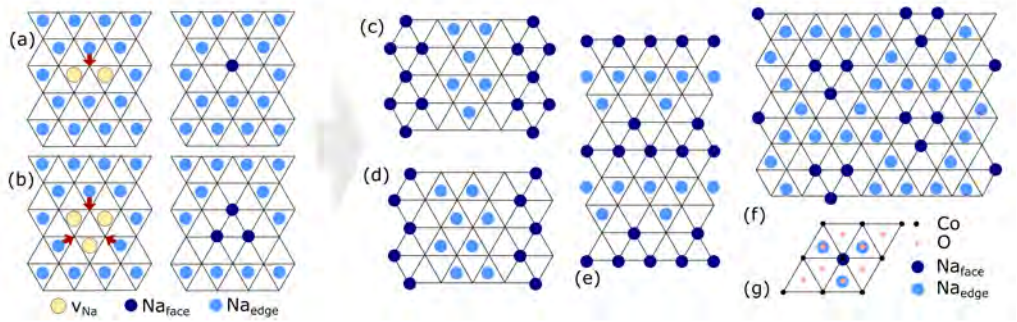

Figure 2.4: Demonstration of the meaning of the (a) di-vacancy and (b) trivacancy model, adapted with permission from Willis et al.[52] These are then used to demonstrate suggested Na-orderings for $x = 0.75$ (3/4) with (c) "diamond" structure,[60] (d) "zigzag" structure,[66] (e) "stripe" pattern[65] and (f) "droplet" structure.[55] (g) Placement of all atoms in the grid, with Co in the corners, Na_f directly above, Na_e in the tetrahedral void between. Picture adapted from Meng et al. with permission.[61]

Na_xCoO_2

Na_xCoO_2 is an often studied material, with more special properties like the superconducting state in the hydrated form,[68] but also as the layered oxide has the most amounts of ordered Na-substructures. The Na-content is inherently linked to the electronic structure of Na_xCoO_2, as this is a direct way to tune the Co valence.[69]

The space group of Na_xCoO_2 is $P6_3/mmc$. One Na position is face sharing with two CoO_6 octahedra, Na_f, and one is edge sharing with six, Na_e. The former is slightly less favourable due to the increased ionic repulsion to Co^{3+}/Co^{4+}. Due to the higher probability of the Na_e, a common way to characterize the Na-structures is to imagine a lattice with Na_e and then impose vacancies. The vacancies are compensated by moving adjacent Na into the Na_f-positions, as shown in figure 2.4, which distributes the charge of the vacancies over a larger area. These are described by the number of vacancies that are compensated: di-vacancies have one Na_f, and tri-vacancies have three.

A selection of Na orderings for different Na/v_{Na} is shown in table 2.1, which includes both experimental[55,60,63,65,70] and theoretical[59,61,71] work. While the structure at $x = 0.5$ is generally agreed on, there are many suggestions for different structures at e.g. $x = 0.71$,[59,61,63,64] 0.75[55,59,60,64–66] and ≈0.83.[55,59,64,66,67] Meng et al. describe the $x = 0.75$ fraction to have a perfect balance between Na^+-Na^+ repulsion and the energy difference of the sites, making

Table 2.1: Ordering patterns of Na in Na_xCoO_2. Na_f is face sharing with CoO_6, Na_e is edge sharing. The di-, tri and quadri-vacancies described by Roger et al. acre created by moving one, three, six and ten Na to the Na_f position in a triangle shape, distributing the charge of the of vacancies in a Na_e grid over a larger area. An example of the di- and trivacancy is shown in figure 2.4.

x	Fraction	Lattice	Supercell	Comment
0.11	$1/9$	3×3 triangular Na_f	$\sqrt{3}a \times \sqrt{3}a$	[59]
0.11	$1/9$	3×3 triangular Na_e	$\sqrt{3}a \times \sqrt{3}a$	[60]
0.20	$1/5$	Na_e	$\sqrt{7}a \times \sqrt{7}a$	[59,60]
0.25	$1/4$	2×2 triangular Na_e	-	[59,60] 0.1 meV from ground state.
0.3	$3/10$	Na_e		[55,59]
0.3	$3/10$	Na_f in layer 1 Na_e in layer 2		[59]
0.33	$1/3$	3×3 triangular Na_e	$\sqrt{3}a \times \sqrt{3}a$	[59,60]
0.40	$2/5$	Na_f/Na_e	-	[59] 0.6 meV from ground state.
0.50	$1/2$	Closely packed di-vacancies of 1/1 Na_f/Na_e	$\sqrt{3}a \times 2a$	[55,59–61]
0.5 - 0.71		Divacancies		[55]
0.54	$7/13$	Zigzag and rows of Na_e, rows of Na_f		[61] Combinations of 0.5 and 0.6 orderings at $(2+5)/(4+9)$.
0.56	$5/9$	Zigzag and rows of Na_e, rows of Na_f		[61] Combinations of 0.5 and 0.6 orderings at $(2+3)/(4+5)$.
0.57	$8/14$	Zigzag and rows of Na_e, rows of Na_f		[61] Combinations of 0.5 and 0.6 orderings at $(5+3)/(9+5)$.
0.60	$3/5$	1/2 Na_f/Na_e	$\sqrt{7}a \times \sqrt{7}a$	[59]
0.60	$3/5$	Zigsag of Na_e, Row of Na_f	$\sqrt{7}a \times \sqrt{7}a$	[59]
0.67	$2/3$	-	3×1	[59]
0.67	$2/3$	Large zigzag of Na_f, with Na_e droplets between		[61]

Table 2.1: Cont. ordering patterns of Na in Na_xCoO_2.

x	Fraction	Lattice	Supercell	Comment and source
0.67	$2/3$	-	$\sqrt{12}a \times \sqrt{12}a \times 3c$	[62]
0.71	$5/7$	$3\times$Na$_e$2-v$_{Na}$-2$\times$Na$_f$-v$_{Na}$	$\sqrt{13}a \times \sqrt{13}a$	[59,63]
0.71	$5/7$	-	$\sqrt{12}a \times \sqrt{12}a$	[64]
0.71	$5/7$	Large zigzag of Na$_f$, with Na$_e$ connected droplets between	-	[61]
0.75	$3/4$	$n\times$Na2-v$_{Na}$-3$\times$Na1-v$_{Na}$, "diamond" shape	$\sqrt{3}a \times 4a$	[59,60] $\sqrt{3} \times (n + 5)/2, n = 3$
0.75	$3/4$	Divacancy droplets	$\sqrt{13}a \times \sqrt{13}a$	[64]
0.75	$3/4$	Tri-vacancies with Na$_f$/Na$_e$	$2\sqrt{3}a \times 2\sqrt{3}a$	[55]
0.75	$3/4$	Stripes	$2 \times 2\sqrt{3}$	[65]
0.75	$3/4$	"Zigzag" structure with 1/1 Na$_f$/Na$_e$	$4a \times \sqrt{3}a$	[66]
0.75 - 0.85		Tri-vacancies		[55,61] $10/13$, $13/16$ and $16/19$ mentioned by Meng et al.
0.80	$4/5$	$n\times$Na$_e$-v$_{Na}$-3$\times$Na$_f$-v$_{Na}$		[59] $\sqrt{3} \times (n + 5)/2, n = 5$.
0.80 - 0.85		Quadri-vacancies		[55,66] Multiple stable phases found for 0.8.
0.83	$5/6$	$n\times$Na$_e$-v$_{Na}$-3$\times$Na$_f$-v$_{Na}$		$\sqrt{3} \times (n + 5)/2, n = 7$.[59]
0.83	$5/6$	-	6×1	[67] Model includes twinning, which can be wrongly interpreted as 6×6.
0.84	$11/13$	Trivacancy droplets with 5/7 Na$_f$/Na$_e$	$\sqrt{12}a \times \sqrt{12}a$	[64] Either in-phase or out of phase stacking.

multiple structures available.[61] A selection of the suggested structures is shown in figure 2.4. This is also true for $x \approx 0.83$,,[55] but here multiple fractions at approximately the same concentration occur. This results in different structures from very small variations in the Na-content. The same material is shown to have a square-to-stripe reordering for the Na droplets in $x \geq 0.78$ near room temperature.[72] The di-vacancy droplets are either disconnected islands (square) or connected channels (stripe). This is connected to a change in diffusion type from 2D to 1D, as the ions must move in restricted paths due to the Co-layers, which will be discussed in section 2.3. Hinuma et al. suggest that the order-disorder transition temperatures are revealed to be below room temperature.[71]

Berthelot et al suggest three influences on the Na-structure: The electrostatic repulsion which tries to maximize the Na^+/Na^+ separation within the layer, the increased repulsion between the face sharing $Na_f{}^+/Co^{3+}$ and electron-electron interactions in the Co-layer.[73] Roger et al. suggest that the Na ordering is governed by pure electrostatics, and propose charge droplets as the structure.[55] The one remaining question is why the Na_xCoO_2 has so many more ordered states than other transition metal oxides. If only electrostatics govern Na-Na interactions, one would expect to see similar mechanisms in other transition metal oxides.

Na_xVO_2

The O3-type Na_xVO_2 was studied with $1/2 \leq x \leq 1$. The material goes from an O3 phase to an O'3.[74] The structure is revealed to go through a distortion between $1/2 \leq x \leq 2/3$. O3-type Na_xVO_2 was shown to have a Na-ordering for x = 1/2, with a zigzag of Na_e (the only available Na site in the O3 type). The Na was shown to be displaced due to Na^+/Na^+ repulsion, which increases these distances. There is a displacement of V from the octahedral centre giving a slight deformation of the layers. The $Na^+/V^{3/4+}$ repulsion likely plays an important role, as the v_{Na} is found to be next to the shortest V-V distances while Na is found between the longest.

P2-Na_xVO_2 was shown by Guignard to be ordered at x = 1/2, 5/8 and 2/3. Na^+ is perfectly ordered to decrease Na-Na repulsion,[75] for example with the zigzag ordering of alternating Na_f and Na_f for x = 1/2. Both of these suggest that as for Na_xCoO_2, the electrostatic interactions dominate the Na-structure.

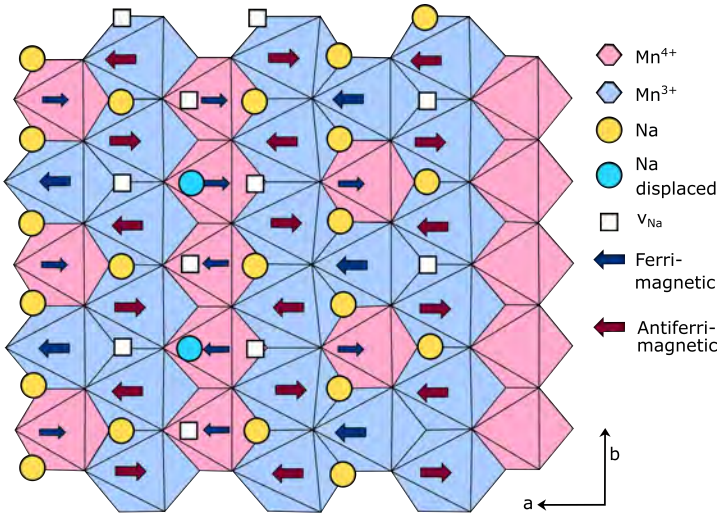

Figure 2.5: Superstructure of O3-$Na_{5/8}MnO_2$, with Na/v_{Na} ordering, shown as yellow circle and white squares respectively, and Na-deformations, shown as blue circles. The Mn layer includes charge ordering, with $Mn^{3+}O_6$ as blue hexagons and $Mn^{4+}O_6$ as red. The magnetic spin stripe ordering has ferrimagnetic stripes as blue arrows and antiferrimagnetic stripes as red. Figure adapted from Li et al.[76]

Na_xMnO_2

The Na_xMnO_2 has a direct interest as a battery material, with a high working potential vs Na^+/Na and high capacity. However, it suffers from phase transformations that happen at high voltages and at low Na content. The phase transformations happen by a simple O-layer glide. Contrary to the Na_xCoO_2 and Na_xVO_2, the Na_xMnO_2 has other influences dominating the Na-structure. The Mn^{3+} has one of the largest Jahn Teller distortions of transition metals, and forms anti-ferromagnetic atomic stipes with the non-Jahn-Teller active Mn^{4+}.[76] This means that Na ordering is a complicated combination of Na-ion ordering, charge ordering, magnetic ordering and cooperative Jahn Teller distortion. This is quite different from other materials where electrostatics is the dominant factor. Li et al. show that x = 5/8 in the O3-type has a complicated Na-structure. There are striped ordering of of Mn^{3+} and Mn^{4+}, anti- and ferrimagnetic ordering with Na^+/v_{Na} and Na-displacements, as seen in figure 2.5.[76]

Apart from this study, most focus on the Mn-types is based around suppressing the ordering by Mn-substitution rather than a focus on characterizing the ordering type as for the Na_xCoO_2. The x = 2/3 has been demonstrated to have a $a \times \sqrt{3}a \times c$ superstructure, in line with the orthorombinc phase (*Cmcm*) and a monoclinic phase (*C2/n*).[77] This superstructure

was connected to the distortions from the Jahn-Teller active Mn^{3+}. The distortions can be suppressed by very slow cooling, allowing more Mn vacancies. More Mn^{4+} is then present and thus suppresses the cooperative Jahn-Teller distortion. Lui et al. show that the Jahn-Teller distortion from the Mn^{3+} causes local strain upon desodiation. The local strain can be compensated either by Li- or Mg-substitution. Li substitution also keeps the Na^+/v_{Na} disordered upon cycling.[78] The Mg substitution on the Mn site smooths the steps in the charge/discharge curve and keeps the high capacity.[77] This is achieved by increasing the average oxidation state towards Mn^{4+}, and dilutions of the Mg^{3+}-centers.

Loung et al. describe that when a Na-ion is removed from the full $NaMnO_2$, it is accompanied by a polaron at the third nearest Mn-octahedra to the vacancy, implying Mn^{3+} is oxidized to Mn^{4+}.[79] This migrating polaron then interferes with Na^+ diffusion. At lower Na-concentrations, Na-diffusion is easier due to the lower activation energy compared to the Na-rich materials. The Na-ions favour the Na_{edge}-prism at high and low concentrations, but the intermediate is a stable mix between the two. This is due to the presence of both Mn^{3+} and Mn^{4+} increasing the layer distance, giving a 2:1 ratio of Na_e to Na_f. The same is true for Co-substitution, which lowers the energy differences between orderings and reduces the number of phase transformations observed.[80] This simulation probes different substitution concentrations at x = 1/2. This is particularly interesting due to the strong ordering tendency at this Na-content. The influence through the face-sharing position is demonstrated, where Mn is shown to increase the Na_f energy, while Ni and Fe decrease compared to Co.

Dang et al. demonstrates that $Na_2Ti_3O_7$ coating on $Na_{0.67}Mn_{0.67}Ni_{0.33}O_2$ can suppressed both Na-ordering and the P2-O3 transition.[81] This is due a tiny amount of Ti^{4+} substitution along the interphase.

A different ordering is found in the P2-types of $Na_{0.62}Mn_{0.75}Ni_{0.25}O_2$ (x = 0.62) and $Na_{2/3}Mn_{2/3}Ni_{1/3}O_2$ (x = 2/3) by Gutierrez et al.[82] The face sharing Na-site can be distinguished by the Mn/Ni coordination. One type between two Mn and one type between one Mn and one Ni (analogous to the NZTO shown in figure 2.2). These sites are not energetically equivalent, as Na is likely to avoid the increased electrostatic repulsion at the Mn^{4+}-Mn^{4+}, found in x = 0.62. There is a superstructure of $\sqrt{3} \times \sqrt{3} \times 1$ from Ni/Mn intralayer ordering which is preserved for both ratios. The difference between the two is from a larger number of the high energy Mn-Na_f-Mn for x = 0.62, which Na avoids and the low energy electrostatic Na-ordering (a large zigzag type ordering) is disrupted.

2.3 Na-dynamics and disorder

Studies on the ordered Na_xMO_2 typically address issues of fundamental nature, like interactions, ordering of atoms and vacancies, and intercalation reactions (and reactivity). The latter has in some cases given rise to spectacular findings like the existence of superconductivity in $Na_xCoO_2 \doteq yH_2O$ ($x \approx 0.35$, $y \approx 1.3$),[68] which lead to more detailed explorations of phase diagrams and emergent properties. The main interactions Na can be determined from looking at the site distribution, and thus the ordered materials can give insight into the whole material class.

On the other hand, the disordered states are of high relevance for understanding Na-ion dynamics, a key parameter when considering ionic conductivity. The requirement of a good ionic conductor is mobile species that have vacant sites (or intermediate sites) with a low activation energy between them.

Some structural deviations from the general structures shown in figures 2.1 and 2.2 are worth noting before going into the studies of the Na-dynamics. Smirnova et al. demonstrate an off-centering of the Na in the O3-type $Na_{0.8}Ni_{0.6}Sb_{0.4}O_2$.[83] Variable temperature NMR between 197-288K reveals two types of Na-sites: the centred *3b* and the off-centred *18g*. The ratio of the Na-environments changes with temperature, with a 2:1 ratio from 215 until it the ratio changes to 4:1 at 230K. The driving force for the offset *18g*-site is speculated to be as a compensation of adjacent vacancies in the partially filled layer. Bianchini et al. demonstrates a disordered Na-sublattice in NZTO, without much influence from the ZnO_6 and TeO_6 on the Na-ordering.[48] They also demonstrate that the pattern has a wide range of configurations for the Na-lattice at room temperature, giving a high mobility of Na-ions.

The diffusion pattern for both the quasi-1D and 2D type can be understood locally as the stabilization of multi-vacancy clusters over both Na_e and Na_f (figure 2.7) as opposed to isolated vacancy hopping. Due to the similarity to the Li-cathode Li_xCoO_2, there have been a lot of studies on the Na-dynamics in Na_xCoO_2. However, Na_xCoO_2 is not analogous to Li_zCoO_2 in terms of ionic conductivity. This is due to the ordered states described in the previous section, which limits ionic conduction. Simulations by Mo et al. demonstrated this multi-vacancy cluster mechanism for P2 Na_xCoO_2, which gives the honeycomb sublattice with very low activation energy for Na-diffusion (figure 2.6).[84] This is demonstrated to be different from the O3-phase, which has the di-vacancy mechanism. This phase has lower ionic conductivity than P2 for all x, except at very high Na-concentrations, where the Na-Na repulsion limit conduction in the P2 phase.

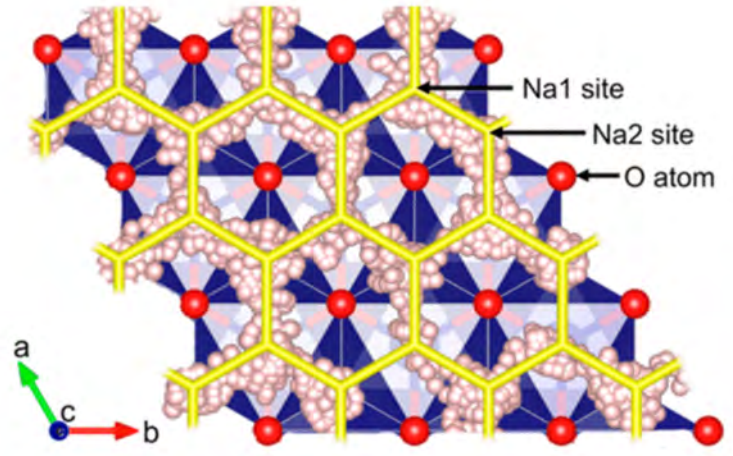

Figure 2.6: Pathway for migration in $Na_{0.56}CoO_2$. Figure is from Mo et al.[84] and reproduced with permission.

Weller et al. has performed NMR relaxation measurements on $Na_{0.8}CoO_2$ at a 7T magnetic field.[85] Between 291K and 292K there is an abrupt change in the magnetization recovery rate, but no change in the narrow peak. A reappearance of satellite peaks demonstrates that this is not a structural change. Instead, this is explained as a "melting" of the Na-layer into a 2D-liquid state, which is known from Na^+-dynamics in β-alumina.[86] Another study on $Na_{0.8}CoO_2$ by Wills et al. shows two significant temperatures by XRD, QENS and *ab-initio* MD.[52] At 290, the material goes from a partially disordered stripe pattern, while at 370K they observe a melting of the 2D layers. Transitions at the approximately same temperatures for x = 0.7 was demonstrated by Medarde et al. using neutron diffraction.[87] Below 290K, the Na-ions are static, with a transition to quasi-1D diffusion along the a-direction at 290K and full 2D diffusion at 400K. The apparent discrepancy in the explanation from Wills, Medarde and Weller is purely due to slight differences in the meaning of the terms used in different fields (which changes the length scale probed). 2D in NMR is Na-jumps along both the x and y-direction, while this is observable as the "partially disordered stripe pattern", which still has symmetry and a fully disordered state is first reached at 370K.

Shu et al. have shown that the diffusion of different P2 Na_xCoO_2 phases are strongly related to the Na-ratio x.[63,88] The average diffusion coefficient is shown to be up to five times higher for $x > 0.5$ than for $x < 0.5$. This demonstrates a difference from the diffusion species, where the former has v_{Na}, following the multi-vacancy hopping (figure 2.7), and the latter has Na^+ as the diffusing species.

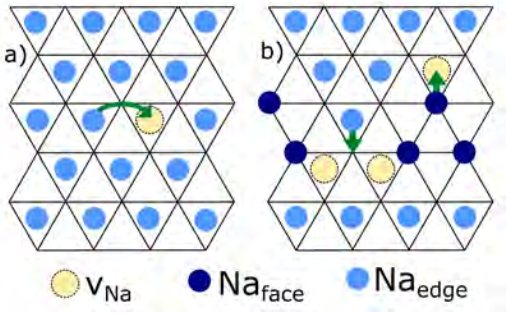

Figure 2.7: Comparison between Na diffusion mechanisms: a) isolated vacancies hopping between only the Na_{edge} (*2d*) and b) multi-vacancy hopping between Na_{edge} and Na_{face} (*2b)*), adopted from Willis et al. and reproduced with permission.[52]

Carlier et al. demonstrated the difference in the Na-coalescence between P2 and P3-type Na_xCoO_2 phases.[26] At high temperatures, the former Na peaks coalesce into a single second-order quadropolar line shape. The latter changes towards a Gaussian shape, as the exchange is between sites symmetric in the ab-plane but antisymmetric in the c-direction. This leads to a cancellation of the V_{zz} contribution and suppression of the quadropolar line shape. P2-$Na_x[Li_yNi_zMn_{1-y-z}]O_2$ display the same coalescence, where the Na_{edge} and Na_{face} mix into a single average gaussian.[89]

The influence of Na-Na correlations and disorder in the Na-lattice between Na_e and Na_f was investigated by Sau and Kumar for a different family of oxides. Ion conduction in Na_2M_2TeO2 with *M* = Ni, Co, Zn and Mg was therefore shown to be highly correlated.[28] They also show that the two Na_f sites are distinguished by the coordination to different cations in the framework layer, in turn showing a clear influence on the energy landscape and the population profile. One of the Na_f-sites in both possible stacking variants *$P6_322$* and *$P6_3/mcm$* are virtually unoccupied due to the high energy of the site. Further references to Na_f is therefore referring to the other Na_f: placed in the mixed column (*M*/Te) for the *M* = Zn, Co, Mg (*$P6_322$*) and the pure Ni-column for *M* = Ni (*$P6_3/mcm$*).

The energy landscape was further investigated by over- and underloading the layers in the *M* = Ni variant, which shows a clear change in the population profile towards the Na_f.[36] The same was shown by tuning the Na-Na repulsion, where the higher ionic conductivity was increased by an order of magnitude for the lower short-range ionic repulsion.[51] This experiment tunes physical parameters such as the Na-Na repulsion and is therefore only done to demonstrate the influence of ionic radius on the ionic conductivity. They also

demonstrate the absence of the disordered Na-distribution over Na_e and Na_f without ionic repulsion, where the population is set to the more energetically favourable Na_e.

^{23}Na NMR of the $Na_{2/3}Ni_{1/3}Ti_{2/3}O_2$ show a relatively symmetrical ^{23}Na NMR peak shape at room temperature, suggesting a fast Na^+ motion.[90] There is no quadropolar line shape at lower temperatures, which is suggested to be due to a dominance of magnetic susceptibility anisotropy and paramagnetism over quadropolar interaction. Chen et al. compare the ionic conductivity of this Na composition with a Na-poor (x = 5/9) and a Na-rich (x = 7/9) by QENS and MD.[91] They demonstrate that Na migrates between the Na_e to Na_f through the faces of the prisms. Simulations show a decrease in diffusivity with increasing Na-content, attributed to decreased vacancies. However, measures of ionic conductivity using QENS show an increase for both the Na-poor and -rich compared to the pristine material (x = 2/3).

The dynamics can also be characterized by NMR relaxometry, explained in depth in section 3.3.2. Two articles by Li et al. characterizes Ga-substituted NZTO[29] and pure NMTO[92] by ^{23}Na NMR relaxometry and electrical impedance spectroscopy (EIS). The ionic conductivity of the two is found to be 0.63 and 0.23 mS cm^{-1} at room temperature. Variable temperature EIS find activation energy of 0.32 and 0.34 respectively. Another EIS study on NZTO from Li et al. gives an activation energy of 0.29 eV for pure NZTO.[25] They also show that samples with a phase fraction of O'3 have a larger activation energy, both when this is achieved from lower synthesis temperatures and when the Na content is increased.

NMR relaxometry is not the same as the total conductivity, because it excludes macroscopic effects like grain boundary. The results of NMR relaxometry are instead compared to the calculated bulk conductivity from EIS, finding the order of magnitude to be correct. NZTO have 0.12 eV and 0.14 eV and NMTO have 0.18 eV and 0.23 eV from NMR and EIS, respectively. However, the activation energy from NMR is likely underestimated, as they are taken from the low-temperature side of the T_1 vs T curve, where the slope is reduced by any degree of correlation (deviation from free movement, explained in section 3.3.2). The slope of the high-temperature region yields much higher activation energy: $\approx$ 0.26 (NZTO) and 0.4 eV (NMTO).

Li et al. also demonstrate the effects of the Ga-substitution of NZTO, which is compensated by a reduction in the Na-content on the formula $Na_{2-x}Zn_{2-x}Ga_xTeO_6$. They find the sample with x = 0.1 showing a maximum: Full ionic conductivity of 1.1 mS cm^{-1}, giving an activation energy of 0.27 eV. The bulk conductivity is even more reduced, with of 0.05 eV (NMR) and 0.07 eV (EIS). They suggest the discrepancy is from a slight underestimation by NMR, which is correct as the low-temperature side is still used. However, it is clear that

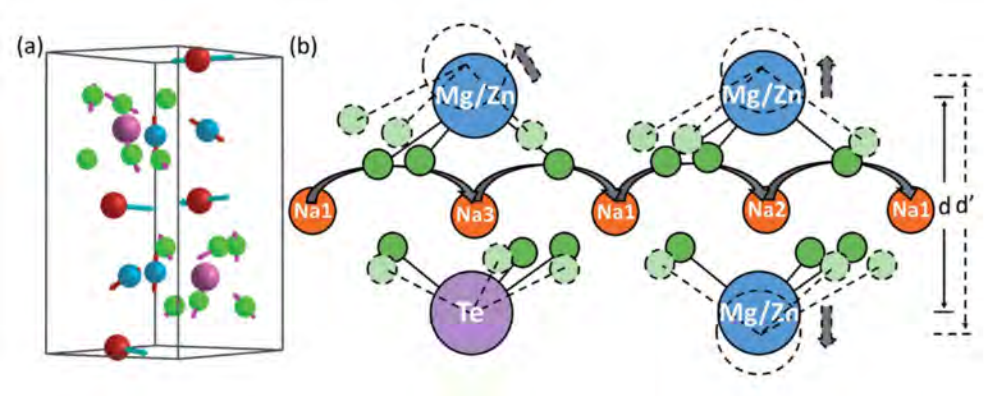

Figure 2.8: Phonon modes for NZTO and NMTO reported by Huang et al. Reproduced with permission.[93]

the high-temperature slope is also decreased significantly, suggesting that reduction in E_a from Ga-substitution is a real feature.

Wu et al expanded the discussion of Ga-substitution by demonstrating the different effects on grain boundary and bulk conductivity.[94] The grain boundary resistance is found to be two orders of magnitude lower compared to bulk in unsubstituted NZTO. They use the established model of grain boundaries from oxides.[95,96] The grain boundary is composed of the core (crystallographic mismatch zone) and two adjacent space charge layers. The core will carry an electric charge at thermal equilibrium due to excess oxygen vacancies, as established for oxides.[95,96] A Schottky barrier is established by the depletion of Na-ions in the space layer, which compensate for the oxygen vacancies. This lowers ionic conductivity across the barrier. The grain boundary resistance is significantly improved by Ga-substitution, as it introduces an effective positive charge into the lattice. This reduces the charge density in the space-charge layer, decreasing the Schottky barrier height. The ionic conductivity is improved from 0.57 to 0.83 mS cm^{-1} for a substitution of only $x = 0.05$, which is a factor of 1.5.

Huang et al. have simulated the local differences in activation energies of the different local diffusion paths in both NZTO and NMTO.[93] They show a slightly lower activation energy for the Na_e-$Na_{f,\ Te+Zn/Mg}$-Na_e diffusion path, which has a 0.23 eV and 0.27 eV E_a from NEB calculations in NZTO and NMTO, respectively. The other diffusion path Na_e-$Na_{f,\ 2xZn/Mg}$-Na_e has a 0.33 and 0.39 eV activation energy, which is less common but not unaccessed. They also reveal the role of the framework cations, where the Na-conduction

is helped by a cooperative ion vibration mechanism. When the Na-ions hop to the Na_f sites between the Mg/ZnO_6 or TeO_6 octahedra, the octahedra vibrate away or towards each other to enlarge or shrink the diffusion channels, as shown in figure 2.8. They connect the superior conductivity of NZTO to the larger interlayer spacing and the softer phonon band centre and therefore suggest that substitution with larger cations leads to better conductivity. This has previously been demonstrated by increasing lattice spacing by small concentrations of Ca-substitution in NZTO, increasing ionic conductivity.[97]

2.4 Solid-state electrolytes and its competitors

This work focuses on material-specific properties like ordering, Na-structure and mobility of certain layered oxides. This is to gain insight into the ionic conductivity of the layered Na-conductor NZTO, understand the limitations and thus create strategies for improvement. This section will review this material class up against some of the main alternatives for use in batteries, which should give some insight into the progress needed for the development of NZTO, but also of SSEs as a whole.

Goodenough and Kim suggest that an electrolyte needs an ionic conductivity of at least 10^{-3} S cm^{-1} and an electric conductivity of 10^{-10} at room temperature.[98] Additionally, the electrolyte will need a large electrochemical window, a large thermal stability window, no reactivity towards any of the other battery components, low cost and be non-hazardous for the environment and human health. Some groups of alternative electrolytes are inorganic solid (the main focus of this work), aqueous and non-aqueous LE, solid polymer electrolytes, quasi solid-state electrolytes and organic ionic plastic electrolytes, shown in figure 2.9.[99] Of these groups, it is clear that the aqueous and non-aqueous LE has the best ionic conductivity at RT, usually some orders of magnitude over the value demanded by Goodenough ($\approx 10^{-1}$ S cm^{-1}). SSEs are however preferred in the case of high temperatures, due to their stability and high ionic conductivity, and are already commercialized. However, next-generation batteries require use at ambient temperatures, for which ionic conductivity must be increased. In addition, there are concerns with scale-up (when taking the material from the lab to industrial scale) for example in regards to processing. This section will review the advantages and challenges for the alternative candidates for SSE, focusing on the more mature technologies of LE, inorganic solid and solid polymers.

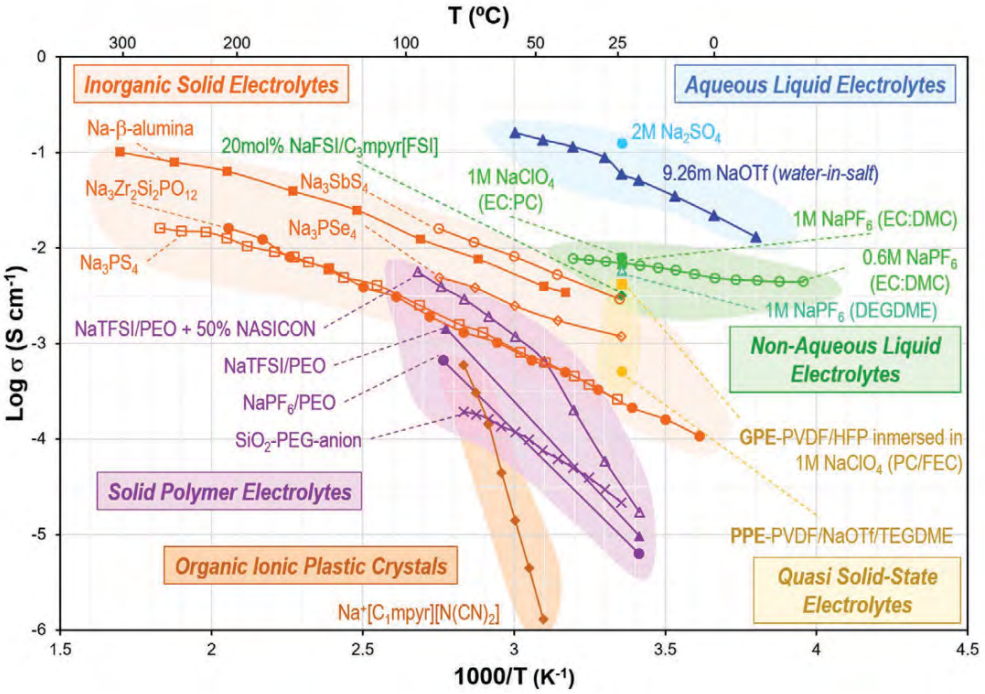

Figure 2.9: Summary of temperature dependent ionic conductivity of a few Na-based electrolytes. Figure reproduced with permision from Goikolea et al.[99]

2.4.1 Liquid electrolytes

The standard for LIB is to use Li-salts, usually $LiPF_6$, combined with different solvents. The same recipe is being developed for NIBs, with Na-salt being an area of immense interest. Some possibilities are $NaPF_6$, $NaClO_4$, NaTFSI, NaFSI, NaFTFSI with two first being the better performers.[100] The salts are relatively cheap and have good electrochemical behaviour, but exhibit some explosion hazards. The solvents are usually mixes of EC, PC or DEC.

The solid electrolyte interphase (SEI) is a very important field in all battery research. This is where the electrolyte is reduced on the anode surface, forming a passivating layer which hinders further degradation (figure 2.10).[102] The cathode has an analogous layer, the cathode electrolyte interphase (CEI), from the oxidation of solvents. The SEI layer remains a matter of debate, with multiple formation mechanisms proposed. The Na-system is even less understood.[99] With the functional electrode protection it can provide, this knowledge gap will need to be addressed before further use.[101]

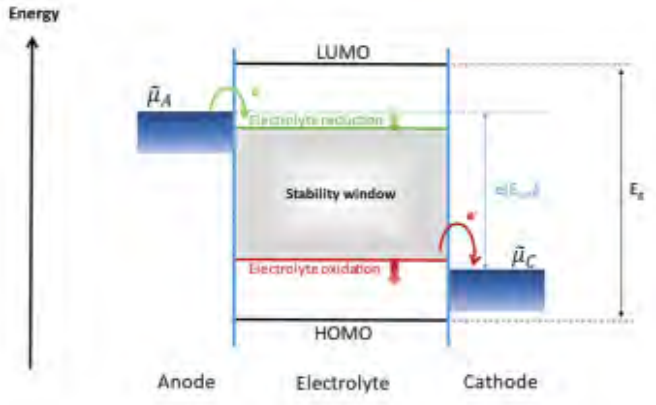

Figure 2.10: Electrolyte stability window defined in terms of potential of electrolyte reduction at negative potentials, and of the potential of solvent oxidation at positive potentials. Figure adapted from Munoz-Marquez et al and Peljo et al. with permission.[101,102]

One of the large drawbacks of the LEs is their flammability. They can both ignite and accelerate a battery fire.[103] In addition, the breakdown of the ionic salt and other components lead to emissions of toxic gasses, hydrogen fluoride (HF), hydrogen cyanide (HCN) and carbon monoxide (CO), posing a significant health hazard.[104]

Aqueous electrolytes are also of interest, with the advantages of low cost, good safety and low environmental impact compared to their organic solvent counterparts. The recipe is similar to non-aqueous types, with a combination of some type of salt like Na_2SO_4 and water as the solvent.[105] The main limitation is the narrow voltage window of 1.23V, which is dictated by the electrochemical decomposition of H_2 and O_2. The stability can be significantly increased, for example by changing the ratio of salt to water, giving a so-called ”water in salt”.[106] This leaves no ”free” water outside the solvation shell of the dissolved ions, increasing stability to 2.5V.[105] As $NaPF_6$ will create HF in contact with water, this recipe must use other salts like NaTFSI and $NaCF_3SO_3$. These electrolytes might also become a problem in combination with intercalation cathodes, which become water sensitive at lower Na-contents.[107–110]

Ionic liquids are another technology that could expand the use of LEs. They are especially interesting due to their wider electrochemical stability window, which could both enable metal anodes and high-voltage cathodes.[111] They are also not flammable, giving increased battery safety.

2.4.2 Polymer-based and composite solid state electrolytes

One material type that is generally viewed as a simpler transition for SSEs is polymer-based electrolytes, which combine the ionic salt with a flexible polymer matrix. These increase the temperature stability window compared to their liquid counterpart. The main drawback is the low ionic conductivity at room temperature. The standard salts are the same as for the liquid electrolytes ($NaPF_6$, NaTFSI, NaFSI) and combined with a polymer like polyethylenoxide (PEO).

Another strategy is to combine a polymer with an inorganic material, which improves ionic conductivity by decreasing the crystallinity of the polymer. This has been demonstrated for PEO combined with NaSICON[112,113] and Ga-substituted NZTO.[114] Both improved ionic conductivity compared to the inorganic material. In addition, the polymer matrix helps with electrode contact, one of the major drawbacks of the inorganic SSEs.

2.4.3 Layered oxides

This thesis work is related to layered oxides as the material class for SSEs. They have been discussed in depth in previous sections and will therefore only be covered briefly here. The structure is similar to the layered cathodes but uses framework cations without adjacent oxidation states to ensure negligible electric conductivity. Some of the hope here is to exploit the vast knowledge of research and processing of the cathode materials. Layered oxides are generally less moisture sensitive than the other electrolytes, especially for higher Na-contents which are the ones usually investigated for use as SSEs.[107–110] This would vastly simplify processing, which usually now requires dry rooms or inert atmospheres.

A major issue with the layered oxides is the electrochemical stability window. While early predictions used electrochemical stability as a selling point, recent results of poor cycling performance challenged this view.[115] Calculations on NMTO and NZTO found the electrochemical stability window to be 1.41 and 0.98V respectively. However, the decomposition products are electrically insulating, meaning a good SEI could be formed and extend battery life.[93] This demonstrates the necessity of studying the SEI and CEI layers for improvements of all possible electrolytes. The electrochemical stability window of the layered oxides is higher than for sulfides, but lower compared to NaSICON structures.

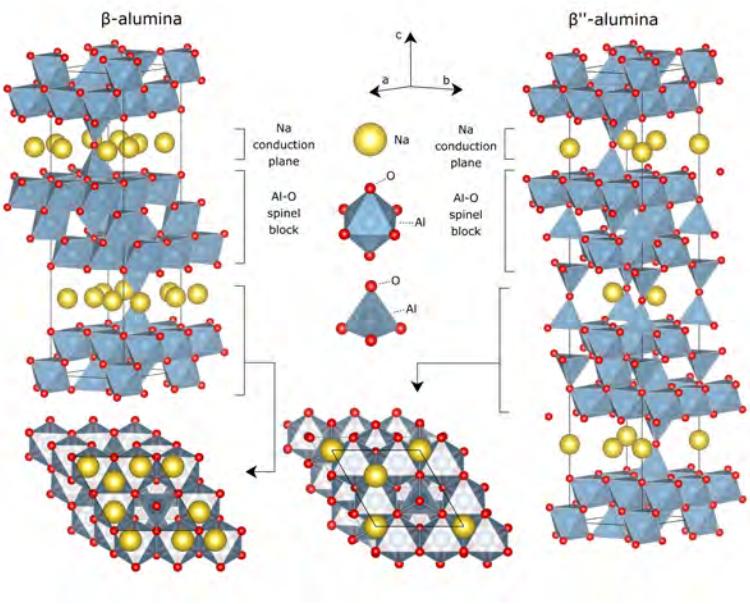

Figure 2.11: Structure of β-alumina (space group *P6$_3$/mmc*) and β"-alumina (space group *R*$\bar{3}m$). Reproduced from Chi et al. with permission.[120]

2.4.4 Aluminates

One of the earliest described Na-SSE is β-alumina. The discovery of the fast ion transport was a milestone in the development of solid-state electrolytes.[116] β-alumina has a measured ionic conductivity in the 10^{-2}Scm^{-1} range at room temperature, which makes it a great alternative for a SSE.[117] It has been incorporated in multiple technologies, for example, the sodium sulfur battery[118] and in the sodium/nickel chloride (ZEBRA) battery.[119] It has also been used in pacemakers, an application where safety is prioritized above all else.[116]

The superior ionic conductivity is connected to the 2D mobility of Na in planes perpendicular to the c-axis. The chemical form $Na_2O \cdot xAl_2O_3$ varies *x* depending on the stacking of the Na- and spinel layers. This results in two distinct crystal structures: One is on the form *P*6$_3$/*mmc*[121] with *x* = 11, and the other, often denoted β"-alumina, is in the space group *R3m* with *x* = 5.[120] Both structures consist of layers where Na^+ ions lie in a mirror plane between two spinel blocks of aluminium oxide.[86]

The main limitation of the use of β-alumina is the high sintering temperature of 1600 ℃, which makes the material energy intensive and therefore costly to produce. This is also a problem for the β"-alumina, which has an even higher conductivity of 0.2-0.4 Scm^{-1} at

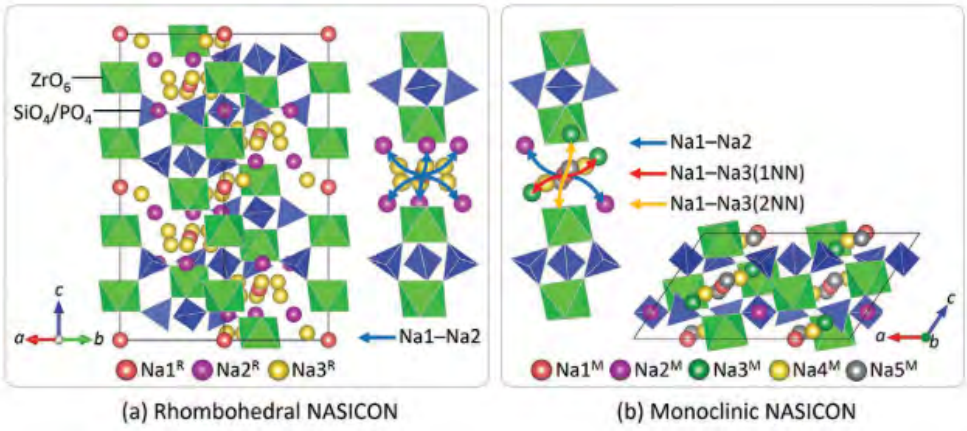

Figure 2.12: Conventional unit cells and the Na+ ion migration channels of a) rhombohedral NASICON and b) monoclinic NASICON. The crystallographic data for rhombohedral NASICON and monoclinic NASICON are derived from ref. [36] and ref. [37], respectively. Superscript R indicates rhombohedral and superscript M represents monoclinic. The $O2-$ ions are not shown for clarity. Adopted from Zou et al[123]

300℃, but it is unstable at these sintering temperatures and usually decomposes to the β-phase and Al_2O_3. The stability is low, both against mechanical stress and as it is very sensitive to moisture, which is why mixes of the two phases are common. Other methods of stabilization are by insertion of mono- or divalent ions such as Li^+ and Mg^{2+} and with Al-substitution.[120,122]

2.4.5 NaSICON-type conductors

The NASICON (Na Super Ion CONductors) are a material type ($Na_{1+x}Zn_2Si_{2-x}P_xO_{12}$ with $0 \leq x \leq 3$) first described by Hong and Goodenough in 1976.[124,125] They are a subset of the $NaZr_2(PO_4)_3$, where the P is substituted with Si. This is balanced by increasing the Na content. The structure have been expanded into a large class of multiple different compositions, with the general form $A_xMM'(XO_4)_3$ and tested elements being *A* = Li, Na, K, Mg, Ca; *M* and *M*' = Fe, V, Ti, Zr, Sc, Mn, Nb, In; and *X* = S, P, Si.[126] The structure is a framework of ZnO_6 octahedra sharing O with P/SO_4 tetrahedra, with NaO_6 octahedras face sharing with ZnO_6. With varying Na-content, the material can crystallize in two different symmetries: The rhombohedral ($R\bar{3}c$) and the monoclinic (*C2/c*). These two phases are separated by Na-content, with the intermediate $1.8 \leq x \leq 3$ Na-contents giving the monoclinic type. This

monoclinic type gives the highest conductivity, especially at $x = 2$. This structure have three distinct sites, the Na1, Na2 and Na3, which is connected in 3D diffusion channels with the conduction path Na1-Na2-Na1 and Na1-Na3-Na1. The rhombohedral structure have no distinction between the Na2 and Na3 sites, and have therefore a conduction channel of Na1-Na2-Na1.

The ionic conductivity of the $x = 2$ type has the highest measured conductivity of this material, at $2 \times 10^{-1} \mathrm{Scm}^{-1}$ at $300\,^{\circ}$ and $6.7 \times 10^{-4} \mathrm{Scm}^{-1}$ at room temperature. Improvements of the conductivity to has been made by substitution of the framework cations with Sc, Fe, Co and Ni,[127,128] by removing poorly conducting secondary phases and by tuning microstructural phases.[129]

One of the notable drawbacks of the oxides like layered, aluminates and NaSICON is their brittleness. This complicates integration into a battery cell where the SSE must have good contact with both electrodes. If contact is not sufficient, processing steps like coatings or hierarchical structures could be integrated, but both would likely increase cost. Sufficient interphase (grain boundary) conductivity is also a must. It can be solved through densification, making a single phase, or synthesis tailoring of a suited secondary phase along the grain boundaries.[123]

2.4.6 Sulfides

The crystalline $Li_{10}GeP_2S_{12}$ (LGPS)[130] and the glass-ceramic $Li_7P_3S_{11}$ has an ionic conductivity of $\approx 10^{-3}$ S cm^{-1}. The Na-types have a lower conductivity than Li-types, often accredited to the larger ionic radius,[131] but both the bond type and polarizability will also have an influence. The Na analogue $Na_{10}GeP_2S_{12}$ has a very moderate ionic conductivity of 0.01 mS cm^{-1},[132] demonstrating materials with good Li-conduction is not directly transferrable to the Na-variants in sulfides.

The glass-ceramic Na_3PS_4 has a conductivity of $\approx$1 mS cm^{-1} at room temperature,[133] increased by inclusion of Si or Ca.[134,135] Changing P to Sb (Na_3SbS_4) increases ionic conductivity to 1 mS cm^{-1}.[136] Inclusion of W to $Na_{2.88}Sb_{0.88}W_{0.12}S_4$ further increased to 32 mS cm^{-1}.[137] This was at the time higher than the highest LGPS. The Sb types is present in nature as well, suggesting it is stable in contact with air. Many other sulfides react with moisture to form the harmful H_2S.

One of the most important features of the sulfides is their formability.[138] The Na-types have higher formablitiy than the Li-types, due to the larger ionic radius give weaker inter-

actions with the P_2S_5, allowing for easier rearrangement. Another desirable quality of the sulfides is that they can be processed through room temperature pressure sintering.[138] The Na-types are even denser than the Li types, due to the higher ionic radius.[139] The low temperature processing is desirable due to the higher chance of side reactions for high temperature processing.

Chapter 3

Methods

This section will give a brief introduction to the methods used in this thesis work. An in-depth explanation of the main techniques is provided to give the reasoning behind their use. We also give a very brief overview of the simulation techniques, although they are not the focus of this work. We also give a summary of the experimental work of each of the articles, with detailed descriptions provided in the experimental sections of the respective experimental sections (Article I and II and Manuscript I and II).

3.1 Synthesis

This work was on two systems, derived from the well-known P2-$Na_2Zn_2TeO_6$ (NZTO) and O3-$Na_3Zn_2SbO_6$ (NZSO). One system is the Ga-substituted NZTO, with the formula $Na_{2-x}Zn_{2-x}Ga_xTeO_6$ with x = 0.05, 0.10, 0.15, 0.2. The other system is for mixed samples of NZTO and NZSO. This is described as Sb-substituted NZTO to avoid confusion (but note that all Sb-substituted samples are in O3-phase, not P2 as NZTO). This gives material on the formula $Na_{2+x}Zn_2Sb_xTe_{1-x}O_6$ with x = 0.1, 0.5 and 1.

The main work of the synthesis work is to ensure homogeneous substitution and ensure no secondary phases. Solid-state synthesis is the standard way to synthesize the layered oxides, due to the relatively few steps. However, this technique gives very little control over the distribution of reactants, which can give an inhomogeneous distribution of substituents and secondary phases. The previous Ga-substitution in NZTO using solid-state synthesis has unidentified secondary phases.[29] Bianchini et al. describe that for layered oxides, the solid-state reaction is compositionally unrestrained at the interface and could therefore form

other stable phases before reacting with the rest of the precursors.[32] As substitution is often forcing a system away from the most stable thermodynamic state. The step-wise reaction path easily gives a two-phase system if the kinetic stable phase is formed first and the rest of the precursor reacts with that product.

Sol-gel synthesis is a well-known synthesis method for creating high-purity phases. The method ensures mixing at the atomic level by dissolving all precursors in acid. Through heating steps the cations are embedded in a carbonate matrix, ensuring a homogeneous distribution of all precursors. This avoids the compositionally unconstrained phase where the reaction is driven to the kinetically stable phases. The chance of secondary phases is also decreased, as they would require long diffusion paths against the gradient.

Citric acid synthesis is a subset of the sol-gel synthesis method. It is a versatile tool for making structures of different complexities, from simple powders to ceramic films to more complex materials like Xerogel and Aerogel. The method works by taking dissolved cations species and adding citric acid as a complexing agent. The solution is then dried, which yields an amorphous powder of the cations homogenously dispersed in a carbon network. The method is often used for the synthesis of materials with small substitutions, with the homogeneously dispersed starting point helping to avoid two-phase systems or inhomogeneous doping. The method is also used for unstable phases, needing mild synthesis conditions. Solid state synthesis of $Na_{0.6}MnO_2$ would give bronzes with three-dimensional structure.[109] But Caballero et al demonstrates a successful sol-gel synthesis with $Mn(acac)_3$ and Na_2CO_3 in propionic acid.

The different precursors needed slightly different methods to ensure complete dissolution. Na_2CO_3 and ZnO is easily dissolved in nitric acid. The TeO_2 is much harder to dissolve, but with increasing the amount of nitric oxide and heating to ≈ 50℃, the solution turns transparent. $Ga(NO_3)_3$ was dissolved in water and added to the Ga-substituted samples. The Sb_2O_3 is dissolved directly in citric acid monohydrate melt for the Sb-substituted samples. All precursors are added in stoichiometric amounts, except for a 10% excess of Na_2CO_3 to account for evaporation. Citric acid is added in a 5:1 ratio to all cations in the solution. The solution was heated to 180℃ to allow NO_x evaporation and gel formation, before drying the gel at this temperature overnight. The resulting powder was heat treated at 450℃ for 12h, ball milled at 600 rpm for 20 min and pressed into pellets before final sintering. The pellets are covered by their mother powder to limit crucible contact and evaporation. Ga-substituted samples $x = 0.2$ and 0.15 was heated to 800℃, while $x_{Ga} = 0.1$-0.0 and $x_{Sb} = 0.1$ and 0.5 are all heated to 900℃.

The NZSO sample was synthesized by solid-state synthesis. This experimental protocol uses sintering at 1100℃ for 3h as the only heat treatment. Ball milling and pellet pressing were otherwise as described above.

3.2 X-ray diffraction

X-ray diffraction (XRD) is a characterization technique based on Bragg's law of diffraction, a description of the reflection of X-rays by sets of lattice planes. The X-rays are high-energy photons with a wavelength of similar order of magnitude as most lattice distances and the lattice planes are crystallographic planes of equally distanced atoms. Bragg analysis treats the reflection of the atoms as a reflection of visible light on a mirror, meaning all X-rays are reflected in the same direction and a superposition of the X-rays occurs. As seen in figure 3.1, the scattered X-ray from the lower plane has to travel a distance that is slightly longer than the one from the plane above, both before and after reflection. Constructive interference is only possible when the difference is a multiple of the wavelength $\Delta = n\lambda$. In all other cases, the large number of crystal planes means that there is some lower plane exactly out of phase, giving destructive interference. This means that only certain angles will give reflected X-rays from the crystal, with no intensities between them. The angles are related to the interplanar spacing by $\Delta = 2d_{hkl}sin\theta$, which gives Bragg's law of diffraction:

$$n\lambda = 2d_{hkl}sin\theta \tag{3.1}$$

In a crystal, there are many different lattice planes, indexed by the Miller indices *h k l*. The full set of diffraction peaks is therefore characteristic of the specific crystal symmetry. There are nine primitive crystal lattice systems, defined by the number of distinct lattice vectors **a, b, c** and specific lattice angles α, β and γ, with atoms only placed on the unit cell vertex. Within each of these, atom placement gives some extra non-primitive cells which contain more than one atom. From this, we define the 14 Bravais lattices, which combined with the 32 crystallographic point groups give 230 space groups which are used to describe all crystals. Additional changes are often described as modulations of the average structure, in which positional, compositional, occupational and orientational (for magnetic moments) variations are described using a set number of vectors. Commensurate modulations have a different multiplicity and are described as a superstructure, while incommensurate have no shared factor.

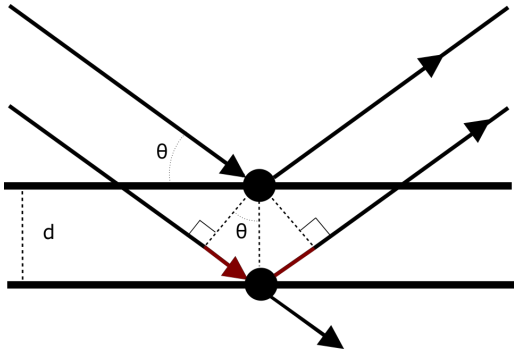

Figure 3.1: Illustration of Bragg's law with two identical incoming beam (same wavelength and phase). The X-ray beam scattered by the lower plane must travel an extra distance of $2d_{\text{hkl}}sin\theta$, marked in red on figure. This distance will only give constructive interference when this distance is equal to a multiple of the wavelength, $n\lambda$.

The amplitude and phase of the diffracted beam are determined by the structure factor

$$F_{hkl} = \sum_{j-1}^{N} f_j e^{-2\pi i(hx_j+ky_j+lz_j)} \tag{3.2}$$

where x_j, y_j, z_j is the positional coordinates and f_j is the scattering factor of the *j*-th atom, *h, k, l* is the Miller indices and this is summed over all atoms in the unit cell.

The most common technique is powder XRD, where the sample is made up of randomly oriented crystallites that scatter in random directions. At the correct angles, the scattered X-rays will instead form cones, called the Debye-Sherrer rings. These are integrated over the full circle, which forms a 1D pattern, plotted as a function of angles 2θ. As described above, the intensity of each peak contains information on the species and occupation in each lattice plane. The peak intensities can also be influenced by the preferred orientation (texturing) in the sample, which influences the probability distribution of the lattice planes. The peak shape usually deviates from the expected Gaussian distribution, which in addition to instrumental parameters contains information on the crystallite size and defects like microstrain.

3.2.1 Rietveld refinement

The diffractogram can be directly interpreted from peak position and width. But the common method is to generate a diffractogram of a theoretical structure and fit this to the measure to extract structural information. This is especially true for powder patterns, which usually

have overlapping, broad peaks, influenced by both the material structure and instrument. Common methods for simulating a diffractogram is Le Bail, Pawley method and Rietveld refinement, where the latter is the most common technique for powder XRD and the focus of this work. The method is based on a simulated diffraction pattern from a symmetric model of the structure, where both instrumental and structural parameters can be defined and fitted to a measured pattern,[140] performed in programs like Topas.[141] The fitting is performed using a least squares algorithm, which minimizes the function *M* using a weighing factor W_i and a scaling factor *c*

$$M = \sum_i W_i \left(I_i^{obs} + \frac{1}{c} I_i^{calc} \right) \tag{3.3}$$

The goodness of the fit is usually characterized with the weighed profile residual R_{wp}

$$R_{wp} = \sqrt{\frac{\sum w_i (Y_{o,i-c,i})^2}{\sum w_i Y_{o,i}^2}} \tag{3.4}$$

but other assessments like the standard profile residual R_p and $\chi^2 = R_p/R_{exp}$ are also employed. None of these parameters is a complete, standalone measure of a good fit, as noise can decrease the quality of the fit or very good data can be impossible to get good models for.[142] The fit is therefore usually assessed with a combination of the fit parameters and a visual inspection of the discrepancy between the calculated and measured diffractogram, especially for high 2θ.

3.2.2 Total scattering XRD and pair distribution function

XRD provides a great description of the average structure but is constrained to be highly ordered and very rigid in form. A real material under standard conditions always includes some form of disorder. Total scattering is a method using the complete diffraction pattern, which includes both the Bragg peaks and signal from diffuse components. The Fourier transform of this signal (which is in itself a Fourier transform from the real space) gives the pair distribution function (PDF). PDF is the atomic density as a function of radial distance, or the probability of finding an atom at a given distance *r* from any other. The resulting function is therefore a description of the local structure. It is a standard technique to characterize both liquid and amorphous materials but is also employed to describe nano-materials and highly disordered systems.

There is some disagreement in the literature on the notation used, with the same or

similar symbols used for different functions. This work will therefore follow the formalism described by D. Keen.[143]

The wave vector Q is related to the diffraction angle by

$$Q = 4\pi sin(\theta)/\lambda \tag{3.5}$$

The coherent scattering vector $I(Q)$ is usually given in its normalized form $S(Q)$, which is $I(Q)$ divided by the number of scatterers *N* and the average scattering power per atom. For X-rays, this is the square of the atomic form factor $f(Q)$, while for neutrons this is the coherent scattering cross-section. The Fourier transform of this is the reduced pair distribution function

$$G(r) = 4\pi r\left[\rho(r) + \rho_0\right] = \frac{2}{\pi}\int_0^\infty Q[S(Q)]sin(Qr)\mathrm{d}Q \tag{3.6}$$

with macroscopic pair density $\rho(r)$ and average number density ρ_0.

The atomic probability distribution gives insight into the local structure of a crystal, as opposed to the diffractogram which is the average crystal structure. An interesting feature of PDF is that the lower interatomic distances *r* provide very local structure information, but at higher *r* include more atoms and are thus more averaged. PDF can therefore be used to investigate structures from the very local, and up to some nm. This is in opposition to NMR, which only gives information on the very closest atomic neighbours. XRD, PDF and NMR are therefore a powerful combination, as they give structural information on all different length scales.

3.3 Nuclear magnetic resconance spectroscopy

Nuclear magnetic resonance (NMR) spectroscopy is a characterization technique based on the behaviour of nuclei with a magnetic moment, i.e. a nuclei with a spin quantum number different from 0, in a magnetic field. It exploits the Zeeman effect, which is a splitting of degenerate energy states in an external magnetic field. When nuclei are placed in a magnetic field, it becomes slightly more favourable to align the spin of the nuclei with the field. When the sample is allowed to reach thermal equilibrium, the nuclei spin distribute according to a Boltzmann distribution. The slight increase in the probability of alignment with the external field creates a net magnetization, which is used in the vector model to explain simple principles and concepts of NMR experiments.

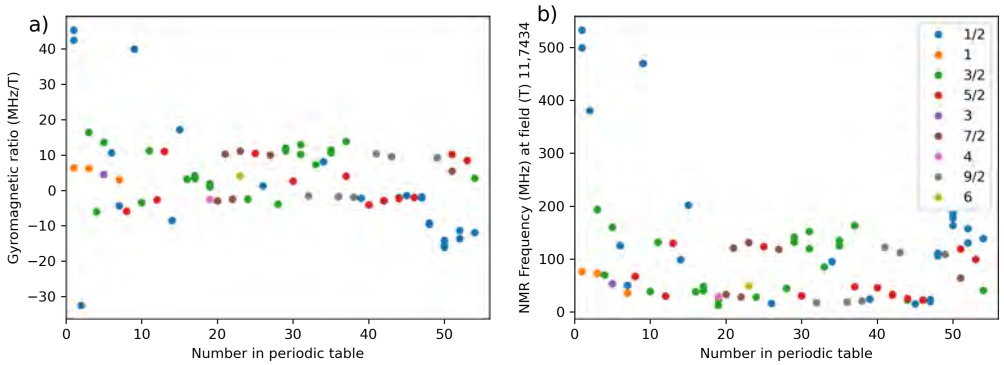

Figure 3.2: a) Gyromagnetic ratio and b) frequency (in an 11.7 T magnetic field) of different iosotopes, plotted by their number in the periodic table.

If the object in the field additionally has an angular momentum, the object will not align with the field. The combined effect of a nuclei's magnetic moment and the spin of the nuclei is a precession around the applied magnetic field. The frequency of this precessional motion is named the Larmor frequency, ω_0, which is given by

$$\omega_0 = -\gamma B \tag{3.7}$$

where γ is the gyromagnetic ratio and *B* is the external magnetic field. The gyromagnetic ratio is the ratio of magnetic moment to angular momentum, and it varies a lot between elements, as shown in figure 3.2. This allows isotope-specific characterization and does not scale with the weight. This allows for measurements that are difficult for many methods, like light elements or contrast between elements with similar weights.

Any nuclei in a real sample are surrounded by electrons, and an external magnetic field will induce an electric current, with a magnetic field opposing the external field. The nuclei will therefore experience different magnetic fields depending on the electronic environment. NMR can therefore be used to characterize the immediate environment surrounding each element.

As the Larmor frequency and the chemical shift is both dependent on the external magnetic field, it is common to convert the value so the fixed ratio between the two is clear. The chemical shift is given by

$$\delta = \frac{\omega_0 - \omega_{0,ref}}{\omega_{0,ref}} \tag{3.8}$$

where $\omega_{0,ref}$ is the chemical shift of the reference compound specific for the isotope.

The chemical shift is small and is therefore usually given in ppm, which scales the shift by 10^6.

The isotope that is measured needs to be NMR active, meaning the nuclei has spin $\neq$ 0. The most intuitive version is the nuclei with spin 1/2, but there are also nuclei with spin $\geq$ 1/2 (see figure 3.2). These nuclei are not spherical, meaning that their interactions must include a quadrupole for a satisfactory mathematical description. They are therefore called quadropolar nuclei. The quadropolar nuclei will have additional broadening from interaction with any electric field gradient (EFG), giving rise to the so-called quadropolar lineshapes. These quadropolar lineshapes can disappear in sufficiently high fields or very fast motion.

3.3.1 The NMR experiment

The NMR experiment is performed by placing the sample in the external magnetic field, magnetizing the sample as explained above. Then a radio frequency pulse is applied, which flips the directions of some spins, and makes the precession in phase. From an average view, this moves the magnetization into the *xy*-plane, usually measured in a rotating reference frame. The precessing magnetization induces a current in a coil surrounding the sample, while the magnetization relaxes back to the thermal equilibrium. The mechanisms for relaxation are described in section 3.3.2. The rotating frame is both a way to simplify the calculation and also mirrors the real electrical processing. The oscillating signal has a very high frequency (of the order of $\approx$500 MHz at 11.7 T field), so a reference frequency in that order of magnitude is subtracted for processing.

The r.f. pulse will exert a magnetic field on the sample, orders of magnitude smaller than the external magnetic field. It influences the system because the r.f. field is resonant with the spin precession. With the time development of the precession, the weak field is allowed to build up over time and have a large influence over the spin system. The duration and the strength of the pulse will therefore have different effects on the state of the spin system. A simple description of the different pulses is the effect it has on the average magnetization in a system of upcoupled spin 1/2. A 90°pulse will flip the equilibrium state into the *xy*-plane (or the *-y*-direction in the rotating frame), and a $180°$ pulse will flip it into *-z*. These pulses can be combined into different and relatively complicated pulse sequences, which can give complex measurements. The simplest is the single pulse sequence, which consists of a 90°pulse and then acquisition, as shown in figure 3.3. The acquired spectra are Fourier transformed to give the component of different frequencies, which is broadened

by the decaying spectra.

Most solid-state NMR uses magic angle spinning, or MAS, where the sample is rotated at $\approx$ 54.74°($cos2\theta_m = 1/3$) with respect to the external magnetic field. This averages some of the orientation-dependent interactions, giving more narrow peaks and thus better resolution. The most important interactions are dipole-dipole interactions, chemical shift anisotropy and the first order quadropolar interactions.

The relaxation time T_1, which will be explained in section 3.3.2, is measured typically by either the inversion recovery or saturation recovery methods, where the latter is explored here. This pulse sequence is performed by applying multiple 90°pulses with short intervals, which saturates the system. Then a 90°pulse is applied after a variable wait time τ, before spectre acquisition. The experiment is repeated for 15-20 τ, which then gives the relaxation curve, following the relation

$$\begin{aligned} I &= I_0(1 - exp(-\tau/T_1)) \\ I &= I_0 + Pexp(-\tau/T_1). \end{aligned} \tag{3.9}$$

The latter equation is an approximation which can include experimental errors. This experiment is repeated for different temperatures, giving information about the dynamic processes in the material.

The multi-quantum magic angle spinning, or MQMAS, is a 2D NMR method for half-integer quadropolar nuclei. As the quadropolar peaks can be very broad, the method can help separate the peak into distinct components. As the experiment is performed using only a single spinning angle, it requires less expensive equipment than other methods like DOR (DOuble Rotation), where the sample is spun at two angles simultaneously.

A general pulse sequence consists of a multi-quantum excitation pulse before an evolution period (t_1), before a new pulse which is a conversion back to single quantum coherence, a new mixing period (this delay is sometimes mentioned to be extremely short), before a selective 90°pulse for the central transition.

The result is a 2D spectra, which projected onto both of the axes gives the 1D spectra. Then a shearing operation is done, so the direct frequency dimension is the same as the 1D spectra, while the indirect frequency dimension places the individual peaks on different frequencies depending on the strength of the quadropolar interaction.

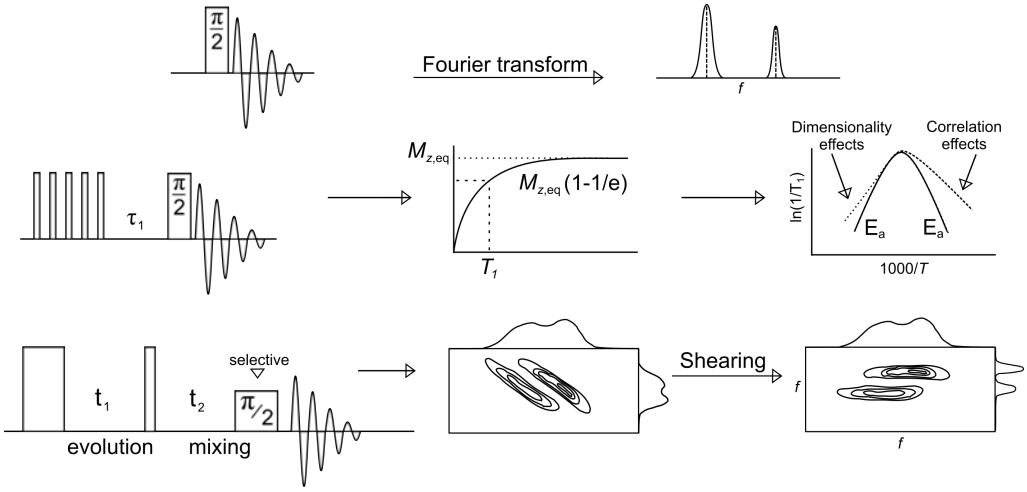

Figure 3.3: NMR pulse sequences. a) single pulse sequence with a 90°pulse. (b) saturation recovery pulse sequence, with the exponential decay of the z-magnetization as a function of time. (c) MQMAS pulse sequence, with an imaginary example of the resulting 2D spectra after shearing.

3.3.2 Characterization of motion

It is possible to detect motional processes by NMR if they change the nuclear spin Hamiltonian. This is true for a large variety of motional processes. Some have a very high frequency, like molecular vibrations, rotations and the rapid oscillations of the H-atom (called librations). Some are slower, like chemical exchange, some molecular rotations, and the very slow diffusion.

The motional averaging of these mechanisms works on different time scales. The faster motional vibrations are usually motionally averaged. Chemical exchange is a movement that involves making and breaking bonds, which can be one atom moving between two, or in some cases, multiple sites, represented as

$$\mathrm{A} \underset{\mathrm{k}}{\overset{\mathrm{k}}{\rightleftharpoons}} \mathrm{B} \tag{3.10}$$

As seen in figure 3.4, the chemical exchange happens over a wide timescale, and some of this is observed by line shape perturbations. Depending on the frequency of the movement, this can change the line shape. If the exchange is much slower than the rate constant *k*, usually described as the rate constant τ_c in NMR, the nuclei are effectively frozen on the NMR time scale. The spectra will have one peak from each site. If the exchange is much

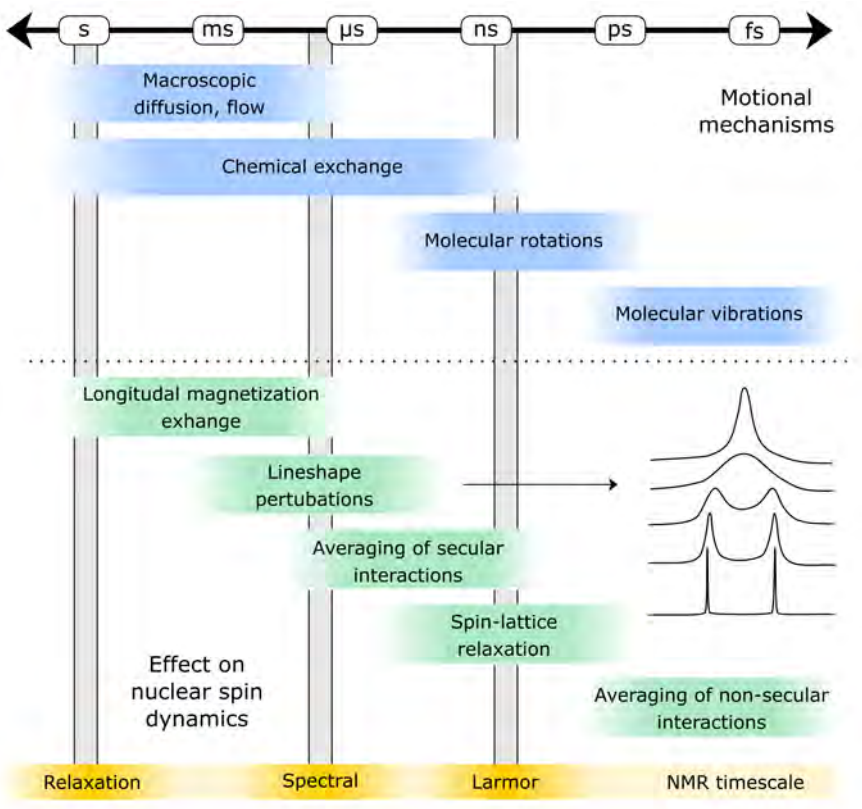

Figure 3.4: Typical motional timescales for physical processes and the effect on the nuclear spin dynamics. Adopted from Wilkening[144] and Levitt with permission.[145]

faster than the rate, the result will be one Gaussian peak positioned at the average isotropic shift. In the intermediate stage, spectra will be a mix of the peaks, either as one or two very broad peaks. Some quadropolar nuclei can have one region where the peak is not a broad one, but the intermediate mixing peak is visible as a quadropolar line shape with a quadropolar coupling constant that is an average of the two.[26]

While slower dynamics are visible through line-shape perturbations, the ultra-fast ion jumps in ionic conductors are best probed by NMR spin-lattice relaxometry (SLR). SLR can probe dynamic rates up to the order of the Larmor frequency ω_0 ($\approx 10^9$ s^{-1}).[146] This measures how fast the system goes back to thermal equilibrium after the perturbation from the r.f. pulse. In a spin 1/2 system, it is simply understood as how fast magnetization in the z-direction is re-established. Relaxation is driven by random fluctuations of the magnetic field around the nucleus caused by thermal motion. The relaxation time in the laboratory

frame, T_1, measures the fastest processes, but slower processes can be measured by SLR in the rotating frame ($T_{1\rho}$),[147] and by spin-spin relaxation (T_2).[148]

If we measure T_1 or $T_{1\rho}$ of the material over a wide temperature range (where no phase transitions occur), we can extract the activation energy E_a and jump rates τ^{-1} of the underlying process. The jump rates follow the Arrhenius behaviour

$$\tau^{-1} = \tau_0^{-1} e^{\frac{E_a}{k_B T}} \tag{3.11}$$

with a pre-exponential factor in the order of phonon frequencies.[149] The relaxation rate T_1 is related to the correlation time τ_c as in the following equation

$$T_1^{-1} \propto \frac{\tau_c}{1 + (\omega_0 \tau_c)^2} \tag{3.12}$$

Over a set of temperatures, this yields the diffusion-induced relaxation rate peak, which has a maximum where $\omega_0\tau_c \approx 1$. The curve for an uncorrelated dynamic process with no directional limitation will be symmetrical, a so-called BPP behaviour (after Bloembergen, Purcell, and Pound).[150] The activation energy E_a for the dynamic process can be determined directly from the slope of the relaxation rate peak.

BPP behaviour is however rarely true in a real material. Especially the low-temperature region ($\omega_0\tau_c \gg 1$) is influenced by the deviation from free unhindered movement and will usually have a reduced slope (indicated in figure 3.3). This correlated motion can be caused by vacancy diffusion mechanisms, structural disorder and Coloumbic interactions.[146] The high-temperature region ($\omega_0\tau_c \ll 1$) is frequency independent for a 3D process, but conduction mechanisms with a reduced dimensionality will have a reduced slope.[151,152] By using models for the reduced dimensionality, the E_a can still be determined on the high-temperature slope, provided the dimensionality is known. An empirical equation for a 2D conductor has been put forward,[144,153] and changes equation 3.12 to

$$T_1^{-1} \propto \tau_c * ln(1 + \frac{1}{(\omega_0 \tau_c)^\beta}) \tag{3.13}$$

The sample in the magnetic field is in a thermal equilibrium, where the populations are given by the Boltzmann distribution for the given temperature. When the RF pulse is applied, the sample is pushed out of this equilibrium state. Spin populations deviate from their equilibrium values and typically coherences are created. The process of regaining thermal equilibrium is called relaxation.

There are two main types of relaxation: The previously described spin-lattice relaxation (SLR) measures the spin population's movement back to the Boltzmann distribution. This is also called the longitudinal relaxation, as it follows the average magnetization in the *z*-direction (along the external magnetic field). The other type is spin-spin relaxation (SSR), or the loss of coherence. This is also called transverse magnetization, as it is related to the loss of average magnetization in the *xy*-plane.

A sample with uncoupled spin 1/2 will only have one value for each of these categories: the spin-lattice relaxation time constant T_1 and the spin-spin relaxation time constant T_2. With any coupled system or spin $>$ 1/2, the processes are more subtle and can have multiple different values depending on the coupling. The two values are still often used for a sample average.

The driving force for relaxation in a spin 1/2 system is the random fluctuation of the magnetic field. There are many origins for these magnetic fields. This can be from the chemical shift anisotropy, where the external field induces a molecular electron current, thus inducing an opposing magnetic field (to the external). A direct dipole-dipole coupling is also one nucleus' magnetic field having an influence on the adjacent nucleus. Any type of movement, for example, molecular tumbling in a liquid or thermal vibrations in solids, creates a change in the direction and magnitude of the local fields referenced to the external field. Most of these changes are very small, but still large enough to cause spin-lattice relaxation.

For nuclei with quadropolar moments, there is an additional relaxation mechanism from the quadropolar coupling. In most quadropolar systems this mechanism will dominate, creating a much faster relaxation than the previously discussed mechanisms.

Relaxation is directly connected to the physical movement in the sample. This method gives great insight into the molecular dynamics in a sample and is therefore a common tool for studying ionic conductors.

The temperature dependence of the value of T_1 follows the relation shown in figure 3.3. The peak has a maximum when the relation $\omega_0\tau_c = 1$ is fulfilled. If this measurement is combined with the same curve in a different magnetic field, the relation of the peak maxima can be used to find the activation energy of the dynamic process. Preferably, we would like to go to very low fields, but this is not possible due to experimental constraints of the NMR machine. Instead, we measure the spin-lattice relaxation in the rotating frame. This means that the magnetic field from the r.f. pulse is used as the external magnetic field for the experiment. As previously stated, the r.f. field is orders of magnitude below the external

magnetic field. The sample can thus be measured in a low field, even without changing NMR machine. This relaxation rate is the $T_{1\rho}$.

In the case of an uncorrelated dynamic process moving in all directions, the activation energy of the dynamic process can be found from the slope of the high- and low temperature regions. The high temperature region for a 3D process is independent of field, but the slope is reduced for either 2D or 1D conductors. The dimensionality in this context describes the directions that an atom can move. Layered materials are typical 2D conductors and materials with channels are 1D. For sufficiently high temperatures, the dimensionality effects vanish and the activation energy can be directly determined. The low temperature region slope is reduced by any degree of correlation, which is almost always present. The simplest example of correlation is if a hopping ion is blocked by another. However, there are more complicated correlation mechanisms. This slope can therefore not be used for determination of the activation energy.

3.4 Modeling and simulations

This section gives a superficial introduction to different simulation methods and how they are employed in this work. The main focus of this work is the experimental work. The simulations only support the findings. The technical details are provided in the experimental sections of the different articles.

3.4.1 Density functional theory

Density functional theory modelling (DFT) has gained massive popularity as it adequately described a wide variety of atomic and molecular properties. DFT assumes that a sufficient approximation of the ground state electronic state can be made using the electron density. Instead of a $3N$ variables of the wave function, only three variables are used to describe the electron density.[154] This relatively simple assumption has been extremely successful and has taken quantum mechanical systems from a specialized field to the building block of much of physics and chemistry.

It is almost impossible to point out areas where DFT is not employed, as it is currently a building block in most areas of materials research. In battery materials, DFT is used to support most steps that involve material research. There are simpler versions like phase stability and synthesis conditions, simulated by simple energy minimization calculations, to

ionic conductivity using ab-initio molecular dynamics, where every frame in the ”film” is a minimized DFT structure.

3.4.2 Reverse Monte Carlo

Monte Carlo methods are a type of algorithm that uses a random sampling strategy to generate structure models. In molecular modelling, the goal is to generate a very large quantity of structures using very simple conditions, and then make statistical predictions about the system. This strategy can also be used ”in reverse”, called reverse Monte Carlo (RMC), where a model is constructed and parameter values are adjusted to fit experimental measurements until a satisfactory solution is reached.

There are many approaches to modelling PDFs. The simplest version is to use the symmetric space group and simulate the resulting PDF, which can be performed using programs such as Topas.[141] This can be useful in some cases, where the local structure is very similar to the average, but with distinct deviations in certain aspects. It can also model crystalline nanoparticles well, as the size limitation gives broad unsolvable Bragg peaks. However, this method is not suitable if the local structure deviates from the average to a large degree. Positions that are modelled as partially occupied in the average structure are for example often modelled as all positions occupied but weighed depending on the occupation. However, if the partially occupied positions have some ordering, this method will not produce the correct intensity for the different bond lengths.

In cases where the deviations cannot be described using the average structure, RMC can be a great option. The starting point is usually a large supercell, in which the atoms are moved until the PDF generated fits the experimental observations. An advantage of RMC is that the conditions for accepting a move are generally very simple, and it is therefore relatively easy and cheap to generate a large number of structures. The supercell usually needs to be relatively large to be able to model features like thermal disorder, which increase cost and time use. Another disadvantage is that there are no physical restraints beyond very simple ones, like interatomic distances, and the method can therefore generate very unrealistic situations.

3.4.3 NMR spectral fitting

Simulating NMR spectra from a model structure is quite challenging, as explained in section 4.1. The spectra are often instead modelled by positioning peaks with well-known line

shapes, visually fitting to the spectra and then reading out parameters. Using programs such as DMfit, the parameters can be fitted using a least square method.[155] For spin = 1/2 and highly dynamic systems, simple peak shapes like the Voight distribution, which is mixes of Gaussian and Lorenzian distributions. Spin ¿ 1/2 systems are modelled using the well-known quadropolar lineshapes, where the asymmetry parameter, position and quadropolar coupling are the fitting parameters. Any broadening from dipolar coupling and magnetic permeability inhomogeneities are usually modelled using a Gaussian/Lorenzen broadening on top.

One peak distribution worth noting is the Czezk distribution, which is an analytical expression of a distribution of both the quadropolar parameters coupling strength v_Q and asymmetry ν:[156,157]

$$v_Q = \frac{3eQ}{2I(2I-1)h} \text{ and } \nu = \frac{V_{XX} - V_{YY}}{V_{ZZ}} \tag{3.14}$$

This distribution is recognizable in the peak shape as a distinct tailing towards lower frequencies.

Chapter 4

Summary of articles

This chapter summarizes the main findings of two articles and two manuscripts. Article I, II and Manuscript I all concern NZTO and Ga-substituted variations. These materials have decreasing amounts of Na as compensation for the increased Ga^{3+} substitution on Zn^{2+}. Manuscript II is focused on the influence of increasing the Na-content, which is achieved through Sb^{5+}-substitution on the Te^{6+} position.

Article I investigates the influence of Ga-substitution on the local structure. The materials are made using an alternative synthesis method, employed to ensure homogeneous substitution. This homogeneity is investigated using ^{125}Te NMR as a probe to directly observe the substitution mechanism on the neighbouring Zn-sites to Te. The analysis is further expanded by DFT simulation showing an influence from the neighbouring Na on the chemical shift of Te. This demonstrates changes in the Na-distribution with increasing Ga-substitution, but no more detailed solution of the structure is possible.

Article II continues the work on Ga-substituted samples, but now focuses on the influence on the Na-dynamics from Ga-substitution and reduced Na-content. The distribution of Na-ions on Na-sites is resolved using low-temperature NMR, finding three differently occupied sites. The Na-dynamics are studied with variable temperature NMR and relaxometry, demonstrating a reduction in activation energy of Na-dynamics for samples with a higher degree of Ga-substitution. This finding is supported by DFT simulations on ionic conductivity.

Manuscript I concerns a superstructure in NZTO. Additional supercell peaks were identified in the diffractogram, fitted to a $2\times2\times3$ supercell. The work compares a modulated superstructure fitted to the diffractogram with an RMC fit of the PDF and identifies the main

deviations from the average unit cell.

Manuscript II demonstrates the variations with increased Na-content, with Sb-substituted variations of NZTO (all in the O3-type phase). The substitution characterization is the same as in Article 1, demonstrating that the Na structure is determined by the charge compensation of the framework layer. The Na structure is characterized using ^{23}Na NMR and MQMAS.

4.1 The effect of Ga-susbtitution on the local structure of NZTO

This article is focused on demonstrating sol-gel synthesis as a reliable method to create homogeneously substituted samples. This work is motivated by the difficulty of synthesizing single-phase materials, especially with some degree of substitution.[25,29] This difficulty is likely due to the large influence of Na-content on phase, requiring homogeneous Na-distribution.[27] A special emphasis is put on identifying a method of verifying a successful substitution, as XRD often has issues with elemental contrast between light elements and elements of similar weight.

The second part of this work is focused on investigating some of the structural changes from the Ga-substitution and especially the influence on the Na-structure. The article combines XRD, NMR and DFT calculations to gain insight into the severely disordered system.

4.1.1 Structure and phase purity from the sol-gel synthesis method

The diffractograms of Ga-substituted NZTO are well described in space group $P6_322$, shown in figure 4.1, consistent with previous reports for both the parent and deviated structures.[24,25,29,31,48]

The samples x = 0.00 and possibly x = 0.05 have a small ZnO impurity. The most impure phase is calculated to be 1.22%, but this is below the limit for quantification.[158] With increasing Ga-content, the ZnO impurity is reduced. No peak is visible in either x = 0.10, 0.15, 0.20. The reason for this could be a higher rate of evaporation of Te compared to Zn, leaving small amounts of ZnO behind. This is further discussed in section 5.

The Ga-substitution has the expected trend on the lattice parameters (figure 4.1), with decreasing Na-content expands the *c*-direction (layer), while the *a, b* plane contracts. The *c*-axis expansion could be from a myriad of reasons: Increased repulsion to the higher

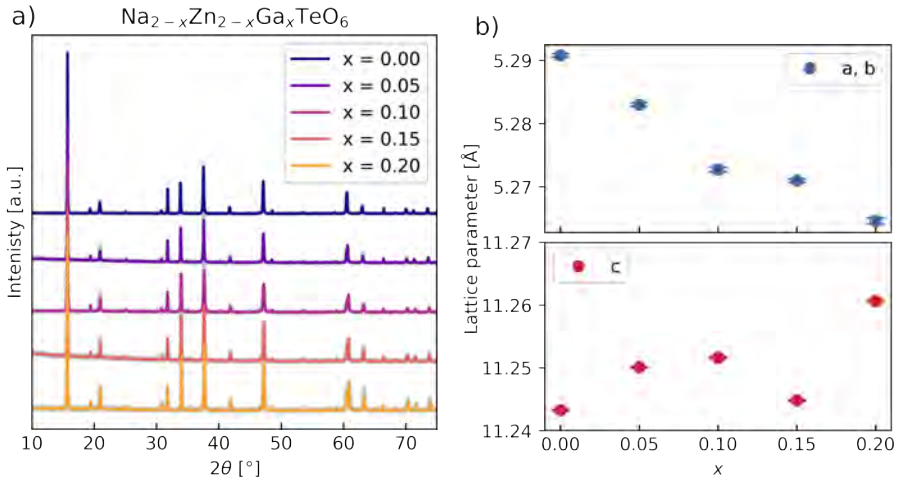

Figure 4.1: Result of Rietveld refinement of $Na_{2-x}Zn_{2-x}Ga_xTeO_6$ with x = 0.00, 0.05, 0.10, 0.15 and 0.20. (a) fitted diffractogram and (b) lattice parameters (of which *a* and *b* is equivalent in the hexagonal crystal system). The bars is the estimated standard deviation calculated by Topas.

charged Ga^{3+}, weaker Na-O bonding or increased O-O repulsion with decreasing Na content. At the same time, the *ab*-plane contracts, decreasing unit cell volume, likely a result of a lower number (on average) of atoms in the unit cell.

Note the anomalously short *c*-axis of the x = 0.15 sample, which is the only deviation from the otherwise clear upward trend. The lattice parameter has previously been directly tied to the Na-content in Na_xCoO_2,[26] suggesting this was an unsuccessful substitution. This is likely not the case for this material as the Ga/Zn ratio was confirmed very close to the nominal, demonstrated with the ^{125}Te NMR below. It should be noted that the errors reported are the estimated standard deviation from the Rietveld refinement in Topas and not the full experimental errors. The errors estimated in Topas are expected to be underestimated.[158] However, the result is reproduced by repeated synthesis, suggesting a real difference in the lattice parameter around this Na-fraction. One important difference between this material system and Na_xCoO_2 is that this system has two types of face-sharing Na-sites with very different coordinated cations (either two Zn^{2+} or one Zn^{2+} and one Te^{6+}). This might influence the Na-structure and might then not coordinate the nominal Na-ratio with the layer distance as clearly. Another possible origin is an inhomogeneous Na-distribution between the layers, which are both suggested by the DFT calculations in this section and

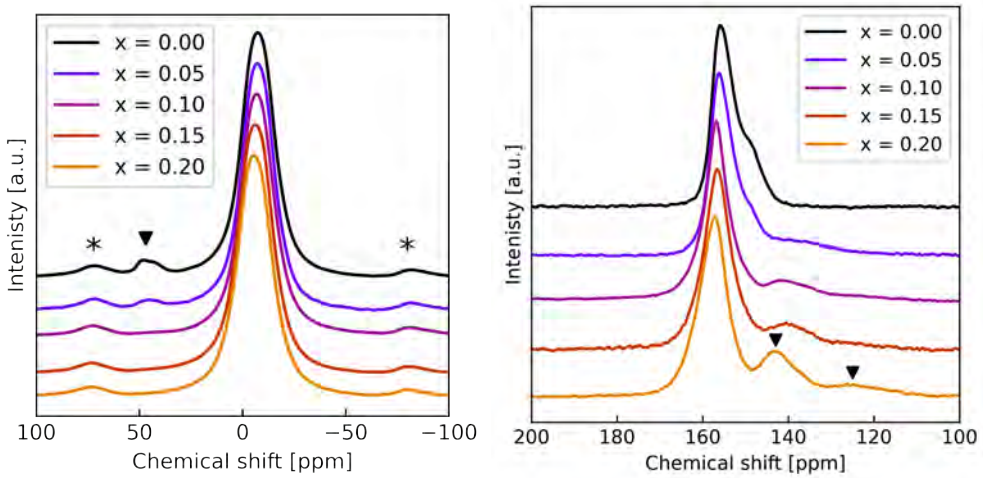

Figure 4.2: ^{125}Te MAS NMR spectra in 11.75 T field for all Ga-substituted samples. Side peak connected to Ga-substitution marked with two black arrows.

by the superstructure in section 4.3. This could give a series of different layer distances which are underestimated by the average.

The occupancy fits are quite unreliable and give very low improvement on the R_{wp}. Previous reports have a large distribution of reported the *6g*/*4f* ratio.[24,31,48] This could be related to the high mobility, degree of disorder and weak scattering contrast of Na. The Na structure for an ionic conductor is difficult to fit, as the large thermal parameter of Na is correlated with the occupancy. In addition, Na is a weaker scatterer than the other elements in the structure.

4.1.2 ^{23}Na and ^{125}Te NMR spectra

The ^{23}Na NMR spectra is lacking the quadropolar line shape expected from ^{23}Na NMR. Instead, the shape seems almost symmetric, which might be due to the dynamic nature of Na. If chemical exchange of Na takes place at a faster frequency than the Larmor frequency, this would result in a mixed signal. This will be further explored in section 4.2.

The structural changes from Ga-substitution can be observed in the ^{125}Te spectra. As seen in figure 4.2, the spectra can be split into two separate regions. The first is the multi-component peak that is present for the pure NZTO, and the other is the two features at lower ppm that grow with increasing Ga-substitution. The feature is only present in the Ga-substituted samples is natural to assume it to be Te with substituted Ga neighbours.

Table 4.1: Integration of Te spectra. The multi-component at 155 ppm is integrated as one, and all components below are summed up. This is compared to the expected number of Ga neighbors to Te from structural considerations.

	Nominal		Integrated	
x	$Te_{Ga=0}$ [%]	$Te_{Ga=\geq 1}$ [%]	I (155 ppm) [%]	Sum small peaks [%]
0.00	100	0.0	100	0.0
0.05	92.5	7.5	86.4	11.1
0.10	85	15.0	83.9	16.1
0.15	77.5	22.5	75.0	25.0
0.20	70	30.0	71.2	28.9

One Zn/Ga position has three Te-neighbours (see figure 2.2) and substituted Ga will thus have an influence on these. Integration of the spectral components should give three times the substituted percentage, reported in table 4.1. It is clear that the integration is close to the expected from nominal amounts. This also means that the Ga^{3+} must be within the closest coordination sphere of a given Te atom, suggesting Ga to be correctly positioned in the structure. There is some uncertainty in the phasing of the spectra, which influences very small peaks. This can explain the discrepancy of the x = 0.05 sample. With some uncertainty, the exact nominal amounts should thus not be considered confirmed.

The main peak observed alone in the x = 0.00 spectra, is clearly a multi-component peak. This is likely from the different Na-coordination environments around Te. This must however be investigated further, which is done through DFT-calculations of Na- influence on the ^{125}Te NMR chemical shift below.

It is also clear by the change in peak shape that no region of the substituted samples is unaffected by the doping, suggesting that there is no pure NZTO region left. NMR is an additive method, so if there were unsubstituted regions in the higher substituted samples, the spectra should have a shoulder feature like the one at 145ppm in x = 0.00. The shoulder feature clearly disappears with increasing substitution, suggesting that the whole sample is affected by the Ga substitution. This supports the interpretation that the substitution is homogeneous.

4.1.3 DFT calculations of Na-influence on ^{125}Te-spectra

DFT simulations of the chemical shift were performed to test if the surrounding Na could influence the chemical shift of ^{125}Te. If this is the case, the surrounding Na-neighbours

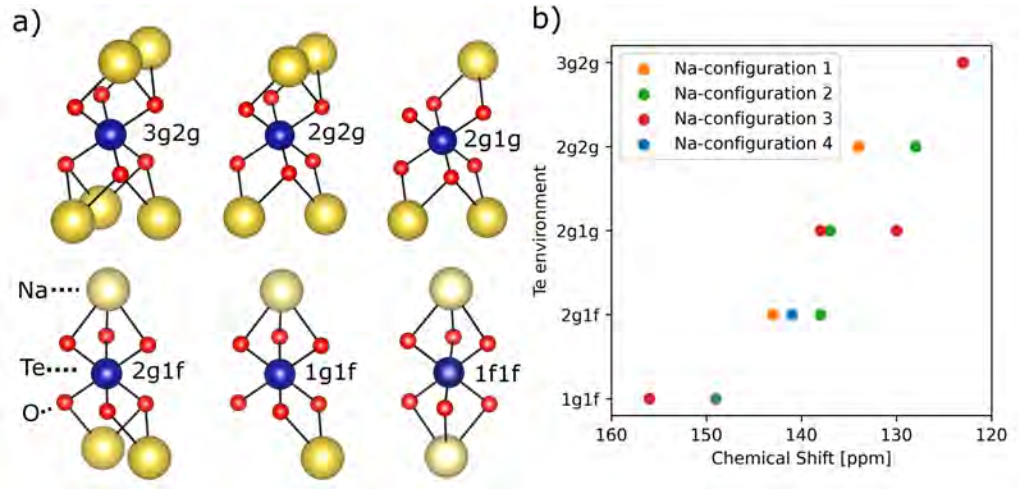

Figure 4.3: a) Structural overview of the different possible Na-environments surrounding Te. b) Influence of Na-configurations (combinations of the invironments in a) on chemical shift ^{125}Te NMR spectra, calculated by DFT.

could be the reason for the peak shape of the x = 0.00 and the main peak of the substituted derivatives. Three compositions of $Na_{2-x}Zn_{2-x}Ga_xTeO_6$ type with x = 0.000 (NZTO), 0.083 (2Ga), 0.167 (4Ga) were explored with *ab-initio* MD simulation. The latter two had respectively 2 and 4 Ga^{3+} ions in a supercell with 24 formula units.

Note that this section uses a *namb* notation to refer to the Te-environments. *na* and *mb* refer to two neighbouring sodium layers on either side of a Te-atom. *a, b* denotes the type of Na site (f or g) using the letter of the Wyckoff site, but omitting multiplicity. and *n, m* describes the number of Na in the said type of site (0, 1, 2, 3). This is not the same as the Wyckoff sites (*6g, 4f* and *2a*) used in other sections of this thesis.

This section only concerns the simulation at 750K, which is high enough to gain a statistical distribution, but low enough to still see the influence of the Ga-substitution. Other temperatures are discussed in section 4.2. The chemical shift of Te was calculated for the coordination environments 1*g*1*f*, 2*g*1*f*, 2*g*1*g*, and 2*g*1*g*. The 3*g*2*g* environment is included to better account for the influence of the number of Na-ions in the Te-coordination environment even though it is rarely observed. The calculated chemical shifts are shown in figure 4.3a.

Two trends emerge for the chemical shift. The first is that better shielding is provided by the configuration environment with a larger number of Na-neighbors, shifting them to a lower frequency. The second trend is from the difference between the face- and edge-sharing Na-

prisms. This is seen in 2*g*1*f* and 2*g*1*g* as these are the only instances where the number of neighbours is the same and one side has 2*g* for both. This shows that better shielding is provided by the Na in the edge-sharing *g*-position, compared to the closer face-sharing *f*.

The first point about the number of neighbours is only applicable to the layers containing *g*-sites. There is only one *f*-site available around a Te-atom, and the *f*- and *g*-sites in one layer cannot be simultaneously filled.

There is a large spread of calculated shifts for the same coordination environment. To force each configuration to produce the desired coordination environments, the lattice is not allowed to relax and the different Na-distributions may exert distortions on the lattice. This is therefore expected to be a simulation feature, and not that the Te-chemical shift is influenced beyond the closest Na-ions.

We can draw some more conclusions about the effect of the Ga-influence on the Na-distributions from the insights gained from the ^{125}Te NMR spectra. Te-environments with a higher number of neighbours have a higher degree of shielding and are therefore shifted to lower frequencies. Looking at the baseline of the peak of sample x = 0.2 the higher frequency side of the peak shifts about 8 ppm higher compared to the unsubstituted sample. This is consistent with what is expected for a reduction in the Na-content, where the low Na-environments become more common with increasing substitution. However, the peak maxima does not change much, only 2 ppm from x = 0.00 to 0.20. There is clearly a shift in the ratio between the different environments, not just a linear shift of an effect being reduced on all.

4.1.4 *Ab Initio* MD simulations on structural changes from Ga-substitution on NZTO

The 4Ga system shows a clear preference for uneven Na distribution across the Na layers. In this case, a 23:21 distribution of the 44 Na ions has an energy gain of 0.2 eV with respect to a system with an even (22:22) distribution. As these should be discussed separately, the simulation was repeated to gain better statistics on both layers. The Na-structure is shown in figure 2.2 and demonstrates one clear trend: increased Ga-substitution gives an increased percentage of Na in the *a*-site. It is important to keep in mind the multiplicity of the sites, where equal filling of the different Na-sites would still give a distribution with 3:2:1. The change in Na-structure demonstrates the trend where the sites move towards equal occupancy.

The calculated Te-coordination environments are shown in figure 4.4. The first to note is the disorder between samples, where there is no clear trend with increasing Ga-substitution. This lack of linearity is in line with the observed trends in the ^{125}Te NMR shifts, where the peak maxima shift very little, but the edges shift approximately 10 ppm. The disorder is also a demonstration of no long range Na-ordering, which would be expected to produce fewer environments.

The cumulative distribution sorts the environment from the calculated shielding calculated in the section above, which reveals a trend of the environment type with Ga-substitution. The 4Ga is much higher in the environment with only one Na-neighbor, whereas the 2Ga has the larger increase around 3 neighbours and NZTO at four neighbours. This demonstrates the reduction in Na-content with Ga-substitution. The Na-rich environments are less common for higher substitution. When looking at the ^{125}Te spectra in figure 4.2, we observe the same. The weight of the spectra shifts to the left with increasing substitution, due to an increase of Te-environments with fewer Na neighbours.

Note that the 1*f*1*f* is not populated at all in any sample. The *f*-site was found to have a high occupancy, which indicates that the Na layers are not independent, but that Na in one layer influences the structure in adjacent layers. This will be further explored in section 4.3. In 4Ga it is interesting to note that the 1*f* environment becomes very populated as the *f* and *a*-sites become more favourable.

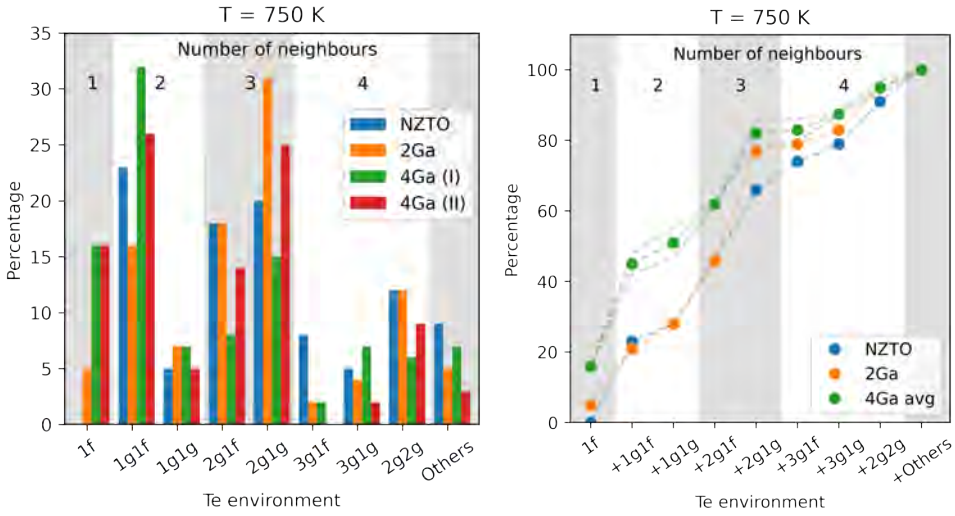

Figure 4.4: Te-environments from 50ps MD at 750K. The number of Na neighbours around Te is marked by grey and white areas as a guide to the eye. (a) Relative percentages of each Te-environment, (b) Cumulative distribution, where amounts of each environment is added in the order of calculated shielding from section 3.4. The average of two 4Ga runs is plotted, with the two individual runs indicated by grey dotted lines.

4.2 Na-dynamics and structure in Ga-substituted NZTO

This section continues the work from section 4.1, with a focus on the influence of Ga-substitution on Na-dynamics. To investigate the mobile ions which have indistinguishable peaks due to chemical exchange, we employ a variable temperature NMR from 100K up to 500K. At low temperatures, the dynamic process of the mobile ions is slowed down. The Na-ions appear frozen at the NMR time scale so that the Na-ratio between the different environments can be quantified.

The following analysis investigates changes in the Na-dynamics with temperature. It also compares the static and MAS spectra, which gives great insight into the dynamic processes of the individual samples with different levels of Ga-substitution. The results are compared to the relaxation behavior, measured between room temperature and 500K. Relaxation is modelled using an empirical equation that considers low dimensional diffusion.[144,153] Lastly, all results are compared to AIMD DFT calculations of the ionic conductivity of Ga-substituted samples.

The main goal of this work is to investigate the influence on the very local dynamics from the substitution and consequential lower Na-content. Previous works have often used impedance measurements as a characterization method for ionic conductivity.[29,94] This method gives insight into the long range transport necessary for total conductivity of Na-ions in an SSE. However, this technique is not necessarily the best to investigate the effect of substitutions on the local scale. Ga-substitution is motivated by assuming that an effect on the local Na-dynamics will translate into an increase in long-range conductivity. Removing Na reduces Na-Na repulsion. This will decrease the activation energy of Na-hopping and increase the local dynamic movement of Na.[51] However, Li et al. found a limited increase in the ionic conductivity from Ga-substitution.[29] We have three possible hypotheses. First, activation energy is not decreased by reduced Na content. Second, the activation energy of Na-hopping was never the bottleneck for bulk ionic conductivity, as the number of vacancies is already high. Third, there is not a simple proportional relationship between local hopping and long-range movement, and there are other effects which can counteract the gains in the former. We thus employ variable temperature NMR and relaxometry to gain the necessary insight into the changes on the local scale.

Note that this section uses kelvin as a unit for temperature, as this is the standard for variable temperature NMR and relaxometry. This is not in line with other sections, which uses °C for readability.

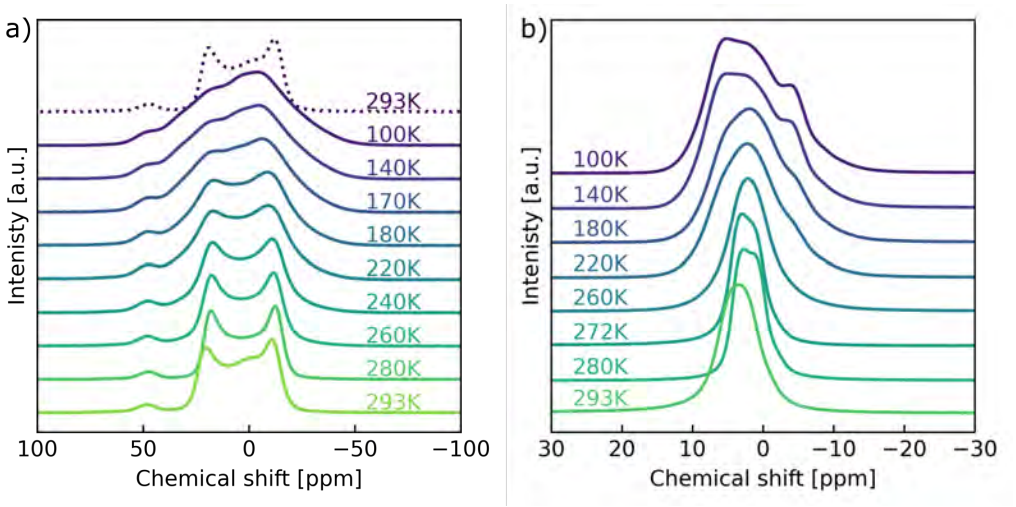

Figure 4.5: (a) Static and (b) MAS (12.5 kHz) ^{23}Na NMR of the x = 0.00 at 100K to room temperature in a 18.8 T field.

4.2.1 Low temperature ^{23}Na NMR

This section will start by looking at the unsubstituted sample in detail, before moving on to the substituted samples to investigate the changes. Figure 4.5a shows the static ^{23}Na NMR of x = 0.0 sample. A static NMR measurement has all line-broadening effects present, such as dipole-dipole interactions, quadrupole interactions, chemical shift anisotropies, and susceptibility broadenings. These typically create broad, indistinguishable peaks which can not be used for a typical peak shape analysis. It is instead a good starting point for dynamic analysis since the only narrowing effects with temperature will be motional. The general trend observed is the gradual narrowing from an almost featureless spectrum at 100 K to a distinct peak shape for 293 K. The similarity between 100 and 140 K suggests that the Na ions are frozen out in the NMR time scale at this temperature for this specific field strength, sample and method. We also note the lack of the quadropolar line shape, which will be explored below.

The line shape narrows as temperature increases, which is expected with increased Na dynamics. The exact point of coalescence is hard to estimate, but seems to be somewhere between 200 K and 240 K. This gives a lower temperature limit of the frequency for the dynamic process. The peak is approximately 25000 Hz wide at 100 K, and therefore the frequency of the dynamic process must be at least half of this, which is 12500 Hz at the temperature of coalescence. The static spectra also change between 280 K and 293 K, with

a shift to the left and the appearance of a central peak. At 280 K, the shape is best described as two maxima with a small component at 45 ppm. At 293 K, an extra component is visible at approximately 0 ppm. This peak is not distinguishable at lower temperatures but is visible both before and after cooling. This could suggest that the peak is a result of a dynamic process. It is safe to assume some additional broadening due to magnetic susceptibility, so the extracted values for dynamic processes from the spectra are overestimated.

MAS spectra reduce dipole-dipole and field anisotropicy broadenings. 1^{st} quadropolar couplings become spinning sidebands, while the 2^{nd} is reduced by a factor of four. The decreased line shape makes MAS spectra better suited for peak shape analysis. The full temperature MAS spectra are shown in figure 4.5b. The 100 K spectra are a composite of at least three components. What kind of Na-environment these three components relate to is a very important aspect of this thesis work. This section will only discuss which distribution which will be used to model the peaks, and thus give some information on the Na-environments, but the nature of the Na-positions investigated further in section 4.3 and both are discussed in section 5.3. One easy suggestion is that the three components relate to the three sites in the space group (*6g, 4f* and *2a*), but this is not a sufficient description as revealed in section 4.3. This section will instead use the *6g-, 4f-* and *2a*-prisms as a shorthand for the approximate positions.

The first significant peak shape change happens between 140 and 180 K. The peak narrows slightly and the ratio of the components shift (as the middle becomes the peak maxima). This change in peak shape is evidence of Na dynamics between different environments at these conditions. Further heating to 260 K shows an expected narrowing of the peak shape and also a coalescence into practically one peak at a chemical shift of 35 ppm with an FWHM of 7 ppm.

The MAS spectra at 100 K are a composite of the Na environments, with the integrated intensity correlating to the Na distribution. When Na-ions become dynamic for higher temperatures, the peak position becomes a weighted average of the non-dynamic peaks (i.e. those observed at 100K). In a static spectrum, all narrowing is from motional averaging, but in MAS spectra the increased dynamics also influence relaxation times, dipole-dipole and quadropolar interactions. This lead to peak shape narrowing and additional leftward shift from the reduced quadropolar coupling.

The changes between 280 and 293K are even more pronounced for the MAS spectra compared to the static spectra. From 272K the symmetric peak splits into two components with a slightly higher point on the left side. Then at 293 K, the peak shifts to higher fre-

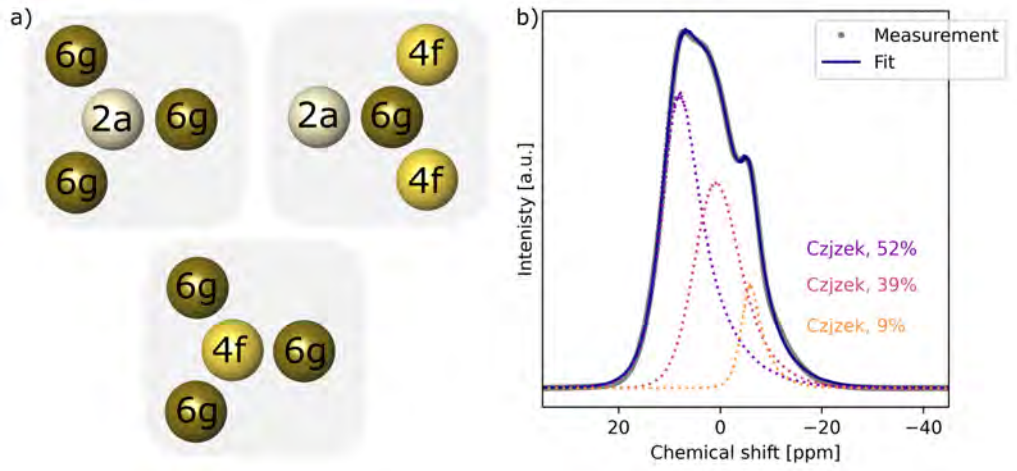

Figure 4.6: a) All symmterical Na-sites with closest Na-neighbours, demonstrating that only the *6g*-site is adjacent to both other positions. b) Decomposition of ^{23}Na MAS NMR spectra at 100 K in 18.8T field, with a MAS rate of 12.5 kHz. The decomposition use three Czjzek distributions.

quencies and the features disappear. This development is best understood by realizing that the exchange is not between only two sites, but three as seen from the components. The exchange is also likely not symmetrical, as not all are adjacent. As seen in figure 4.6a, only *6g* is neighbouring both *4f* and *2a*, while both the latter are only surrounded by *6g*. The weighted average is therefore not a simple combination but is the complex combination of multiple sites with different exchange rates. This analysis is further expanded in the SI, where similar peak shapes are reproduced with a Matlab script in the SI of article 2. In conclusion, the observed spectra are all a result of a complex interplay and influence by coupling interactions, relaxation times, relative amounts and available routes to jump, especially at low temperatures.

The 100K Mas spectra can be decomposed into three components (figure 4.6b). ^{23}Na is a quadropolar spin 3/2 nuclei, and one would therefore expect a quadropolar lineshape. However, the spectra are not possible to break into a reasonable combination of quadropolar lineshapes. One explanation is that the high field reduces the quadropolar coupling. This cannot be the case because the line width of the static spectra is approximately four times the MAS spectra. It is therefore clear the sample is dominated by quadropolar interactions since dipole-dipole interactions would give a line difference of $\approx$100. Decomposing the spectra shows that the peaks are not Gaussian, but are well-fitted using Czjzek distribu-

tions. This is a model describing a distribution of quadropolar lineshapes.[156] This suggests that there is a variety of small deviations within one type of chemical environment. As previously stated, this will be further investigated in section 4.3, and the following section use *2a, 4f* and *6g*-prisms to describe the three different approximate Na-positions, while -site is used for the crystallographic position.

With the understanding of the low-temperature measurements of the pure NZTO, we can move to the substituted samples. Figure 4.7 static and MAS spectra of sample x = 0.2 from 100 to 293 K and a comparison between the static spectra of all Ga-substituted samples at 100 and 293 K. Sample x = 0.2 is the other extrema compared to x = 0.0, so it is a good comparison. The first to note is that the point of coalescence is clearly at a lower temperature compared to x = 0.0, likely closer to 220 K (compared to 260 K). This is congruent with the theory about substitution since reducing the Na content is assumed to reduce Na-Na repulsion and increase the dynamic rates. Another striking feature is the new middle peak, which is clear in both 4.7a and c. x = 0.0 has no feature at 0 ppm before 293, while this middle feature is the maxima up to higher temperatures for at least samples x = 0.1-0.2. A direct interpretation of the origin of this feature is not possible, as we do not have assigned the features to chemical environments.

The static spectra show a clear difference from the degree of substitution at 100K. These differences are not visible with increasing dynamics, excluding the small peak at 50 ppm which disappears with substitution. The origin of this feature is unknown. The peak disappears with increasing temperature (see below) it must be Na in some position where it can still participate in the dynamic process, and thus not a secondary phase. The high amount also suggests it is not from standard defects like surfaces and interphases. Lastly, it is very unlikely to be from Na-defects into the framework layer, since an octahedral coordination is likely to result in a leftward shift. Excluding this feature, the peak width of the main peak seems to be similar both at 100 and 293 K for all samples.

4.2.2 High temperature ^{23}Na NMR

Figure 4.8 shows both the stacked plot of ^{23}Na NMR of x = 0.0 for different temperatures and the highest temperature for all samples x. Note that this is measured in a lower magnitude field of 11.7 T, compared to the 18.8 T field used for the low-temperature series. The peaks are thus broader, as the lower field cannot reduce the quadropolar coupling to the same degree.

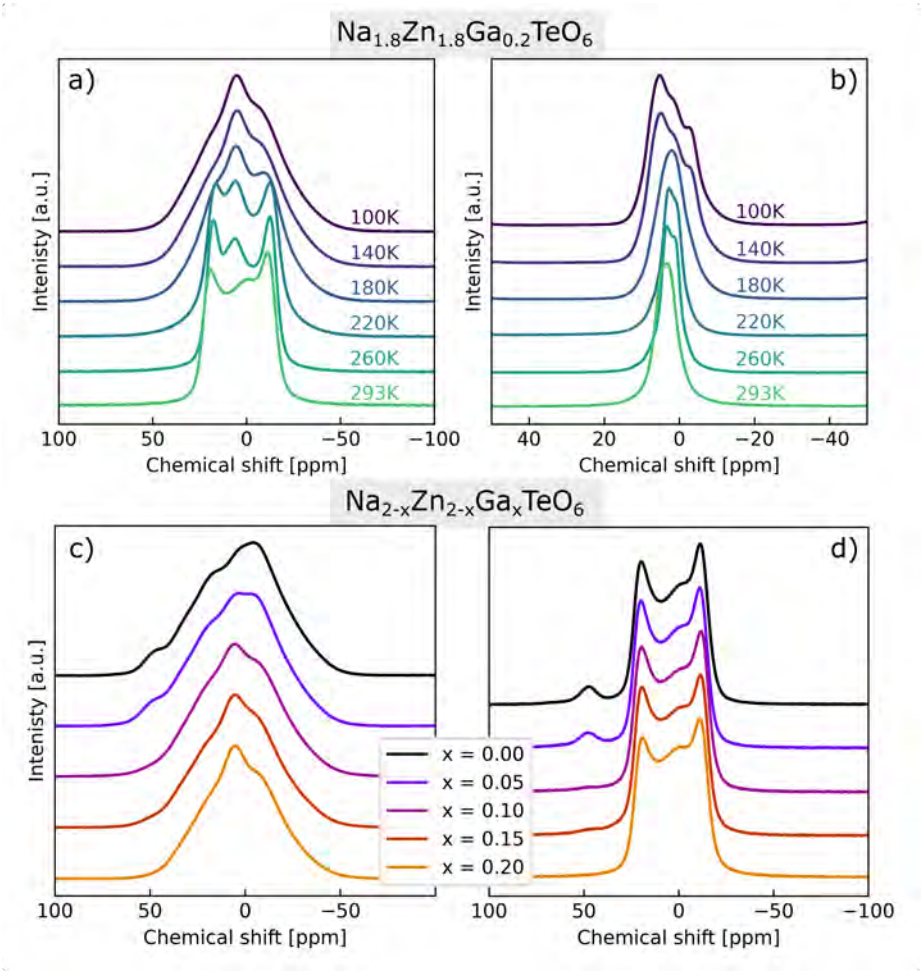

Figure 4.7: (a) Static and (b) MAS at a rate of 12.5 kHz, and ^{23}Na NMR spectra of $Na_{2-x}Zn_{2-x}Ga_xTeO_6$ (x = 0.20) in the temperature range of 100−293 K, in a 18.8 T field. Static ^{23}Na NMR spectra (18.8 T) of $Na_{2-x}Zn_{2-x}Ga_xTeO_6$ (x = 0.00, 0.05, 0.10, 0.15, 0.20): (c) 100 K and (d) 293 K

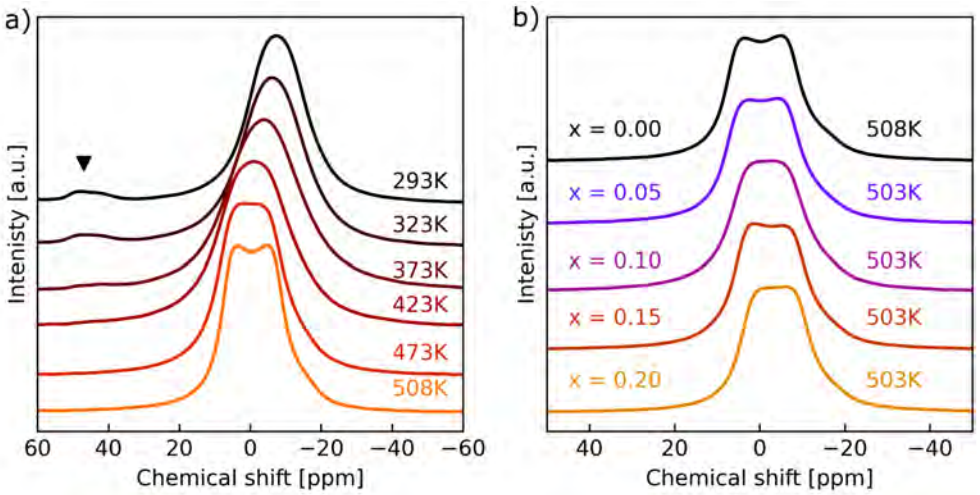

Figure 4.8: a) ^{23}Na MAS NMR of NZTO at temperatures (293-208) and b) Highest temperature measurements of all samples x = 0.00-0.20. Both measured in a 11.75 T field

The peak shifts slightly left, which is likely both due to mixing with the component at 50 ppm and a slight further reduction in quadropolar coupling. The most striking feature is the peak splitting at higher temperatures, with some intensity at the right foot of the peak. There is no phase change identified in this temperature region, but between 573 and 673 there has been some observation of the Na-distribution going from an orthorhombic to a hexagonal structure.[Li2019a, 24] From the line shape discussion above, one can suggest this to be from the three-site exchange combined with reduced dipole-dipole and quadropolar interactions. This is present for all substituted samples to a smaller degree. Note that the x = 0.0 sample is measured at 5 K higher than the others, suggesting an increased splitting is a temperature effect.

4.2.3 Relaxation measurements

The T_1 relaxation for all Ga-substituted samples is shown in figure 4.9, with only the measurements from 293 to 508 K shown. Each temperature is measured multiple different times and averaged. The uncertainty within one temperature is estimated to be smaller than the difference between different temperature averages, even when remeasuring on different days. Therefore, the trends in the T_1 have very low uncertainty.

Looking at the development in the T_1 curve, some trends are directly visible. The peak maxima are shifted down with increasing doping from sample x = 0.00 to 0.10. This means

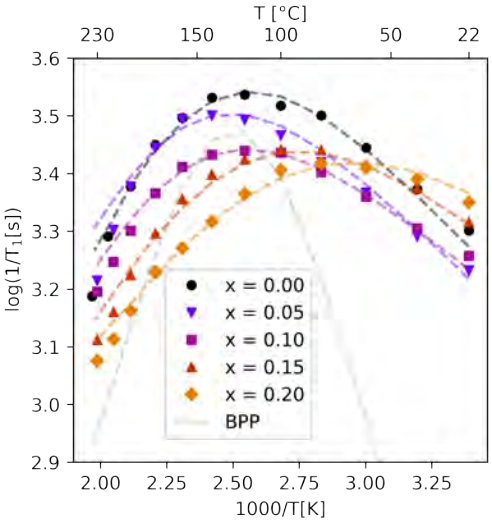

Figure 4.9: Temperature dependence for diffusion induced ^{23}Na SLR rates T_1 for all Ga-substituted samples. The reduced slope on the high temperature side is connected to a 2D dimensional diffusion process, and is modeled using equation 3.3.2, shown in dotted lines. The grey dotted line shows the temperature dependence of a BPP.

that the relaxation time is decreased. This is very likely due to dipole interaction between Na and Ga, where 60% of the nuclei have a magnetic moment compared to 4% of the Zn. The maxima are shifted to the right for higher substitutions, as the condition $\omega_0\tau_c = 1$ is reached at a lower temperature. This must be due to an increase in the jumping frequency of Na. This increase is clearly not linear with temperature, as the x = 0.05 is shifted to a higher temperature compared to the unsubstituted, suggesting a lowering of the Na-dynamics compared to the unsubstituted sample.

In an uncorrelated 3D process, the peak shape of the temperature dependence curve is symmetrical, with the slope of each side determined by the activation energy. This is shown in figure 4.9. In most solids, the curves are influenced by correlated motion on the low-temperature side and dimensionality effects on the high-temperature side. The activation energy in a 2D conductor can be modelled using an empirical model (equation 3.3.2). In the case of NZTO and the Ga-derivates, it is assumed that both sides should have a reduced slope compared to the BPP curve, as it is a layered 2D conductor and the Na-Na interactions should give correlated movement. The activation energies of all samples are calculated from equation 3.3.2 shown in table 4.2. These are compared with the values

Table 4.2: Activation energy for all samples with $Na_{2-x}Zn_{2-x}Ga_xTeO_6$ calculated from the point approximately straight slope and equation 3.3.2. Two values are given for x = 0.00 and 0.05, as no straight region is reached.

x	Ea [eV] Arrhenius (points used)	Ea [eV] 2D model (β value in eq. 3.3.2)	Max temperature
0.00	0.34/0.25 (2/3)	0.32 (1.30)	393
0.05	0.28/0.25 (2/3)	0.32 (1.29)	413
0.10	0.17 (3)	0.30 (1.25)	393
0.15	0.17 (4)	0.26 (1.28)	373
0.20	0.14 (4)	0.20 (1.35)	353

from the standard Arrhenius relation using linear regression over a few points.

As seen in table 4.2, the activation energy decrease with the Ga-substitution. The activation energy of higher substitutions is significantly lower than previously reported by Li et al.[29] This difference cannot be explained by the additional components in the total conductivity, as Wu et al. reports grain boundary conductivity significantly decreases with Ga-substitution. However, as noted in the low-temperature NMR spectra, the point of coalescence is drastically lower for $x = 0.20$ in difference, which supports the calculated low activation energy. As previously noted, the uncertainty in the measurements is low and there are more points for determining the $x = 0.20$. This suggests that the low activation energy is a real feature. To investigate the activation energy further, we compare the measured values to an *ab-initio* molecular dynamics simulation (AIMD).

4.2.4 *Ab-initio* MD simulations for ionic conductivity

The same supercells as described in section 4.1 are used for investigating the ionic conductivity, called NZTO 2Ga and 4Ga. For each composition *x*, we consider five simulation temperatures: 500, 750, 1000, 1250 and 1500 K. The AIMD trajectories are used to compute the mean square displacement and, thus, the ionic mobility. The diffusion coefficients increase slightly, but the three cases exhibit very similar values at different temperatures. One thing to note is that the 4Ga structure shows clear indications of inhomogeneous Na distribution across layers, which is distinctly more favourable than homogeneous distribution. The 4Ga is calculated twice for better statistics, with the two layers being reported separately.

The calculated activation energy for NZTO is 0.33 eV, in very good agreement with the

Table 4.3: AIMD calculation of Na diffusion in an average lattice. Diffusion coefficient and mobility are calculated at room temperature.

System	Act. Energy [eV]	Diff coeff. 10^{-9} [cm2/s]	Mobility 10^{-4} [S/cm]
NZTO	0.33 ± 0.03	2.0	1.8
2Ga	0.33 ± 0.04	3.7	3.3
4Ga (23 Na)	0.31 ± 0.03	5.5	4.8
4Ga (21 Na)	0.30 ± 0.03	6.9	5.6

fitted values from the relaxation measurements of 0.32 eV. As this translate to an ionic mobility of 1.8 10^{-4} S/cm, it confirms the reported experimental range for NZTO of $\approx 10^{-4}$-10^{-3} S/cm.[25,29,94]

The Ga-derivates have a low decrease in activation energy, with 0.32, 0.31 and 0.30 eV for 2Ga and the two 4Ga layers. The calculated difference between the structures is within the margin of error, and should therefore be carefully considered. They do however suggest a decrease in activation energy from reduced Na content, as expected.

The calculated activation energies are closer to estimates from impedance spectroscopy, which find that samples with Ga-substitution x = 0.05 - 0.15 have activation energies of respectively 0.30 - 0.27 eV.[29] Since the calculated activation energy is based on the mean square displacement, both of these methods measure long-range movement, whereas relaxation is only affected by local fluctuations in the magnetic field. The values for a 2D conductor are also relatively close, but notably lower than either model which uses longer-range movement.

Previous nudged elastic band (NEB) calculations for pure NZTO give activation energy for one jump of a single Na in an empty lattice to be 0.09 eV.[25] This supports the hypothesis that the Na-Na repulsion is the limiting factor for ionic conductivity. It is also clear that the activation energy is lower at the local scale compared to what is measured and simulated for a longer scale. This discrepancy is easy to explain when comparing what Na-movement is actually measured. The relaxometry measures the activation energy of a single Na-jump. Long-range movement, on the other hand, requires multiple jumps, without significant movement back to the starting position. A Na-jump is due to thermal energy and is therefore stochastic, so both directions are equally likely. With decreasing Na-content, there are fewer surrounding Na and the Na-Na distances are longer. This means the probability is much lower for the correct series of reorganization for long-range movement. The decreasing Na-content is reducing Na-Na repulsion from Na-ions blocking each other, which was assumed to increase the Na-conductivity.[51] But it might simultaneously increase the chance

of backward movement after the initial jump. This leaves a situation where the Na-dynamic is faster, as Na moves between sites at a higher frequency. But this local movement appears not to translate to long-range movement. This will be further discussed in section 5.

This work investigated the Ga-substitution and, more importantly, following the reduction of Na-content as a mechanism for improving ionic conductivity. Simulations have shown that in the similar material $Na_2Ni_2TeO_6$ ionic conductivity can be increased either by underloading the Na layer by 20%[36] or decreasing the Na-Na repulsion in the simulations.[51] However, these were done by altering physical properties or breaking electroneutrality. In a real material, the suggested route for achieving the same effect was a reduction of the Na-content. We have shown that reducing Na content leads to an unexpected trade-off between quick motion and directional motion.

4.3 Superstructure of locally disordered $Na_2Zn_2TeO_6$

Both previous sections have hinted at a more complex Na-structure than described by the simple unit cell. The Te-environments in section 4.1 demonstrate that no Te has both adjacent *4f*-position occupied, and section 4.2 demonstrate correlated Na-dynamics for all samples. Both of these results suggest Na-Na correlations to be further investigated. Additionally, previous reports of Na-site occupancy in NZTO vary significantly between sources.[24,25,48] This could be due to a weak scattering power of Na, the high thermal disorder or due to a large deviation between the symmetrical and the real Na-positions. The latter is supported by the presence of additional peaks in the diffractogram, previously tied to the Na-structure, but not resolved.[31,159]

This section explores the superstructure of NZTO. We approach this superstructure by describing it using two different methods: a commensurate modulated $2\times2\times3$ supercell fitted to the average XRD and one supercell found by RMC fitting to the PDF.

The resulting structure gives a highly complex Na-structure. No Na is found in the *2a* site, instead a new offset site is identified between *6g* and *2a*. In addition, we identify a disorder in the Te/Zn columns, that is selectively present in two out of the eight of the Zn/Te columns in the supercell.

4.3.1 X-ray diffraction and superstructure

The structure of NZTO has previously been refined to the space group *$P6_322$*,[24,25] but there are a few peaks that are not fitted by the average structure, as seen in figure 4.10. These peaks have previously been explained as displacements of the Na-structure, both for $Na_2LiFeTeO_6$[159] and NZTO.[25] However, the reported structures have an unphysical placement of Na, typically too close together or into the framework layer. The reported Na-structures also have a high degree of disorder. With Na's weak scattering power these structures are unlikely to produce such narrow peaks in the diffractogram. The two small peaks between 2θ = 6-7°were previously fitted to an O'3-type phase.[25] This phase should also have a shoulder on the 5 2θ peak, which is not present here. This makes an O'3 phase an unlikely source of these peaks.

We expand the unit cell to see if the satellite Bragg peaks can be indexed by a larger supercell. A $2\times2\times3$ supercell is sufficient to describe all peaks, with respect to a hexagonal unit cell with a = 5.2906 Å and c = 11.2457 Å within the $P6_322$ spacegroup. A $2\times2\times3$ superstructure in hexagonal lattice and $P6_322$ spacegroup have 2 possible (3+3)D dimensional

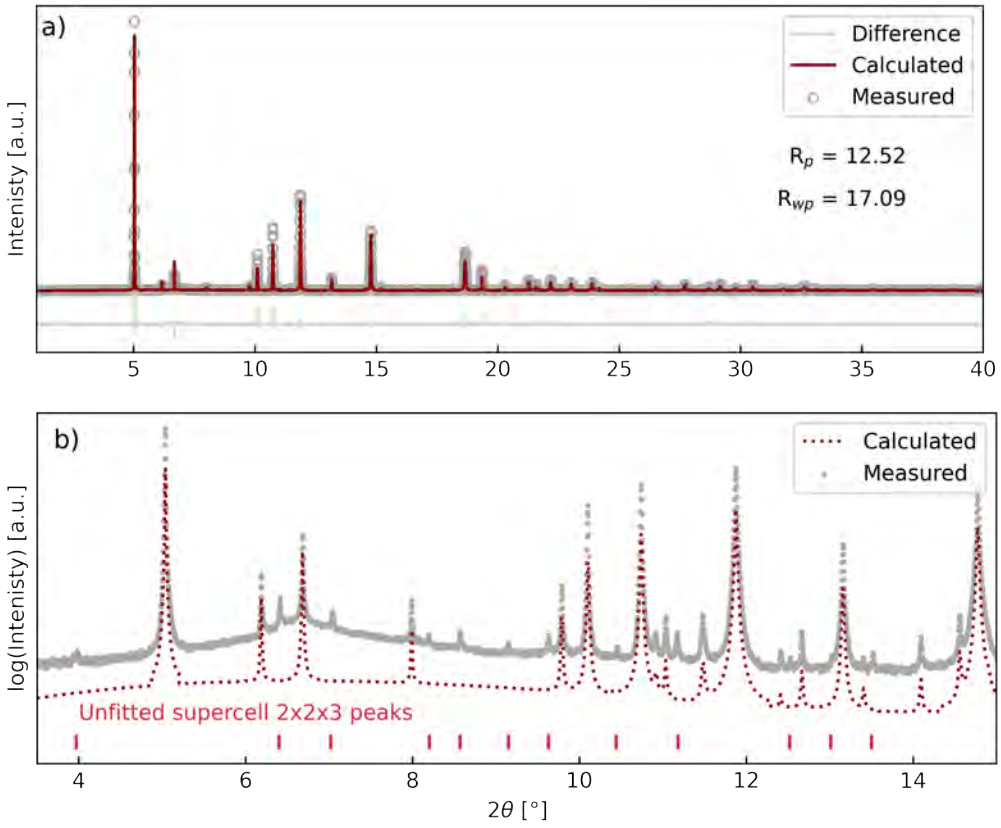

Figure 4.10: Measured diffractogram of NZTO compared to a simple fit using the $P6_322$ space group. a) is plotted with intensity on a linear scale and b) uses a logarithmic scale (with a small mismatch) to demonstrate the mismatch.

superspacegroups,[160–162] defined in equation 4.3.1

$$\begin{aligned} &182.3.200.3 \qquad P6_322(\alpha_1,0,0)000(\bar{\alpha}_1,\alpha_1,0)000(0,0,\gamma_1)000 \\ &182.3.200.4 \qquad P6_322(\alpha_1,0,0)000(\bar{\alpha}_1,\alpha_1,0)000(0,0,\gamma_1)-h00 \end{aligned} \tag{4.1}$$

In both superspacegroups, there are 3 independent modulation vectors. However, to have a complete set, a fourth vector $q_3 = -q_1 - q_2$ has to be included. The full set of modulation vectors is therefore

$$\begin{aligned} q_1 &= (1/2 \quad 0 \quad 0) \\ q_2 &= (-1/2 \quad 1/2 \quad 0) \\ q_3 &= (0 \quad -1/2 \quad 0) \\ q_4 &= (0 \quad 0 \quad 1/3) \end{aligned} \tag{4.2}$$

The superstructure could in principle be described by expanding the unit cell by 2×2×3. However, this would give much too many parameters to be possible to use in a refinement. The larger structure is better described by the superspacegroup formalism, where the atomic occupancy and positions are commensurately modulated. These keep the total number of parameters down, in addition to restrictions on the supercell structure derived from the symmetry. It is important to say that the number of additional, superstructure Bragg peaks predicted by the spacegroup is very large but only a limited number of them are observed. Our superstructure model is reliable as it is not only based on observed satellites but also on a large number of unobserved Bragg peaks.

The superstructure was obtained by JANA2020.[163] To ensure that the global minimum was found, we randomly generated different sets of starting modulation amplitudes before refinement. The search was performed in both possible superspace groups (equation 4.3.1), but the best results were obtained in $P6_322(\alpha_1,0,0)000(\bar{\alpha}_1,\alpha_1,0)000(0,0,\gamma_1)000$. All modulation amplitudes lower than a threshold 3σ were fixed and set to 0, with a visual inspection to ensure this did not have any influence on the fit. To fix the origin of the modulation wave all positional modulation amplitudes for modulation vectors 1, 2 and 3 for $\sin$ modulation function were set to 0. A full list of the average crystal structure detail and all modulation amplitudes are provided below, the average, non-modulated structure in table 4.4, the occupancy modulation amplitudes in table 4.5 and positional in table 4.6.

Table 4.4: Average crystal structure description of of $Na_2Zn_2TeO_6$. List of atomic positions in crystallographic unit cell, isotropic displacement factor U_{iso} and average site occupancy.

average structure					
	position			U_{iso}	occupancy
atom	x	y	z		
Na1	0.7060(39)	0	0	0.0221(20)	0.5
Na2	2/3	1/3	0	0.0221(20)	0.25
Zn1	0	0	1/4	0.0000(7)	1.0
Zn2	1/3	2/3	3/4	0.0187(6)	0.9
Te2	1/3	2/3	3/4	0.0187(6)	0.1
Zn3	1/3	2/3	1/4	0.0086(4)	0.1
Te3	1/3	2/3	1/4	0.0086(4)	0.9
O1	0.3449(11)	0.3236(10)	0.6543(4)	0.0116(11)	1.0

Table 4.5: Occupancy modulation amplitudes in $Na_2Zn_2TeO_6$ (*o*sin1, *o*sin2 and *o*sin3 are all equal to 0 and omitted).

occupancy modulation amplitude					
atom	*o*cos1	*o*cos2	*o*cos3	*o*sin4	*o*cos4
Na1	-0.082(24)	-0.082(24)	-0.096(24)	0	0
Na2	0.139(20)	0.139(20)	0.139(20)	-0.509(14)	0
Zn1	0	0	0	0	0
Zn2	0.106(13)	0.106(13)	0.106(13)	0	0
Te2	-0.106(13)	-0.106(13)	-0.106(13)	0	0
Zn3	-0.062(12)	-0.062(12)	-0.062(12)	0	0
Te3	0.062(12)	0.062(12)	0.062(12)	0	0
O1	0	0	0	0	0

Table 4.6: Atomic position modulation amplitudes in $Na_2Zn_2TeO_6$, (*x*sin1-3, *y*sin1-3 and *z*sin1-3 are all equal to 0 and omitted).

	position modulation amplitude					
atom	xcos1	ycos1	zcos1	xcos2	ycos2	zcos2
Na1	0.098(5)	0.023(5)	0	0.075(5)	-0.023(5)	0
Na2	0	0	0.028(3)	0	0	0.028(3)
Zn1	0	0	0	0	0	0
Zn2	0	0	0	0	0	0
Te2	0	0	0	0	0	0
Zn3	0	0	0	0	0	0
Te3	0	0	0	0	0	0
O1	0	0	0	0	0	0
atom	xcos3	ycos3	zcos3	xsin4	ysin4	zsin4
Na1	0.030(4)	0	0	0	0	0
Na2	0	0	0.028(3)	0	0	0
Zn1	0	0	0	0	0	-0.008(1)
Zn2	0	0	0	0	0	-0.003(1)
Te2	0	0	0	0	0	-0.003(1)
Zn3	0	0	0	0	0	0
Te3	0	0	0	0	0	0
O1	0	0	0	0.019(3)	0.011(3)	0
atom	xcos4	ycos4	zcos4			
Na1	-0.034(6)	0	0			
Na2	0	0	0			
Zn1	0	0	0			
Zn2	0	0	0			
Te2	0	0	0			
Zn3	0	0	0			
Te3	0	0	0			
O1	0	0	0			

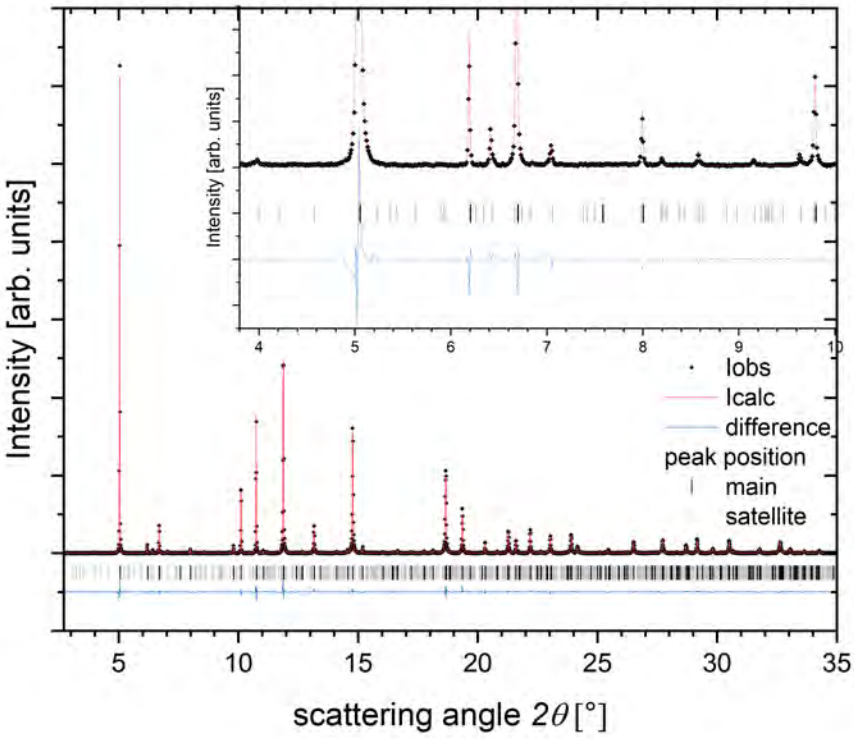

Figure 4.11: Synchrotron radiation powder diffraction pattern of $Na_2Zn_2TeO_6$: experimental (points) and calculated (line). The calculation performed using commensurate superstructure model. Below difference curve and Bragg peak positions: main reflections (black) and superstructure (grey) are shown. The inset shows low angle region of diffraction pattern where small superstructure peaks are clearly visible.

Figure 4.11 shows the comparison of the measured diffractogram (as shown in figure 4.10) compared to the calculated pattern based on the best commensurate $2\times2\times3$ superspace model. Immediately recognizable are the very sharp diffraction peaks both for average structure (marked with black tick-marks) and superlattice (grey tick-marks). The inset shows a low scattering angle region of the patterns with several superstructure Bragg reflections. The model gives a good agreement with the experimentally measured intensities of the satellite peaks, but also with a lack of calculated intensity for unobserved reflections.

It is important to note that the measured diffraction pattern cannot be described by using either occupancy modulation or occupancy modulations. Those two types of modulations have to be combined to get a reasonable agreement with the data. Na is a weak scat-

terer and is expected to have a significant degree of disorder, both in the positional and in occupancy since the Na-layer is just partially occupied.

Note that no improvement of the fit was provided by Na in the *2a* Wyckoff site, and this site was therefore removed in subsequent analysis. This is in line with earlier reported Rietveld refinement with very low occupancy for the *2a*-site.[24,25] However, section 4.2 with ^{23}Na NMR data at 100K demonstrates about 10% of the Na in a third environment. This fraction should have a significant influence on the diffractogram. The validity of removing this site will be explored further in section 5.

The structure is not easily understood directly from the modulation vectors. The structure should therefore be explored visually. For simplicity, the modulated structure is separated into three discussions: the framework cations Zn and Te, the Na sublattice of the Wyckoff sites *6g* and *4f* separately.

4.3.2 Modulated structure of Zn and Te

We start by looking at the modulations of Te and Zn-atoms. Neither has significant positional modulations, but there is a clear change in occupation from the average structure. In the original unit cell, three symmetrical positions align with the different columns. The *2b* is the pure Zn-column with the *2a* sites between. The alternating Te/Zn columns are comprised of *2c* and *2d* sites, which have the *4f* Na-sites between. These are out of phase so in addition to the Zn from the pure Zn column, every layer has one Zn and one Te.

The observed modulation has two types of alternating columns: Out of the eight columns in the 2×2 supercell, six exhibit a small disorder of the Zn and Te compared to the ideal structure, with a 0.95/0.05 relative occupation. These are termed high-order columns. The last two columns, centred on opposite sides of the central pure Zn column of the supercell, show a much higher cation exchange. Each position has a 0.6/0.3 relative occupancy of either atom type. These columns are termed low order columns.

The following discussion of the Na-sublattices will use the columns as reference points. The columns are highlighted using this terminology and the colour coding shown in figure 4.12. The two Na-sublattices are easier to understand related to the position of the high and low order columns.

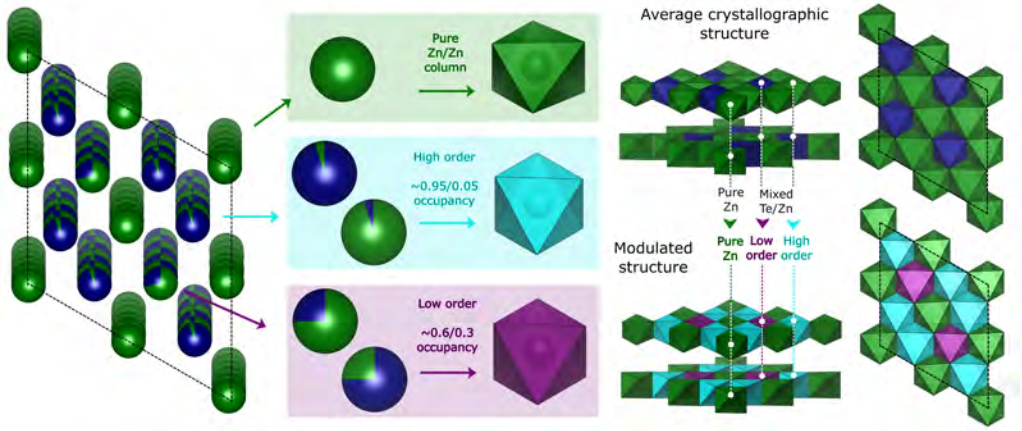

Figure 4.12: The modulated Te/Zn structure, with three types of columns: Pure Zn, high order Zn/Te and low order Zn/Te. This is compared to a $2\times2\times1$ representation of the average structure, with color coding to denote the three different column types.

4.3.3 Modulated structure of Na

The Na-structure and modulations are complicated. For a better understanding, we provide a reminder of the average structure (shown in figure 2.2). The average Na-structure is shown in figure 4.13a with a comparison to one modulated Zn/Te layer. Then we demonstrate the comparison between Wyckoff sites and a single layer of modulated Na and finally show the full modulated Na-structure of the full six-layer supercell, all seen along the *c*-direction. As mentioned, the *2a*-site (light red) was not included in the fit.

To understand the changes from the average structure to the modulations, we consider the Na approximately in the two Wyckoff sites *4f* and *6g* separately. This grouping is structurally relevant as the modulations are different between these two groups: The positional modulation of the *6g* gives displacements in the *xy*-plane, while *4f* is only displaced along *z*.

The Na in the *6g* group are shown in figure 4.14a. All *6g*-sites are modulated in the *xy* plane, but there are different magnitudes of the displacement. Most of the Na is displaced very little and is close to the average positions. All have a medium occupancy of ≈ 0.5. This is the case for all but one of the *6g*-sites in the 2×2 layer. The last position is very different: It has a very large offset in *xy* towards the empty *2a*-position, and a much smaller occupancy of ≈ 0.3. Only half of the *2a*-sites have this type of displacement towards it, while the other *2a* is surrounded by the normal *6g* displacements. This offset towards the *2a* site

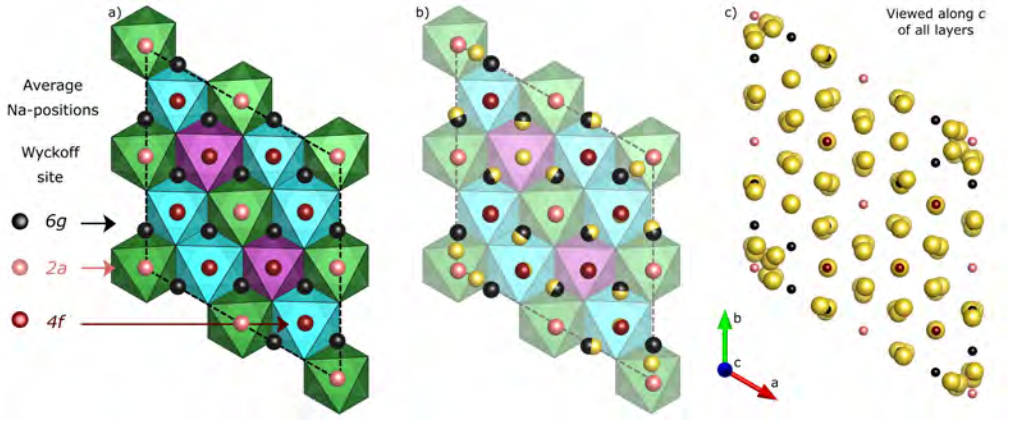

Figure 4.13: a) Average Na-structure in relation to the framework layer, in one layer. *6g* is shown in black, *4f* in dark red and *2a* in light red. b) Average and refined Na-positions of a single layer (at z = 0.83) and c) full modulated 2×2×3 Na-structure viewed along z. The full projection includes all *6g*-Na, which is placed in alternating *xy*-coordinates between layers, as seen from figure b).

raises the question of whether it was correct to exclude the *2a*-site. The fit could be trying to accommodate two different Na-sites, but this is considered highly unlikely. The inclusion of the *2a* sites gave no improvements on the fit, while the modulations only included those with a large influence on the fit. The displacement is therefore assumed to be a real feature.

The other type of Na is the approximate *4f*-sites, shown in figure 4.14b. There are multiple empty *4f* sites, which was not the case for the *6g*-site. The *4f*-sites also have some of the highest occupancies in the model ($\approx$ 0.7-0.8).

The *4f*-site is face sharing with the framework octahedra, and is clearly differentiated by the type of column they are placed in. While all Na in *4f*-sites are displaced along the *z*-direction, the Na placed in the low order Zn/Te columns have a much higher degree of displacement than those placed in the high order Zn/Te columns. The *4f*-Na are also differentiated by the layer they are placed in. Four of the layers are structurally equivalent but with mirrored placement and the opposite offset direction. All high-order columns are filled in the last two layers but with some minor differences: The occupancy of one layer is approximately double that of the other, and the high occupancy layer has some additional Na in the low order column. The high-order columns have higher occupancy of the *4f* these and they have a lower fraction of empty positions. This suggests that Na is more stable in the high-order columns than in the low order columns.

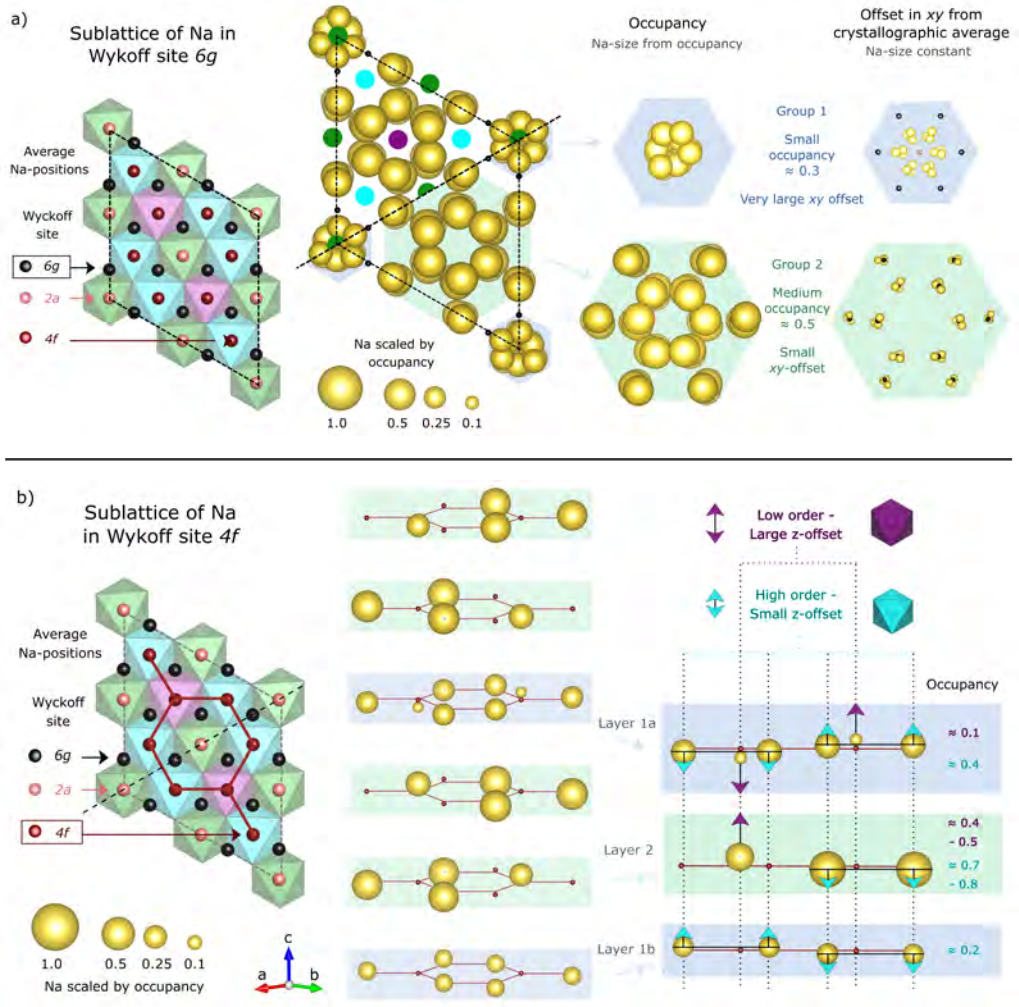

Figure 4.14: Na modulations of the a) *6g* and b)*4f*-sublattice. Both sublattices are split into two groups based on occupancy and magnitude of displacement, indicated by blue and green background. Layer 1 in the *4f*-sublattice has both layers displayed, as there are small variations between them. Note that the *6g*-sublattice is a projection of all six layers along the c-axis, but each individual layer has only half of the positions filled. The Na-radii are scaled by occupancy, except where otherwise stated.

We can summarize the main findings regarding the cation distributions and displacements for the modulated structure:

- There are two types of Zn/Te mixed columns, where one type is significantly more ordered than the other.
- The Na surrounding half of the *2a* sites (in the pure Zn-column) is massively offset and located in between *6g* and *2a* sites.
- The Na in *4f* in low order columns are more offset along *z* than Na located in high order columns.
- The set of *4f*-sites has empty Na-positions, while the *6g*-sites are all fully filled with Na-cations.

4.3.4 Total scattering XRD and RMC modeling

To verify the validity of the modulated structure described above, it needs to be compared to a measurement of the local structure. While previous sections have used NMR for local structure characterization, it is not suited to characterize the large supercell of $2\times2\times3$. NMR typically characterize distances of the closest coordination sphere, while the longest distances in $2\times2\times3$ is a few nm. We instead employ total scattering XRD. It gives the atomic pair distribution function (PDF) of all of the bond lengths in the structure. Due to the high complexity and large deviation from the average structure, the fitting of the structure is performed by reverse Monte Carlo (RMC) modelling. We generate a $9\times9\times18$ supercell from the modulated structure and adjusted it until a high-quality fit of the PDF is achieved. One feature of RMC is the inability partial occupancy of any site. RMC must instead generate real atomic positions in the correct fraction. This decreases the sensitivity to smaller occupational differences, as very large supercells are necessary to model the fractional difference.

Figure 4.15 shows a comparison of the generated PDF from the average $P6_322$-structure, the modulated structure and the result of the RMC-fit (referred to as the RMC-structure) to the measured PDF of NZTO. Comparing the average structure to the experimental, the intensity and some of the peak widths are clearly mismatched. Notably, the peak positions are well estimated. This is in accordance with the trend of the mismatched intensities of the diffractogram. The average bond distances and to some extent the distribution are approximately correct, but there is a mismatch in the scattering power of the atoms at various sites.

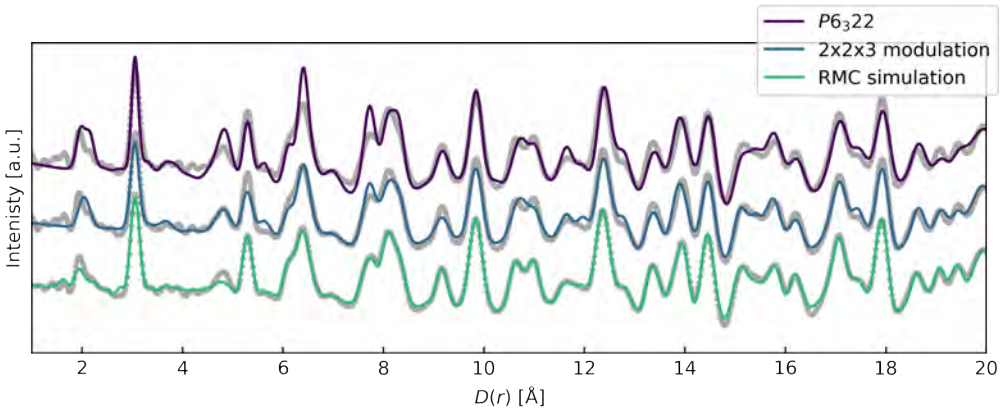

Figure 4.15: The measured (grey circles) and calculated (colored lines) $D(r)$ for the average, modulated and simulated structures. The $D(r)$ ($= G(r)r$) is used as it provides a better visual inspection for the peaks at higher *r*.

This suggests that most of the differences are from some site disorder (or Na/v_{Na} ordering) that is not captured by the average structure.

Some of the observed mismatches in intensity are expected from the description of the partially occupied Na-layer in the average structure. The PDF is calculated as if all Na-positions were occupied, and then scaled based on relative occupancy. This is an adequate description for a completely disordered Na-layer with reduced site occupancies. However, for the real material, atomic correlations exist. Adjacent Na-sites cannot be simultaneously occupied, a 1.7 Å separation is too short owing to strong Na-Na repulsion.[48] Furthermore, it is likely that the weak scattering from Na-cations is not the sole contribution to the intensity mismatch. Hence, the observed differences are also due to heavier atoms like Zn and Te. The intensity discrepancies are also present at the higher *r*-ranges, showing that the structural deviations are not averaged out over just a few unit cells.

The PDF generated from the modulated superstructure is made using the supercell as the periodic unit cell, and will thus have the same insufficient description of the Na-intensities as described above. The fit is improved, especially at high *r*, but discrepancies remain in the low *r*-range. This we can understand given the applied model: The peaks at high *r* are a composite of more bonds than those at low *r*, and will therefore be better described by the partial occupancy model. The higher mismatch at low *r* demonstrates that the near neighbour bonds are still poorly described.

The PDF of the RMC-fitted structure is as expected very close to the measured PDF.

However, even in this case, we observe deviations for the peaks around 2 and 5 Å. The ripples below 2 Å that most likely represent inaccuracy introduced by the Fourier transform of the data. This raises the question of whether the 2 Å peak, which describes the Zn/Te-O bonds, is really a double peak describing distinct Zn/Te-O bonds or whether also this is a result of Fourier ripples. In this case, the data might be slightly overfitted.

The simulated RMC structure is visualized in figure 4.16. In order to create it, the large supercell was projected into a $2\times2\times3$ supercell. The atomic clusters around the average crystallographic position are fitted to both structural disorder and a temperature displacement parameter. These are indistinguishable in RMC modelling.

One difference between the modulated structure and RMC modelling is their ability to give an adequate description of order. The RMC has intrinsically a much higher degree of disorder, like site disorder, thermal displacements and non-periodic displacements. The higher degree of disorder is likely the main reason for the improved description of the PDF. The modulated supercell is not suited to describe the disorder at a local level. It is reasonable that the highly dynamic and likely disordered $Na_2Zn_2TeO_6$ material will deviate from the modulation vectors on the local scale. However, the supercell model describes variations in site occupancies well, giving a probability distribution of the partially occupied Na-substructure. The RMC structure model is constructed from the $18\times18\times9$ supercell. With the small variations between different Na-positions, the size of the model does not have a sufficient number of atoms to give the statistics necessary to recreate complicated occupancy modulations described in the previous section.

As the RMC structure was generated from the modulated structure, it is useful to investigate structural features present in both, as these are features that are preserved through both refinements. The RMC preserve the proposed Zn/Te order-disorder, where two of the eight alternating Zn/Te columns have a larger degree of site disorder compared to the other six. Note that the actual position of the low order columns is on opposite sides of a pure Zn-column. The placement of this column is just due to an arbitrary shift in origin. This confirms the main result from the modulated structure model, namely that the disorder is higher in two of the eight Zn/Te-columns. Both Zn and Te seem to have some thermal displacements, which might have some directionality (see SI). This reflects anisotropic thermal parameters, consistent with the anisotropy of the crystal structure.

The offset position around half of the *2a*-sites are also well preserved in the RMC refinement. The Na distribution forms a connected circle around the *2a*-site in the centre of the supercell. The crystallographic *2a* site is in the centre of this circle, which has very low

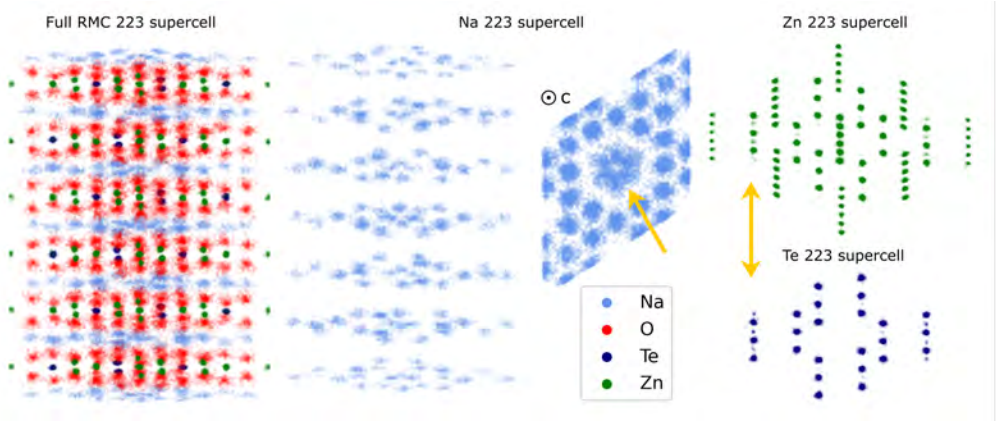

Figure 4.16: RMC simulated structure. All atoms from the RMC simulation is plotted with a high degree of transparency, to make regions with higher density clear. Arrows indicate the two main features, the offset Na surrounding a Zn column and the disorder in two of the six Te/Zn columns.

occupancy. The placement of this feature is also shifted in relation to the origin, as the low order Zn/Te columns. This suggests that the positional orientation of these two features is real. This highly offset *2a*/*6g*-position is conserved through the RMC fitting and should therefore be considered a real feature. This aspect will be further explored in 5.

Neither the empty *4f*-sites nor the selective *z*-offset magnitude is observed in the RMC structure. This suggests that these features do not exist, or that we cannot observe them in the RMC fitting due to the relatively small supercell. The latter point is likely why any variations in the occupancy cannot be confirmed, with an $18\times18\times9$ supercell not having enough atoms to be able to capture subtle differences described by the modulated structure.

4.4 Substitution mechanism in Na-deficient O3-phases

This section investigates the influence of increasing the Na contents in the NZTO system. This was achieved through Sb/Te substitution. As in section 4.1, the substitution was characterized by ^{125}Te NMR. The following Na-structure is best described by a simple conditional probability from the substitution, demonstrating that the Na-structure is fully dominated by the electrostatic interactions with the framework layer. The phase stability is demonstrated to be connected to the Na-structure.

This work was motivated by gaining a fundamental understanding of the influences on the Na. The O3-phase has fewer Na-sites and vacancies, in addition to slower kinetics and can therefore be used as a simpler baseline system. Previous studies on simple layered transition metal oxides have revealed multiple ordering phenomena. Some show maximized Na-Na distance, but other structures have patterned Na-structure, demonstrating other factors must influence.[57,58] We identify no ordering phenomena. Instead we demonstrate the the electrostatic interactions with framework layer is the main influence on the Na-structure.

4.4.1 Phase stability

It is well known that the Na content determines the phase of the layered material.[27] NZSO is a variant of the O3-NaMO$_2$ material. Here, Na is octahedrally coordinated, all Na-sites filled and all Na-octahedra is edge-sharing with the framework octahedra. NZTO is a variation of the P2-Na$_{2/3}M$O$_2$, with prismatic Na-coordination, double the amount Na-sites compared to O3, and Na-prisms both edge- and face-sharing with framework octahedra. Both structures are well studied as cathodes, but the P2-phases have superb ionic conductivity and are therefore also the most investigated for solid-state electrolytes.[25,29,164,165] Both of these structures are shown in figure 2.2.

This section investigates materials with Sb/Te substitution and can be seen as mixes between the two endpoint materials NZSO and NZTO. To determine which structural aspects are important for phase stabilization, we start the investigation by looking at the phase stability of these two materials and how the stability relates to Na content.

The partial occupancy of the Na-layer of the P2 phase complicates the phase stability computations, which are thoroughly explained in our previous works.[25,48] Previous calculations of NZTO found a non-hexagonal reconstruction of the Na-lattice. This means one Na is filling one Na$_{edge}$ and a non-adjacent Na$_{face}$.[48] The non-hexagonal reconstruction is included in this calculation as the P2$_1$2$_1$2$_1$ phase. Two different P2-type structures are in-

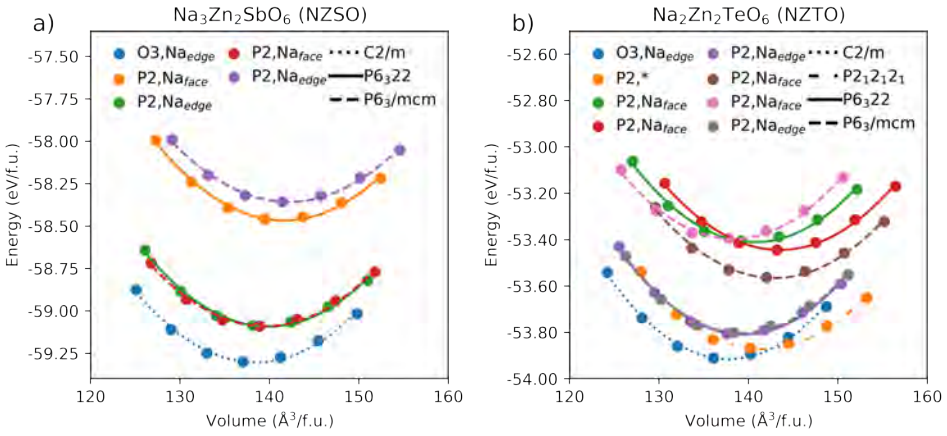

Figure 4.17: DFT calculated energy/volume curves for the edge cases (a) NZSO and (b) NZTO. The Na-sites are simplified to Na_{edge} and Na_{face}. Na structure denoted * is a doubled unit cell where both the Na_{edge} and Na_{face} are occupied. The color of the marker refers to the phase type and the Na-placement, while the line type refers to the space group.

cluded, differentiated by the interlayer cation order. One P2-type have the alternating Zn/Te columns described in section 4.3, while the other has only pure columns of either Zn or Te, as in the NNTO-structure.

The energy/volume curves for NZTO and NZSO are shown in figure 4.17. For NZSO the O3-type phase is about 0.2 eV lower in energy than the closest P2-type phase and is thus clearly the most stable. NZTO does not have a similarly clear stability difference. The curves overlap more in energy, suggesting less difference between phases in terms of stability. The O3 is the lowest in energy, which is not in line with experimental data as NZTO is well known to yield the P2-type. However, the O3 curve overlaps with multiple curves for P2-type phases with different Na-arrangements. One of these differ in the stacking and transformations would require bond breaking. The two others differ only in the Na-structure, with small energy differences. This suggests that Na-mobility will be favoured, in accordance with experimental findings for the P2-phase.[25,29] To explain the experimentally observed stabilization of the P2 phase, we probably need to go beyond the enthalpy-based E-V curves. To gain a measure of the total energy, entropy contributions have to be added. Several distributions of Na-cations are possible for the P2-phases, some being described in terms of E-V curves in figure 4.17. We therefore expect a substantial configurational entropy contribution at the high temperatures at which these layered materials are synthe-

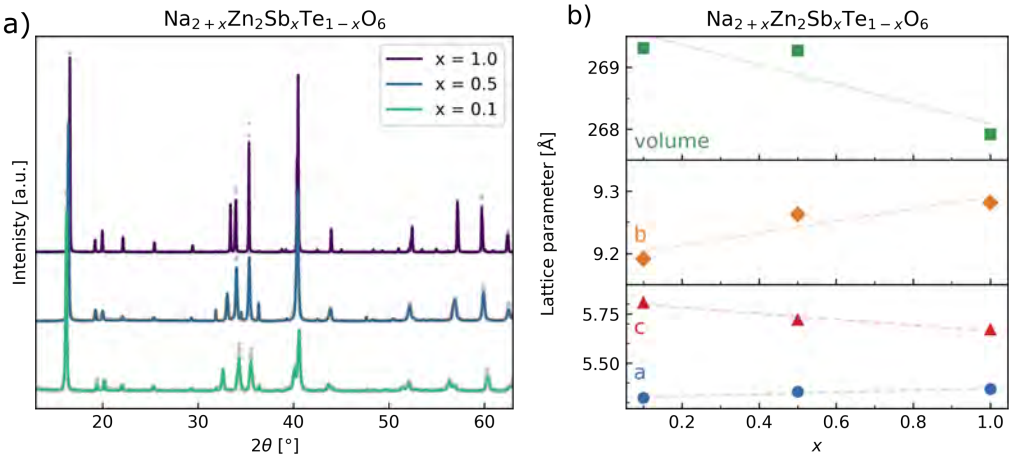

Figure 4.18: a) Comparison between measured and calculated diffractogram of samples with substitution $Na_{2+x}Zn_2Sb_xTe_{1-x}O_6$, x = 0.1, 0.5 and 1.0, and b) lattice parameters.

sized.[25,27,32] Unless the current simulations have failed in selecting low-energy Na-cation distributions, we conclude that entropy stabilization at synthesis conditions is key for favouring the formation of P2-type products.

4.4.2 Crystal structure and substitution

The Sb-substituted samples are all fitted well to the *C2/m* space group, a monoclinic distortion of O3. The ”distortion” in this case is the ordering of Sb/Zn, in which the *c*-axis is not perpendicular to the layer but points along the translation between the cations in the layer. The distortion is often denoted as O’3 to mark the difference between the multiple O3-phases with different orderings. As this section only has one phase type, we will use O3 to avoid confusion. The unit cell in this space group is only one single layer, compared to the two of $P6_322$, figure 2.2. The *c*-axis of the two phases can therefore not be directly compared.

The lattice parameters follow the same trend as the Ga-substituted samples. The *c*-axis increases with decreasing Na-content, while the *ab*-plane decrease. The layer expansion is related to the c-axis expansion by $d_{lattice} = c\,sin(\beta)$, with β being the angle between the layer direction and the *c*-axis. The mechanism for this expansion is likely the same as for the Ga-substituted samples, where lower Na-contents provide less shielding for the high O-O repulsion in the prismatic cell.

The mixed samples (x = 0.1 and 0.5) have a high phase fraction of ZnO, about ≈2 % and ≈5%. Changes in sintering temperature or time did not remove the ZnO fraction. The reason is unknown, but it could be an influence by the partial pressures from the precursors. This is supported by the fact that previous solid state synthesis methods report the same phase fraction of ZnO.[25,31] This additional phase will be discussed further in section 5. However, since the characterization is based on NMR, a local scale method, this is not thought to influence the following characterization. However, this does mean that the nominal substitution could be different from the real. The substitution must therefore be further investigated.

The peak shape in the diffractogram is broader for low substitution levels. The broadening can be fitted using microstrain broadening, but not by size broadening. The Na-content in the x = 0.1 sample is likely right on the edge of the stability of O3 to P2. This could create a highly strained material, maybe with a high degree of local deformations. Previous reports of a Li-doped NZTO are refined to a mix between P2 and O3 for the same Na-ratio, with only ≈10% in the O3 phase.[25] The Zn/Te fractions are confirmed using ICP-MS, and the diffractogram in this report shows much sharper peaks. As will be discussed below, this material is found to be homogeneously substituted. The difference could be due to the material being forced into a much less stable phase fraction, while previous two-phase reports are due to inhomogeneous Na-fractions stabilizing different phases.

4.4.3 Sb-substitution on NZTO

As explained in section 4.1, ^{125}Te NMR has been used to confirm the nominal substitution in $Na_{2-x}Zn_{2-x}Ga_xO_6$. This is from the large number of electrons surrounding the Te nuclei, which makes this sensitive to relatively minor differences.[33] In addition, we have to confirm that the Na-structure change with substitution.

To characterize the whole series of all the O3-phases including NZSO, $^{121/123}$Sb NMR might seem like a better option. But somewhat low Larmor frequency, abundance and quadrupolar coupling made NMR experiments on these nuclei in these samples hard.[34] However, the substituted samples are of main interest for substitution characterization. ^{125}Te NMR on the samples x = 0.5 and 0.1 should thus be sufficient.

The measured ^{125}Te spectra of the x = 0.5 and 0.1 are shown in figure 4.20. The decomposition of these ^{125}Te NMR spectra into two components is unambiguous. The x = 0.5 spectra could be mistaken for a one-component peak, but the peak has some asymmetry

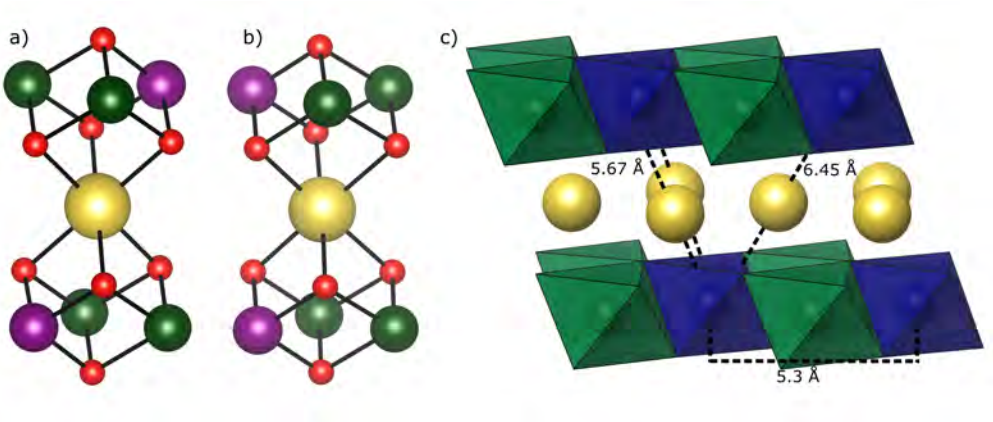

Figure 4.19: a) The *2d*Na site, b) the *4h* Na site, c) One Te with all closest neighboring Te-sites in the same and adjacent layers

that is present with phasing. As *125*Te is a spin $\frac{1}{2}$ nuclei, the asymmetry requires two components to be able to replicate this asymmetry. The integration of the peak components gives very close to the nominal ratios of Sb and Te in each sample, but this is deceptive. In the Sb/Te case, the substitution takes place at the site of the "observer" nuclei, and not at the neighboring site as for Ga-substitution. Every Sb/Te-position has 6 surrounding Te/Sb positions in the same layer at a separation of 5.3 Å. Further, there are two neighbours in adjacent layers at a distance of 5.7 Å and then the following at 6.4 Å, see figure 4.19. Even for sensitive ^{125}Te nuclei, these distances are probably too long to have the influence observed in the spectra. Hence, we rather claim that the peak components are due to adjacent Na-configurations, in line with our previous DFT modelling for NZTO. In the O3 phase, there are three Na-sites edge sharing with every Te-octahedra in each layer, which gives six in total per site. The following sections will explain the hypothesis of how these sites influence the ^{125}Te NMR spectra. But first, some assumptions about the material must be stated.

Any significant Zn/Te-site disorder is unlikely due to the large charge difference between Zn^{2+} and Te^{6+}.[24] In the Rietveld refinements we evaluated the possibility of simple Sb^{5+} located to Zn-sites, potentially benefiting from the strong scattering contrast between Zn and Sb atoms. But no improvement in fit was obtained. It is therefore probable that the Sb substitutes Te on the same Wyckoff site. This heterovalent substitution affects the amount of Na-charge compensating ions between the Zn-Sb/Te layers but could also influence the distribution of Na. This has previously been related to stacking faults,[31] which is congruent with the different P2 phases that are very close in energy, as seen in the phase stability

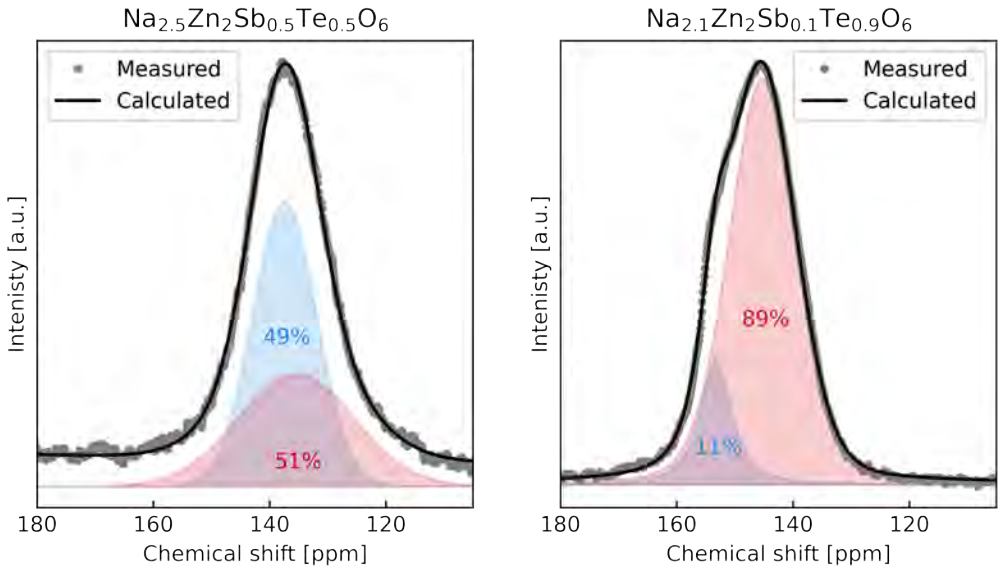

Figure 4.20: ^{125}Te NMR MAS spectra at a MAS rate of 10 kHz in a 11.7 T field, combined with the most stable peak decomposition. The fit was repeated with multiple starting points to ensure the global minima was found.

calculations. The Sb/Te distribution will be assumed to be random as a starting point for our analysis.

Some assumptions can be made considering local charge neutrality. Na^+ is more likely to surround the Sb^{5+} coordination polyhedral than the Te^{6+}, as it provides charge compensation. Any Te^{6+} should therefore have more vacancies at adjacent Na sites than Sb^{5+}. We chose to consider the situation of adding vacancies with increasing Te-content, following $Na_{3-x}Zn_2Sb_{1-x}Te_xO_6$, instead of $Na_{2+x}Zn_2Sb_xTe_{1-x}O_6$ where additional Na is added to vacant sites with the increasing Sb-substitution.

For the simplest starting point, we suggest that the placement of the Na/v_{Na} is guided completely by the electrostatic interactions with the framework layer. The high formal charge of Te^{6+} implies the presence of Na-vacancies, v_{Na}, within the nearest surroundings of the Na-layers. However, the localization of v_{Na} is unknown and we will therefore consider two placements of the v_{Na}.

The two types of Na-sites in the O3-phase are differentiated by their coordination to the Sb/Te and Zn-octahedra, see figure 4.19. All Na-octahedra are edge-sharing with two Sb/TeO_6 and four ZnO_6 from both adjacent layers. One (*2d*) has the Sb/TeO_6 on opposing

sides, while the other (*4h*) has the two Sb/TeO_6 on the same side. The ratio between these sites is 1:2. If we only consider the Sb/Te-sites that are connected to the same Na-sites, we only have to consider the two Sb/Te sites in the adjacent layer on one side. One Sb/Te position is connected through the two *4h* positions, with a distance of 5.67 Å. The *2d*-position is connected to another Te/Sb position with a distance of 6.45 Å. The difference in distance to the adjacent Sb/Te positions must be included in the analysis, as a vacancy in the closer positions would give a higher local charge. This can give preference for Na-placement in the *4h*-position, as it provides better charge compensation. We will therefore consider the placement of the v_{Na} in only the *4h*-position, where only the two closest Te/Sb-neighbors on either side have an influence on the Te-environment. The second scenario is where both the *4h* and *2d* can contain the vacancy, where all four connected Sb/Te positions can influence the Na distribution.

Because the Sb/Te distribution is assumed to be stochastic, the probability of a given number of Sb/Te neighbours is just given by the probability of finding either in each position. This is determined by the degree of substitution. The probabilities of the different possible neighbours are only the probability of each series. Considering only Te/Sb connected through the *4h*, there are eight possible combinations of Sb and Te. Of these, only the four with a central Te-atom are relevant for analyzing the ^{125}Te NMR spectra. The central atom represents the measurement nuclei, and thus ^{125}Te NMR measures only series with a central Te. These series are shown in figure 4.21. There are 32 possible combinations for the situation with *4h* and *2d* can contain the vacancy, which gives 16 series with Te as the central atom.

For simplicity, the following discussion focuses on the situation with only *4h*-connected Te. The principle is the same for both situations but is easier to understand with the simpler structure. An expanded explanation is provided in the SI. Looking at the Na-layers in figure 4.21, two situations can be determined right away. The Te-Te-Te sequence must have a v_{Na} in both Na-layers, giving an environment of four Na-cations neighbouring the central Te (R_{4Na}). The Sb-Te-Sb-series must have one v_{Na} in one of the two layers, giving an environment of five Na-cations the central Te-atom (R_{5Na}). The other two sequences are equivalent: The two Na-layers are determined by two Te neighbours and by one Te and one Sb neighbour. Assuming no directional preference this gives a probabilistic situation: 50% chance of R_{4Na}, and 50% of R_{5Na}. An overview of the probability of $R_{i\mathrm{Na}}$ for all series is shown in table 4.7.

It is now clear that the probability for the different Te-environments can be calculated

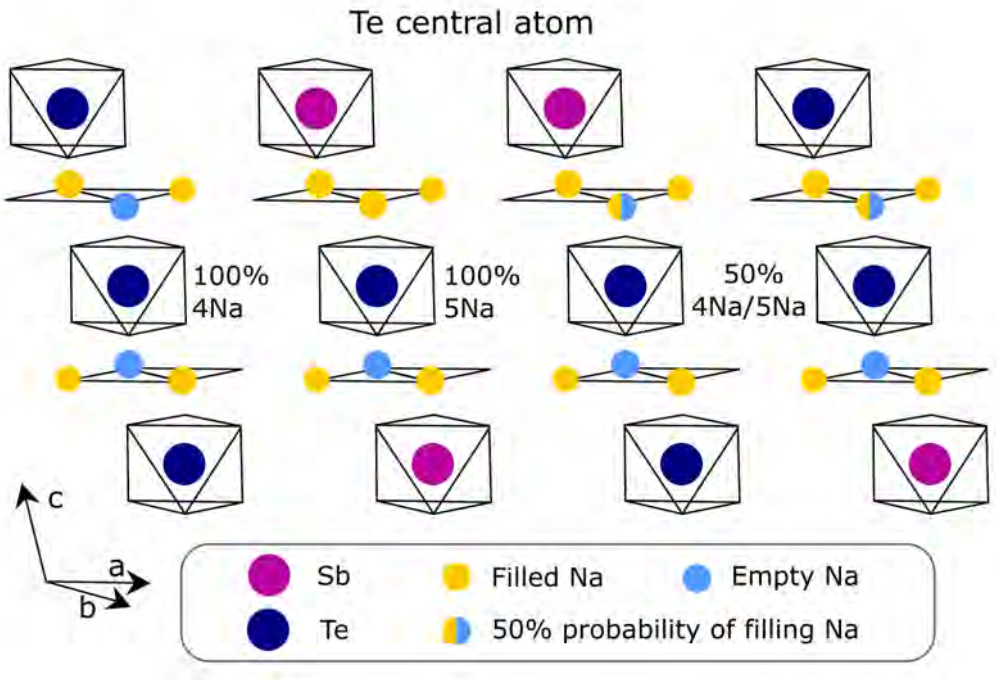

Figure 4.21: All possible Sb/Te series with the corresponding Na-environments. Only the environments with Te as the central atom gives a contribution to the ^{125}Te NMR spectra. Table 4.7 shows the probability of different R_{Na} whan considering both *4h* and *2d*.

Table 4.7: Probabilities of different possible Te-configurations and the resulting probabilities of number of Na-neighbours to Na, with models considering only the closest Te neighbour (called *4h* from the connecting Na-position) and one considering both (called *4h* + *2d*). This set only considers the same subset of the possible Sb/Te series as shown in figure 4.21, only considering the Te as the central atom as this would be the relevant series for the ^{125}Te NMR. Note that R_{6Na} is not possible when considering only *4h*, and is therefore excluded. Due to the large number of possible series whe considering both *4h* and *2d*, the details of the calculation is moved to SI of article 4 and results are summarized here.

Model		x = 0.5	x = 0.1
	p(Sb)	50	10
	p(Te)	50	90
4h	p(Te+Te)	0.25	0.81
	p(Sb+Sb)	0.25	0.01
	p(Sb+Te)	0.25	0.09
	p(Te+Sb)	0.25	0.09
	$P(R_{4Na})$	0.5	0.9
	$P(R_{5Na})$	0.5	0.1
4h + 2d	*Probabilities of different Sb/Te series shown in the SI of article 4*		
	$P(R_{4Na})$	0.25	0.81
	$P(R_{5Na})$	0.5	0.18
	$P(R_{6Na})$	0.25	0.01

from the combination of the probability of the series and the following probability of the number of Na given in this series. This is simply obtained from the substitution level of Sb, as this gives the probability of finding either the Sb or Te species in a given position. The probability for a given number *i* of Na-cations located in the surroundings of the central Te-atom is denoted R_{iNa} and is given by

$$P(R_{i\text{Na}}) = \sum_{j=0}^{3} p(j\text{Te}) p(R_{i\text{Na}}|j\text{Te}) \qquad i \in 4,5,6 \tag{4.3}$$

where p(jTe) is the probability of a given number of Te-neighbors, and p($R_{iNa}|j$Te) is the probability of a given number of Na-neigbors given that number of Te-neighbors. The results summarized in table 4.7.

If the Te and Sb atoms in the x = 0.5 sample are randomly distributed, all positions have an equal chance of being filled by either atom. In this scenario, all four sequences have a probability of 0.25. The probability of either Na-environments R_{4Na} and R_{5Na} is thus 0.5.

This is in excellent agreement with the two decomposed components of the ^{125}Te NMR for the x = 0.5 sample in figure 4.20, which has 51% of one and 49% of the other.

The sample with 90% Te and 10% Sb (x = 0.1), will expectedly have 81% Te-Te-Te sequences, 1% Sb-Te-Sb and 9% of each of the two other equivalent sequences. Assuming the same conditions for charge neutrality holds, Te has R_{4Na} 90% and R_{5Na} 10%. This corresponds very well to the decomposed ^{125}Te experimental peak ratio for x = 0.1.

This is not the case when considering all four neighbouring Sb/Te-atoms. Both substitution concentrations include all three possible number of Na-neighbours, which is not in line with the two observed distributions. The relative ratios of the different peaks are also not corresponding with the observed peak ratios.

From this, we conclude that the ^{125}Te-NMR spectra are influenced by adjacent Na-ions, in good agreement with a probabilistic model. The vacancies seem to selectively be positioned in the *4h* position, as the shorter distance between the Te-atoms creates a larger local charge difference, which is compensated by this vacancy. This is in line with the assumption that the Na-placement is mainly governed by the electrostatic interactions with the framework. It is also quite unlikely to get any in-layer Na-order, as these would distribute the v_{Na} more homogeneously and not be placed around Te^{6+} in the correct amounts. One can imagine ordering types for giving the correct ratios, however, to produce only two environments in the correct amounts require this to be R_{4Na} and R_{6Na} around any Sb/Te-position. This is highly unlikely as it would produce a large local charge difference, and the more likely option is that the Na-distribution is mainly influenced by the electrostatic interaction with the framework cations, and not the Na-Na repulsion.

Some more conclusions on the substitution mechanism can be made. First, the assumption of a random distribution of Te and Sb cation is very likely correct, and we believe this also reflects the good atomic mixing during the soft chemical synthesis. Any clustering, island formation or simple orderings would otherwise fail in obtaining correct ratios for different Sb/Te-sequences, and hence also not an appropriate ratio of chemical environments. This also suggests that the real Sb/Te ratio is very close to the nominal, and is not hampered by potential evaporation issues that appeared to give a secondary phase of ZnO.

4.4.4 ^{23}NMR MAS NMR

Figure 4.22 the single pulse ^{23}Na MAS NMR spectra of the various Sb-concentrations. The x = 1 sample is a composite spectrum, which we could assume to be a multi-component

quadrupolar lineshape. This cannot be decomposed without a significant amount of ambiguity, therefore this peak will be decomposed using MQMAS, which separates the peaks from the magnitude of the quadropolar coupling.

The substituted samples are easier to understand from single pulse NMR. The peaks shift to the right, and the peak shape is smoothed. These materials have an observed expansion of the *z*-axis (figure 4.18). This is expected as less Na can compensate for the O-O repulsion with reducing Na-content, instead compensated for by an increase in layer distance. The following stretched NaO_6 octahedra have increased anisotropy. This explanation is supported by the similarity between the x = 0.1 and 0.0. The Na is octahedrally coordinated in O3, but prismatically coordinated in P2, which is expected to give a different anisotropy. However, a severely stretched octahedra will give a higher anisotropy and thus might explain the gradual transition between the phases instead. The same trend was also observed for Ga-substituted samples (section 4.1). This octahedra stretching could be the explanation for the broad peaks observed in the diffractogram of x = 0.1, which could only be fitted using microstrain broadening. The right shift is most likely due to an increase in quadropolar coupling.

The fast Na-dynamics was the explanation for the lack of features in x = 0.0 in section 4.2. With 16% vacancies for x = 0.5 and 30% for x = 0.1, there is a large enough concentration of vacancies to give fast Na-movement leading to some degree of peak coalescence at room temperature. This chemical exchange observation complies with previous measurements of ionic conductivity in the Na-deficient O'3 phase at room temperature.[25]

4.4.5 ^{23}NMR MQMAS

Figure 4.23 show the ^{23}Na MQMAS NMR for all samples. The x = 1 is the only sample without significant movement, and will therefore give an insight into the coordination of Na. There are two distinct groups, Probably corresponding to the two crystallographic Na-positions in O3. MQMAS spectra should generally not be integrated for peak quantification, as small variations in peak excitation can give large differences in the intensity of the components. Determination of the peak intensity is therefore not possible. However, the peak has a higher intensity than the other. This could correspond to the two sites with a 2:1 ratio if peak excitation is similar. Without any other structural variation to produce differences in the Na-environment, the two groups are likely from the two Na-environments described by the symmetrical positions.

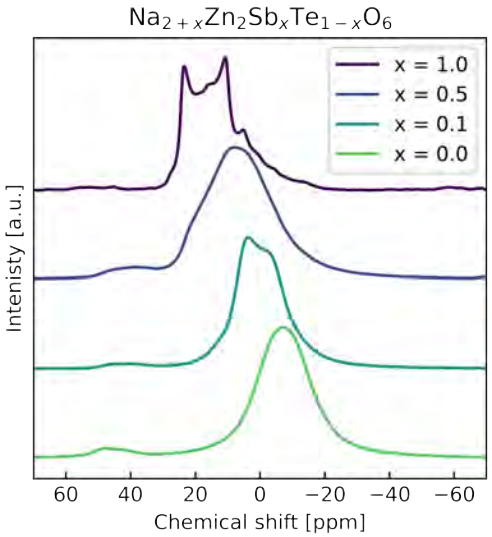

Figure 4.22: ^{23}Na NMR of the samples on formula $Na_{2+x}Zn_2Sb_xTe_{1-x}O_6$ with x = 1, 0.5, 0.1 and 0.0, where the three former is the O3-types and the latter is P2.

However, the inset for x = 1.0 reveals a much more complex structure than previously assumed. If the peak shape was due to quadropolar coupling, the peak maxima of one quadropolar peak shape are positioned at the exact same indirect frequency. The inset in figure 4.23 show that the three maxima are not at the same indirect frequency. This means that the spectra are a composite of peaks from different chemical environments. The similar placement in the indirect frequency suggests that the chemical environments are very similar. The most likely candidate is structural variations of the same crystallographic environment. One of these environments can be further described. The peak at 0 ppm at sample x = 1.0 is likely from Na in highly symmetrical octahedral coordination. This environment must deviate slightly from a perfect symmetrical octahedron, which would have no quadropolar coupling and is therefore not measurable in the MQMAS spectra.

The peaks from the 2nd Na-site are not as intense as the other, so it is not possible to determine if this also has three distinct maxima. However, it seems to span a similar range in the direct frequency and seems to vary in intensity, so we can assume some structural variations in these Na environments as well. The deviation from the symmetrical positions is significant since it is in the x = 1.0 sample, which has a full Na-lattice. One previous description of structural deviations in O3-type materials describes Na off-centering as a response to adjacent vacancies.[83] Another describe bending of the full Na-layers,

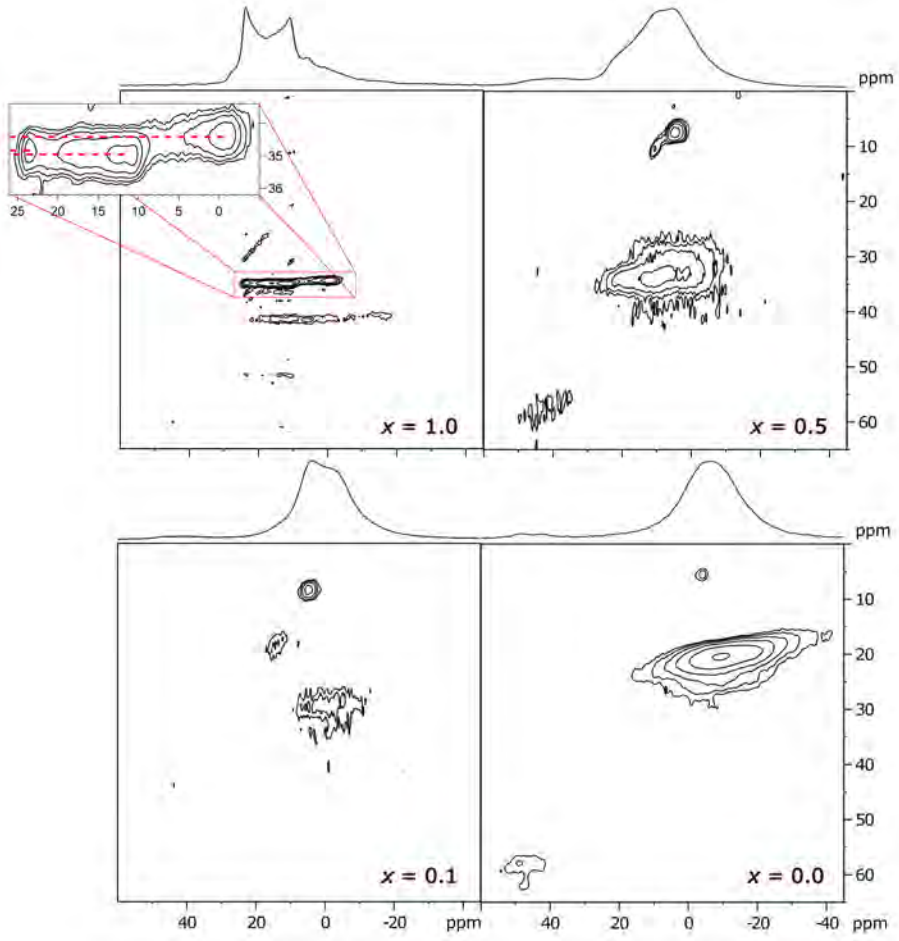

Figure 4.23: ^{23}Na MQMAS of the samples on formula $Na_{2+x}Zn_2Sb_xTe_{1-x}O_6$ with x = 1.0, 0.5, 0.1 and 0.0. Inset is of the most intense peak in x = 1, with red dotted lines marking the indirect frequency of the peak maxima.

but in this situation the framework cations are red-ox active, allowing inhomogeneous Na-distribution.[56] The x = 1.0 sample has no red-ox active cations and has a full Na-layer, so neither of these previously reported mechanisms can be the origin of deformations in this material.

The diagonal peak straight above the most intense peak is likely from a real component with a large chemical shift distribution. No additional phases are present in the diffractogram. It is therefore much more likely that the additional peaks are due to stable defects and surfaces in the material, although the high amount makes both of these origins slightly improbable. Another option is other distinct Na sites, as we have already established a variety of slightly deformed Na sites.

The mixed materials have a gradual development towards the x = 0.0. The two Na sites can no longer be distinguished at x = 0.5, which is very likely due to the chemical exchange of Na between the sites from the introduced vacancies. This is consistent with the expectations from the single pulse spectra. All of these samples also have one symmetrical peak around 5 ppm in the indirect frequency. The lower intensity of the main component in the x = 0.1 sample is a little misleading, as this sample has a lower signal-to-noise ratio, and the 45 ppm component is not visible. The ratio between the two peaks still seems to have changed, and an additional component is visible between them. The origin of all these additional positions is unknown. In this case both changes in the Na-position from adjacent vacancies or bending of the framework layer as a response to vacancies are possible candidates.

The peak of the x = 0.0 is much wider compared to the mixed samples (x = 0.1 and 0.5). The P2 phase has the face-sharing Na-sites in addition to the edge-sharing (figure 2.2), giving a greater distribution of Na-environments. The component is diagonally oriented, suggesting a chemical shift distribution combined with the chemical exchange.

Chapter 5

Discussion

5.1 Sol-gel synthesis

A very important part of this work was identifying a reliable synthesis method to make single-phase substituted samples with a high degree of homogeneity. Previous efforts of similar layered materials used solid-state synthesis. The wet-chemical synthesis methods are highly appropriate for high-purity versions of (non-substituted) stoichiometric compounds like NZTO and NZSO for which solid solution derivatives so far have proven difficult to synthesize as pure single-phase materials.

One previous report on Ga-substitutions of a similar concentration has an as currently unidentified secondary phase.[29] This phase increases in proportion with increasing substitution. The material reported still has a significant increase in ionic conductivity, which suggests some substitution has been achieved by the solid-state synthesis. The Ga-substituted materials reported by Wu et al are completely phase pure,[94] although much lower degrees of substitution than those reported by Li et al or in this work.[29]

Substitutions of Li^{+} on Zn^{2+}-site in NZTO gives a two-phase material around 10% Li. The equivalent substitution level in this work, with 10% Sb^{5+} on Te^{6+}, gives a single O3-phase. The two substitution routes should yield the same Na-content, and could therefore be expected to give the same product. The Li-substitution is in line with the behaviour of Na_xCoO_2 described by Lei et al.[27] The phase diagram (reproduced in figure 2.3) has large multi-phase regions for different Na-content and synthesis temperatures. This reaction is however not constrained by framework ions, as the Co can charge compensate for Na-concentration. The chemical composition of the NZTO derivatives is completely determined

by the distribution of the substituted ions, which is likely to be inhomogeneously distributed in the solid-state synthesis. Bianchini et al. report the in-situ synthesis of P2-$Na_{2/3}CoO_2$ from solid precursors. An O3-$NaCoO_2$ phase forms at the interphase after minutes only. This reaction is not compositionally constrained at the interphase and thus forms the most thermodynamically stable phase with secondary phases of the other precursors. The precursors and products then react through slow nucleation and growth of the stable P2 phase. The sol-gel synthesis likely diverts from this reaction pathway, as the reaction happens in the dried gel, with a homogeneous distribution of all precursors and not interphase. The reaction *is* therefore compositionally constrained, as opposed to the reaction described by Bianchini et al. The material can therefore directly form the equilibrium phase for the given Na-composition.

Itaya et al investigated the influence of excess Na-precursor.[166] They demonstrate that while lower excess gives a better sample density, the ionic conductivity is increased. The mechanism might be from secondary phases decreasing the grain boundary resistance. In the annealing steps, Na-loss due to volatilization may result in the formation of ZnO as an impurity phase. This is also the main impurity observed in this work. This suggests that the ZnO impurity we observed insufficient Na-excess for the sintering temperature and -time used in this work. We used 10% excess, which was found by Itakaya et al. to be sufficient. The differences between this work and theirs are they use lower sintering temperature (850 to 900 ℃), longer sintering time (12h to 3h) and different precursors (solid-state synthesis). The amount of the ZnO impurity in this work also varies between samples that have the same sintering program. We therefore suggest that the volatility precursors are influenced by the ratio of other species present. However, finetuning the Na-excess could remove the ZnO impurity observed in NZTO and the Sb-substituted samples.

5.2 Characterization of solid solution derivates

Tailoring of material properties is often achieved through chemical tuning, for example through substitution. However, the atomic consequence of chemical substitutions on the local and average atomic arrangement can only be assessed by the use of a combination of methods, each individually having its limitation, e.g. diffraction versus IR/RAMAN or NMR spectroscopy. Standard characterization techniques like diffraction or spectroscopy have limitations with respect to resolution. Two different substitution mechanisms have been investigated using ^{125}Te NMR in this work. Ga^{3+} substitution on the Zn^{2+} position in *$P6_322$*

NZTO and Te^{6+} on Sb^{5+} in *C2/m* NZSO. For internal consistency, this method is called Sb^{5+} substitution on Te^{6+} in NZTO in the following discussion. ^{125}Te NMR is a suitable element probe for measuring due to a large number of surrounding electrons, making it sensitive to very small variations in the chemical environment.[33]

The two substitution situations have significant differences. In the Ga^{3+}-case, the substitution takes place on neighbouring position to those of the measuring nuclei ^{125}Te. In the case of Sb^{5+}, the substitution occurs at Te sites that are being measured. These measurements must be approached and analyzed in different ways, which demonstrates both the limitations and versatility of NMR.

The nominal amounts of the substituents are easily explored in the Ga-substitution. The substituted Ga^{3+} is positioned adjacent to Te^{6+} and thus gives additional peaks in the Te-spectra, as seen in figure 4.2. The integrated signal of the different peaks is matched with the nominal substitution. This is done by considering the number of Te-neighbors to any Ga-sites, and thus calculating the fraction of Te with a neighbouring substituent. This is a relatively straightforward and robust analysis but does not give further structural information about the Na distribution in the material. In order to gain insight into the Na-substructure, we need to include other techniques or modelling like DFT.

The nominal amounts of Sb-substituents could also be confirmed using NMR. The analysis is more complex because the incorporated ion is located too far from the Te-nuclei to influence the ^{125}Te spectra directly. Nevertheless, a realistic model can be constructed by some simple chemical assumptions: i) The Sb/Te distribution is stochastic, ii) the Na-sites surrounding any Sb/Te-position will have a specific probability of Na/v_{Na} filling depending on the specie at the Sb/Te site, to compensate for the larger charge differences, and iii) the Na in the second coordination sphere of the Te atom will have an influence on the Te chemical environment, and can therefore be observed in the ^{125}Te spectra. The latter point is relatively likely, as this is similar to the situation described for the case of the Ga-substituted samples above.

Using these simple assumptions, we demonstrate that the Te-environments are described by conditional probability: The probability of having either Sb or Te at the two neighbouring positions (p(Te)) and the probability of the number of Na-neighbors given the Sb/Te neighbours ($p(R_{i\mathrm{Na}}$—$j\mathrm{Te})$). The correct ratios of Te-environments are only produced when we consider the two closest Te/Sb positions in adjacent layers. This is calculated in section 4.4, but can also be understood more intuitively. Both ^{125}Te spectra are decomposed to two components, while there are three possible combinations of neighbours ($R_{4\mathrm{Na}}$, $R_{5\mathrm{Na}}$

and R_{6Na}) if assuming no v_{Na} is placed in adjacent positions within a layer. The situation with only the closest neighbours will always exclude the R^{6Na} configurations, as one v^{Na} must compensate for the central Te. If all connected Na is included, all three configurations should be present. The ratios of the peaks would also be different, as reported in table 4.7. It is therefore clear that the compensating Na og v_{Na} is only determined by the closest neighbours.

It is interesting to consider what we actually understand with a homogeneous solid substitution. In NZTO this would mean stochastic distribution over the relevant Sb/Te-sites. But, at the local scale, the distribution of Na is not random. It is rather a direct result of the local Sb-Te distribution. The same reasoning cannot be followed for the Ga/Zn distribution. We only know that Te is neighbouring a correct amount of Ga, but not the further distribution of Ga and Zn. It is clear that all regions are influenced by the substitution, as the centre peak of ^{125}Te changes with increasing substitution and is assigned to Te without Ga-neighbors. If we would have regions exactly as the unsubstituted NZTO, the spectrum should be a composite containing the exact peak shape of the unsubstituted spectrum. As the distinct shoulder feature is absent (the whole spectral weight is moved to higher frequencies), the whole sample is clearly influenced by the substitution. This excludes regions without any Ga-substitutions and demonstrates that all Na in the material is influenced by the substitution.

It might be problematic to prove the existence of small amounts of secondary phases that could occur as a result of a heterovalent substitution by standard techniques. XRD is great at identifying the presence of crystalline phases, but amorphous and nano-sized particles can easily escape detection. They would be distinct in NMR, which is a local probe. Amorphous or nano-sized secondary phases will have distinct chemical environments, with respect to neighbouring specie and relevant coordination polyhedra.

5.3 The validity of Wyckoff sites as approximation for Na-sites

In this work, we have put special emphasis on deriving a satisfactory description of the unsubstituted NZTO structure. The average structure, as defined by the space group $P6_322$, has three non-equivalent positions for Na: *6g*, *4f* and *2a*. Na atoms are placed in the centre of the three different coordination trigonal prisms. All these three Na-sites represent special

positions. While the Na-structure was revealed to be more complex, it is still useful to consider these positions as a good approximation of unsubstituted NZTO when a detailed description is not necessary.

The most important findings in this work concerning Na-positions refer to the ^{23}Na NMR data collected at 100K, and the description of the modulated Na-substructure and the RMC simulated structure based on synchrotron powder diffraction data. The NMR demonstrate that the Na-atoms in NZTO are separated into three distinct groups. These groups are described by the Czjzek distribution, which describes the distribution of quadropolar peak shapes. This demonstrates a clear internal distribution of chemical environments.

It is interesting to compare the findings from ^{23}Na NMR, the modulated average structure and the disordered structure generated by RMC modelling. However, we first need to emphasize the difference in temperature between these experiments. The three distributions are only visible in the NMR spectra at 100K, and any changes with respect to number, ratio or internal distribution of sites with increasing temperature are not possible to confirm by ^{23}Na NMR. We can therefore not say if the distribution of three distinct groups of sites is still present at room temperature. The XRD and PDF data are measured at room temperature and no low temperature data are at hand. It is therefore important to note that there might exist different Na-substructures due to temperature effects. Temperature must therefore be considered when comparing the structure models. Note that thermal disorder could have major effects on the RMC structure, but thermal vibrations are always averaged on the NMR timescale and is therefore not the source of the distribution described by the Czjzek model.

The degree of filling of the ideal Wyckoff sites, as well as atomic displacement relative to the ideal coordinates, has been elucidated by RMC modelling and the modulated structure description. The results from the two methods both suggest that Na is rarely positioned in the centre of the prismatic sites. There is either an offset in the modulated structure or a broadening of the distribution suggested by the RMC structure. This offset is expected to correlate with the measured internal site distribution of the ^{23}Na NMR at 100K. More importantly, the new ”hybrid” Na-site is preserved in both X-ray-based approaches, where the Na is positioned between the *6g* and the *2a* site and surrounding half of the *2a*-sites. The occupancy of this hybrid *6g/2a*-site sums up to a very similar value as the integrated intensity of the smallest component in the ^{23}Na NMR data at 100K (14% to 9%). The NMR decomposition does not include spatial information which can confirm the features to be the same. We would however expect the ”hybrid” *6g/2a* environment to produce a distinct

Table 5.1: Comparison of Na-distributions reported in literature between different measurement techniques. The Na-distribution refers to the percentage of Na in each site.

Na-distribution ordered from similarity			
Peak 1	Peak 2	Peak 3	Reference
52	39	9	^{23}Na NMR at 100K, this work
62	24	14	Supercell XRD, this work
Na-distribution assigned to sites			
6g	4f	2a	Reference
43	55	2	XRD[24]
58	30	12	DFT, this work
67	28	5	XRD[31]
71	22	7	DFT[31]

chemical environment from the other Na-positions identified in the modulated structure. This together with the integrated similarity does suggest that the different measurements could identify the same structural deviation.

There are significant variations in reported values for site occupancies, see table 5.1. The reported thermal parameters are usually quite high,[25] as could be expected for an ionic conductor. However, the anisotropic thermal parameters indicate displacement from Na-movement, and not only thermal vibrations. In Rietveld analysis of powder diffraction data, the thermal parameters are highly correlated with site occupancy. Rietveld refinement therefore requires constraints on the total Na-content. The current finding shows that the Na-displacements have different directions and magnitudes for the various sub-groups of Na-atoms. The frequent use of one common displacement (”temperature”) parameter for non-equivalent Na-atoms is inadequate.

It should be noted that for a realistic description of the Na-substructure of NZTO, a single-unit cell is not sufficient. As the ”hybrid” *6g/2a* position is only present around half of the *2a*-sites. The proper description needs at least a $2\times2\times1$ supercell to describe the correct Na-positions, even in instances where the full modulated structure is unnecessary. In summary, the *4f* and *6g* are good approximants for positions with Na-atoms, although the details are much more complex. The *2a*-site appears to not be filled with any Na-atoms in the NZTO structure.

The hybrid *2a*/*6g* position has, to our knowledge, not been considered earlier. Hence, previous DFT simulations did not take note of this possibility when assigning Na-atoms to either of the non-equivalent symmetrical sites.[28,93,167] The same is true for the previous analyses of the Na-substructure from XRD data.[24,25] The only exception could be Karna et

al., who report that the Na-positions in NNTO are split into multiple surrounding sites.[168] This could be seen as a similar feature to the ”new” hybrid position reported here.

5.4 Na-disorder in Sb- and Ga-substituted variants

The previous section relates to the average structure and the approximation of average sites in NZTO. Some of the structural differences described for the pure NZTO could likely be present in the substituted materials, but no detailed description is made. This section will therefore look at indications of structural variations in the Sb- and Ga-substituted materials which are not described by the average structure.

In this work, the detailed RMC and modulation structure descriptions have only been obtained for pure NZTO. However, the ^{23}Na NMR spectra at 100 K have been recorded for Ga-substituted NZTO with x = 0.10, 0.15 and 0.20, figure 5.1. As discussed in section 4.2, the NMR signatures for these could also be described using the Czjzek distribution, demonstrating the same disorder within the three groups of positions. The integrated intensities of the three NMR deconvoluted signals illuminate aspects not previously discussed. In section 4.1, the DFT calculations predicted that upon increasing Ga-substitution, the *2a* site will become increasingly occupied. This can provide more shielding by forcing layers apart because it places more Na in positions that are face-sharing with the framework cations. It is unclear if the hybrid *2a*/*6g*-site will provide the same local charge compensation.

It should be emphasized that we have no measurement which demonstrates a modulated structure in the Ga-substituted samples. We have the options that i) NZTO is a special case and is the only material exhibiting such complex structure, ii) the Ga-substituted samples have the exact same modulated structures or iii) the substituted materials also have some sort of superstructure that changes with Ga-substitution. The only indication we have of either is the 100K NMR which has the distribution of chemical environments as for NZTO. This points to either of the latter two options. This is also more likely as we have few indications of larger structural changes from the Ga-substitution. The NNTO structure reported by Karna also displays structural deviations, which could be similar to what is described in this work.[168]

The ^{23}Na NMR spectra at 100 K for Ga-substituted samples were not discussed in detail in section 4.2, shown in figure 5.1. However, these can be better understood with greater insight from the Na-site discussion. Looking at the ratios reported in table 5.1, multiplicity considerations do suggest that the left peak is related to the *6g*-site, the middle is to the

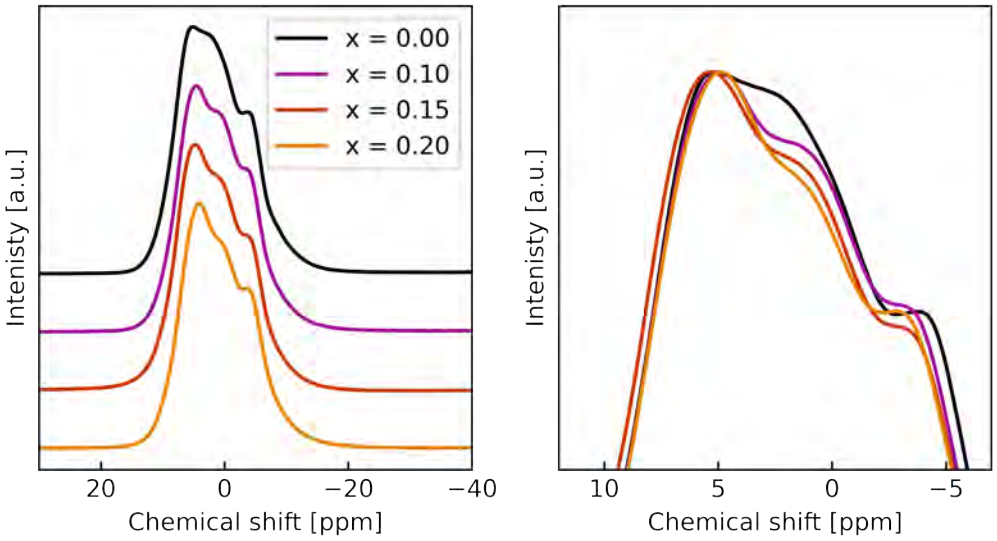

Figure 5.1: a) Normalized ^{23}Na MAS NMR of samples (x = 0.00, 0.10, 0.15, 0.20) at 100K in a 18.8T field, and b) same spectra moved in ppm to position normalized maxima at the same ppm for simple visual comparison of change in components.

4f and the right is due to the *6g/2a* hybrid site. The middle component, assigned to *4f*, decreases linearly with increasing Ga-substitution. The right component changes between samples, but is non-linear between samples. The decrease of the *4f* is the opposite of the trends predicted in sections 4.1, suggesting that the more complex Na-structure must be included in simulations predicting Na-site distribution.

We do not know the source of the environment distribution identified by the Czjzek distribution and the modulated Na-substructure. One explanation could be that the displacements are a response to the surrounding Na distribution. Na is displaced towards empty adjacent sites and simultaneously pushed away from surrounding Na-ions because of strong Na-Na repulsions. However, from the MQMAS in section 4.4, we know that the fully sodiated NZSO also has multiple deviations between the symmetrically equivalent sites. This cannot be due to an identical mechanism since all Na-sites are filled according to the compound stoichiometry. The high intensity of NMR signals excludes common sources of disorder, like grain boundaries and interfaces, which cannot account for a large fraction of the Na positions. Instead, there might be several structural deformations, which are not caused by Na-Na interactions alone. It is worth noting that the peak positioned at 0 ppm in NZSO suggests Na-atoms in a nearly perfect octahedron, rather than deformed (elongated) poly-

hedral as described by the average structure. This indeed supports some type of structural deformations and indicates that the average structure model is insufficient.

5.5 Interlayer interactions

Indications of significant interactions between neighbouring Na-layers were provided by DFT simulations of the Te-environments. Very few Na-atoms were found in a 1*f*1*f* configuration, meaning that almost no Na is positioned in the 4f-sites on both sides of a Te-octahedron. This is highly unlikely because the *4f* site has a high degree of occupancy. Assuming the layers are independent, the Na-placement in adjacent layers is stochastic. The chance of two *4f*-sites on either side of a Te-atom (1*f*1*f*) being occupied simultaneously would be relatively high. However, this environment is not found in the simulations. This could suggest that the Na-placements in the layers are not completely independent of the adjacent layers.

The proposed modulated structure also suggests this kind of interlayer interaction. A $2\times2\times3$ cell is necessary to describe the modulated structure, which means the supercell spans six layers. From the general trends of the modulated structure, the *4f*-sublattice shows modulations along the *z*-direction. Of the Na-sites described by the superstructure, *4f*-position is face sharing with the framework-octahedra, as no Na is found in the *2a*-position. The face-sharing position is known to be the less stable configuration from Pauling's third rule, which could be a driving force for deformations. However, the stability calculations from section 4.4 demonstrates that the P2-phase is stabilized by the occupation of both the Na_{edge} and Na_{face}, as observed for other layered materials such as Na_xCoO_2.[27] One mechanism could be similar to what is described by Roger et al. for Na_xCoO_2. They demonstrate that the framework layer displaces in the *z*-direction as a response to a trivacancy (which is three adjacent Na_{face}). This would be a mechanism where an occupied position of Na displaces Te or Zn, and thus blocking the adjacent sites.

A similar Na-to-Te/Zn displacement is mirrored by the description of the cooperative Na-diffusion mechanism described by Huang et al. for both NZTO and NMTO.[93] The phonon vibration mode of $ZnO_{6/3}$ moves so the Na-prisms are shrinked or enlarged up to 1.2%, as they move away or towards each other when Na is situated between (figure 2.8) They also find that the Te and Zn vibrate symmetrically around their average position. This is in line with observations from the modulated structure, where Te and Zn are not offset. The mechanism identified by Huang et al. specifically mentions the Zn vibration as the one that

moves the most, while Te is not found to similarly move. However, we started this section by pointing out the lack of the 1*f*1*f* Te-environment in our DFT calculations. This could suggest a similar mechanism as Huang et al. describe for the Zn vibration for the Te-vibration. Te moving as a response to face-sharing Na is thus blocking Na-sites in adjacent layers. Na-ions in one layer would then effectively block Na-positions in adjacent layers, which is what is suggested in this work. Note that in the modulated structure, only the *4f*-sublattice has empty sites, while the *6g*-sublattice has no empty sites (figure 4.14). This is what we would expect from the mechanism discussed above, as the *4f*-sites are the only face-sharing sites, and should therefore be more influenced by the Zn/Te vibrations.

5.6 Investigating changes in Na-dynamics from Ga-substitution

This work has been focused on improving the Na-dynamics by Ga-substitution. This reduces the Na-content and thus also the Na-Na interactions. The general hypothesis is that the Na-Na repulsion is the main bottleneck for ionic conductivity. Underloaded Na-layers improve ionic conductivity and changes the energy landscape.[36] As the general hypothesis is about the local scale, our methods are also focused on the local dynamics of the Na movement. We hypothesized that the Ga-substituted samples would have a visible decrease in the activation energy of Na-dynamics, which is exactly what was observed in section 4.2.

Contrary to this, Li et al. observe a limited increase in the ionic conductivity.[29] There is already a large Na-vacancy concentration in the original NZTO structure. Therefore the limiting factor for ionic transport was not assumed to be vacancies (and sites for jumping), but strong Na-Na repulsion. Na-Na repulsion should be radically reduced when the Na content is decreased by 10%, as for the highest substitution $x = 0.20$. Previous simulations with a reduced Na-Na repulsion suggest a drastic conductivity increase.[51] Simulations are well known to easily under- or overestimate E_a, however, there is a genuine question whether there are any overlooked effects from the Ga-substitution that must be included to properly model and explain ionic conductivity.

The first to note here is the result of the relaxation measurements. The activation energy of Na-dynamics of the $x = 0.00$ sample was calculated value very close to previous measurements at 0.30 eV, both by DFT and relaxometry, suggesting that this is the correct value. When using equation 3.3.2, we found a limited effect on the activation energy for

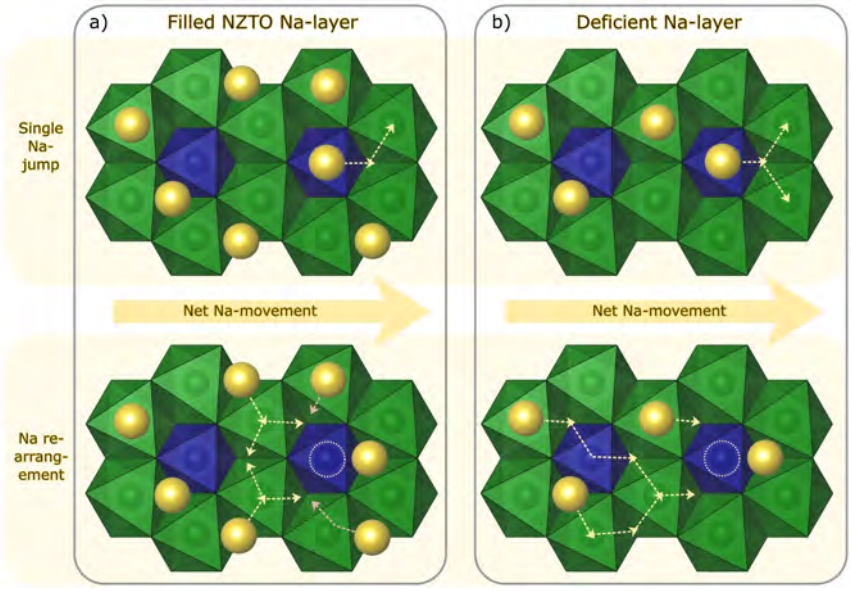

Figure 5.2: Na-jumps in in (a) filled Na-layer and (b) emptied Na-layer (highly exaggerated). Moves with jumps that moves by a position adjacent to a filled one, additional jump by the adjacent Na would be required. For simplicity, only movement in one direction is considered, but as it is a stochastic process the first jump in b) have multiple available jump directions.

the lower substituted samples, but an increasing Ga-substitution decreases the activation energy significantly. However, the high-temperature curve is clearly a little flatter compared to the measured point, which tapers off. In that case, we must refer to the activation energies of the Arrhenius equation. This calculation gives much lower activation energy for the higher substituted samples. The x = 0.20 sample has activation energy at 0.14 eV using the Arrhenius equation and 0.2 eV using the more sophisticated 2D model. The former is close to previous NEB calculations of NZTO at 0.09 eV.[25] NEB-calculations only model a single ion moving between sites and do not include the interactions between moving ions. It is therefore known to underestimate activation energy. The low activation energy for the substituted samples could be from fewer Na-neighbors blocking the Na-movement, and individual jumps are thus more unconstrained. However, an increase in jumping frequency does not necessarily translate to increased net transport.

The Sb-substituted samples reveal something useful about the Na-structures. These samples are an O3-type phase, and all Na are positioned in the Na_{edge}-type site, the same as the *6g*-site analogue. We demonstrated that the Na-structure was regulated by the cations in the framework. We demonstrate that the charge compensating Na for Te^{6+} and Sb^{5+} was selectively placed in the two Na-sites shared by the closest Sb/Te neighbours, and not in the other shared Na-position. This suggests that the material has a short range of charge compensation. Na thus has a small region in which it can move, without additional compensation from another Na. One could expect this localized feature in Sb-substituted samples to be due to a result in lower ion diffusion. However, the ^{23}Na NMR reveals dynamic mixing at room temperature for both Sb and Te mixes.

We hypothesize that the long-range movement of Na is a product of the charge compensation. Increasing facile Na-ion movement is dependent on making individual jumps more energetically favourable, reducing activation barriers and having available empty sites. Long-range Na movement also requires a constant rearrangement of Na so that no region is charge depleted or filled up by surplus positive Na-ions. This aspect is easily overlooked since the materials discussed in this aspect are often cathode materials. They have red-ox active cations which can change charge state and therefore allow regions to be depleted (or have a surplus) of positive charge. This is not true for the currently considered solid-state electrolytes, where no cation is red-ox active and hence the Na-distribution is much more constrained. If one Na jumps to contribute to the long-range movement (ionic transport), it is necessary that another Na is jumping to the now depleted region to keep charge neutrality. With the stochastic nature of the Na-jump, driven by thermal energy, it is quite likely

that the original Na-ion jumps back to its original position, resulting in no net movement. This is illustrated in figure 5.2, where a correct Na-filling for NZTO is compared to a highly exaggerated depleted Na-layer. It is clear that for the initial jump, the Na in NZTO has only one possible route that will give long-range movement in the correct direction, as the sites adjacent to other filled Na are blocked. In the deficient layer, there are fewer Na-atoms to block movement and there are therefore multiple possible directions.

When looking at the rearrangements, the full layer is more favourable. There are multiple close Na, and only one or two jumps are needed to move into the positions close to the vacated Na-position. This is not true for the depleted layer. The Na is positioned further apart, and most Na needs multiple jumps to move within the depleted region. In addition, there are fewer Na which can move. This lowers the probability of the correct movement. The Na that just vacated the position is therefore the most likely to move back. Although this figure is severely exaggerated, fewer Na and therefore longer Na-Na distances are present in all substituted samples.

How these two separate processes balance is unknown, but it is clear that they could to some extent counteract each other. This is in line with the reduction in activation energy but yet has a limited impact on the ionic conductivity in Ga-substituted samples. However, an SSE would always operate along a concentration gradient. This could be where there is a real driving force for the ionic diffusion in one direction. This additional driving force could counteract some of the effects described in this section, and the lower activation energy for the higher substituted materials could be exploited.

5.7 Comparison of Ga-substituted NZTO with other Na-ion conductors

This work has had a mechanistic focus on the local Na-dynamics to gain insight into a method using cation substitution to decrease Na-content, often assumed to improve ionic conductivity. The overarching goal is moving towards improving NZTO for use as an SSE. In this section, we will discuss the properties of Ga-substituted NZTO as an ionic conductor in light of the status of some other SSEs candidate materials. Note that only the Ga-substituted P2 materials are discussed in this section. The O3-phase has a much lower ionic conductivity than the P2,[25] and is therefore not viable as an SSE.

Table 5.2 provides a comparison of our findings as well as literature data on NZTO with

Table 5.2: Activation energy and ionic conductivity for NZTO and some selected SSE-candidates. The type of measurements are split into local (NMR) and average (grain boundary and bulk conductivity of EIS techniques). Materials denoted with *x* only are substituted variants of NZTO.

Composition	Activation energy [eV]	Ionic Conductivity [mS cm^{-1}]	Reference
Local measurement techniques			
NZTO	0.32	0.18	This work
	0.14/0.12		Li 2018[29]
x_{Ga} = 0.05	0.30	0.33	This work
x_{Ga} = 0.10	0.32		This work
	0.05/0.07		Li 2018[29]
x_{Ga} = 0.15	0.26	0.48/0.56	This work
x_{Ga} = 0.20	0.20		This work
Average measurement techniques			
NZTO	0.32	0.63	Li 2018[29]
		0.63	Deng 2019[97]
		0.57	Wu 2018[94]
x_{Ga} = 0.05	0.29	0.74	Li 2018[29]
		0.83	Wu 2018[94]
x_{Ga} = 0.10	0.27	1.1	Li 2018[29]
x_{Ga} = 0.15	0.28	0.73	Li 2018[29]
x_{Ca} = 0.02		0.75	Deng 2019[97]
NMTO	0.23	0.34	Li2018[92]
Na_3PS_4 (cubic)		0.2	Hayashi 2012[133]
Na_3SbS_4		1.0	Hayashi2019[137]
$Na_{2.88}Sb_{0.88}W_{0.12}S_4$	0.18	32	Hayashi2019[137]
$75\,Na_2S \cdot 25\,P_2S_5$		0.1	Nose 2015[138]
$94\,Na_3PS_4 \cdot 6\,Na_4SiS_3$		0.74	Tanibata 2014[134]
$Na_3Zr_2Si_2PO_{12}$	0.385	2.7	Samiee 2017[129]

corresponding data for other SSE materials candidates. The slight differences in reported values for NZTO are expected because NMR relaxometry, EIS and DFT probe slightly different features of the mechanisms. Wu et al. report a large influence on total conductivity from grain boundaries for NZTO. This suggests that synthesis type and conditions might have a large influence on the measured values for EIS.[94]

Pure NZTO has a higher ionic conductivity than pure NASICON, but substitutions have been successful in improving average ionic conductivity in the latter. The same is true for the sulfide system, with the development from Na_2PS_4 to Na_2SbS_4 to $Na_{2.88}Sb_{0.88}W_{0.12}S_4$ giving an improvement of two orders of magnitude in ionic conductivity. Understanding the substitution mechanism has thus been fundamental in improving other classes of SSEs, and, likely, further improvements could also be realized in the layered oxide system.

The current findings support the hypothesis that the removal of Na-cations from the 2D structure by creating vacancies as a result of heterovalent substitution decreases Na-Na interactions and lowers the activation barrier for Na-hopping (figure 4.9). However, this strategy is not sufficient to increase the actual ionic conductivity. The local Na-substructure can show disorder, however, major redistribution and movement appear to be hindered. Na-ions are required for the general reduction of repulsion between the neighbouring O-layers. If other strategies could be used to decrease the O-O repulsion, the large decrease in activation energy for local Na-movement could be translated to long-range movement.

One strategy could be to introduce the Ca substitution for the smaller *M* (Zn in our case) as described by Deng et al.[97] It gave a significant decrease in activation energy with very small Ca-substitutions, due to the larger Ca substituting Zn (1.14 Å vs 0.74). Another possibility is introducing larger monovalent cations in the Na-layer. To our knowledge, there is no report on the potential effect of tiny amounts of divalent substituents in the Na-layer (Mg, Ca possibly), which locally may help reduce Na-ion concentration (creating vacancies) as well as provide charge balance.

The concentration of vacancies is often emphasized to be an important factor for increasing ionic conductivity, but the situation appears to be more complex for NZTO-based materials. In pure NZTO, there are four vacancies for every two Na-ions, but this is not the real situation. Two adjacent sites cannot be simultaneously occupied, due to the high Na-Na repulsion. When considering the change in site only, the number of vacancies is only increased by 5 % for the highest adopted Ga-substitution in this work. But as one Na atom would block its own site, and the three adjacent, the number of vacancies created is thus much larger.

An often overlooked problem with SSEs is their electrochemical stability. Huang et al demonstrate that the NZTO is stable in a relatively narrow voltage window from 2.25 to 3.23V.[93] The stability window of NZTO can be increased by incorporating Mg. The decomposition products at 0V are of the highest interest, as this would be the voltage at the SSE/anode interphase. Huang et al. demonstrate that most of the decomposition products at 0V are electronically insulating.[93] This would create an electronically insulating SEI phase, which creates a stable metal-electrolyte interphase and thus extend the operating voltage window beyond that of the material (see figure 2.10). However, Tian et al. demonstrate that it is not sufficient to consider the thermodynamically stable phases. Intermediate products can form instead of the thermodynamically stable phases.[169] This can thus widen the effective electrochemical window, which was demonstrated by Huang to be widened to

3.57V.[93] Compared to other alternatives, the electrochemical stability window for NZTO is much wider than that of the sulfides (0.21-0.46 V), but other oxides like NASICON (2.53), $Na_2Ti_2(PO_4)_3$ (2.97V) or $NaZr_2(PO_4)_3$ (3.10V) have even wider stability windows.[93]

Chapter 6

Concluding remarks and outlook

Layered oxides are currently popular candidates for solid-state electrolytes. We have in our fundamental approach with the objective to better explore and understand such materials at the atomic scale. This work has focused on Na-substructure and mobility in a layered oxide class, for the possible applications as solid-state electrolytes. We used techniques and tools such as NMR, DFT and PDF to characterize the local structure. We can thus focus on aspects which cannot be characterized in the more standard battery material measurement techniques like impedance spectroscopy and battery cycling. However, the chosen materials are not redox active and are in that sense not relevant as electrode materials. This expands the fundamental understanding of the mechanism of Na-mobility. Ideally, the findings will enhance the current understanding of limiting factors for high-rate ionic conductivity in layered oxides and thereby provide synthetic pathways to improved SSE. This understanding should build on the atomistic understanding of the Na interactions in all layered oxides. The layered oxides used for SSEs contain only elements with fixed oxidation states in the framework layer. To achieve local charge neutrality, this means the Na distribution must be homogeneous at all times, reducing the degree of freedom for the Na structure. The behaviour of Na in these layered materials might therefore help with the understanding of the cathode materials with red-ox active cations that allow for inhomogeneous Na distribution.

The most important motivation for this investigation was to gain insight into how Na-non-stoichiometry influences Na mobility. If Na-Na interactions are a major contributor to the activation energy for Na-ion jumps, then we would expect a reduction in the activation energy on removal of Na-cations from the Na-substructure, to be achieved via heterovalent

substitution. This has however not been confirmed in measurements on Na-mobility and long-range Na-diffusion only very slightly increased.[29] Removing Na is the method often chosen to reduce the Na-Na interactions, assumed to be the limiting factor. Previous investigations physically tune the Na-Na interactions,[51] which is not equivalent to removing Na. The work suggests that the activation energy is lowered by the removal of Na and thus the frequency of local hopping is increased, it does not necessarily translate to a higher ionic conductivity.

We suggest that this lack of translation from lower activation energy for Na-hopping to long-range diffusion is due to the role Na is playing in charge compensation. This is supported by insight from the Sb-derivatives, where Na-content is increased instead of reduced (as for Ga). We demonstrate a quite small area from Te/Sb where the Na and vacancies must be placed to compensate. This suggests that when Na is sparse, the more mobile Na has a higher probability of jumping back to the region it just left and thus limiting long-range movement. Further work on Na-conductivity must therefore not only address Na-Na interactions but also the role of charge compensation. A possible way to counteract these effects partially could be the introduction of a larger cation, e.g. Ca-substitution, as demonstrated by Deng et al., which increases interlayer distances even at small amounts of substitution.[97] Ca-substitution could therefore decrease the local charge density and maybe increase the freedom of the Na. As a divalent cation, the local structure of Ca-ions with respect to the heterovalent substituents (Ga, Sb) would be different from that of the Na-ions, and worthwhile exploring in future studies.

The currently applied wet chemical / sol-gel synthesis routes provide homogeneous products with expected nominal compositions, including for the substituents. This allows substitution without creating secondary phases, or regions in the crystallites with non-equilibrium compositions of the substituents. We also wanted to find a method to verify substitution. In this respect, we need to go beyond conventional powder X-ray diffraction which is limited in quantitative resolution and where local inhomogeneities just show up as peak broadening (strain). ^{125}Te NMR was demonstrated in two instances to characterize the substitution method. The Ga-substituted materials get an additional peak in the ^{125}Te NMR spectra, confirming the nominal composition. The Sb-substituted materials observe the Na-distribution surrounding the observation nucleus ^{125}Te, which is modelled by a simple conditional probability.

Elemental substitution appears as a fully appropriate route to improve the layered material class for use as SSE. However, in line with the efforts put into this project on synthe-

sis, the obtained products must be homogeneous, both for any fundamental studies and for more applied screening. The strategy on heterovalent substitution is of course quite generic. However, the NMR characterization would require suitable NMR active nuclei as observers. There are many factors influencing if nuclei would be good for similar characterization. One factor making Te a very good candidate is the many surrounding electrons making it sensitive to very small variations in the second or third coordination sphere.[33] However, we have demonstrated that both the substituted and the surrounding elements can be used for such verification, meaning that many SSEs can be characterized with NMR.

This work has in addition made an in-depth study of complex ordering schemes that may occur in multicomponent layered oxides. The real situation can indeed be very complex, compared to the rather simple average picture description. We demonstrate a very long range of Na interactions resulting in a very large $2\times2\times3$ supercell, spanning six full layers of NZTO. This work should be expanded to investigate how Ga-substitution and reduced Na-content influences the superstructure. The face-sharing Na-positions are suggested to be the source of the long-range interactions, causing the superstructure. this is supported by the adopted modulated structure descriptions, in which the *4f*-site is the only one with any offsets in the *z*-direction. A similar effect was observed by Roger et al. $Na_{0.8}CoO_2$, where trivacancies of Na_{face} create an offset in the framework layer.[55] It would be of great interest to expand the work on the superstructure into the other materials described by Evstigneeva et al. ($Na_2M_2TeO_6$ for M = Ni, Mg and Co in addition to Zn). If Na in the Na_{face} positions creates this long-range superstructure, it would be expected that these materials also display a similar long-range structure. However, the superstructure can be changed by differences in the cation size of *M*. Additionally, the Ni-variant has a different stacking (Te-Te and Ni-Ni columns only), which could change both the column disorder and the Na-substructure. Expanding on the superstructure could further expand on the understanding of the cooperative nature of the Na movement.

From a practical point of view, substantial R&D work remains before layered oxides will have properties making them realistic alternatives for SSE in Na-ion batteries. This work is focused on ionic conductivity, which is currently too low to completely replace a liquid electrolyte. Other solid electrolytes have seen improvements in ionic conductivity of many orders of magnitude, but it is yet unknown if the oxides can be similarly improved. It is however likely that these could already be high enough for certain applications, where rate is not the main limitation. The largest challenge for the oxide class is however likely to be the cell integration. It needs to be integrated into a real cell design, mainly ensuring

good contact with both electrodes. Designing a compound with good enough contact on the interfaces is a complicated process. The SSE material must then be included in the material synthesis, increasing fabrication costs. It could be applied as a coating or as a matrix surrounding one of the electrodes. The sol-gel synthesis should be a good method for either of these applications, as it is easier to take the gel stage to hierarchical structures like thin films or coatings compared to solid-state synthesis. The sol-gel synthesis is also a well-known synthesis method, which is an advantage when increasing the synthesis/fabrication from the lab scale to the industry scale.

The NZTO system remains a promising candidate for SSEs, with an ionic conductivity comparable to products in the process of commercialization. As an oxide, it has the advantage of being stable in air, and with the high Na content, it is less sensitive to water than layered oxides.[107] This would simplify the production process of the battery cells significantly, where significant power consumption is needed to keep the atmosphere either inert or dry depending on the material choice. Even with the same anode and cathode, a significant part of the production can thus be moved into less sensitive synthesis conditions. This will give a lower environmental footprint of batteries with NZTO as the SSE compared to today's technology, which is significant in the electrification of society.

Bibliography

[1] R. P. Allan, E. Hawkins, N. Bellouin, and B. Collins. *IPCC, 2021: summary for Policymakers*. Tech. rep. IPCC, 2021.

[2] A. Ekhtiari, D. Flynn, and E. Syron. “Gas networks, energy storage and renewable power generation”. *Chem. Eng. Trans.* 76 (2019), 889–894.

[3] A. I. Osman, M. Hefny, M. I. Abdel Maksoud, A. M. Elgarahy, and D. W. Rooney. “Recent advances in carbon capture storage and utilisation technologies: a review”. *Environ. Chem. Lett.* 19.2 (2020), 797–849.

[4] B. Wagner, C. Hauer, and H. Habersack. “Current hydropower developments in Europe”. *Curr. Opin. Environ. Sustain.* 37 (2019), 41–49.

[5] L. Fan, Z. Tu, and S. H. Chan. “Recent development of hydrogen and fuel cell technologies: A review”. *Energy Reports* 7 (2021), 8421–8446.

[6] M. Guarnieri. “Before Lithium-Ion Batteries: The Age of Primary Cells”. *IEEE Ind. Electron. Mag.* 16.2 (2022), 73–77.

[7] J. B. Goodenough and K. Mizuchima. *Electrochemical cell with new fast ion conductors*. 1981.

[8] A. Yoshino, K. Sanechika, and T. Nakajima. *Secondary Battery*. 1987.

[9] A. Manthiram. “An Outlook on Lithium Ion Battery Technology”. *ACS Cent. Sci.* 3.10 (2017), 1063–1069.

[10] *Special issue on strategic battery raw materials*. Tech. rep. 13. UN Conference on Trade and Development, 2020, 63.

[11] G. André and M. Godin. “Child labour, agency and family dynamics: The case of mining in Katanga (DRC)”. *Childhood* 21.2 (2014), 161–174.

[12] B. Farber, B. Krause, and R. S. De La Sierra. *Artisinal Mining, Livelihoods, and Child Labour in the Cobalt Supply Chain of the Democratic Republic of Congo*. Tech. rep. Center for Effective Global Action Policy Report, 2017.

[13] T. Yusaf, L. Fernandes, A. R. A. Talib, Y. S. Altarazi, W. Alrefae, K. Kadirgama, D. Ramasamy, A. Jayasuriya, G. Brown, R. Mamat, H. A. Dhahad, F. Benedict, and M. Laimon. "Sustainable Aviation - Hydrogen Is the Future". *Sustain.* 14.1 (2022), 548.

[14] H. Barthelemy, M. Weber, and F. Barbier. "Hydrogen storage: Recent improvements and industrial perspectives". *Int. J. Hydrogen Energy* 42.11 (2017), 7254–7262.

[15] T. Placke, R. Kloepsch, S. Dühnen, and M. Winter. "Lithium ion, lithium metal, and alternative rechargeable battery technologies: the odyssey for high energy density". *J. Solid State Electrochem.* 21.7 (2017), 1939–1964.

[16] S. R. Ovshinsky, M. A. Fetcenko, and J. Ross. "A Nickel Metal Hydride Battery for Electric Vehicles". *Science* 260.5105 (1993), 176–181.

[17] L. Ouyang, J. Huang, H. Wang, J. Liu, and M. Zhu. "Progress of hydrogen storage alloys for Ni-MH rechargeable power batteries in electric vehicles: A review". *Mater. Chem. Phys.* 200 (2017), 164–178.

[18] C. Vaalma, D. Buchholz, M. Weil, and S. Passerini. "A cost and resource analysis of sodium-ion batteries". *Nat. Rev. Mater.* 3 (2018).

[19] T. Wang, D. Su, D. Shanmukaraj, T. Rojo, M. Armand, and G. Wang. "Electrode Materials for Sodium-Ion Batteries: Considerations on Crystal Structures and Sodium Storage Mechanisms". *Electrochem. Energy Rev.* 1.2 (2018), 200–237.

[20] X. Wang, S. Roy, Q. Shi, Y. Li, Y. Zhao, and J. Zhang. "Progress in and application prospects of advanced and cost-effective iron (Fe)-based cathode materials for sodium-ion batteries". *J. Mater. Chem. A* 9.4 (2021), 1938–1969.

[21] A. Rudola, C. J. Wright, and J. Barker. "Reviewing the Safe Shipping of Lithium-Ion and Sodium-Ion Cells: A Materials Chemistry Perspective". *Energy Mater. Adv.* 2021 (2021), 1–12.

[22] P. Desai, J. Huang, D. Foix, J. M. Tarascon, and S. Mariyappan. "Zero volt storage of Na-ion batteries: Performance dependence on cell chemistry!" *J. Power Sources* 551.July (2022), 232177.

[23] J. Lamb, C. J. Orendorff, E. P. Roth, and J. Langendorf. “Studies on the Thermal Breakdown of Common Li-Ion Battery Electrolyte Components”. *J. Electrochem. Soc.* 162.10 (2015), A2131–A2135.

[24] M. A. Evstigneeva, V. B. Nalbandyan, A. A. Petrenko, B. S. Medvedev, and A. A. Kataev. “A new family of fast sodium ion conductors: $Na_2M_2TeO_6$ (M = Ni, Co, Zn, Mg)”. *Chem. Mater.* 23.5 (2011), 1174–1181.

[25] X. Li, F. Bianchini, J. Wind, C. Pettersen, D. S. Wragg, P. Vajeeston, and H. Fjellvåg. “Insights into Crystal Structure and Diffusion of Biphasic Na 2 Zn 2 TeO 6”. *ACS Appl. Mater. Interfaces* 12.25 (2020), 28188–28198.

[26] D. Carlier, M. Blangero, M. Ménétrier, M. Pollet, J. P. Doumerc, and C. Delmas. “Sodium ion mobility in Na_xCoO_2 ($0.6 < \times < 0.75$) cobaltites studied by ^{23}Na MAS NMR”. *Inorg. Chem.* 48.15 (2009), 7018–7025.

[27] Y. Lei, X. Li, L. Liu, and G. Ceder. “Synthesis and stoichiometry of different layered sodium cobalt oxides”. *Chem. Mater.* 26.18 (2014), 5288–5296.

[28] K. Sau and P. P. Kumar. “Ion transport in $Na_2M_2TeO_6$: Insights from molecular dynamics simulation”. *J. Phys. Chem. C* 119.4 (2015), 1651–1658.

[29] Y. Li, Z. Deng, J. Peng, E. Chen, Y. Yu, X. Li, J. Luo, Y. Huang, J. Zhu, C. Fang, Q. Li, J. Han, and Y. Huang. “A P2-Type Layered Superionic Conductor Ga-Doped $Na_2Zn_2TeO_6$ for All-Solid-State Sodium-Ion Batteries”. *Chem. - A Eur. J.* 24.5 (2018), 1057–1061.

[30] R. J. Clément, P. G. Bruce, and C. P. Grey. “Review—Manganese-Based P2-Type Transition Metal Oxides as Sodium-Ion Battery Cathode Materials”. *J. Electrochem. Soc.* 162.14 (2015), A2589–A2604.

[31] X. Li, F. Bianchini, J. Wind, P. Vajeeston, D. Wragg, and H. Fjellvåg. “ P2 Type Layered Solid-State Electrolyte Na 2 Zn 2 TeO 6 : Crystal Structure and Stacking Faults ”. *J. Electrochem. Soc.* 166.15 (2019), A3830–A3837.

[32] M. Bianchini, J. Wang, J. Wang, R. J. Clément, B. Ouyang, P. Xiao, D. Kitchaev, T. Shi, Y. Zhang, Y. Wang, H. Kim, M. Zhang, J. Bai, F. Wang, W. Sun, and G. Ceder. “The interplay between thermodynamics and kinetics in the solid-state synthesis of layered oxides”. *Nat. Mater.* 19.10 (2020), 1088–1095.

[33] P. Woodward, A. Sleight, L.-S. Du, and C. Grey. “Structural Studies and Order-Disorder Phenomenon in a Series of New Quaternary Tellurates of the Type $A^{2+}M^{4+}Te^{6+}O_6$ and $A_2{}^{+}M^{4+}Te^{6+}O_6$”. *J. Solid State Chem.* 147.1 (1999), 99–116.

[34] A. Faucher, V. V. Terskikh, and R. E. Wasylishen. “Feasibility of arsenic and antimony NMR spectroscopy in solids: An investigation of some group 15 compounds”. *Solid State Nucl. Magn. Reson.* 61-62 (2014), 54–61.

[35] S. J. L. Billinge. “Local Structure from Total Scattering and Atomic Pair Distribution Function (PDF) Analysis”. *Powder Diffraction, Theory Pract.* Ed. by R. E. Dinnebier and S. J. L. Billinge. Royal Society of Chemistry, 2008. Chap. 16, 464–493.

[36] K. Sau and P. P. Kumar. “Role of Ion-Ion Correlations on Fast Ion Transport: Molecular Dynamics Simulation of $Na_2Ni_2TeO_6$”. *J. Phys. Chem. C* 119.32 (2015), 18030–18037.

[37] A. Weiss. “A Secret of Chinese Porcelain Manufacture”. *Angew. Chemie Int. Ed. English* 2.12 (1963), 697–703.

[38] G. Centi and S. Perathoner. “Catalysis by layered materials: A review”. *Microporous Mesoporous Mater.* 107.1-2 (2008), 3–15.

[39] M. M. Hanczyc, S. M. Fujikawa, and J. W. Szostak. “Experimental Models of Primitive Cellular Compartments: Encapsulation, Growth, and Division”. *Science (80-.).* 302.5645 (2003), 618–622.

[40] P. K. Auerbach, Scott M and Carrado, Kathleen A and Dutta. *Handbook of layered materials*. CRC press, 2004, 2–4.

[41] A. H. Castro Neto, F. Guinea, N. M. Peres, K. S. Novoselov, and A. K. Geim. “The electronic properties of graphene”. *Rev. Mod. Phys.* 81.1 (2009), 109–162.

[42] J. Zhang and L. Gao. “Synthesis of antimony-doped tin oxide (ATO) nanoparticles by the nitrate-citrate combustion method”. *Mater. Res. Bull.* 39.14-15 (2004), 2249–2255.

[43] S. Manzeli, D. Ovchinnikov, D. Pasquier, O. V. Yazyev, and A. Kis. “2D transition metal dichalcogenides”. *Nat. Rev. Mater.* 2 (2017).

[44] K. S. Novoselov and A. H. Castro Neto. “Two-dimensional crystals-based heterostructures: Materials with tailored properties”. *Phys. Scr.* 146 (2012).

[45] L. Guo, H. Guo, G. Ma, M. Abbas, and S. Gong. “Ruddlesden-Popper structured BaLa 2Ti 3O 10, a highly anisotropic material for thermal barrier coatings”. *Ceram. Int.* 38.5 (2012), 4345–4352.

[46] F. S. Galasso and M. Kestigan. “Aurivillius ceramics: $Bi_4Ti_3O_{12}$-based piezoelectrics” (2007), 112–113.

[47] K. R. Kendall, C. Navas, J. K. Thomas, and H.-C. zur Loye. “Recent developments in Oxide Ion Conductors: Aurivillius phases”. *Chemistry of materials* 8.3 (1996), 642–649.

[48] F. Bianchini, H. Fjellvåg, and P. Vajeeston. “Nonhexagonal Na Sublattice Reconstruction in the Super-Ionic Conductor $Na_2Zn_2TeO_6$: Insights from *Ab-Initio* Molecular Dynamics”. *J. Phys. Chem. C* 123.8 (2019), 4654–4663.

[49] C. Delmas, C Fouassier, and P Hagenmuller. “Structural classification and properties of layered oxides”. *Physica B+ c* 99 (1980), 81–85.

[50] Y. Biecher, D. L. Smiley, M. Guignard, F. Fauth, R. Berthelot, C. Delmas, G. R. Goward, and D. Carlier. “Original Layered OP4-$(Li,Na)_xCoO_2$ Phase: Insights on its Structure, Electronic Structure, and Dynamics from Solid State NMR”. *Inorg. Chem.* 59.8 (2020), 5339–5349.

[51] K. Sau. “Influence of ion–ion correlation on Na^+ transport in $Na_2Ni_2TeO_6$: molecular dynamics study”. *Ionics (Kiel).* 22.12 (2016), 2379–2385.

[52] T. J. Willis, D. G. Porter, D. J. Voneshen, S. Uthayakumar, F. Demmel, M. J. Gutmann, M. Roger, K. Refson, and J. P. Goff. “Diffusion mechanism in the sodium-ion battery material sodium cobaltate”. *Sci. Rep.* 8.1 (2018), 1–10.

[53] N. A. Katcho, J. Carrasco, D. Saurel, E. Gonzalo, M. Han, F. Aguesse, and T. Rojo. “Origins of Bistability and Na Ion Mobility Difference in P2- and O3-$Na_{2/3}Fe_{2/3}Mn_{1/3}O_2$ Cathode Polymorphs”. *Adv. Energy Mater.* 7.1 (2017), 1–9.

[54] M. D. Radin and A. Van Der Ven. “Stability of Prismatic and Octahedral Coordination in Layered Oxides and Sulfides Intercalated with Alkali and Alkaline-Earth Metals”. *Chem. Mater.* 28.21 (2016), 7898–7904.

[55] M. Roger, D. J. Morris, D. A. Tennant, M. J. Gutmann, J. P. Goff, J. U. Hoffmann, R. Feyerherm, E. Dudzik, D. Prabhakaran, A. T. Boothroyd, N. Shannon, B. Lake, and P. P. Deen. “Patterning of sodium ions and the control of electrons in sodium cobaltate”. *Nature* 445.7128 (2007), 631–634.

[56] X. Lu, Y. Wang, P. Liu, L. Gu, Y. S. Hu, H. Li, G. P. Demopoulos, and L. Chen. “Direct imaging of layered O3- and P2-$Na_xFe_{1/2}Mn_{1/2}O_2$ structures at the atomic scale”. *Phys. Chem. Chem. Phys.* 16.40 (2014), 21946–21952.

[57] A. J. Toumar, S. P. Ong, W. D. Richards, S. Dacek, and G. Ceder. “Vacancy Ordering in O3 -Type Layered Metal Oxide Sodium-Ion Battery Cathodes”. *Phys. Rev. Appl.* 4.6 (2015), 1–9.

[58] A. J. Toumar. *Phase Transformations in Layered Electrode Materials for Sodium Ion Batteries by*. Doctor of Philosophy, Massachusetts Institute of Technology, 2017.

[59] P. Zhang, R. B. Capaz, M. L. Cohen, and S. G. Louie. “Theory of sodium ordering in Na_xCoO_2”. *Phys. Rev. B - Condens. Matter Mater. Phys.* 71.15 (2005), 1–4.

[60] H. W. Zandbergen, M. Foo, Q. Xu, V. Kumar, and R. J. Cava. “Sodium ion ordering in Na_xCoO_2: Electron diffraction study”. *Phys. Rev. B - Condens. Matter Mater. Phys.* 70.2 (2004), 1–8.

[61] Y. S. Meng, Y. Hinuma, and G. Ceder. “An investigation of the sodium patterning in Na_xCoO_2 ($0.5 \leq x \leq 1$) by density functional theory methods”. *J. Chem. Phys.* 128.10 (2008).

[62] T. A. Platova, I. R. Mukhamedshin, H. Alloul, A. V. Dooglav, and G. Collin. “Nuclear quadrupole resonance and x-ray investigation of the structure of $Na_{2/3}CoO_2$”. *Phys. Rev. B - Condens. Matter Mater. Phys.* 80.22 (2009).

[63] G. J. Shu, A. Prodi, S. Y. Chu, Y. S. Lee, H. S. Sheu, and F. C. Chou. “Searching for stable Na-ordered phases in single-crystal samples of γ- Na_xCoO_2”. *Phys. Rev. B - Condens. Matter Mater. Phys.* 76.18 (2007), 1–9.

[64] F. C. Chou, M. W. Chu, G. J. Shu, F. T. Huang, W. W. Pai, H. S. Sheu, and P. A. Lee. “Sodium ion ordering and vacancy cluster formation in Na_xCoO_2 (x = 0.71 and 0.84) single crystals by synchrotron X-ray diffraction”. *Phys. Rev. Lett.* 101.12 (2008), 1–4.

[65] J. Geck, M. V. Zimmermann, H. Berger, S. V. Borisenko, H. Eschrig, K. Koepernik, M. Knupfer, and B. Büchner. “Stripe correlations in $Na_{0.75}CoO_2$”. *Phys. Rev. Lett.* 97.10 (2006), 2–5.

[66] Y. S. Meng, A. Van Der Ven, M. K. Chan, and G. Ceder. “Ab initio study of sodium ordering in $Na_{0.75}CoO_2$ and its relation to $Co^{3+}Co^{4+}$ charge ordering”. *Phys. Rev. B - Condens. Matter Mater. Phys.* 72.17 (2005), 4–7.

[67] P. Foury-Leylekian, V. V. Poltavets, N. Jaouen, J. P. Rueff, J. E. Lorenzo, P. Auban-Senzier, C. R. Pasquier, C. Mazzoli, and M. Greenblatt. "Sodium ion and cobalt charge ordering in Na_xCoO_2 ($x \approx 5/6$)". *Phys. Rev. B - Condens. Matter Mater. Phys.* 79.11 (2009), 1–7.

[68] K. Takada, H. Sakurai, E. Takayama-muromachi, F. Izumi, R. Dilanian, and T. Sasaki. "Superconductivity in two-dimensional CoO_2 layers". *Lett. to Nat.* 422.March (2003), 53–55.

[69] T. Wu, K. Liu, H. Chen, G. Wu, Q. L. Luo, J. J. Ying, and X. H. Chen. "Rearrangement of sodium ordering and its effect on physical properties in the Na_xCoO_2 system". *Phys. Rev. B - Condens. Matter Mater. Phys.* 78.11 (2008), 1–5.

[70] Q. Huang, J. W. Lynn, B. H. Toby, M. L. Foo, and R. J. Cava. "Characterization of the structural transition in $Na_{0.75}CoO_2$". *J. Phys. Condens. Matter* 17.12 (2005), 1831–1840.

[71] Y. Hinuma, Y. S. Meng, and G. Ceder. "Temperature-concentration phase diagram of P2 -Na_xCoO_2 from first-principles calculations". *Phys. Rev. B - Condens. Matter Mater. Phys.* 77.22 (2008), 1–16.

[72] D. J. Morris, M. Roger, M. J. Gutmann, J. P. Goff, D. A. Tennant, D. Prabhakaran, A. T. Boothroyd, E. Dudzik, R. Feyerherm, J. U. Hoffmann, and K. Kiefer. "Crystal-to-stripe reordering of sodium ions in Na_xCoO_2 ($x > 0.75$)". *Phys. Rev. B - Condens. Matter Mater. Phys.* 79.10 (2009), 2–5.

[73] R. Berthelot, D. Carlier, and C. Delmas. "Electrochemical investigation of the P2-Na_xCoO_2 phase diagram". *Nat. Mater.* 10.1 (2011), 74–80.

[74] C. Didier, M. Guignard, J. Darriet, and C. Delmas. "O'3$-$$Na_xVO_2$ System: A Superstructure for $Na_{1/2}VO_2$". *Inorg. Chem.* 51 (2012), 11007$-$11016.

[75] M. Guignard, C. Didier, J. Darriet, P. Bordet, E. Elkaïm, and C. Delmas. "P2-Na_xVO_2 system as electrodes for batteries and electron-correlated materials". *Nat. Mater.* 12.1 (2013), 74–80.

[76] X. Li, X. Ma, D. Su, L. Liu, R. Chisnell, S. P. Ong, H. Chen, A. Toumar, J. C. Idrobo, Y. Lei, J. Bai, F. Wang, J. W. Lynn, Y. S. Lee, and G. Ceder. "Direct visualization of the Jahn-Teller effect coupled to Na ordering in $Na_{5/8}MnO_2$". *Nat. Mater.* 13.6 (2014), 586–592.

[77] J. Billaud, G. Singh, A. R. Armstrong, E. Gonzalo, V. Roddatis, M. Armand, T. Rojo, and P. G. Bruce. "$Na_{0.67}Mn_{1-x}Mg_xO2$ ($0 \leq x \leq 0.2$): A high capacity cathode for sodium-ion batteries". *Energy Environ. Sci.* 7.4 (2014), 1387–1391.

[78] Y. Liu, C. Wang, S. Zhao, L. Zhang, K. Zhang, F. Li, and J. Chen. "Mitigation of Jahn-Teller distortion and Na^+/vacancy ordering in a distorted manganese oxide cathode material by Li substitution". *Chem. Sci.* 12.3 (2021), 1062–1067.

[79] H. D. Luong, V. A. Dinh, H. Momida, and T. Oguchi. "Insight into the diffusion mechanism of sodium ion-polaron complexes in orthorhombic P2 layered cathode oxide Na_xMnO_2". *Phys. Chem. Chem. Phys.* 22.32 (2020), 18219–18228.

[80] C. Zheng, B. Radhakrishnan, I. H. Chu, Z. Wang, and S. P. Ong. "Effects of Transition-Metal Mixing on Na Ordering and Kinetics in Layered P2 Oxides". *Phys. Rev. Appl.* 7.6 (2017), 1–12.

[81] R. Dang, M. Chen, Q. Li, K. Wu, Y. L. Lee, Z. Hu, and X. Xiao. "Na^+-Conductive $Na_2Ti_3O_7$-Modified P2-type $Na_{2/3}Ni_{1/3}Mn_{2/3}O_2$ via a Smart in Situ Coating Approach: Suppressing Na^+ /Vacancy Ordering and P2-O2 Phase Transition". *ACS Appl. Mater. Interfaces* 11.1 (2019), 856–864.

[82] A. Gutierrez, W. M. Dose, O. Borkiewicz, F. Guo, M. Avdeev, S. Kim, T. T. Fister, Y. Ren, J. Bareño, and C. S. Johnson. "On Disrupting the Na^+-Ion/Vacancy Ordering in P2-Type Sodium-Manganese-Nickel Oxide Cathodes for Na^+-Ion Batteries". *J. Phys. Chem. C* 122.41 (2018), 23251–23260.

[83] O. A. Smirnova, J. Rocha, V. B. Nalbandyan, V. V. Kharton, and F. M. Marques. "Crystal structure, local sodium environments and ion dynamics in $Na_{0.8}Ni_{0.6}Sb_{0.4}O_2$, a new mixed antimonate". *Solid State Ionics* 178 (2007), 1360–1365.

[84] Y. Mo, S. P. Ong, and G. Ceder. "Insights into diffusion mechanisms in P2 layered oxide materials by first-principles calculations". *Chem. Mater.* 26.18 (2014), 5208–5214.

[85] M. Weller, A. Sacchetti, H. R. Ott, K. Mattenberger, and B. Batlogg. "Melting of the Na layers in solid $Na_{0.8}CoO_2$". *Phys. Rev. Lett.* 102.5 (2009), 6–9.

[86] M. Villa and J. L. Bjorkstam. "^{23}Na and ^{27}Al in β-alumina solid electrolytes". *Phys. Rev. B* 22.11 (1980), 5033–5042.

[87] M. Medarde, M. Mena, J. L. Gavilano, E. Pomjakushina, J. Sugiyama, K. Kamazawa, V. Y. Pomjakushin, D. Sheptyakov, B. Batlogg, H. R. Ott, M. Månsson, and F. Juranyi. "1D to 2D Na+ion diffusion inherently linked to structural transitions in $Na_{0.7}CoO_2$". *Phys. Rev. Lett.* 110.26 (2013), 1–5.

[88] G. J. Shu and F. C. Chou. "Sodium-ion diffusion and ordering in single-crystal P2-Na_xCoO_2". *Phys. Rev. B - Condens. Matter Mater. Phys.* 78.5 (2008), 3–6.

[89] R. J. Clément, J. Xu, D. S. Middlemiss, J. Alvarado, C. Ma, Y. S. Meng, and C. P. Grey. "Direct evidence for high Na^+ mobility and high voltage structural processes in P2-$Na_x[Li_yNi_zMn_{1-y-z}]O_2$ (x, y, z $\leq$ 1) cathodes from solid-state NMR and DFT calculations". *J. Mater. Chem. A* 5.8 (2017), 4129–4143.

[90] O. H. Han, J. K. Jung, M. Y. Yi, J. H. Kwak, and Y. J. Shin. "Sodium ion dynamics in the nonstoichiometric layer-type oxide $Na_{0.67}Ni_{0.33}Ti_{0.67}O_2$ studied by ^{23}Na NMR". *Solid State Commun.* 117.2 (2000), 65–68.

[91] C. Chen, Z. Han, S. Chen, S. Qi, X. Lan, C. Zhang, L. Chen, P. Wang, and W. Wei. "Core-Shell Layered Oxide Cathode for High-Performance Sodium-Ion Batteries". *ACS Appl. Mater. Interfaces* 12.6 (2020), 7144–7152.

[92] Y. Li, Z. Deng, J. Peng, J. Gu, E. Chen, Y. Yu, J. Wu, X. Li, J. Luo, Y. Huang, Y. Xu, Z. Gao, C. Fang, J. Zhu, Q. Li, J. Han, and Y. Huang. "New P2-Type Honeycomb-Layered Sodium-Ion Conductor: $Na_2Mg_2TeO_6$". *ACS Appl. Mater. Interfaces* 10.18 (2018), 15760–15766.

[93] H. Huang, Y. Yang, C. Chi, H. H. Wu, and B. Huang. "Phase stability and fast ion transport in P2-type layered $Na_2X_2TeO_6$(X = Mg, Zn) solid electrolytes for sodium batteries". *J. Mater. Chem. A* 8.43 (2020), 22816–22827.

[94] J. F. Wu, Q. Wang, and X. Guo. "Sodium-ion conduction in $Na_2Zn_2TeO_6$ solid electrolytes". *J. Power Sources* 402 (2018), 513–518.

[95] J. F. Wu and X. Guo. "Origin of the low grain boundary conductivity in lithium ion conducting perovskites: $Li_{3x}La_{0.67-x}TiO_3$". *Phys. Chem. Chem. Phys.* 19.8 (2017), 5880–5887.

[96] X. Guo and R. Waser. "Electrical properties of the grain boundaries of oxygen ion conductors: Acceptor-doped zirconia and ceria". *Prog. Mater. Sci.* 51.2 (2006), 151–210.

[97] Z. Deng, J. Gu, Y. Li, S. Li, J. Peng, X. Li, J. Luo, Y. Huang, C. Fang, Q. Li, J. Han, Y. Huang, and Y. Zhao. “Ca-doped $Na_2Zn_2TeO_6$ layered sodium conductor for all-solid-state sodium-ion batteries”. *Electrochim. Acta* 298 (2019), 121–126.

[98] J. B. Goodenough and Y. Kim. “Challenges for rechargeable Li batteries”. *Chem. Mater.* 22.3 (2010), 587–603.

[99] E. Goikolea, V. Palomares, S. Wang, I. R. de Larramendi, X. Guo, G. Wang, and T. Rojo. “Na-Ion Batteries - Approaching Old and New Challenges”. *Adv. Energy Mater.* 10.44 (2020), 1–21.

[100] A. Ponrouch, E. Marchante, M. Courty, J. M. Tarascon, and M. R. Palacín. “In search of an optimized electrolyte for Na-ion batteries”. *Energy Environ. Sci.* 5.9 (2012), 8572–8583.

[101] M. Á. Muñoz-Márquez, M. Zarrabeitia, S. Passerini, and T. Rojo. “Structure, Composition, Transport Properties, and Electrochemical Performance of the Electrode-Electrolyte Interphase in Non-Aqueous Na-Ion Batteries”. *Adv. Mater. Interfaces* 9.8 (2022).

[102] P. Peljo and H. H. Girault. “Electrochemical potential window of battery electrolytes: The HOMO-LUMO misconception”. *Energy Environ. Sci.* 11.9 (2018), 2306–2309.

[103] G. G. Eshetu, S. Grugeon, S. Laruelle, S. Boyanov, A. Lecocq, J. P. Bertrand, and G. Marlair. “In-depth safety-focused analysis of solvents used in electrolytes for large scale lithium ion batteries”. *Phys. Chem. Chem. Phys.* 15.23 (2013), 9145–9155.

[104] P. Sun, R. Bisschop, H. Niu, and X. Huang. “A Review of Battery Fires in Electric Vehicles”. *Fire Technol.* 56.4 (2020), 1361–1410.

[105] K. Nakamoto, Y. Kano, A. Kitajou, and S. Okada. “Electrolyte dependence of the performance of a $Na_2FeP_2O_7$//$NaTi_2(PO_4)_3$ rechargeable aqueous sodium-ion battery”. *J. Power Sources* 327 (2016), 327–332.

[106] L. Suo, O. Borodin, Y. Wang, X. Rong, W. Sun, X. Fan, S. Xu, M. A. Schroeder, A. V. Cresce, F. Wang, C. Yang, Y. S. Hu, K. Xu, and C. Wang. ““Water-in-Salt” Electrolyte Makes Aqueous Sodium-Ion Battery Safe, Green, and Long-Lasting”. *Adv. Energy Mater.* 7.21 (2017), 1–10.

[107] D. Buchholz, L. G. Chagas, C. Vaalma, L. Wu, and S. Passerini. “Water sensitivity of layered P2/P3-$Na_xNi_{0.22}Co_{0.11}Mn_{0.66}O_2$ cathode material”. *J. Mater. Chem. A* 2.33 (2014), 13415–13421.

[108] Z. Lu and J. R. Dahn. “Intercalation of water in P2, T2 and O2 structure $A_z[Co_xNi_{1/3-x}Mn_{2/3}]O_2$”. *Chem. Mater.* 13.4 (2001), 1252–1257.

[109] A. Caballero, L. Hernán, J. Morales, L. Sánchez, J. Santos Peña, and M. A. Aranda. “Synthesis and characterization of high-temperature hexagonal P2-$Na_{0.6}Mno_2$ and its electrochemical behaviour as cathode in sodium cells”. *J. Mater. Chem.* 12.4 (2002), 1142–1147.

[110] O. A. Smirnova, V. B. Nalbandyan, M. Avdeev, L. I. Medvedeva, B. S. Medvedev, V. V. Kharton, and F. M. Marques. “Crystal structure, conductivity and reversible water uptake of new layered potassium antimonates $K_xL_{(1+x)/3}Sb_{(2-x)/3}O_2$ (L = Ni^{2+}, Mg^{2+}, Co^{2+})”. *J. Solid State Chem.* 178.1 (2005), 172–179.

[111] M. Forsyth, L. Porcarelli, X. Wang, N. Goujon, and D. Mecerreyes. “Innovative Electrolytes Based on Ionic Liquids and Polymers for Next-Generation Solid-State Batteries”. *Acc. Chem. Res.* 52.3 (2019), 686–694.

[112] “A ceramic/polymer composite solid electrolyte for sodium batteries”. *J. Mater. Chem. A* 4.41 (2016), 15823–15828.

[113] Z. Zhang, K. Xu, X. Rong, Y. S. Hu, H. Li, X. Huang, and L. Chen. “$Na_{3.4}Zr_{1.8}Mg_{0.2}Si_2PO_{12}$ filled poly(ethylene oxide)/$Na(CF_3SO_2)_2N$ as flexible composite polymer electrolyte for solid-state sodium batteries”. *J. Power Sources* 372 (2017), 270–275.

[114] J.-F. Wu, Z.-Y. Yu, Q. Wang, and X. Guo. “High performance all-solid-state sodium batteries actualized by polyethylene oxide/$Na_2Zn_2TeO_6$ composite solid electrolytes”. *Energy Storage Mater.* 3.July (2019).

[115] R. Chen, Q. Li, X. Yu, L. Chen, and H. Li. “Approaching Practically Accessible Solid-State Batteries: Stability Issues Related to Solid Electrolytes and Interfaces”. *Chem. Rev.* 120.14 (2020), 6820–6877.

[116] B. B. Owens. “Solid state electrolytes: Overview of materials and applications during the last third of the Twentieth Century”. *J. Power Sources* 90.1 (2000), 2–8.

[117] M. Stanley Whittingham and R. A. Huggins. “Measurement of sodium ion transport in beta alumina using reversible solid electrodes”. *J. Chem. Phys.* 54.1 (1971), 45–51.

[118] T. Oshima, M. Kajita, and A. Okuno. “Development of Sodium-Sulfur Batteries”. *Appl. Ceram. Technol.* 76 (2004), 269–276.

[119] J. L. Sudworth. “The sodium / nickel chloride (ZEBRA) battery”. *J. Power Sources* 100 (2001).

[120] C. Chi, H. Katsui, and T. Goto. “Effect of Li addition on the formation of Na-β/β”-alumina film by laser chemical vapor deposition”. *Ceram. Int.* 43.1 (2017), 1278–1283.

[121] C. R. Peters, M. Bettman, J. W. Moore, and M. D. Glick. “Refinement of the structure of sodium β-alumina”. *Acta Crystallogr. Sect. B Struct. Crystallogr. Cryst. Chem.* 27.9 (1971), 1826–1834.

[122] W. Roth, J. Briant, and B Dunn. “Li and Mg Stabilized beta Aluminas”. *Solid State Ionics* 5 (1981), 163–166.

[123] Z. Zou, N. Ma, A. Wang, Y. Ran, T. Song, B. He, A. Ye, P. Mi, L. Zhang, H. Zhou, Y. Jiao, J. Liu, D. Wang, Y. Li, M. Avdeev, and S. Shi. “Identifying Migration Channels and Bottlenecks in Monoclinic NASICON-Type Solid Electrolytes with Hierarchical Ion-Transport Algorithms”. *Adv. Funct. Mater.* 31.49 (2021).

[124] H. Y. P Hong. “Crystal Structures and Crystal Chemistry in the system $Na_{1+x}Zr_2Si_xP_{3-x}O_{12}$”. *Mater. Res. Bull.* 11.2 (1976), 173–182.

[125] J. B Goodenough, H. Y. P Hong, and J. A Kafalas. “Fast Na^+-ion Transport in Skeleton Structures”. *Mater. Res. Bull.* 11 (1976), 203–220.

[126] Z. Jian, Y. S. Hu, X. Ji, and W. Chen. “NASICON-Structured Materials for Energy Storage”. *Adv. Mater.* 29.20 (2017).

[127] T. Asai, K. Ado, Y. Saito, H. Kageyama, and O. Nakamura. “Mixed conductivity of $Na_{1+4x}M^{II}{}_xFe^{III}{}_{2x}$ $Zr_{2\text{-}3x}P_3O_{12}$, M^{II}: Fe^{2+}, Co^{2+} and Ni^{2+}”. *Solid State Ionics* 35 (1989), 319–322.

[128] Q. Ma, M. Guin, S. Naqash, C. L. Tsai, F. Tietz, and O. Guillon. “Scandium-substituted $Na_3Zr_2(SiO_4)_2(PO_4)$ prepared by a solution-assisted solid-state reaction method as sodium-ion conductors”. *Chem. Mater.* 28.13 (2016), 4821–4828.

[129] M. Samiee, B. Radhakrishnan, Z. Rice, Z. Deng, Y. S. Meng, S. P. Ong, and J. Luo. “Divalent-doped Na3Zr2Si2PO12 natrium superionic conductor: Improving the ionic conductivity via simultaneously optimizing the phase and chemistry of the primary and secondary phases”. *J. Power Sources* 347 (2017), 229–237.

[130] N. Kamaya, K. Homma, Y. Yamakawa, M. Hirayama, R. Kanno, M. Yonemura, T. Kamiyama, Y. Kato, S. Hama, K. Kawamoto, and A. Mitsui. “A lithium superionic conductor”. *Nat. Mater.* 10.9 (2011), 682–686.

[131] J. L. Souquet, E. Robinel, B. Barrau, and M. Ribes. “Glass formation and ionic conduction in the M_2S-GeS_2 (M = Li, Na, Ag) systems”. *Solid State Ionics* 3-4.C (1981), 317–321.

[132] F. Tsuji, N. Tanibata, A. Sakuda, A. Hayashi, and M. Tatsumisago. “Preparation of sodium ion conductive $Na_{10}GeP_2S_{12}$ glass-ceramic electrolytes”. *Chem. Lett.* 47.1 (2018), 13–15.

[133] A. Hayashi, K. Noi, A. Sakuda, and M. Tatsumisago. “Superionic glass-ceramic electrolytes for room-temperature rechargeable sodium batteries”. *Nat. Commun.* 3.May (2012), 2–6.

[134] N. Tanibata, K. Noi, A. Hayashi, N. Kitamura, Y. Idemoto, and M. Tatsumisago. “X-ray Crystal Structure Analysis of Sodium-Ion Conductivity in 94Na3PS4 * 6Na4SiS4 Glass-Ceramic Electrolytes”. *ChemElectroChem* 1.7 (2014), 1130–1132.

[135] C. K. Moon, H. J. Lee, K. H. Park, H. Kwak, J. W. Heo, K. Choi, H. Yang, M. S. Kim, S. T. Hong, J. H. Lee, and Y. S. Jung. “Vacancy-Driven Na^+ Superionic Conduction in New Ca-Doped Na_3PS_4 for All-Solid-State Na-Ion Batteries”. *ACS Energy Lett.* 3.10 (2018), 2504–2512.

[136] H. Wang, Y. Chen, Z. D. Hood, G. Sahu, A. S. Pandian, J. K. Keum, K. An, and C. Liang. “ An Air-Stable Na_3SbS_4 Superionic Conductor Prepared by a Rapid and Economic Synthetic Procedure ”. *Angew. Chemie* 128.30 (2016), 8693–8697.

[137] A. Hayashi, N. Masuzawa, S. Yubuchi, F. Tsuji, C. Hotehama, A. Sakuda, and M. Tatsumisago. “A sodium-ion sulfide solid electrolyte with unprecedented conductivity at room temperature”. *Nat. Commun.* 10.1 (2019).

[138] M. Nose, A. Kato, A. Sakuda, A. Hayashi, and M. Tatsumisago. “Evaluation of mechanical properties of Na2S-P2S5 sulfide glass electrolytes”. *J. Mater. Chem. A* 3.44 (2015), 22061–22065.

[139] A. Sakuda, A. Hayashi, and M. Tatsumisago. “Sulfide solid electrolyte with favorable mechanical property for all-solid-state lithium battery”. *Sci. Rep.* 3 (2013), 2–6.

[140] H. M. Rietveld. “A profile refinement method for nuclear and magnetic structures”. *J. Appl. Crystallogr.* 2.2 (1969), 65–71.

[141] A. A. Coelho. “TOPAS and TOPAS-Academic: An optimization program integrating computer algebra and crystallographic objects written in C++: An”. *J. Appl. Crystallogr.* 51.1 (2018), 210–218.

[142] B. H. Toby. “ R factors in Rietveld analysis: How good is good enough? ” *Powder Diffr.* 21.1 (2006), 67–70.

[143] D. A. Keen. “A comparison of various commonly used correlation functions for describing total scattering”. *J. Appl. Crystallogr.* 34.2 (2001), 172–177.

[144] M. Wilkening and P. Heitjans. “Li jump process in h-$Li_{0.7}TiS_2$ studied by two-time ^{7}Li spin-alignment echo NMR and comparison with results on two-dimensional diffusion from nuclear magnetic relaxation”. *Phys. Rev. B - Condens. Matter Mater. Phys.* 77.2 (2008), 1–13.

[145] M. H. Levitt. *Spin Dynamics: basics of nuclear magnetic resonance*. John Wiley & Sons, 2013.

[146] A. Kuhn, M. Kunze, P. Sreeraj, H. D. Wiemhöfer, V. Thangadurai, M. Wilkening, and P. Heitjans. “NMR relaxometry as a versatile tool to study Li ion dynamics in potential battery materials”. *Solid State Nucl. Magn. Reson.* 42 (2012), 2–8.

[147] V. Epp, S. Nakhal, M. Lerch, and M. Wilkening. “Two-dimensional diffusion in $Li_{0.7}NbS_2$ as directly probed by frequency-dependent ^{7}Li NMR”. *J. Phys. Condens. Matter* 25.19 (2013).

[148] M. Wilkening and P. Heitjans. “From Micro to Macro: Acess to Long range Li^+ diffusion parameters in solids via Microscopic ^{6,7}Li Spin alignment echo NMR spectroscopy”. *Phys. Chem. Chem. Phys.* 13.13 (2012), 53–65.

[149] P. Heitjans, A. Schirmer, and S. Indris. “NMR and β-NMR studies of diffusion in interface-dominated and disordered solids”. *Diffus. Condens. Matter Methods, Mater. Model.* (2005), 367–415.

[150] N. Bloembergen, E. M. Purcell, and R. V. Pound. “Relaxation effects in nuclear magnetic resonance absorption”. *Phys. Rev.* 73.7 (1948), 679–712.

[151] P. M. Richards. “Effect of Low Dimensionality on Prefactor Anomalies in Superionic Conductors”. *Solid State Commun.* 25.3 (1978), 1019–1021.

[152] V. Epp and M. Wilkening. “Fast Li diffusion in crystalline LiBH4 due to reduced dimensionality: Frequency-dependent NMR spectroscopy”. *Phys. Rev. B - Condens. Matter Mater. Phys.* 82.2 (2010), 4–7.

[153] M. Gombotz, S. Lunghammer, S. Breuer, I. Hanzu, F. Preishuber-Pflügl, and H. M. R. Wilkening. “Spatial confinement - Rapid 2D F-diffusion in micro- and nanocrystalline $RbSn_2F_5$”. *Phys. Chem. Chem. Phys.* 21.4 (2019), 1872–1883.

[154] P. Hohenberg and W. Kohn. “Inhomogeneous Electron Gas”. *Phys. Rev.* 136.3 (1964), B864.

[155] D. Massiot, F. Fayon, M. Capron, I. King, S. Le Calvé, B. Alonso, J. O. Durand, B. Bujoli, Z. Gan, and G. Hoatson. “Modelling one- and two-dimensional solid-state NMR spectra”. *Magn. Reson. Chem.* 40.1 (2002), 70–76.

[156] J. B. d’Espinose de Lacaillerie, C. Fretigny, and D. Massiot. “MAS NMR spectra of quadrupolar nuclei in disordered solids: The Czjzek model”. *J. Magn. Reson.* 192.2 (2008), 244–251.

[157] A. P. Kentgens. “A practical guide to solid-state NMR of half-integer quadrupolar nuclei with some applications to disordered systems”. *Geoderma* 80.3-4 (1997), 271–306.

[158] I. C. Madsen and N. V. Scarlet. “Quantitive Phase Analysis”. *Powder Diffraction, Theory Pract.* Ed. by R. E. Dinnebier and S. J. L. Bilinge. Royal Society of Chemistry, 2008. Chap. 11, 298–311.

[159] V. B. Nalbandyan, A. A. Petrenko, and M. A. Evstigneeva. “Heterovalent substitutions in $Na_2M_2TeO_6$ family: Crystal structure, fast sodium ion conduction and phase transition of $Na_2LiFeTeO_6$”. *Solid State Ionics* 233 (2013), 7–11.

[160] H. T. Stokes, S. Van Orden, and B. J. Campbell. “ISOSUBGROUP: An internet tool for generating isotropy subgroups of crystallographic space groups”. *J. Appl. Crystallogr.* 49.5 (2016), 1849–1853.

[161] H. T. Stokes, B. J. Campbell, and S. Van Smaalen. “Generation of (3 + d)-dimensional superspace groups for describing the symmetry of modulated crystalline structures”. *Acta Crystallogr. Sect. A Found. Crystallogr.* 67.1 (2011), 45–55.

[162] S. Van Smaalen, B. J. Campbell, and H. T. Stokes. “Equivalence of superspace groups”. *Acta Crystallogr. Sect. A Found. Crystallogr.* 69.1 (2013), 75–90.

[163] V. Petrícek, M. Dušek, and L. Palatinus. “Crystallographic computing system JANA2006: General features”. *Zeitschrift fur Krist.* 229.5 (2014), 345–352.

[164] W. L. Pang, X. H. Zhang, J. Z. Guo, J. Y. Li, X. Yan, B. H. Hou, H. Y. Guan, and X. L. Wu. “P2-type $Na_{2/3}Mn_{1-x}Al_xO_2$ cathode material for sodium-ion batteries: Al-doped enhanced electrochemical properties and studies on the electrode kinetics”. *J. Power Sources* 356 (2017), 80–88.

[165] D. Carlier, J. H. Cheng, R. Berthelot, M. Guignard, M. Yoncheva, R. Stoyanova, B. J. Hwang, and C. Delmas. “The P2-$Na_{2/3}Co_{2/3}Mn_{1/3}O_2$ phase: Structure, physical properties and electrochemical behavior as positive electrode in sodium battery”. *J. Chem. Soc. Dalt. Trans.* 40.36 (2011), 9306–9312.

[166] A. Itaya, K. Yamamoto, R. Inada, and Y. Sakurai. “Effect of excess Na contents in precursor on the property of Na2Zn2TeO6 ceramic solid electrolyte”. *Mater. Lett.* 284 (2021), 128941.

[167] F. S. Hempel, F. Bianchini, B. Arstad, and H. Fjellvåg. “Effects of Ga Substitution on the Local Structure of $Na_2Zn_2TeO_6$”. *Inorg. Chem.* 61.33 (2022), 13067–13076.

[168] S. K. Karna, Y. Zhao, R. Sankar, M. Avdeev, P. C. Tseng, C. W. Wang, G. J. Shu, K. Matan, G. Y. Guo, and F. C. Chou. “Sodium layer chiral distribution and spin structure of $Na_2Ni_2TeO_6$ with a Ni honeycomb lattice”. *Phys. Rev. B* 95.10 (2017), 1–9.

[169] Y. Tian, T. Shi, W. D. Richards, J. Li, J. C. Kim, S. H. Bo, and G. Ceder. “Compatibility issues between electrodes and electrolytes in solid-state batteries”. *Energy Environ. Sci.* 10.5 (2017), 1150–1166.

I

Inorganic Chemistry

pubs.acs.org/IC

Article

Effects of Ga Substitution on the Local Structure of $Na_2Zn_2TeO_6$

Frida Sveen Hempel, Federico Bianchini, Bjørnar Arstad,* and Helmer Fjellvåg*

Cite This: *Inorg. Chem.* 2022, 61, 13067−13076

Read Online

ACCESS | Metrics & More | Article Recommendations | Supporting Information

ABSTRACT: In the work presented here, we prepared Ga-substituted NZTO ($Na_{2-x}Zn_{2-x}Ga_xTeO_6$, x = 0.00, 0.05, 0.10, 0.15, 0.20) layered materials with a soft chemical, citric acid-based synthesis method and characterized these by means of X-ray diffraction (XRD), ^{23}Na and ^{125}Te NMR, and by density functional theory (DFT) modeling. The influence of randomly distributed Ga cations on the ^{125}Te NMR spectra confirms the successful synthesis. With DFT-based linear response computations, we show that the local distribution of Na ions in the two neighboring interlayers influences the ^{125}Te chemical shift, consistent with observations. DFT modeling suggests that some of the Na sites are rarely occupied in pure NZTO but become favorable upon Ga substitution. There are clear indications that Ga substitution gives an uneven distribution of Na ions in neighboring interlayers and that the Na structure in one layer affects the adjacent layers.

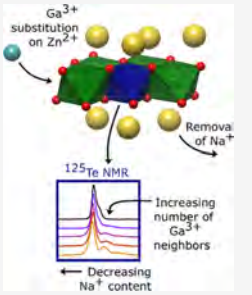

1. INTRODUCTION

Layered oxide materials have been of interest for use in battery technology since the introduction of Li_xCoO_2 (LCO) as an early cathode material.[1] While Li-ion batteries are currently dominating, Na-based technology is an interesting candidate for certain applications. This can be attributed to Na's greater global distribution[2] and the negligible weight difference in the larger picture of all battery components. Layered oxides may exhibit a negligible electronic conductivity while still having good ionic conductivity and may thus be candidates as solid-state electrolytes (SSEs). SSEs would replace the organic liquid electrolyte, which is highly flammable and can emit toxic gases in the case of fires,[3] in addition to unwanted reactions with the electrodes.[4] SSE materials should exhibit high ionic conductivity, low electron conductivity, and good stability[5] and can be amorphous, polymeric or crystalline-like NASICON-types, certain sulfides, or Na-β-alumina.[6]

A structural classification for A_xMO_2 layered oxides was proposed by Delmas et al., with A being an alkali cation and one or several cations M located within $(MO_2)_n$ layers of edge-sharing octahedra.[7] Depending on the stacking of the MO_2 layers, the intercalated alkali ion may take octahedral (O) or prismatic (P) coordination. Furthermore, a number in combination with O or P refers to the number of distinct $(MO_2)_n$ layers in the stacking sequence, with two prominent stacking variants being the O3- and P2-types. An interesting family of quaternary layered oxides $Na_2M_2TeO_6$ (M = Ni, Co, Zn, and Mg) was first described by Evstigneeva et al. in 2007[8] and further characterized by Berthelot et al.[9] These P2-type materials have 12 possible Na positions available in face-sharing trigonal prisms in each unit cell, although on average only four of them are filled with Na ions. The distance between adjacent Na sites is 1.7 Å, which is too short for the simultaneous occupation of Na ions. The M = Co, Ni members of $Na_2M_2TeO_6$ are redox-active and are relevant as cathode materials,[10] whereas M = Zn[11] and Mg[12] are candidates for solid-state electrolytes. The focus of our work has been on the Zn variant $Na_2Zn_2TeO_6$ (NZTO) shown in Figure 1, which is in the space group $P6_322$ and has an alternating arrangement of the Te atoms across consecutive layers.[8]

This structure has three different crystallographic Na sites, with a multiplicity of three, two, and one in the interlayer gallery and below and above the layers of octahedrally coordinated Zn/Te. Hence, the central atoms of the octahedra have several possible local configurations with respect to the surrounding Na cations residing in the neighboring interlayers.

The three different Na prisms are differentiated by their coordination to the framework octahedra. A prism can either be positioned between two octahedra, where it will face-share its two ends with the octahedra on each side, or in the tetrahedral voids between the octahedra, where it is edge-sharing with the surrounding octahedra. The latter of these is the g-site, but the former is further differentiated by the cations in the framework layer: The a-site has a Zn octahedra on each side, and the f-site has one Zn octahedra on one side and one Te on the other. These sites are labeled using the symbols from the Wyckoff sites but omit the multiplicity. Any number in

Received: April 26, 2022
Published: August 9, 2022

https://doi.org/10.1021/acs.inorgchem.2c01431
Inorg. Chem. 2022, 61, 13067−13076

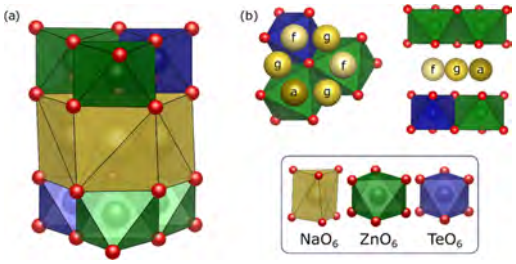

Figure 1. (a) Perspective view of the P2-type NZTO structure and space group $P6_322$. Coordination polyhedra of Te, Zn, and Na are shown (bottom). (b) Crystallographic Na positions, labeled as Wyckoff *a*-, *f*-, and *g*-sites. Note, on average, four out of 12 Na positions per unit cell are filled, and two adjacent sites cannot be simultaneously occupied due to distance constraints.

combination with *a*, *f*, and *g* denotes the number of filled sites instead, in line with our previous work on NZTO.[11,13]

$Na_2Zn_2TeO_6$ shows Na conductivity, and by impedance spectroscopy, it has been reported to be 6.29×10^{-4} S cm^{-1}. By introducing Ga at Zn sites, an increased conductivity of up to 1.1×10^{-3} S cm^{-1} has been reported.[14] This substitution is reported to reduce the grain boundary resistance;[15] however, Sau and Kumar et al. report that the main effect is decreased Na−Na repulsion due to the increased Na vacancy concentration.[16−18] Karna et al. observed indications for Na ordering in a similar layered $Na_2Ni_2TeO_6$ based on Fourier maps of synchrotron X-ray and neutron diffraction data.[19] On the other hand, *ab initio* molecular dynamics studies of NZTO supported a disordered Na distribution.[13]

Solid-state synthesis is the most common synthesis method for the abovementioned layered oxides.[9,11,20−22] This methodology is based on diffusion between and inside reactant/product grains, which makes the homogeneous substitution of elements in low concentrations challenging, as shown in previous reports, which indicate that the amount of unknown secondary phases increases with Ga substitution.[23] The synthesis reaction pathway for the similar Na_xCoO_2 material is complex and depends on several factors and was reported by Bianchini et al. as an interplay between thermodynamically stable phases and nonequilibrium kinetic phases, with a multistage, compositionally unrestrained reaction pathway.[20] To ensure homogeneous substitution, wet chemical sol−gel methods are preferable as they shorten the diffusion paths and mix easily to form a homogeneous distribution of precursors.

In this article, we present a detailed experimental and computational study of Ga-substituted NZTO materials. The motivation behind the work has been to investigate an alternative synthesis route, ensuring homogeneous substitution, combined with a characterization method for verification of the nominal substitution, which must also ensure that no regions are unsubstituted. We have applied the citric acid method, where all cations are presumably mixed at the atomic scale in the form of complexes and precipitated in a homogeneous gel during heat treatment. The substitution of Ga^{3+} for Zn^{2+}, leading to $Na_{2-x}Zn_{2-x}Ga_xTeO_6$, modifies the sodium content in the interlayer galleries and may, in turn, affect the local Na substructure, within and between neighboring two-dimensional (2D) intergalleries, thereby impacting the environment of Zn/Ga and Te cations. Special attention is therefore given to Ga's effect on the average and local structure. For this, ^{23}Na and ^{125}Te magic angle spinning (MAS) solid-state NMR spectroscopy was applied to obtain information on the local environment of Na and Te and changes induced by Ga substitution. The energetics of different interlayer Na configurations has been determined from structural optimization calculations using density functional theory (DFT). Furthermore, DFT linear response calculations of NMR chemical shifts are used to help analyze and interpret NMR spectra. The results obtained on the basis of high-quality samples made by the sol−gel method are discussed in relation to the existing literature on NZTO and related 2D materials.

2. MATERIALS AND METHODS

2.1. Synthesis. Samples of $Na_{2-x}Zn_{2-x}Ga_xTeO_6$ with x = 0.00, 0.05, 0.10, 0.15, and 0.20 were synthesized using sol−gel synthesis. All precursors were added in relevant stoichiometric ratio, with the exception of Na_2CO_3, which was added in 10% excess to compensate for evaporation. The reactants ZnO (Sigma-Aldrich, 99.99%), Na_2CO_3 (Sigma-Aldrich, >99.5%), and TeO_2 (Sigma-Aldrich, 99.995%) were dissolved by adding nitric acid (Sigma-Aldrich, 65%) using a magnetic stirrer on a hot plate at 50 °C until the solution became transparent. Subsequently, $Ga(NO_3)_3{\cdot}xH_2O$ (Sigma-Aldrich, 99.9%) was dissolved in water and added. The level of hydration of the Ga-precursor was determined from thermogravimetric analysis (TGA). Finally, citric acid (Sigma-Aldrich, 99.5%) was added in a ratio of 5:1 with respect to the cations in the precursors.

The solution was heated to 180 °C while stirring to allow NO_x gas to evaporate, and after gel formation, the beaker was left overnight at 180 °C. The resulting powder was then heated to 450 °C for 12 h. The powder was ball-milled at 600 rpm for 20 min and pressed into pellets prior to final sintering reactions. The samples with x = 0−0.10 were sintered at 900 °C, while x = 0.15 and 0.20 at 800 °C, both using a heating/cooling rate of 5 °C. The top and bottom of the pellet were covered with the parent powder before sintering.

2.2. X-ray Diffraction (XRD). Powder X-ray diffraction (XRD) data were measured on a Bruker D8-A25 diffractometer, using a Cu $K\alpha_1$ radiation source and a Ge(111) Johansson monochromator and a Lynxeye detector. Data were collected for the 2θ range between 10 and 128°, using a step size of 0.005°, and samples were packed in a capillary for reducing preferred orientation. Rietveld refinement against the collected data was performed using Topas v6,[24] and the background was fitted with a 10-term Chebychev polynomial.

2.3. Nuclear Magnetic Resonance (NMR) Spectroscopy. ^{23}Na (I = 3/2) and ^{125}Te (I = 1/2) MAS NMR single transient spectra were collected at 11.74 T with a Bruker Avance AV III spectrometer using a 4 mm double-channel probe head at 295 K and at a MAS frequency of 10 kHz. The applied ^{23}Na resonance frequency was 132.29 MHz, and 400 free induction decays (FIDs) after short pulses were accumulated for each spectrum. For the ^{23}Na experiments, we used 1.5 μs excitation pulses at an RF-field of 33 kHz, calibrated using a 1 M NaCl(aq) solution. For ^{23}Na, we measured, using the saturation recovery method, a T_1 relaxation time constant of ca. 500 μs, and the recycle delay was set to 0.5 s. The applied ^{125}Te resonance frequency was 157.79 MHz, and 2000 FIDs (NS) were accumulated for each spectrum using 90° pulses calibrated using a 1 M $Te(OH)_6$ (aq) solution. Tests with variable recycle delays showed that the maximum intensity in the ^{125}Te spectra were reached using a recycle delay of about 25 s. In addition, we measured with the saturation recovery method a T_1 relaxation time constant of ca. 7 s for ^{125}Te, and the recycle delay was set to 30 s. There were no observable differences between the various ^{125}Te components in the spectra regarding relaxation rates.

The samples have been mainly stored in an Ar/desiccator after preparation/XRD analyses but have been some time in air since we have not worked in a completely inert atmosphere. ^{1}H NMR was carried out to check hydroxyl groups and water level, and the samples showed a small broad peak that can be attributed to water that is

https://doi.org/10.1021/acs.inorgchem.2c01431
Inorg. Chem. 2022, 61, 13067−13076

slightly above the probe background level. The amount of hydroxyl groups was also only slightly above background levels. ^{23}Na experiments with high-power proton decoupling gave identical spectra as those without decoupling. Hence, based on these data, we anticipate very small effects of water/OH groups on the samples, both in regard to structure, ion dynamics, and relaxation times. We also note that studies of water's effect on similar materials show that the interlayer distance (*c*-axis) should increase with the intercalation of water.[25,26] We do not see any sign of this in our XRD data, and hence we are confident that the water present is not of significance. Based on these points, we have decided not to work in a completely inert atmosphere with our materials.

The magnetic field was adjusted by setting the high-frequency peak of Adamantane to 38.48 ppm. In addition to the references 1 M NaCl (aq) for ^{23}Na and $Te(OH)_6$ (aq) for ^{125}Te spectra, TeO_2 (s) was used for comparison with chemical shifts calculated from DFT (*vide infra*). The shift values for aqueous ^{23}Na and ^{125}Te are set to 0 ppm. Before Fourier transform of the averaged FIDs, zero filling and apodization were applied to improve the line shape definitions and signal-to-noise ratio. The apodization was done by multiplying the FIDs with a decaying exponential window function with a processing line broadening (LB) factor of 250 Hz (^{23}Na) and 50 Hz (^{125}Te).

All NMR spectra were adjusted by proper signal phasing and baseline corrections. Curve fitting was performed using DMfit.[27]

2.4. Density Functional Theory Modeling. The DFT calculations were performed using the Vienna Ab initio Simulation package (VASP, version 5.4.4).[28−31] The simulations build upon results and configurations obtained in our previous work[13] and can be divided into two categories: (i) accurate calculations on a relatively small system to compute the Te chemical shift from linear response theory and (ii) AIMD simulations to compute the structural properties under Ga substitution. Structural optimization calculations were carried out to obtain reliable starting configurations compatible with the simulation parameters. All computations make use of the conjugate gradient algorithm.

The chemical shift for Te was evaluated by means of linear response theory using the method developed by Yates, Pickard, and Mauri.[32,33] The shift was computed with respect to TeO_2, which was then referenced back to $Te(OH)_6$. Exchange and correlation were treated using the strongly constrained and appropriately normed (SCAN) semilocal density functional.[34] The projector augmented wave (PAW) method was used to model core states. Additional technical details can be found in Section S1 in the Supporting Information (SI).

The Ga-substituted systems were modeled using a supercell structure of the configuration reported as the most stable in our previous work.[13] A $3 \times 2 \times 1$ supercell system ($16.03 \times 18.48 \times 11.37$ Å^3) of said configuration was constructed, large enough to render the interactions between point defects and their periodic images negligible and to perform molecular dynamics simulation. The system contains 24 formula units (264 atoms).

The AIMD calculations were performed on the supercell model of the original NZTO structure and the two most stable substituted configurations. The stoichiometry of the systems is $Na_{48}Zn_{48}Te_{24}O_{144}$, $Na_{46}Zn_{46}Ga_2O_{144}$, and $Na_{44}Zn_{44}Ga_4O_{144}$. For brevity, the Ga-substituted systems are labeled as 2Ga and 4Ga, respectively. All AIMD simulations used a calculation setup similar to the one chosen to construct the initial configurations, with some minor modifications, as reported in Section S1.

AIMD simulations were performed both within the canonical (NVT) and the microcanonical (NVE) ensemble: the former for thermalization of the system and the latter for production. In both cases, we used the same parameters described in Section S1. Calculations within the canonical ensemble were modeled using the Nosé thermostat for controlling temperature oscillations.[35−37] The Nosé mass parameter was set so that the period associated with these fluctuations was 40 fs. A time-step of 1 fs was found to be sufficiently small to avoid sudden jumps in the total energy of the system during the simulation. This setting was used to thermalize the system using the procedure described in Section S1.

Production calculations, performed in the microcanonical ensemble, compute 50 ps of dynamics. The analysis of the trajectories relies on three packages: MDANSE,[38] the atomic simulation environment (ASE),[39,40] and quippy, the python interface of QUIP.[41] Additional software used in this work includes VESTA[42] for the rendering of ball-and-stick and coordination polyhedra.

We would like to make some comments on the choice of methods when it comes to calculating ^{125}Te NMR parameters from first-principles. Garaga et al. computed chemical shielding of various forms of TeO_2[43] using the methodology developed by Yates, Pickard, and Mauri.[32,33] This work shows that meaningful results can be obtained already at the generalized gradient approximations (GGA) level using the Perdew−Burke−Ernzerhof (PBE) functional. Lizion et al. computed the NMR shift of Ge—Te structures including vacancies.[44] As the large size of the systems considered and the presence of crystal defects render first-principles calculations particularly challenging, the authors opted for the Virtual Crystal Approximation, a less-demanding approach neglecting the distortion of the lattice due to vacancies and only considering one average site for the entire structure. Albeit not accurate, this approach allowed the identification of a large number of vacancies, which is correlated with higher chemical shift values. Furthermore, Alkan et al. showed that for ^{125}Te, it is important to include relativistic effects.[45] They used cluster models and showed that methods that included relativistic corrections had to be applied for accurately modeling the magnetic-shielding principal components of ^{125}Te in a range of different compounds. This work also offers a comparison between results from different functionals, showing that, while hybrid functionals are required to obtain accurate results, GGA-level functionals do provide satisfactory results. Since Alkan et al. studied a range of different compounds and bonding types around Te, it was important to adopt methods that captured the essential parts of electronic structure and energies and magnetic and relativistic effects for heavy nuclei. However, in our case, we investigate very similar compounds and compare configurations that are quite similar both in structure and properties; hence, cancellation of errors is expected to occur. Even with the Ga incorporation, the closest Te surroundings are quite similar and only modulated slightly by the Na ions, and as long as we have found a functional that gives parameters close to experimental findings, other complicating effects will typically be canceled when making comparisons.

3. RESULTS AND DISCUSSION

3.1. Crystal Structure. The diffraction data of $Na_{2-x}Zn_{2-x}Ga_xTeO_6$ are well described in the space group $P6_322$, which is consistent with other experiments.[11,14,15,22] Diffractograms are shown in Figure 2a, with a more detailed Rietveld fit in Figure S1a and information in Table S1. The variation in unit cell dimensions with composition is shown in Figure 2b. Atomic coordinates and derived average bond lengths are listed in Tables S3, S4, respectively.

The SEM image of NZTO particles in Figure S2 shows that the material crystallizes as 1−2 μm thick platelets of some 2−5 μm in lateral size and with well-developed facets. This could give preferred orientation effects, even in the capillary setup. If the crystallites have an anisotropy similar to the particles, anisotropic size broadening could be expected, and adding this to the refinement improves the fit of the intensities. However, as shown in Table S2, either preferred orientation or anisotropic size broadening provided very low improvement in the R_{wp}. This will be further explored in later work.

The elevated background in the 2θ range 16−24°, as shown in an inset in Figure S1b, has previously been ascribed to stacking faults.[32] The two additional weak peaks indicated with blue arrows as $x = 0.00$ were earlier explained by the presence of an O'3 impurity,[22] which, however, is unlikely for our samples owing to the lack of a shoulder/peak at $2\theta = 16°$.

https://doi.org/10.1021/acs.inorgchem.2c01431
Inorg. Chem. 2022, 61, 13067−13076

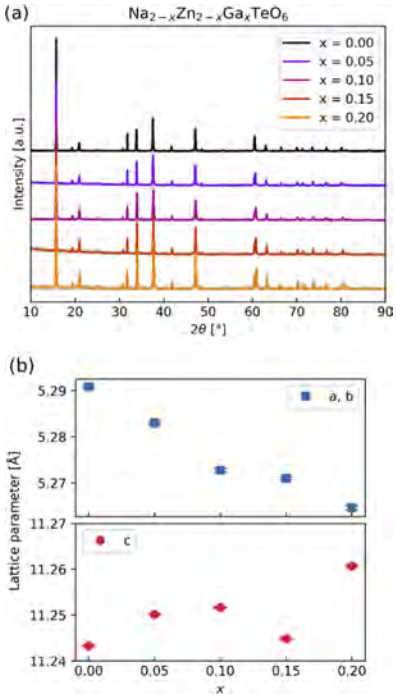

Figure 2. (a) Observed and calculated (Rietveld refinement) X-ray diffractograms of $Na_{2-x}Zn_{2-x}Ga_xTeO_6$, with increasing Ga concentration x; wavelength λ = 1.54 Å. (b) Variation in lattice parameters; space group $P6_322$. Error bars are calculated as standard error.

There is a small, unexplained peak at around 35° for all of the samples, which is tentatively ascribed to the Na substructure.[11,46] A small ZnO impurity is fitted for sample x = 0.00 and may be 0.05, as shown in Figure S1c, but decreases for higher x-contents and is not visible in the patterns for x = 0.10, 0.15, and 0.20.

On increasing Ga substitution at the Zn site, the c-axis expands slightly. This may have different causes: cation repulsions due to higher charged gallium and O−O repulsion due to fewer Na cations or weaker Na−O bonding. The ab-plane contracts, leading to a decrease in the unit cell volume. The average bond lengths from the structure and the bond lengths from the DFT calculations described in Section 3.5 are listed in Table S4. In the average structure, the octahedral O-distances increase upon Ga insertion, but the DFT calculations confirm only the increase in the O−O distance in the Zn octahedra and show that prismatic O−O distances also increase instead of the expected decrease in the average model.

The x = 0.15 sample appears to have an anomalously short c-axis, with c and possibly a deviating from an otherwise clear trend. Repeated synthesis and analysis confirmed this result. As discussed in Section 3.3, we could confirm that the actual Ga/Zn ratio corresponds well to the nominal composition. This suggests that the reason for the anomaly might be rooted in the Na distribution, which has been reported to influence the interlayer distance.[47] As discussed in Section 3.5, modeling reveals a preference for inhomogeneous Na distribution across the layers at high Ga substitution levels. Ga distribution was found to be homogeneous (*vide infra*), suggesting that the Na distribution alternates between layers to uphold charge neutrality. A series of different Na fillings, and therefore different layer distances, could sum up to different averages depending on the degree of filling and the filling/stacking sequence.

The previously reported Na site occupancies for NZTO vary considerably, especially with respect to the f/g ratio.[8,13,22] The currently adopted site distribution is given in Table S3. Attempts to further refine the Na occupancies give no significant improvement in R_{wp}, which probably reflects disorder, mobility, and weak scattering contrast. Note that the actual Ga distribution on Zn sites cannot be determined by XRD due to the low contrast between these neighboring elements in the periodic table, and hence nominal values are reported. To clarify aspects related to local ordering and the effect of Ga substitution, a series of NMR studies were conducted (see below).

3.2. ^{23}Na NMR Study. The ^{23}Na MAS NMR spectra of the studied samples are shown in Figure 3. Curve fitting and

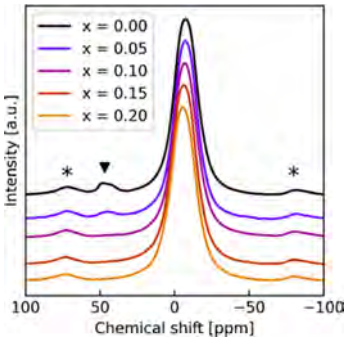

Figure 3. ^{23}Na NMR signals recorded for $Na_{2-x}Zn_{2-x}Ga_xTeO_6$. A peak of unknown origin is indicated with ▼. Spinning sidebands are denoted with *.

superimposed spectra are shown in Section S3. Ideally, the sodium a-, f-, and g-sites with slightly different coordination environments should show up as closely positioned peaks, and one would expect that the prismatic coordination of Na should give an asymmetric environment with an appreciable electric field gradient (EFG) and hence peaks with typical second-order quadrupolar shape. However, the main peaks are quite similar for all samples (peak FWHM ∼ 2.3 kHz), and there are no signs in the line shape of strong quadrupolar couplings. With increasing Ga content, there is a slight shift of peaks to higher ppm values, and the small peaks around 45 ppm decrease and finally disappear. A small shift to higher frequencies may be due to a slight decrease in quadrupolar couplings; however, the low-frequency side (right side) does not change with increasing Ga content. The lack of observed features is interesting and may originate from several phenomena. Atomic disorder around the Na sites will result in a distribution of the chemical environments; however, distributions of quadrupolar couplings and/or chemical shifts will lead to an asymmetric peak shape with a tailing toward lower frequencies, which is not very obvious in our spectra.[48] However, since NZTO and its Ga-substituted derivatives show Na ionic conductivity (*vide supra*),[14] the lack of peak shape

https://doi.org/10.1021/acs.inorgchem.2c01431
Inorg. Chem. 2022, 61, 13067−13076

features could also indicate an exchange of Na cations at rates comparable to, or larger, than the spectral peak widths one would observe for a situation with completely rigid and static Na ions. Increasingly faster jump rates between various sites of prismatic coordination will average the quadrupolar couplings and chemical shift differences until a single peak is observed. To observe such a development, one would have to carry out variable temperature experiments cooling down to such a low temperature that Na ion dynamics were absent and compare with experiments at higher temperatures. The apparent symmetry of the main peak in the stacked plot (Figure 3), is slightly misleading. Fitting shows that the peak cannot be decomposed into one Gaussian/Lorentzian peak for any sample, and hence residual quadrupolar couplings likely remain. For layered Na_xCoO_2, Carlier et al. found that the ^{23}Na signal was not fully averaged at room temperature and could only be fitted as one single peak first at 475 K.[47]

With increased Ga substitution, the peaks at 45 ppm disappear. Since they are located at higher frequencies than the main peak, they probably originate from Na at a lower coordination as this is typical for ^{27}Al and also indicated for ^{23}Na.[48,49] The peaks around 45 ppm could be intrinsic to NZTO or due to a secondary phase. From tabulated values of chemical shift values for Na compounds, no obvious feature appears to explain the peaks.[49] However, upon heating to 200 °C (addressed in another work to be published), the peak at 45 ppm disappears and the main peak shifts slightly to the left. However, the peak reappears upon cooling, suggesting some dynamic effects that exclude a secondary phase.

The integral of the 45 ppm peaks corresponds to about 3% of the total peak areas for pure NZTO. Hence, it is unlikely that the peak is due to the Na situated at a grain boundary, interface, or surface. In these cases, a high surface-to-volume ratio is necessary; however, this is not supported by any broadening of XRD peaks. We consider it unlikely that the peak may emerge from a substitutional defect of Na on either the Zn or Te position, due to the difference in charge and size. Under all circumstances, such a defect is expected to have a chemical shift to the right of the prismatically coordinated Na, considering that Na on the Zn site will be octahedrally coordinated. Due to the ambiguous decomposition of the ^{23}Na MAS NMR spectra, the changes in the Na sublattice from the Ga substitution cannot be described in sufficient detail.

3.3. ^{125}Te NMR Studies. The NZTO-based materials were further characterized by means of ^{125}Te MAS NMR; see spectra in Figures 4 and S4 for curve fittings. The ^{125}Te spectrum of the NZTO (x = 0.00, black line, Figure 4) shows one peak at 155 ppm with a distinct shoulder at approximately 145 ppm. The physical origin of this shoulder feature will be discussed in Section 3.5. Integration of this shoulder feature (145 ppm) in the samples x = 0.00 and 0.05 is counted as part of the main peak (150 ppm) in this section. Furthermore, note that the spectrum cannot be unambiguously decomposed, and at least three Gaussian peaks are needed for a good peak shape description. As Te takes one single crystallographic site (Wyckoff site 2c) and is a spin 1/2 nucleus, the presence of multiple peaks must be due to different local structures around Te atoms. Upon Ga substitution, additional peaks emerge in the region below 140 ppm (Figure 4). All Ga-substituted samples show a feature around 140 ppm, while x = 0.15 and 0.20 show a weaker peak at about 125 ppm as well. Based on charge and size arguments, we claim that Ga substitutes for Zn are in compliance with the intensities of the XRD patterns. A

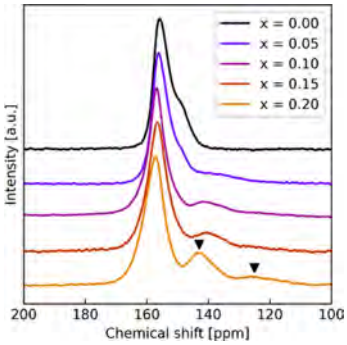

Figure 4. ^{125}Te MAS NMR spectra of $Na_{2-x}Zn_{2-x}Ga_xTeO_6$. Two peaks that appear at higher substitution levels are marked with black arrows for x = 0.20.

Ga atom at a Zn site will therefore be within the second coordination sphere of three Te atoms. By curve fitting and integration, we estimated the relative amounts of the main peak at 155 ppm and the two side peaks at 140 and 125 ppm (see Table 1 below). The integration shows that the theoretical

Table 1. Integrated Peak Intensities and Percentage of Te Atoms with at Least One Close Neighbor Ga Atom for $Na_{2-x}Zn_{2-x}Ga_xTeO_6$[a]

x	theoretical Te with at least one Ga neighbor [%]	I (155 ppm) [%]	I (140 ppm) [%]	I (125 ppm) [%]	sum small peaks [%]
0.00	0.0	100.0	0.0	0.0	0.0
0.05	7.5	86.4	11.1	0.0	11.1
0.10	15.0	83.9	16.1	0.0	16.1
0.15	22.5	75.0	22.4	2.6	25.0
0.20	30.0	71.2	22.3	6.6	28.9

[a]For x = 0.20, 10% of Zn atoms are replaced by Ga. Each Zn site has three Te neighbors, implying that 30% of the Te atoms for x = 0.20 have at least one Ga neighbor.

estimate of the number of Te atoms with different surroundings corresponds very well with the integrated ratio of the observed peaks, assuming the peak at 140 ppm to reflect Te atoms with one Ga neighbor and the 125 ppm peak to reflect two neighbors.

The highest substitution level of x = 0.20 should influence 30% of the Te atoms. The integration shows that the main peak amounts to 71.2%, and the two smaller peaks sum up to 28.8%, which is in good agreement with the expected value. An exception is x = 0.05, for which the integrated value is higher than the theoretical value (11.1 vs 7.5, respectively), which can be attributed to uncertainties in the integration of the weak peak at 140 ppm and the high influence of variations during phasing. The increase in only the two-neighbor peak (at 125 ppm) between x = 0.15 and 0.20 are indications that the Ga distribution is less random at high substitution levels. We note a change in the peak shape also for the main peak with increasing x. Hence, Te atoms with no neighboring Ga atoms are also affected. The nature of the changes is explored in Section 3.4. Note that there are no indications that any ^{23}Na or ^{125}Te peaks are due to significant amounts of a secondary phase. Based on our NMR analyses, it is likely that samples

https://doi.org/10.1021/acs.inorgchem.2c01431
Inorg. Chem. 2022, 61, 13067−13076

correspond to the nominal composition targeted in the synthesis, except for maybe the material with $x = 0.05$. This suggests that the deviation in the c-parameter for the $x = 0.15$ sample is not due to aspects of Ga concentration. Furthermore, the NMR data clearly indicate that the homogeneous substitution of Ga is obtained upon sol−gel synthesis.

3.4. DFT Calculations of ^{125}Te Chemical Shifts. To progress further with analyses of the ^{125}Te spectra, DFT calculations of chemical shifts were carried out as we expected ^{125}Te chemical shifts to be influenced by the distribution of Na ions between the *g*-, *f*-, and *a*-sites due to its many electrons. Out of these sites, Na atoms in the *a*-sites have the largest separation from the Te site. Hence, for the NMR spectra, focus was on the *f*- and *g*-sites. We describe the Te environment with respect to interlayer Na cations with the notation *namb*, where *na* and *mb* refer to two neighboring sodium layers; *a*, *b* denotes the type of Na site (*f* or *g*) and *n*, *m* describes the number of Na in the said type of site (0, 1, 2, 3). In the case of an *f*-site, only *n*, *m* = 0, 1 are possible. When *n* = 0 or *m* = 0, either *na* or *mb* is omitted for simplicity. Some possible coordination environments for Te are shown in Figure 5.

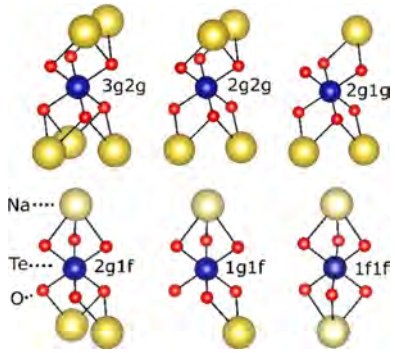

Figure 5. Five Te environments, in addition to the 1*f*1*f*-environment. As noted, the 3*g*2*g* is not common but is included to calculate the influence of the number of Na neighbors to Te. Note: there are 12 distinct Te configuration environments in total.

Calculations to benchmark various approaches were performed on the most stable configuration reported in our previous work.[13] This arrangement is a modification of the hexagonal structure, with twice as many atoms in the unit cell to account for a nonhexagonal reconstruction of the Na sublattice with Na ions equally distributed across the *g*- and *f*-sites and with *a*-sites unoccupied. In this model, all Te atoms exhibit a 2*g*1*f* coordination environment.

Obtained benchmarking chemical shift data are reported in Table 2 and compared with experimental values. The GGA calculation correctly reproduces the sign of the chemical shift and its order of magnitude but deviates clearly from the experimental reference. It is hence tested whether a different setup for the calculation would provide a chemical shift closer to the measured values.

The most accurate set of PAW potential is adopted. In this approach, labeled as "GGA + core states" in Table 2, the most external full shells of p and s electrons are treated as valence electrons, and the associated Kohn−Sham equations are explicitly solved. This method did not provide a shift value

Table 2. Calculated Shifts According to Three Methods for the 2*g*1*f* Environment in NZTO. TeO_2 is Used as a Reference in the Computations, While $Te(OH)_6$ is the Standard Used for Referring Te Shifts and in Experiments

method	shift from TeO_2 [ppm]	shift from $Te(OH)_6$ [ppm]
GGA (standard setting)	−291	460
GGA + core states	−278	473
SCAN + core states	−609	142
experimental span NZTO	−606 to −587	145−164

closer to the experiment. We note that the usage of hybrid functional (i.e., approaches mixing PBE and Hartree−Fock results when computing the exchange portion of the energy) is not viable due to the size of the system (4 formula units, i.e., 44 atoms). A more suitable option is the Meta-GGA functionals using the Laplacian of the density or the kinetic energy on top of the density and its gradient considered by GGA. Within this class of functionals, SCAN recently emerged as an approach capable of an accurate description of bonding in various cases, including oxides such $BaTiO_3$, $PbTiO_3$, and $BiFeO_3$,[50] while maintaining a computational cost comparable to GGA. The reason for this improvement in accuracy is, however, not obvious. While SCAN usually provides more accurate interatomic distances than GGA, the computed values are, in both cases, compatible with experimental data, as shown in Table S5.

The SCAN-based description of the chemical bonding, Table S6, is compatible with the GGA reference and shows a substantial ionic character in good agreement with expectations. The calculated Te shift is fully compatible with experimental references. For this reason, we use the SCAN method and proceed to a modified Te environment to compute the effect on the chemical shift. These environments are constructed to generate different Te coordination environments and are explained in detail in Section S5.

Due to the small size of the system, only a few configurations can be explored. We have opted not to use a supercell system since a large number of atoms in a linear response calculation of this kind significantly increases the computational cost, and convergence of the self-consistent field computation is hard to achieve. The number of atoms is kept constant, and the Na distribution is rearranged to obtain the most frequently observed coordination environments for Te (computed by analysis of MD trajectories described in Section 3.5). These coordination environments are 1*g*1*f*, 2*g*1*f*, 2*g*1*g*, and 2*g*1*g*. The 3*g*2*g* environment, albeit rarely encountered, is also considered to be better, influencing the number of Na ions in the Te coordination environment. Figure 6 below shows the calculated chemical shift values for five different Te environments in NZTO.

There are two noticeable trends for the Te chemical shifts seen in Figure 6. Te atoms with a larger number of Na neighbors are more shielded and therefore shifted to a lower frequency compared to Te atoms with fewer Na neighbors. A comparison of the 2*g*1*f* and 2*g*1*g* environments is the only instance where the difference between the *f*- and *g*-sites can be determined, as one set of neighbors (2*g*) is the same for both, while the second is either *f* or *g*. In this situation, the edge-sharing *g*-position provides better shielding than the face-sharing *f*-site. Overall, the trend in chemical shifts can be summed up as follows:

https://doi.org/10.1021/acs.inorgchem.2c01431
Inorg. Chem. 2022, 61, 13067−13076

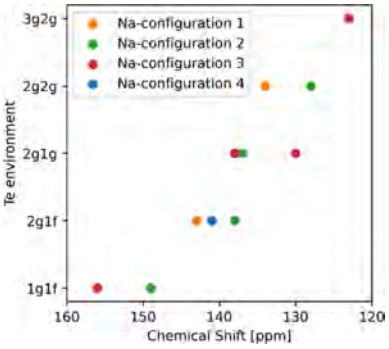

Figure 6. Calculated chemical shift values for five Te environments in NZTO that are produced by four different Na configurations as explained in more detail in Section S5.

1. Less shielding of Te is provided by fewer Na neighbors, which shifts the spectra to higher frequencies/ppm values.
2. Less shielding of Te is provided by Na atoms in the *f*-position (face-sharing) than those in the *g*-position (edge-sharing). This shifts the spectra to higher frequencies/ppm values.

On one side of a Te atom, there can be one, two, or three Na ions in *g*-sites or only one in an *f*-site. Hence, the 1st point is only relevant for environments involving *g*-sites.

We observe that for a given Te environment, the calculated shift is different depending on the Na configuration, i.e., it is influenced by Na positions beyond those that are directly face- or edge-sharing to the given Te atom. Since relatively small periodic systems are used for these computations, the Na distribution exerts certain distortions on the lattice, expectedly to be a feature of the simulations.

Based on these trends, we expect that Ga^{3+} substitution at the Zn^{2+} sites, which in turn will lower the amount of Na^{+}, will result in a change in the peak intensities in the ^{125}Te MAS NMR spectra toward higher frequencies, which is exactly what is observed in Figure 4. The main peak (Te with zero close Ga neighbors) shifts to the left with increasing substitution, consistent with a lower Na content.

Albeit we observe just a moderate shift of 2 ppm in the peak position, the width of the main peak broadens on Ga substitution. This may be due to increased dipolar couplings of Te with substituted Ga, as all Ga atoms have nuclei with magnetic moments, and only about 4% of Zn atoms have nuclear magnetic moments. The Te−Ga interactions, in addition to the already in place Te−Na interactions, and the relative strengths may be discussed by considering the magnetogyro ratios of ^{125}Te, ^{69,71}Ga, and ^{23}Na (all are quite similar) and distances from Te to these elements (see details in SI9). The Te−Na and Te−Zn/Ga distances from the average structure from XRD are 2.81 and 3.05 Å, respectively. Hence, by increasing the Ga content, one could expect a relative increase in nuclear dipole−dipole couplings of Te, albeit complicated due to Ga's relaxation rates. Furthermore, Na is known to be dynamic at room temperature in these materials, and Na's interactions with Te are therefore decreased relative to a static case. The result is that when Ga is substituted into the material, one could expect a broadening of Te peaks due to the increase in dipole−dipole couplings of Te and nearby nuclei.

3.5. *Ab Initio* MD Simulations: Na Distribution and Te Environments. It is not possible to break down ^{125}Te spectra into an unambiguous decomposition, and DFT simulations are performed to gain some insight into the Te coordination environments. Three compositions of $Na_{2-x}Zn_{2-x}Ga_xTeO_6$ type with x = 0 (NZTO), 0.083 (2Ga), and 0.167 (4Ga) were explored with *ab initio* MD simulation, the latter two with, respectively, 2 and 4 Ga^{3+} ions in a supercell with 24 formula units. The construction of the systems is explained in Section S7. For each composition x, we consider two simulation temperatures, 750 and 1000 K. As demonstrated in Section S7, the 4Ga system exhibits a clear preference for an uneven Na distribution when comparing Na layers. In this case, a 23:21 distribution of the 44 Na ions has an energy gain of 0.2 eV with respect to a system with an even (22:22) distribution.

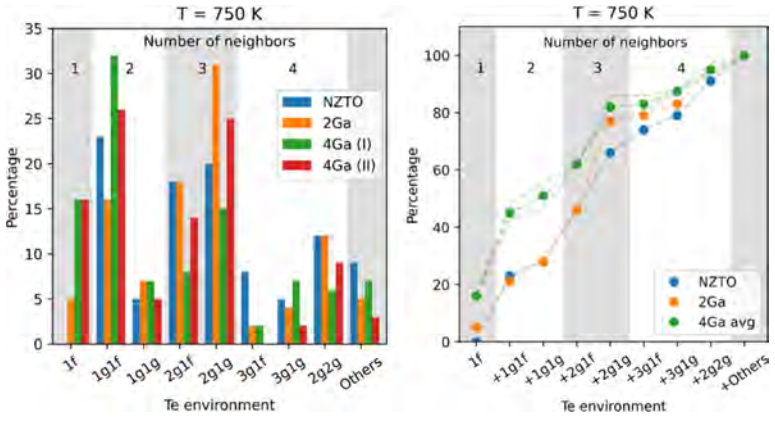

Figure 7. Te environments from 50 ps MD at 750 K. The number of Na neighbors around Te is marked as gray and white areas as a guide to the eye. (a) Relative percentages of each Te environment; (b) cumulative distribution, where amounts of each environment are added in the order of calculated shielding from Section 3.4. The average of two 4Ga runs is plotted, with the two individual runs indicated by gray dotted lines.

https://doi.org/10.1021/acs.inorgchem.2c01431
Inorg. Chem. 2022, 61, 13067−13076

The layer with a larger vacancy concentration exhibits an increased occupancy of the *a*-site.

The average occupation of the Na sites is computed from the AIMD trajectories using an *ad hoc* procedure described in S8 and reported in Table S7. When examining these data, it is important to keep in mind the multiplicity of the three sites: if the occupancy of all of the available sites were equal, the sum of the *g*-sites would be three times as populous as that of the *a*-site. At 750 K, we note that an increased amount of Ga corresponds to a more favorable occupation of the *a*-sites. At 1000 K, the Na site population of all systems is compatible, and it is impossible to identify any effect of Ga substitution. Using the described labeling of the occupied Na sites, we can determine the coordination environments of Te from the AIMD trajectories and compute their abundance using an extension to the algorithm described in Section S8. The resulting population for 750 K is shown in Figure 7a. At this temperature, the Ga substitution influences the Na distribution.

For the pure NZTO, the more populous environments are 1*g*1*f*, 2*g*1*f*, 2*g*1*g*, and, to a minor extent, 2*g*2*g*, whereas the 1*f*1*f* is not populated at all. As the *f*-site has an expected high occupancy, this may then indicate that the Na layers are not independent but that the Na in one layer influences the structure in adjacent layers. In 4Ga, it is interesting to note that the 1*f* environment becomes very populated as the *f*- and *a*-sites become more favorable. As shown in Figure 7b, we further note that the 2*g*1*g* environment becomes highly populated for 2Ga.

With the limited size of the supercell, the amount of each environment is quite low, and the exact number is therefore quite uncertain. Instead, one can look at the general trends, which are clearer when looking at the cumulative distribution of Te environments in Figure 7b, plotted in the order of the shielding calculated in Section 3.4. This plot demonstrates that the samples with the high level of Ga substitution have more of the Te environments with a low number of Na neighbors, while the unsubstituted material has more of Te environments with a high number of Na neighbors. This is fully in line with the interpretation of the ^{125}Te NMR data: the spectra will gain more intensity in the high-frequency region (left part) upon Ga substitution due to an increase of Te environments with fewer Na neighbors. It should be noted that this is not a peak shift but a relative change in the peak intensity ratios for different environments. This could be the explanation for the disappearance of the shoulder peak at 145 ppm, which is due to Te environments with a high number of Na neighbors for the materials with a lower amount of Na. This is also consistent with the observed features in the Te spectra, where the environments do not vary linearly with composition *x*. The peak maxima shift minimally, but the edges of the peak shift to a larger extent. The shift of the high-frequency edge is well in line with the increased population of the 1*f* environment, which is expected to be at a higher frequency than any environment in the pure NZTO. Furthermore, it is very likely that the ^{125}Te NMR spectra consist of multiple overlapping peaks, which are not resolved.

3.6. Comments on Ion Conductivities Based on New Synthesis Protocol: Comparison and Discussion. The homogeneity of Ga in the Ga-substituted materials is likely not to have a large direct influence on the total ionic conductivity as measured by, e.g., impedance measurements. The synthesis method we have reported is employed to control the stoichiometry, ensuring that no region has a lower degree of substitution, which in turn might give a local decrease in ionic conductivity. The bulk (interlayer) conduction is based on the large number of vacancies relative to the Na number, which should be comparable if samples are stoichiometric. A comparison between the ^{23}Na NMR for NZTO synthesized with sol−gel and solid-state synthesis is shown in Section S10, which demonstrates the same local environment. This suggests that the different synthesis methods have very little influence on the local structure, which would result in a relatively similar bulk conductivity. However, there are other influences on the total ion conductivity where the synthesis method is believed to have a greater influence. One is the grain boundary conductivity, which was demonstrated by Wu et al. to be 2 orders of magnitude lower than that of the bulk, greatly limiting the total conductivity.[15] The temperature program used in this work has a shorter heating time than previous studies, which would yield smaller particles, resulting in more grain boundaries and thus might reduce total ionic conduction. Material preparation aiming for high ion conductivity might therefore have to be further optimized to give large particles and dense samples, which should be possible as the sol−gel synthesis method can tailor particle size and morphology.

4. CONCLUSIONS

In this work, we have described sol−gel synthesis and structural characterization of layered NZTO and its Ga-substituted derivatives ($Na_{2-x}Zn_{2-x}Ga_xTeO_6$, x = 0.00, 0.05, 0.10, 0.15, 0.20) by means of XRD, MAS NMR, and DFT methods.

The sol−gel synthesis protocol we applied provided samples with a high level of purity and with a homogeneous distribution of Ga. This is essential for the manufacturing and for the detailed characterization of a solid-state electrolyte candidate material, in particular when it comes to relationships between composition (substituents) and structure (sites).

The NMR data, with the support of DFT modeling, suggest a uniform Ga substitution; hence, we can claim that Ga atoms take the position of the Zn atoms with a concomitant reduction of the Na content. The introduction of heterovalent Ga atoms influences the Na substructure, in a way that the various Wyckoff sites become more energetically similar. The DFT modeling also suggests an inhomogeneous Na distribution between the neighboring layers for higher substitutions, in addition to an influence on the Na distribution in one layer from the Na structure in the adjacent layers.

The ^{125}Te NMR chemical shift values are influenced by both Na and Ga. The effect created by the Na distributions in the two neighboring interlayers was analyzed by DFT calculations. We found that linear response calculation using the SCAN functional gave values for the chemical shifts within the experimental range. The Ga-containing samples showed additional peaks in the ^{125}Te NMR spectra in quantities as expected for a uniform substitution mechanism.

■ ASSOCIATED CONTENT

Supporting Information

The Supporting Information is available free of charge at https://pubs.acs.org/doi/10.1021/acs.inorgchem.2c01431.

Supporting Information with details on DTF modeling, Rietveld refinement, SEM images, curve fitting of ^{23}Na and ^{125}Te spectra, Te configuration for chemical shift

https://doi.org/10.1021/acs.inorgchem.2c01431
Inorg. Chem. 2022, 61, 13067−13076

calculations, discussion of GGA and SCAN functionals, starting points for DFT modeling of Ga-doped materials, dynamical definition of Na and Te coordination environments, notes on evaluation on dipolar couplings, and comparison between ^{23}Na spectra of NZTO synthesized using sol−gel and solid-state synthesis (PDF)

AUTHOR INFORMATION

Corresponding Authors

Bjørnar Arstad − *SINTEF Industry, Oslo 0373, Norway;* orcid.org/0000-0003-0398-786X; Email: bjornar.arstad@sintef.no

Helmer Fjellvåg − *Department of Chemistry and Center for Materials Science and Nanotechnology, University of Oslo, Oslo 0371, Norway*; Email: helmer.fjellvag@kjemi.uio.no

Authors

Frida Sveen Hempel − *SINTEF Industry, Oslo 0373, Norway; Department of Chemistry and Center for Materials Science and Nanotechnology, University of Oslo, Oslo 0371, Norway*

Federico Bianchini − *Department of Chemistry and Center for Materials Science and Nanotechnology, University of Oslo, Oslo 0371, Norway;* Present Address: Center for Bioinformatics, University of Oslo, Gaustadalléen 30, N-0373 Oslo, Norway

Complete contact information is available at: https://pubs.acs.org/10.1021/acs.inorgchem.2c01431

Author Contributions

The manuscript was written through contributions of all authors. All authors have given approval to the final version of the manuscript.

Notes

The authors declare no competing financial interest.

ACKNOWLEDGMENTS

The authors acknowledge the Research Council of Norway for providing the financial support (under project numbers P#272402 and P#255441) and for the computing time (under the project number NN2875k and NS2875k) at the Norwegian supercomputer facility. DFT calculations were performed between June 2019 and August 2020.

REFERENCES

(1) Goodenough, J. B.; Mizushima, K.; Jones, P. C.; Wiseman, P. LixCoO2 (0 < x ∼ < 1): A New Cathode Material for Batteries of High Energy Density. *Solid State Ionics* **1981**, *4*, 171−174.

(2) Development, U. C. on T. *Special Issue on Strategic Battery Raw Materials*; UNCTAD, 2020.

(3) Sun, P.; Bisschop, R.; Niu, H.; Huang, X. *A Review of Battery Fires in Electric Vehicles*; Springer: US, 2020; Vol. *56*.

(4) Eshetu, G. G.; Grugeon, S.; Laruelle, S.; Boyanov, S.; Lecocq, A.; Bertrand, J. P.; Marlair, G. In-Depth Safety-Focused Analysis of Solvents Used in Electrolytes for Large Scale Lithium Ion Batteries. *Phys. Chem. Chem. Phys.* **2013**, *15*, 9145−9155.

(5) Manthiram, A.; Yu, X.; Wang, S. Lithium Battery Chemistries Enabled by Solid-State Electrolytes. *Nat. Rev. Mater.* **2017**, *2*, 1−16.

(6) Fan, L.; Wei, S.; Li, S.; Li, Q.; Lu, Y. Recent Progress of the Solid-State Electrolytes for High-Energy Metal-Based Batteries. *Adv. Energy Mater.* **2018**, *8*, 1−31.

(7) Delmas, C.; Fouassier, C.; Hagenmuller, P. Structural Classification and Properties of Layered Oxides. *Physica B+C* **1980**, *99*, 81−85.

(8) Evstigneeva, M. A.; Nalbandyan, V. B.; Petrenko, A. A.; Medvedev, B. S.; Kataev, A. A. A New Family of Fast Sodium Ion Conductors: Na2M 2TeO6 (M = Ni, Co, Zn, Mg). *Chem. Mater.* **2011**, *23*, 1174−1181.

(9) Berthelot, R.; Schmidt, W.; Sleight, A. W.; Subramanian, M. A. Studies on Solid Solutions Based on Layered Honeycomb-Ordered Phases P2-Na 2M 2TeO 6 (M = Co, Ni, Zn). *J. Solid State Chem.* **2012**, *196*, 225−231.

(10) Gupta, A.; Buddie Mullins, C.; Goodenough, J. B. Na2Ni2TeO6: Evaluation as a Cathode for Sodium Battery. *J. Power Sources* **2013**, *243*, 817−821.

(11) Li, X.; Bianchini, F.; Wind, J.; Pettersen, C.; Wragg, D. S.; Vajeeston, P.; Fjellvåg, H. Insights into Crystal Structure and Diffusion of Biphasic Na 2 Zn2 TeO6. *ACS Appl. Mater. Interfaces* **2020**, *12*, 28188−28198.

(12) Li, Y.; Deng, Z.; Peng, J.; Gu, J.; Chen, E.; Yu, Y.; Wu, J.; Li, X.; Luo, J.; Huang, Y.; Xu, Y.; Gao, Z.; Fang, C.; Zhu, J.; Li, Q.; Han, J.; Huang, Y. New P2-Type Honeycomb-Layered Sodium-Ion Conductor: Na2Mg2TeO6. *ACS Appl. Mater. Interfaces* **2018**, *10*, 15760−15766.

(13) Bianchini, F.; Fjellvåg, H.; Vajeeston, P. Nonhexagonal Na Sublattice Reconstruction in the Super-Ionic Conductor Na 2 Zn 2 TeO 6: Insights from Ab Initio Molecular Dynamics. *J. Phys. Chem. C* **2019**, *123*, 4654−4663.

(14) Li, Y.; Deng, Z.; Peng, J.; Chen, E.; Yu, Y.; Li, X.; Luo, J.; Huang, Y.; Zhu, J.; Fang, C.; Li, Q.; Han, J.; Huang, Y. A P2-Type Layered Superionic Conductor Ga-Doped Na2Zn2TeO6for All-Solid-State Sodium-Ion Batteries. *Chem. - Eur. J.* **2018**, *24*, 1057−1061.

(15) Wu, J. F.; Wang, Q.; Guo, X. Sodium-Ion Conduction in Na2Zn2TeO6 Solid Electrolytes. *J. Power Sources* **2018**, *402*, 513−518.

(16) Sau, K.; Kumar, P. P. Role of Ion-Ion Correlations on Fast Ion Transport: Molecular Dynamics Simulation of Na2Ni2TeO6. *J. Phys. Chem. C* **2015**, *119*, 18030−18037.

(17) Sau, K.; Kumar, P. P. Ion Transport in Na2M2TeO6: Insights from Molecular Dynamics Simulation. *J. Phys. Chem. C* **2015**, *119*, 1651−1658.

(18) Sau, K. Influence of Ion−Ion Correlation on Na+ Transport in Na2Ni2TeO6: Molecular Dynamics Study. *Ionics* **2016**, *22*, 2379−2385.

(19) Karna, S. K.; Zhao, Y.; Sankar, R.; Avdeev, M.; Tseng, P. C.; Wang, C. W.; Shu, G. J.; Matan, K.; Guo, G. Y.; Chou, F. C. Sodium Layer Chiral Distribution and Spin Structure of Na2Ni2TeO6 with a Ni Honeycomb Lattice. *Phys. Rev. B* **2017**, *95*, 1−9.

(20) Bianchini, M.; Wang, J.; Wang, J.; Clément, R. J.; Ouyang, B.; Xiao, P.; Kitchaev, D.; Shi, T.; Zhang, Y.; Wang, Y.; Kim, H.; Zhang, M.; Bai, J.; Wang, F.; Sun, W.; Ceder, G. The Interplay between Thermodynamics and Kinetics in the Solid-State Synthesis of Layered Oxides. *Nat. Mater.* **2020**, *19*, 1088−1095.

(21) Li, X.; Ma, X.; Su, D.; Liu, L.; Chisnell, R.; Ong, S. P.; Chen, H.; Toumar, A.; Idrobo, J. C.; Lei, Y.; Bai, J.; Wang, F.; Lynn, J. W.; Lee, Y. S.; Ceder, G. Direct Visualization of the Jahn-Teller Effect Coupled to Na Ordering in Na 5/8 MnO 2. *Nat. Mater.* **2014**, *13*, 586−592.

(22) Li, X.; Bianchini, F.; Wind, J.; Vajeeston, P.; Wragg, D.; Fjellvåg, H. P2 Type Layered Solid-State Electrolyte Na 2 Zn 2 TeO 6: Crystal Structure and Stacking Faults. *J. Electrochem. Soc.* **2019**, *166*, A3830−A3837.

(23) Zhang, Z.; Shao, Y.; Lotsch, B.; Hu, Y. S.; Li, H.; Janek, J.; Nazar, L. F.; Nan, C. W.; Maier, J.; Armand, M.; Chen, L. New Horizons for Inorganic Solid State Ion Conductors. *Energy Environ. Sci.* **2018**, *11*, 1945−1976.

(24) Coelho, A. A. TOPAS and TOPAS-Academic: An Optimization Program Integrating Computer Algebra and Crystallographic Objects Written in C++: An. *J. Appl. Crystallogr.* **2018**, *51*, 210−218.

(25) Clément, R. J.; Xu, J.; Middlemiss, D. S.; Alvarado, J.; Ma, C.; Meng, Y. S.; Grey, C. P. Direct Evidence for High Na+ Mobility and High Voltage Structural Processes in P2-Nax[LiyNizMn1-y-z]O2 (x, y, z ≤ 1) Cathodes from Solid-State NMR and DFT Calculations. *J. Mater. Chem. A* **2017**, *5*, 4129−4143.
(26) Caballero, A.; Hernán, L.; Morales, J.; Sánchez, L.; Santos Peña, J.; Aranda, M. A. G. Synthesis and Characterization of High-Temperature Hexagonal P2-Na0.6 Mno2 and Its Electrochemical Behaviour as Cathode in Sodium Cells. *J. Mater. Chem.* **2002**, *12*, 1142−1147.
(27) Massiot, D.; Fayon, F.; Capron, M.; King, I.; Le Calvé, S.; Alonso, B.; Durand, J. O.; Bujoli, B.; Gan, Z.; Hoatson, G. Modelling One- and Two-Dimensional Solid-State NMR Spectra. *Magn. Reson. Chem.* **2002**, *40*, 70−76.
(28) Kresse, G.; Hafner, J. Ab Initio Molecular Dynamics for Liquid Metals. *Phys. Rev. B* **1993**, *47*, 558−561.
(29) Kresse, G.; Furthmüller, J. Efficiency of Ab-Initio Total Energy Calculations for Metals and Semiconductors Using a Plane-Wave Basis Set. *Comput. Mater. Sci.* **1996**, *6*, 15−50.
(30) Kresse, G.; Furthmüller, J. Efficient Iterative Schemes for Ab Initio Total-Energy Calculations Using a Plane-Wave Basis Set. *Phys. Rev. B* **1996**, *54*, 11169−11186.
(31) Kresse, G.; Joubert, D. From Ultrasoft Pseudopotentials to the Projector Augmented-Wave Method. *Phys. Rev. B* **1999**, *59*, 1758−1775.
(32) Pickard, C. J.; Mauri, F. All-Electron Magnetic Response with Pseudopotentials: NMR Chemical Shifts. *Phys. Rev. B* **2001**, *63*, 2451011−2451013.
(33) Yates, J. R.; Pickard, C. J.; Mauri, F. Calculation of NMR Chemical Shifts for Extended Systems Using Ultrasoft Pseudopotentials. *Phys. Rev. B* **2007**, *76*, 1−11.
(34) Sun, J.; Ruzsinszky, A.; Perdew, J. Strongly Constrained and Appropriately Normed Semilocal Density Functional. *Phys. Rev. Lett.* **2015**, *115*, 1−6.
(35) Nosé, S. A Unified Formulation of the Constant Temperature Molecular Dynamics Methods. *J. Chem. Phys.* **1984**, *81*, 511−519.
(36) Nosé, S. Constant Temperature Molecular Dynamics Methods Limitations in Simulations in the Microcanonical Ensemble. *Prog. Theor. Phys. Suppl.* **1991**, 1−46.
(37) Bylander, D. M.; Kleinman, L. Energy Fluctuations Induced by the Nose Thermostat. *Phys. Rev. B* **1992**, *46*, No. 13756.
(38) Goret, G.; Aoun, B.; Pellegrini, E. MDANSE: An Interactive Analysis Environment for Molecular Dynamics Simulations. *J. Chem. Inf. Model.* **2017**, *57*, 1−5.
(39) Larsen, A. H.; Mortensen, J. J.; Blomqvist, J.; Castelli, I. E.; Christensen, R.; Dułak, M.; Friis, J.; Groves, M. N.; Hammer, B.; Hargus, C.; Hermes, E. D.; Jennings, P. C.; Jensen, P. B.; Kermode, J.; Kitchin, J. R.; Kolsbjerg, E. L.; Kubal, J.; Kaasbjerg, K.; Lysgaard, S.; Maronsson, J. B.; Maxson, T.; Olsen, T.; Pastewka, L.; Peterson, A.; Rostgaard, C.; Schiøtz, J.; Schütt, O.; Strange, M.; Thygesen, K. S.; Vegge, T.; Vilhelmsen, L.; Walter, M.; Zeng, Z.; Jacobsen, K. W. The Atomic Simulation Environment—a Python Library for Working with Atoms. *J. Phys.: Condens. Matter* **2017**, *29*, No. 273002.
(40) Bahn, S. R.; Jacobsen, K. W. An Object-Oriented Scripting Interface to a Legacy Electronic Structure Code. *Comput. Sci. Eng.* **2002**, *4*, 56−66.
(41) QUIP and Quippy Documentation, 2021. https://libatoms.github.io/QUIP/.
(42) Momma, K.; Izumi, F. VESTA: A Three-Dimensional Visualization System for Electronic and Structural Analysis. *J. Appl. Crystallogr.* **2008**, *41*, 653−658.
(43) Garaga, M. N.; Werner-Zwanziger, U.; Zwanziger, J. W.; Deceanne, A.; Hauke, B.; Bozer, K.; Feller, S. Short-Range Structure of TeO2 Glass. *J. Phys. Chem. C* **2017**, *121*, 28117−28124.
(44) Lizion, J.; Piarristeguy, A.; Laskowski, R.; Blaha, P.; Escalier, R.; Ménétrier, M.; Pradel, A.; Silly, G. 125Te NMR for Structural Investigations in Phase Change Materials: Optimization of Experimental Conditions Coupled to NMR Shift Prediction. *Solid State Nucl. Magn. Reson.* **2021**, *115*, No. 101751.
(45) Alkan, F.; Dybowski, C. Spin-Orbit Effects on the 125Te Magnetic-Shielding Tensor: A Cluster-Based ZORA/DFT Investigation. *Solid State Nucl. Magn. Reson.* **2018**, *95*, 6−11.
(46) Nalbandyan, V. B.; Petrenko, A. A.; Evstigneeva, M. A. Heterovalent Substitutions in Na2M2TeO6 Family: Crystal Structure, Fast Sodium Ion Conduction and Phase Transition of Na2LiFeTeO6. *Solid State Ionics* **2013**, *233*, 7−11.
(47) Carlier, D.; Blangero, M.; Ménétrier, M.; Pollet, M.; Doumerc, J. P.; Delmas, C. Sodium Ion Mobility in NaxCoO2 (0.6 < × < 0.75) Cobaltites Studied by 23Na MAS NMR. *Inorg. Chem.* **2009**, *48*, 7018−7025.
(48) Kentgens, A. P. M. A Practical Guide to Solid-State NMR of Half-Integer Quadrupolar Nuclei with Some Applications to Disordered Systems. *Geoderma* **1997**, *80*, 271−306.
(49) MacKenzie, K. J. D.; Smith, M. E. *Multinuclear Solid-State NMR of Inorganic Materials*, Pergamon Material Series; Elsevier, 2002; Vol. 6.
(50) Sun, J.; Remsing, R. C.; Zhang, Y.; Sun, Z.; Ruzsinszky, A.; Peng, H.; Yang, Z.; Paul, A.; Waghmare, U.; Wu, X.; Klein, M. L.; Perdew, J. P. Accurate First-Principles Structures and Energies of Diversely Bonded Systems from an Efficient Density Functional. *Nat. Chem.* **2016**, *8*, 831−836.

https://doi.org/10.1021/acs.inorgchem.2c01431
Inorg. Chem. 2022, 61, 13067−13076

Supplementary information:

Effects of Ga-substitution on the local structure of $Na_2Zn_2TeO_6$

Frida Sveen Hempel,[a, b] Federico Bianchini,[b,†] Bjørnar Arstad *[a] and Helmer Fjellvåg *[b]

a) SINTEF Industry, Forskningsveien 1, 0373 Oslo, Norway

b) Department of Chemistry and Center for Materials Science and Nanotechnology, University of Oslo, Oslo 0371, Norway

† Current address: Center for Bioinformatics, University of Oslo Gaustadalléen 30 N-0373 Oslo

* bjornar.arstad@sintef.no

* helmer.fjellvag@kjemi.uio.no

S1 DFT modelling

S1.1 Summarized information of calculations

The simulations were performed using VASP version 5.4.4,[1–4] with input/output manipulation and data analysis performed using python version 2.7.17, ase version 3.17.0 and quippy (https://github.com/libAtoms/QUIP.git ad62f721a-dirty) which was compiled on linux_x86_64_gfortran architecture.

Table S1.1: Input keywords for all calculations. Some additional information on the AIMD simulations: The thermalisation uses a *NVT* ensemble, with *T* specified in the INCAR. SIGMA of Fermi function is adjusted to the desired *T*. The MD calculation restarted until the desired thermalisation time is reached, from the CONTCAR to get the positions and momenta. The electronic problem is restarted from scratch every time. This saves time, as we are avoiding writing charge density and wave function, which is extremely time-consuming and disk-space consuming for a system of large size. The production uses a *NVE* ensemble, which is restarted from thermalized configuration. *T* is taken from the momenta of the thermalized system, but the SIGMA of the Fermi function is kept from the *NVT* run, as not to modify the electronic problem. This is restarted until desired time length is reached.

SCAN		Structural optimization	AIMD	
Structural optimization	Chemical shift		Thermalization	Production
KSPACING = 0.4	PREC = A	ENCUT = 500.000000	ENCUT = 400.000000	ENCUT = 400.000000
PREC = A	IALGO = 38	KSPACING = 0.400000	EDIFF = 1.00e-07	EDIFF = 1.00e-07
IBRION = 2	IBRION = -1	SIGMA = 0.100000	PREC = Normal	PREC = Normal
ISIF = 3	ISIF = 2	EDIFF = 1.00e-04	GGA = PE	GGA = PE
ISTART = 0	ISTART = 0	ALGO = Very_Fast	ALGO = Very_Fast	ALGO = Very_Fast
ENCUT = 600.0	LCHARG = .FALSE.	GGA = PE	ISYM = 0	ISYM = 0
EDIFF = 1E-5	LWAVE = .FALSE.	PREC = Normal	NCORE = 10	NCORE = 10

ISMEAR = 0
SIGMA= 0.1
LREAL = A
NSW=40
METAGGA = SCAN
IALGO = 38
LASPH = .TRUE.
LDIAG = .FALSE.
NELM=120
NELMDL = 10

LCHIMAG = .TRUE
ENCUT = 600.0
EDIFF = 1E-8
ISMEAR = 0; SIGMA= 0.1
PREC = A
DQ = 0.001
ICHIBARE = 1
LNMR_SYM_RED = .TRUE.
NSLPLINE = .TRUE.
LREAL = A
KSPACING = 0.4
METAGGA = SCAN
LASPH = .TRUE.
LDIAG = .FALSE.
NELM=200
NELMDL = 10
AMIX = 0.1
BMIX=0.0001
IMIX = 1
ISYM=0

IBRION = 2
ISIF = 2
ISMEAR = 1
ISTART = 0
NSW = 300
NCORE = 8
LCHARG = .FALSE.
LWAVE = .FALSE.
LREAL = Auto

ISTART = 0
NSW = 5000
IBRION = 0
ISIF = 2
LCHARG = .FALSE.
LWAVE = .FALSE.
LREAL = Auto
ISMEAR = -1
SIGMA = 0.086
POTIM=1
SMASS=-1
TEBEG = 1000
TEEND = 1000
NBLOCK = 50

ISTART = 0
NSW = 5000
IBRION = 0
ISIF = 2
LCHARG = .FALSE.
LWAVE = .FALSE.
LREAL = Auto
ISMEAR = -1
SIGMA = 0.086
POTIM=1
SMASS=-3
NBLOCK = 1

All files are available upon request.

S1.2 Parameters for linear response calculations (chemical shift)

The following electron configurations are considered as valence: $2s^2 2p^6 3s^1$ for Na, $3s^2 3p^6 3d^{10} 4s^2$ for Zn, $4s^2 4p^6 4d^{10} 5s^2 5p^4$ for Te, and $1s^2 2s^2 2p^4$ for O. Integration over the Brillouin zone (BZ) is performed using Γ-centred Monkhorst-Pack grids[5] with a resolution of 0.4 $Å^{-1}$. Electronic gaussian smearing[6] with a 0.1 eV broadening width is used. A 600 eV kinetic energy cut-off for the plane wave expansion is chosen. A thick grid for Fast Fourier Transform is used, with twice as many points as the ones required by the cut-off energy. The blocked-Davidson scheme is used for optimising the orbitals and real space projection operators are used to evaluate the non-local part of the pseudopotential. The systems were optimised with an energy convergence threshold of 10^{-4} eV, while the energy convergence threshold of the self-consistent field (scf) calculation is set to 10^{-5} eV. The accuracy of scf calculation is further increased for the linear response calculations, with an energy convergence threshold of 10^{-8} eV.

S1.3 Parameters for structural optimisation

The following electron configurations are considered as valence: $3s^1$ for Na, $3d^{10} 4s^2$ for Zn, $4s^2 4p^1$ for Ga, $5s^2 5p^4$ for Te, and $2s^2 2p^4$ for O. Integration over the Brillouin zone (BZ) is performed using Γ-centred Monkhorst-Pack grids[5] with a resolution of 0.4 $Å^{-1}$. Electronic smearing is introduced using the Methfessel and Paxton method with a 0.1 eV broadening width. A 500 eV kinetic energy cut-off for the plane wave expansion is chosen. The orbitals are optimised using the Residual minimization method direct inversion in the iterative subspace[7] and real space projection operators are used to evaluate the non-local part

of the pseudopotential. The systems were optimised with an energy convergence threshold of 10^{-3} eV, while the energy convergence threshold of the scf calculation is set to 10−4 eV. The volume of the cell is kept fixed upon optimisation.

S1.3 parameters for AIMD simulations

The parameters form 6.1.2 are re-used here with some adjustments: the energy cut-off is decreased from 500 to 400 eV given the computational cost of these calculations. Moreover, the Brillouin Zone is sampled only using the Gamma point. We are consequently using the VASP version with real (not complex) numbers, corresponding to a better computational efficiency for this type of system. The convergence threshold of the scf loop is set to 10^{-7} eV. While this increases the computational cost, it prevents a drifting of the total energy that was observed upon testing. The dielectric function, used as a charge density mixer, is not reset after each ionic update to reduce the number of self-consistent steps after the first ionic interactions. Finally, the electronic smearing is introduced via the Fermi-Dirac distribution matching the electronic temperatures to the desired ionic temperatures.

AIMD simulations are executed for the starting system and two replicas of it, in which the volume has been expanded by 1% and 2% without modifying the shape of the cell (i.e. applying a diagonal strain). The dynamics is then propagated for 5~ps to allow for a (partial) thermalisation. After this step, the dynamics is further propagated for 5 ps more, without changing any parameters and collecting the values of the stress tensor at each step. These are averaged and used to estimate the equilibrium cell shape at a given temperature through linear fitting. This computation of the anisotropic thermal expansion is not accurate, but allows to define a reliable starting system at a reasonable computational cost without modifying the input parameters of the simulation: obtaining a more accurate estimate, e.g. through phonons, would require an entirely difficult setup of the simulation. Moreover, the occupation of the Na sites changes with time, and it is thus advisable to work on system averages rather than considering a structural minimum. A fourth replica of the initial system is then generated using the target lattice parameters. The stress on the cell is verified for this system using the same method. It is found that diagonal stress values are always smaller than 10 GPa and the average values are close to zero. The diagonal elements of the strain tensor are always negligible, being rarely larger than 1 GPa for all the fourth replicas. The simulation for the final replica is then protracted for 10 ps more, before switching to the microcanonical ensemble. The first 10 ps of dynamics in this ensemble are also considered part of the thermalisation stage and not accounted for when computing the physical quantities of interest e.g. the mean square displacement.

S2 Rietveld refinement

Table S1: Measurement and Rietveld refinement, where shared values are given in shared values. Peak

	x				
	0.00	0.05	0.10	0.15	0.20
Chemical formula	$Na_2Zn_2TeO_6$	$Na_{1.95}Zn_{1.95}Ga_{0.05}TeO_6$	$Na_{1.9}Zn_{1.9}Ga_{0.1}TeO_6$	$Na_{1.85}Zn_{1.85}Ga_{0.1}TeO_6$	$Na_{1.8}Zn_{1.8}Ga_{0.2}TeO_6$
Formula weight	400,33	399,40	398,47	397,54	396.6
a, b	5.29034(4)	5.28165(3)	5.27215(5)	5.27085(4)	5.26372(8)
c	11.24233(15)	11.24670(13)	11.25116(19)	11.24508(15)	11.2591(3)
α, β			90		
γ			120		
Source			laboratory X-ray		
Temperature			22°C		
Wavelength			1,540598 Å		
Crystal system			Hexagonal		
Space group			no. 182, *$P6_322$*		
Z			2		
d-space range			0.85 - 8.9		

Table S2: Fit values for inclusion of anisotropic size broadening and preferred orientation, which provides at best marginal improvement, and sometimes increase of R_p values. The particles are clearly anisotropic, as seen in figure S2, and while the size of the crystallites is unknown it is natural to assume some anisotropic size broadening, as described by Katerinopoulou et al.[8] Including this in the model does not improve the fit significantly. Preferred orientation seems to be sufficiently reduced in the capillary geometry. None is therefore included in the further refinement.

Parameter	Model	*x*				
		0.00	0.05	0.10	0.15	0.20
R_p	Normal	18,25	11,08	13,70	11,14	20,54
	Anisotropic size	17,68	11,16	15,43	11,03	20,33
	Preferred orientation	17,51	10,56	17,66	10,69	18,68
R_{wp}	Normal	23,28	14,29	17,66	14,49	25,76
	Anisotropic size	22,88	14,47	19,77	14,57	25,70
	Preferred orientation	22,37	13,65	17,07	13,97	24,01
χ^2	Normal	2,45	2,30	1,99	1,92	2,17
	Anisotropic size	2,36	2,36	2,50	1,94	2,16
	Preferred orientation	2,26	2,10	2,36	1,78	1,88

Definitions of R-factors from Rietveld refinement. R-pattern R_p defined as

$$R_p = \frac{\sum|y_{O,i} - y_{C,i}|}{\sum y_{O,i}}$$

with $y_{o,i}$ and $y_{c,i}$ is the observed and calculated data at data point i. The R-weighted expected pattern, R_{wp} is defined as

$$R_{wp} = \sqrt{\frac{\sum w_i(y_{O,i} - y_{C,i})^2}{\sum w_i {y_{O,i}}^2}} \qquad w_i = \frac{1}{\sigma(Y_{o,i})^2}$$

where w_i is the weighing given to data point *i*, and the $\sigma (Y_{o,i})^2$ is the error is the error in $Y_{o,m}$. The R-expected, R_{exp}, is defined as

$$R_{exp} = \sqrt{\frac{M - P}{\sum w_i {y_{O,i}}^2}}$$

where M is the number of data point and P is the number of parameters. From this, the χ^2 is defined as

$$\chi^2 = \left(\frac{R_{wp}}{R_{exp}}\right)^2$$

This is often redefined to goodness of fit, G, which is defined as $G^2 = \chi^2$.

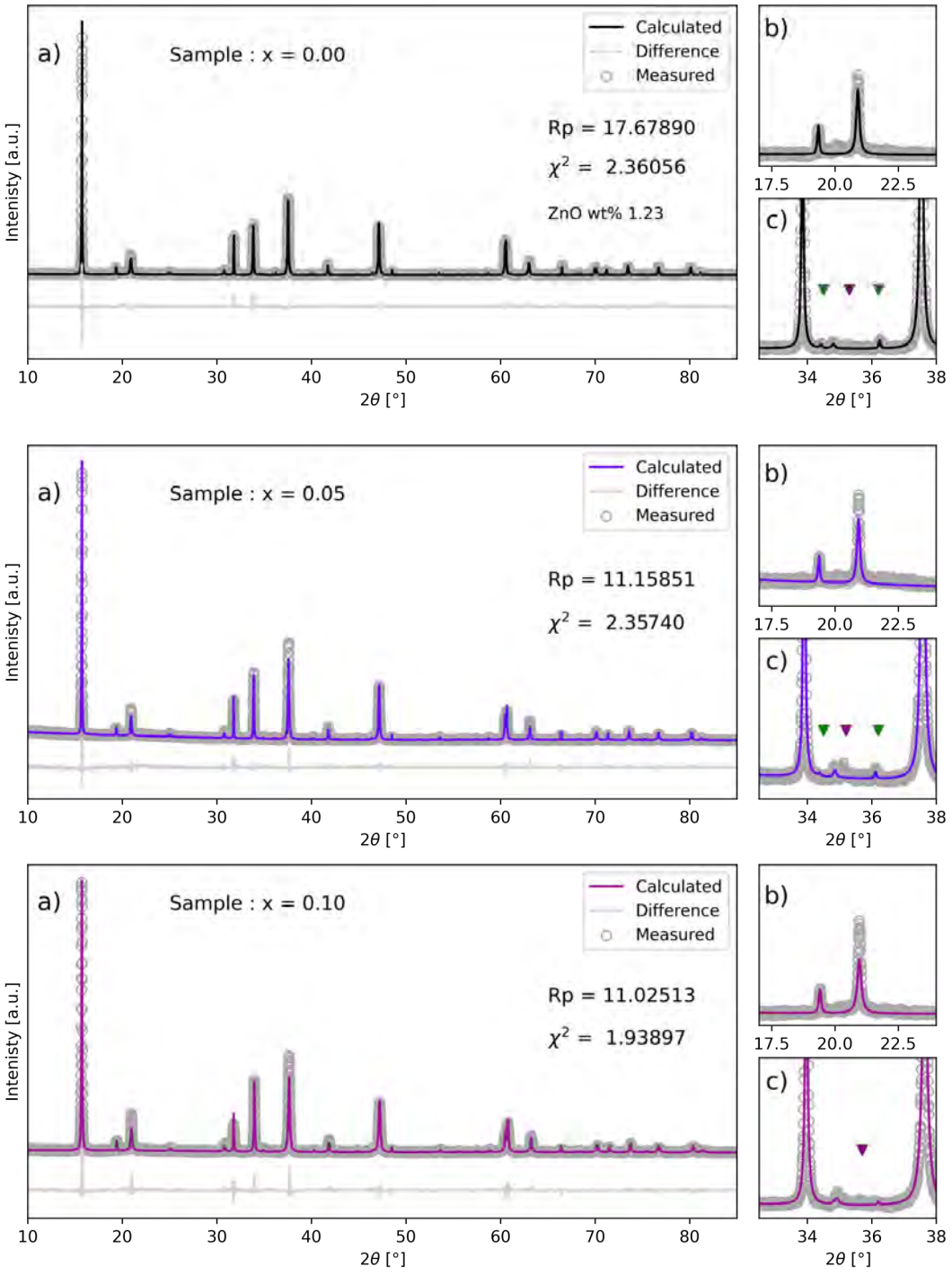
a)
Sample : x = 0.00
Calculated
Difference
Measured
Rp = 17.67890
χ^2 = 2.36056
ZnO wt% 1.23
b)
c)
Intenisty [a.u.]
2θ [°]
a)
Sample : x = 0.05
Calculated
Difference
Measured
Rp = 11.15851
χ^2 = 2.35740
b)
c)
Intenisty [a.u.]
2θ [°]
a)
Sample : x = 0.10
Calculated
Difference
Measured
Rp = 11.02513
χ^2 = 1.93897
b)
c)
Intenisty [a.u.]
2θ [°]

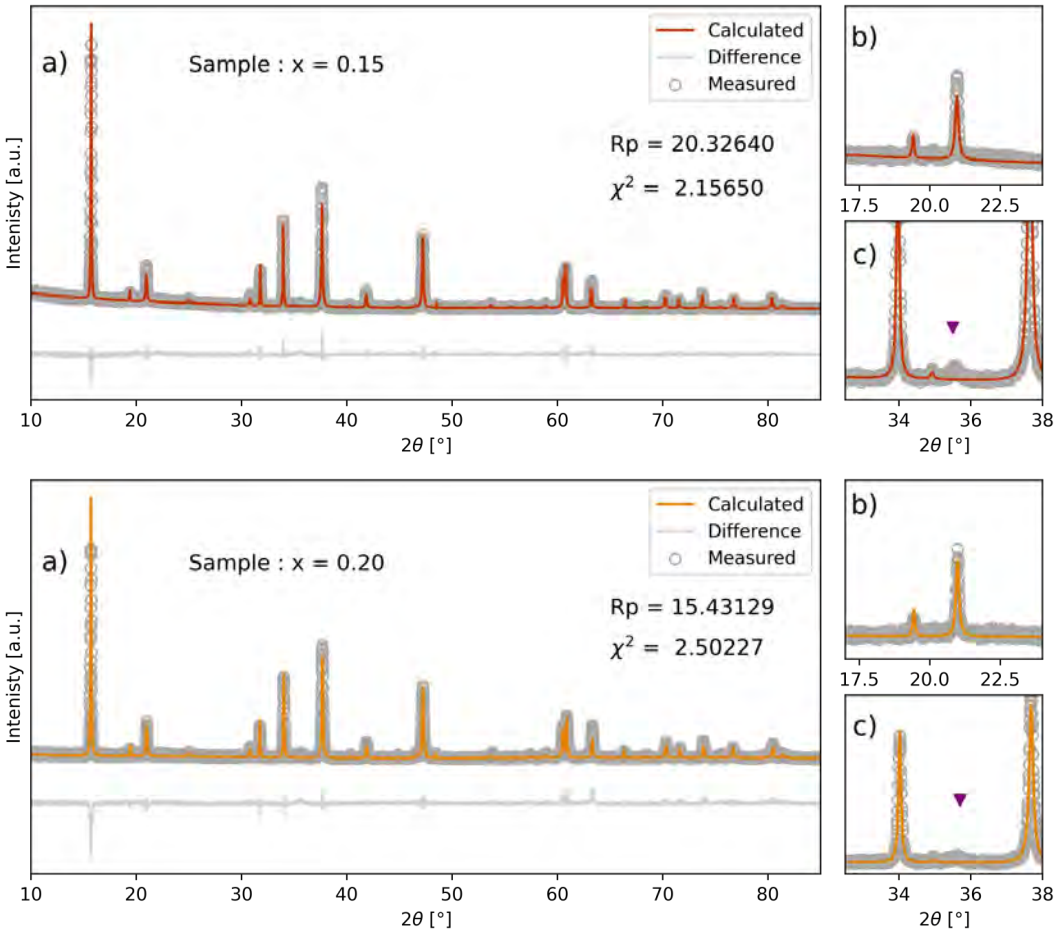

Figure S1: a) Conventional Rietveld refinement of all samples against XRD with the difference in grey. b) Inset of elevated background and extra reflections discussed in section 3.1., marked with blue arrows. c) Reflections from ZnO impurity, marked with green arrows, and unknown peak marked with purple arrow. Phase fractions are calculated by weight percentage, and calculation is not reliable below 3%. Only sample x = 0.00 has clear peaks related to ZnO. Sample x = 0.05 has indication of a peak, but the phase fraction is very low. The unknown peak marked with purple could be due to the Na-displacements previously reported

Table S3: Atomic coordinates and occupancies used in Rietveld refinement. Values adopted from Evstigneeva et al.[9] and not fitted, due to the low scattering power of Na.

Atom	Wyckoff symbol	Coordinates x	y	z	Occupancy	B_{iso}
Na1	6g	0.6615	0	0	0.28	1
Na2	2a	0	0	0	0.043	1
Na3	4f	1/3	2/3	0.5111	0.535	1
Te	2c	1/3	2/3	0.25	1	0.5
Zn1	2b	0	0	0.25	1	0.5
Zn2	2d	1/3	2/3	0.75	1	0.5
O	12i	0.3594	0.3312	0.6501	1	1

Table S4: Bond lengths calculated from DFT compared to experimental values from Rietveld refinement, for NZTO and 4Ga with x = 0.00 and x = 0.20 respectively. In both cases, Na-, Zn- and Te-O bonds decrease upon Ga-insertion, while the octahedral O-O around Zn. The DFT show that the prismatic O-O distance increase, which is the opposite of the decrease in the average structure.

	NZTO	4Ga	x = 0.00	x = 0.20
Na-O, g sites, layer 1	2.48 ± 0.11	2.48 ± 0.14	2.44	2.44
Na-O, f sites, layer 1	2.51 ± 0.18	2.49 ± 0.12	2.43	2.43
Na-O, a sites, layer 1	-	2.53 ± 0.11	2.49	2.49
Na-O, g sites, layer 2	2.48 ± 0.11	2.48 ± 0.18	-	-
Na-O, f sites, layer 2	2.51 ± 0.18	2.49 ± 0.13	-	-
Na-O, a sites, layer 2	-	2.61 ± 0.36	-	-
Zn-O distance	2.16 ± 0.04	2.17 ± 0.08	2.15	2.14
Te-O distance	1.97 ± 0.01	1.97 ± 0.02	1.97	1.97
Na-Zn, f sites, layer 1	2.88 ± 0.01	2.89 ± 0.02	2.69	2.69
Na-Te, f sites, layer 1	3.07 ± 0.01	3.06 ± 0.01	2.94	2.94
Na-Zn, a sites, layer 1	-	3.06 ± 0.09	2.81	2.81
Na-Zn, a sites, layer 2	-	3.1 ± 0.02		
O-O, prism, layer 1	3.47 ± 0.12	3.51 ± 0.08	3.38	3.28
O-O, prism, layer 2	3.48 ± 0.11	3.5 ± 0.08		
O-O, Zn octahedra	2.8 ± 0.11	2.88 ± 0.14	2.9	2.98
O-O, Te octahedra	2.74 ± 0.02	2.73 ± 0.04	2.77	2.86

S3 SEM

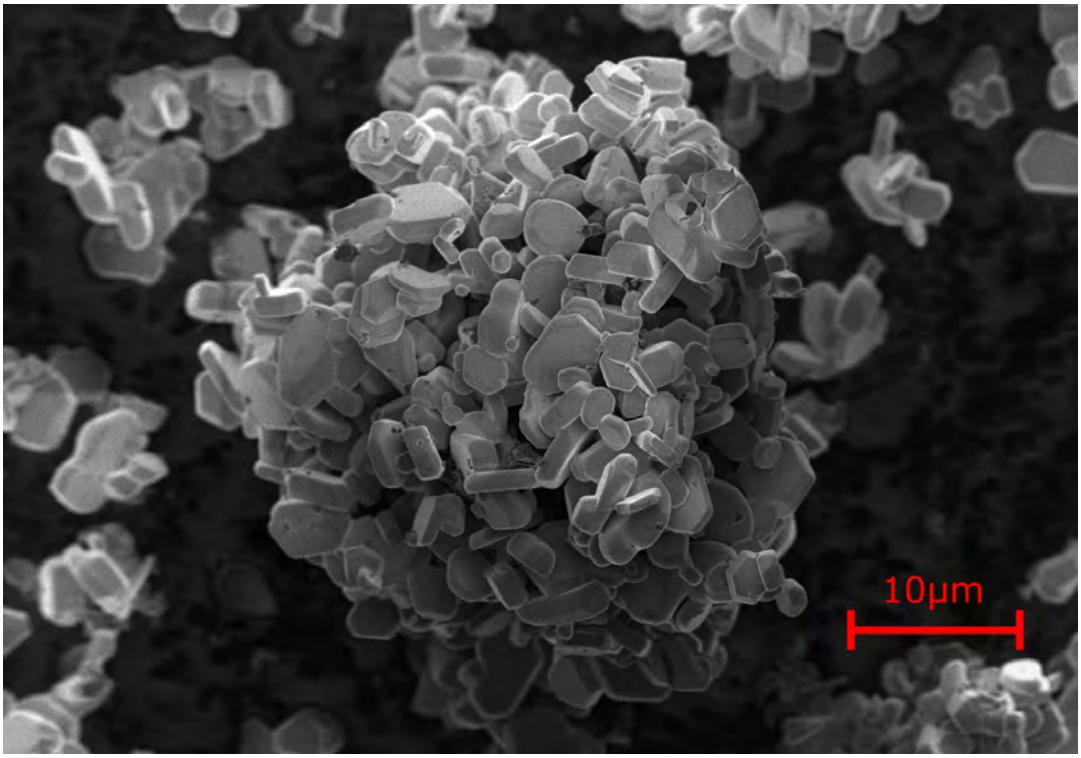

Figure S2: SEM image of NZTO.

S3 ^{23}Na NMR spectra breakdown from curvefitting

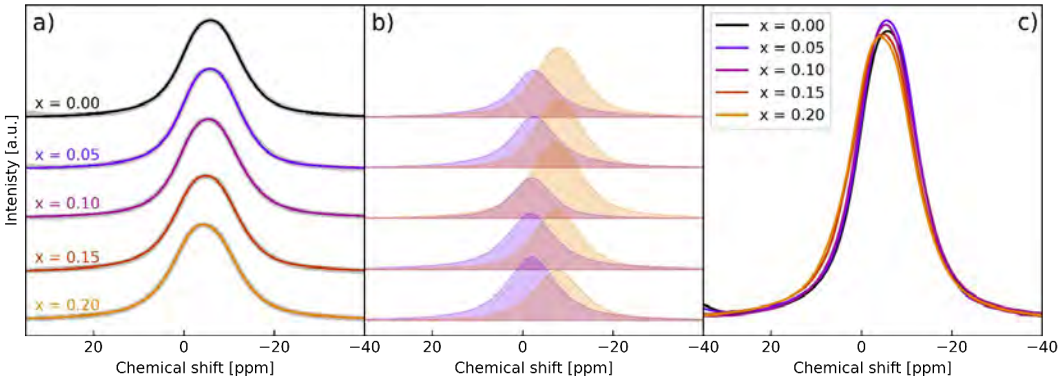

Figure S3: a) Fit of ^{23}Na NMR with grey points for spectrum and coloured line for fit. b) breakdown of ^{23}Na NMR spectra. The peak breakdown has multiple solutions which gives a similar quality fit. The observed peaks are not possible to fit with a single Gaussian peak, which means that if the lack of peak shape is due to a dynamic phenomenon, the peaks have not yet fully coalesced. c) Normalized ^{23}Na NMR spectra with no offset. The higher frequency side of the peaks shift to higher values with increasing substitution.

S4 ^{125}Te NMR spectra breakdown from curvefitting

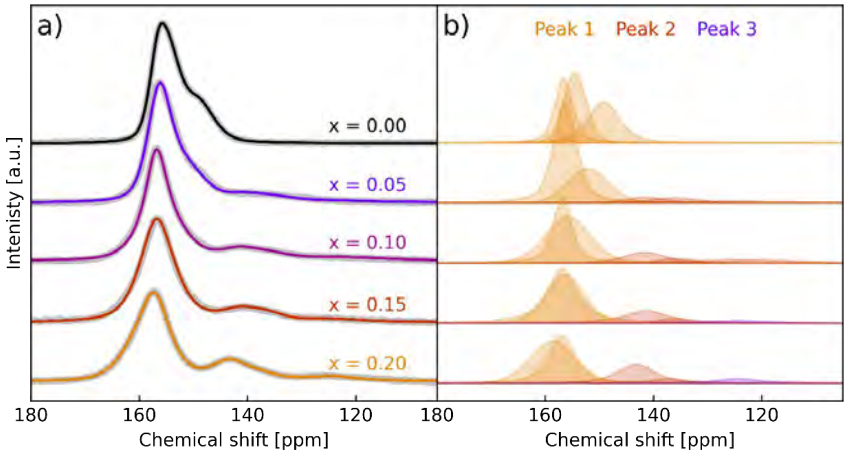

Figure S4: a) Fit and b) breakdown of ^{125}Te NMR. The breakdown is colour coded into the three groups, with the integrated relative frequency reported in Table 1. The peak breakdown has multiple solutions which gives a similar quality fit. The groups are, as explained in section 3.3, interpreted to be due to adjacent Ga-neighbours, but the peak breakdown does not have any physical interpretation and are only selected to fully describe peak shapes.

S5 Te configurations for chemical shift calculations

The first configuration is obtained by rearranging all the Na in one layer according to a honeycomb structure of *g*-sites, while the second layer maintains the non-hexagonal reconstruction. This configuration produces 2*g*2*g* Te coordination environments on top of the previously observed 2*g*1*f*. The second configuration is constructed by arranging the Na in one layer with a 3*g*1*a* pattern, where the three g sites are nearest neighbours and exhibit a triangular pattern. As in the previous case, the second layer maintains the original 2*g*2*f* pattern. This structure produces 4 distinct Te coordination environments: 1*g*1*f* , 2*g*1*g* , 2*g*2*g*, and 2*g*1*f*. In the last case, both Na layers have 3 *g*-sites occupied forming a triangular pattern. The remaining Na are placed in *a* and *f*, thus producing the following Te coordination environments: 1*g*1*f*, 2*g*1*g*, and 3*g*2*g*. After system relaxation, all these configurations have total energies that differ 24 meV or less with respect to the reference, meaning that they are meaningful local minima that can potentially be observed at room temperature. The last system included is the configuration used in the benchmarking.

S6 Comparison between GGA and SCAN results

Some properties of the NZTO systems are reported here to offer a comparison between the GGA and the SCAN functional. In table S3 the lattice parameters and the average Te-O bond length are reported. As expected, GGA overestimates the experimental values. SCAN, on the other hand, is shown to underestimate the values in this case, and it is not evident from these numbers which of the two is the best functional to describe the system. We further report in table S4 the charge population analysis as computed by the Bader method.[10] Also in this case, the results from SCAN and GGA are very similar and they are both very far from the ideal ionic picture. We conclude that GGA and SCAN are equally accurate in describing the basic properties of this system and the superior accuracy of SCAN is made evident only in the more demanding case of the linear response calculation for obtaining the chemical shift.

Table S5: Lattice parameters and interatomic distances as calculated by SCAN and GGA.

axis	SCAN	GGA	Experimental
a	5.25	5.33	5.29
b	9.07	9.21	9.16
c	11.14	11.34	11.24
Average Te-O bond length	1.939 pm 0.008	1.967 pm 0.008	1.971

Table S6: Bader charges computed using SCAN and GGA. The expected values from a purely ionic picture are reported for comparison

Ion	SCAN	GGA	Expected
Na	+0.9	+0.9	+1
Zn	+1.3	+1.4	+2
Te	+3.1	+3.3	+6
O	-1.2	-1.3	-2

S7 Starting points for configurations for Ga-doped NZTO systems

To create the starting point for the Ga-doped systems, each defect, impurity or vacancy, is introduced one after the other in the initial NZTO configuration: a 3x2x1 supercell system contains two Na- and two ZnTe layers. The Na is distributed according to the non-hexagonal pattern described in our previous work.[11] As a consequence of this, the Zn sites are not equivalent and more than one site needs to be considered for substitution with Ga. Two Zn sites are thus considered for the first Ga impurity: one between two unoccupied a sites and one between 2 f sites, one of which is occupied. Other configurations were not considered because (i) occupations for a sites is not so high in pristine NZTO, (ii) the occupation of both the f sites above and below never occurs (as demonstrated in section 3.5) and (iii) two unoccupied f sites sharing the same (x, y) coordinates are also rarely observed. The configuration with impurity between the two a sites is found to be more favourable by a small margin (10 meV). Both systems are thus considered further for generating the starting minima for AIMD calculations. The following step is the introduction of the first Na-vacancy. Since all the Na sites are in principle non-equivalent due to the presence of the impurity, all the possible sites in the structure have been considered and all the structures independently optimised. The optimisation procedure causes symmetry break in the Na sublattice not only in the layer containing the vacancy, but also in the other one. In both cases, the number of occupied g sites increases. This is a behaviour consistent with the g site being energetically more favourable [11] and with experimental evidence [12].

When the vacancy is introduced, the system with Ga over an *a*-site becomes more favourable by 50 meV, while maintaining a lower occupation of the *g*-site. The most favourable configuration is chosen in each case for further insertion of point defects.

The 2nd Ga-dopant is placed at all possible Zn-sites, as they are no longer inequivalent after introduction of the 1st. The system shows a clear preference for the systems with Ga in the previously undoped ZnTe layer, hinting that Ga is expected to be uniformly distributed in the structure. However, this is not conclusive, since our systems do not contain enough layers to further validate this point and, indeed, the integration of the peaks from ^{125}Te-NMR suggest inhomogeneous distribution for the x = 0.2. The most favourable configuration has both Ga impurities above *a*-site type, providing further evidence for the favourability of this site. Notably, also the system with impurity above the *f*-site has a second impurity above the *a*-site. While the two Ga-placements are comparable in energy, both systems show a preference for the placement of the next Na-vacancy in the same Na-layer as the 1st. However, the best 1:1 vacancy distribution is only a few meV above. For MD simulations, the Ga above *a*, 1:1 vacancy distribution will be used as it ensures better statistics (being the two layers equivalent) and is only

marginally less favourable. This is the system labelled 2Ga in the main text.

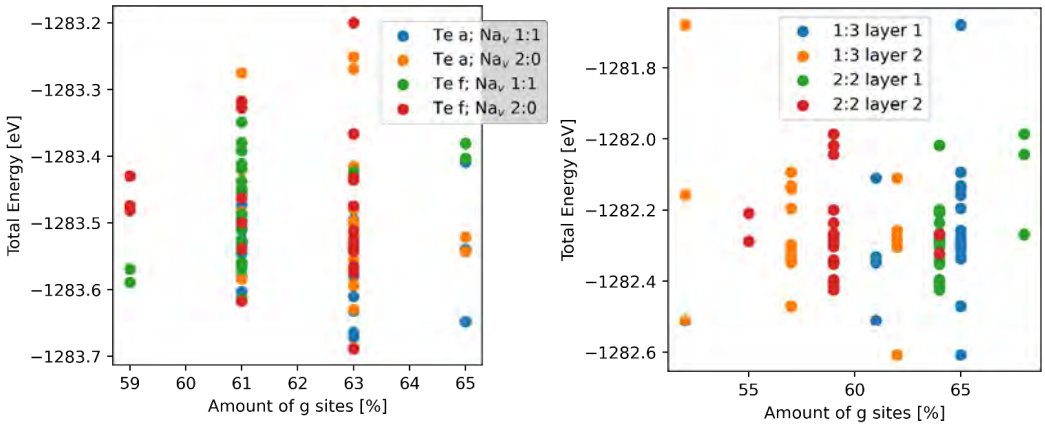

Figure S5: Na-distributions for the 2Ga systems (left) and the 4Ga system (right).

The 3rd most favourable Ga impurity is found to be placed between two *f*-sites where one is filled. The following Na vacancy is placed in the previously undoped layer, giving a 2:1 or 1:2 distribution. The last Ga-impurity exhibits the homogenous distribution, giving a 2:2 distribution between layers. The equilibrium in-layer Ga-distances are 8.16 and 5.3 Å, and there are no configurations with one NaO_6-prism sharing faces with two Ga-octahedra. The last Na vacancy shows a clear preference for unequal distribution, where the energy difference between the most stable 3:1 and 2:2 is quite large (0.2 eV). This 3:1 system, labelled 4Ga, is the one used as starting configuration AIMD simulations. Due to the unequal Na-distribution, the layers might behave differently. In order to obtain better statistics of the behavior of Na as a function of the Na density in the layer, we have decided to run 2 distinct AIMD simulations for this system and average over equivalent layers instead of considering system averages.

S8 Dynamical definition of Na sites and Te coordination environments

For each MD trajectory, we have considered a subset of 1000 configurations separated by 50 fs of dynamics. In each configuration, we define Na sites by averaging the (*x*, *y*) coordinates of atoms sharing the same *z*-coordinate, in particular (i) two Zn for the *a*-site, a Zn and a Te for the *f* site and two O for the *g* sites. This allows us to keep track of the ideal coordinate of the sites when the system is in temperature.

We then measure the distance between the actual positions of the Na during the dynamics and these ideal sites and project it in the (x, y) plane. The Na atoms are labelled *g*, *f* or *a* according to the shortest of these distances. This allows to compute dynamically the amount of Na at each site. The occupation of Na sites is averaged over the 1000 structures considered.

Having the Na atoms labelled by site in the AIMD trajectory, it is now possible to determine the coordination environment of Te and compute their abundance. As in the previous case, we use a subset of 1000 configurations to compute averages. For each Te atom, we have computed the modulus of the planar projection of the distance vector and selected the Na atoms within a 2.3 Å cut-off length. This is in line with the explanation of Te-environments explained in the introduction, where the *a*-sites do not contribute as they are not close enough to the Te atom. The same applies to the second shell of *f*-sites, which are as distant from Te as the *a*-site. The environments are then defined only by the amount of *g*- and *f*-sites, which cannot be simultaneously occupied in the same layer due to the proximity of these sites (≈ 1.7 Å).

Table S7: Na population computed from AIMD trajectories in the considered systems at selected temperatures. The multiplicity of each site is given, as the population will scaled both by the fractional occupancy of each site, as shown in figure 6, and the multiplicity of each site.

	Population [%] T = 750			Population [%] T = 1000		
System	3*g*	2*f*	1*a*	3*g*	2*f*	1*a*
NZTO	62	28	9	58	28	14
2GA (1vNa)	65	22	13	56	28	16
4GA (1vNa)	57	29	14	59	25	16
4GA (3vNa)	48	34	18	58	27	14

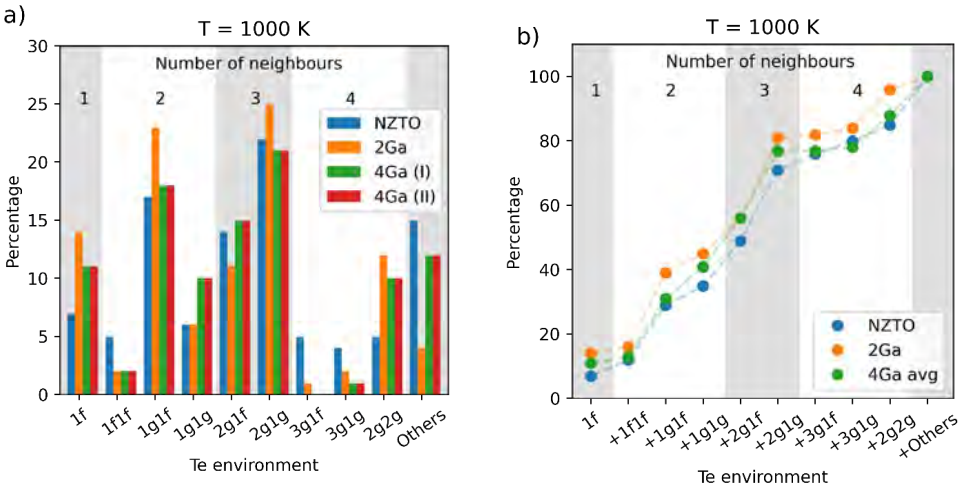

Figure S6: Te-environments from 50ps MD at 1000K. The number of neighbours is marked by grey and white area as a guide to the eye. (a) Relative percentages of each Te-environments, (b) The cumulative distribution, where the amounts of each environments is added together in the order of calculated shielding from section 3.4, which is done to highlight the changes between environments across samples, and how it relates to the Na-content. The two 4Ga runs is the same at 1000K as seen in a), and is therefore plotted as one in b).

S9 Dipolar coupling calculations

Below are average estimated bond lengths in Å extracted from average structures from Rietveld refinement of XRD:

Zn(Ga)-Zn(Ga)	Zn(Ga)-Te	Zn(Ga)-O	Zn(Ga)-Na	Te-Te	Te-O	Te-Na	O-O	O-Na	Na-Na
3.05	**3.05**	2.14	2.60	5.29	1.97	**2.81**	2.76	2.38	3.05

Out of these only those marked in bold should contribute most to interactions between magnetic dipoles of Te and neighbors, in this case Na and Zn/Ga. Both Zn and O are of low natural abundance regarding nuclei with magnetic moments, so we disregard these in this estimate.

From Bruker Table of Isotopes the gyromagnetic ratio, *γ*, for the most relevant nuclei are:

Isotope	Gyromagnetic ratio, γ [10^7 rad s^{-1} T^{-1}]	Natural abundance [%]
^{125}Te	-8.51	7.07
^{69}Ga	6.43	60.11
^{71}Ga	8.18	39.89
^{23}Na	7.08	100

The through space dipolar coupling constant is in angular frequency units:

$$D = \frac{\mu_0}{4\pi}\frac{h}{2\pi}\frac{\gamma_1\gamma_2}{r^3}$$

h is Planck's constant and μ_0 is the vacuum permeability. The interaction is proportional to the product of the magnetogyro ratios of the interacting nuclei and the cube of the inverse of distance.

$\gamma_1\gamma_2$ for Te*Ga or Te*Na are approximate ~ -55 (Te*^{69}Ga), ~ -70 (Te*^{71}Ga), ~-60 for Te*Na. The third power of the distances are respectively 3.08^3= 28, and $2,81^3$ = 22. As can be seen coupling-values are quite similar hence the average distance will be the major controlling factors. The Te-Te interaction has a denominator of about 5.29^3 = 148 and is therefore of significant lower strength.

From these estimates, for otherwise static atoms, the strongest single contribution for dipole-dipole through space interactions of the Te nucleus are with the Na and the Ga nucleus. These interactions are about 4-5 times stronger than a Te-

Te interaction of the same type. However, if Na is dynamic and the stochastic processes have a high rate the through space diploe-dipole couplings of Na and Te will weaken and eventually become sizable with the Te-Te interactions and at a very high dynamic rate of Na only the Te-Te/Ga dipole interaction remains for linebroadening. The Te-Ga interaction may also be influenced by the probable fast relaxation of Ga as the nucleus has a quadrupolar moment that may lead to fast spin-lattice (T1) relaxation.

S10 Comparison of ^{23}Na NMR of solid-state and sol-gel synthesis of NZTO

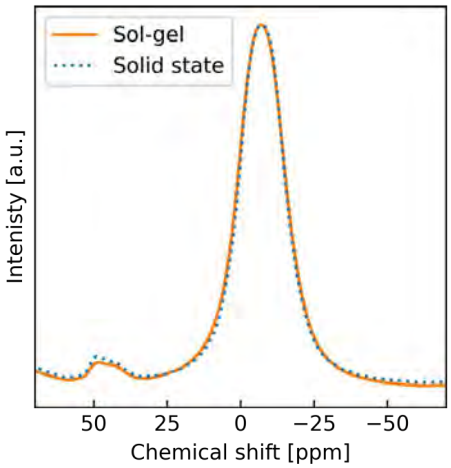

Figure S7: ^{23}Na NMR comparison between NZTO synthesized using sol-gel and solid state synthesis. The similarity of the two spectra demonstrate that while particle morphology and size might be changed by synthesis method, the local structure is clearly similar. There are minor deviations between the spectra, which can either point to very small physical differences from e.g. surfaces or interphases, or be from different phasing of the spectra. The solid-state synthesis was synthesized as reported by Li et al.[12]

References

1 G. Kresse and J. Hafner, Ab initio molecular dynamics for liquid metals, *Phys. Rev. B*, 1993, **47**, 558–561.

2 G. Kresse and J. Furthmüller, Efficiency of ab-initio total energy calculations for metals and semiconductors using a plane-wave basis set, *Comput. Mater. Sci.*, 1996, **6**, 15–50.

3 G. Kresse and J. Furthmüller, Efficient iterative schemes for ab initio total-energy calculations using a plane-wave basis set, *Phys. Rev. B*, 1996, **54**, 11169–11186.

4 G. Kresse and D. Joubert, From ultrasoft pseudopotentials to the projector augmented-wave method, *Phys. Rev. B*, 1999, **59**, 1758–1775.

5 H. J. Monkhorst and J. D. Pack, Special points for Brillouin-zone integrations, *Phys. Rev. B*, 1976, **13**, 5188–5192.

6 C. L. Fu and K. M. Ho, First-principles calculation of the equilibrium ground-state properties of transition metals: Applications to Nb and Mo, *Phys. Rev. B*, 1983, **28**, 5480–5486.

7 P. Pulay, Convergence acceleration of iterative sequences. the case of scf iteration, *Chem. Phys. Lett.*, 1980, **73**, 393–398.

8 A. Katerinopoulou, T. Balic-Zunic and L. F. Lundegaard, Application of the ellipsoid modeling of the average shape of nanosized crystallites in powder diffraction, *J. Appl. Crystallogr.*, 2012, **45**, 22–27.

9 M. A. Evstigneeva, V. B. Nalbandyan, A. A. Petrenko, B. S. Medvedev and A. A. Kataev, A new family of fast sodium ion conductors: Na2M 2TeO6 (M = Ni, Co, Zn, Mg), *Chem. Mater.*, 2011, **23**, 1174–1181.

10 M. Yu and D. R. Trinkle, Accurate and efficient algorithm for Bader charge integration, *J. Chem. Phys.*, 2011, **134**, 064111.

11 F. Bianchini, H. Fjellvåg and P. Vajeeston, Nonhexagonal Na Sublattice Reconstruction in the Super-Ionic Conductor Na 2 Zn 2 TeO 6 : Insights from Ab Initio Molecular Dynamics, *J. Phys. Chem. C*, 2019, **123**, 4654–4663.

12 X. Li, F. Bianchini, J. Wind, P. Vajeeston, D. Wragg and H. Fjellvåg, P2 Type Layered Solid-State Electrolyte Na 2 Zn 2 TeO 6 : Crystal Structure and Stacking Faults , *J. Electrochem. Soc.*, 2019, **166**, A3830–A3837.

II

ACS PHYSICAL CHEMISTRY Au
AN OPEN ACCESS JOURNAL OF THE AMERICAN CHEMICAL SOCIETY

pubs.acs.org/physchemau

Article

Dynamics of Interlayer Na-Ions in Ga-Substituted $Na_2Zn_2TeO_6$ (NZTO) Studied by Variable-Temperature Solid-State ^{23}Na NMR Spectroscopy and DFT Modeling

Frida Sveen Hempel, Charlotte Martineau-Corcos, Federico Bianchini, Helmer Fjellvåg, and Bjørnar Arstad*

Cite This: https://doi.org/10.1021/acsphyschemau.3c00012

Read Online

ACCESS | Metrics & More | Article Recommendations | Supporting Information

ABSTRACT: Local Na-coordination and dynamics of $Na_{2-x}Zn_{2-x}Ga_xTeO_6$; x = 0.00 (NZTO), 0.05, 0.10, 0.15, 0.20, were studied by variable-temperature, ^{23}Na NMR methods and DFT AIMD simulations. Structure and dynamics were probed by NMR in the temperature ranges of 100−293 K in a magnetic field of 18.8 T and from 293 up to 500 K in a magnetic field of 11.7 T. Line shapes and T_1 relaxation constants were analyzed. At 100 K, the otherwise dynamic Na-ions are frozen out on the NMR time scale, and a local structure characterization was performed for Na-ions at three interlayer sites. On increasing the temperature, complex peak shape coalescences occurred, and at 293 K, the Na NMR spectra showed some averaging due to Na-ion dynamics. A further increase to 500 K did not reveal any new peak shape variations until the highest temperatures, where an apparent peak splitting was observed, similar to what was observed in the 18.8 T experiments at lower temperatures. A three-site exchange model coupled with reduced quadrupolar couplings due to dynamics appear to explain these peak shape observations. The Ga substitution increases the Na-jumping rate, as proved by relaxation measurements and by a decrease in temperature for peak coalescence. The estimated activation energy for Na dynamics in the NZTO sample, from relaxation measurements, corresponds well to results from DFT AIMD simulations. Upon Ga substitution, measured activation energies are reduced, which is supported, in part, by DFT calculations. Addressing the correlated motion of Na-ions appears important for solid-state ion conductors since benefits can be gained from the decrease in activation energy upon Ga substitution, for example.

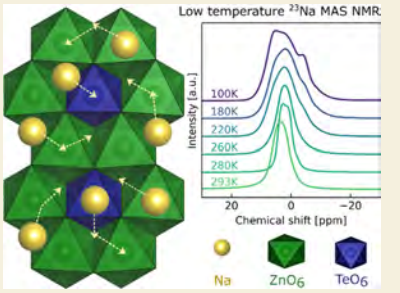

KEYWORDS: *solid-state NMR, ^{23}Na relaxation rates, Na dynamics, NZTO, layered materials, DFT AIMD*

1. INTRODUCTION

Dynamics of ions in solids is essential for many material applications, e.g., ion batteries, membranes, and sensors. In this context, layered oxide (2D) materials are of high interest as they may intercalate ions with mobility within layers in contrast to other materials where mobility takes place between defects, often in three dimensions (3D). Modern Li-ion batteries are examples where layered oxides are used as cathode materials.[1] Furthermore, layered oxides have also come into focus as solid-state electrolytes (SSEs). Compared to liquid electrolytes, SSEs may withstand higher potentials and improve battery properties; they may be less toxic, are more fire-resistant, and allow denser packing of battery cells, as well as making the separator redundant.[2,3] More recently, scientific and technological development of Na-based batteries has been rapid, with certain application areas clearly evident, and the general availability of sodium implies no concern on raw material limitations.[4] Due to the complex situation of ion dynamics in such material classes, a fundamental understanding of controlling factors and structure−dynamic relationships are important for designing improved materials with high performance.

For this purpose, nuclear magnetic resonance (NMR) spectroscopy is one of a few powerful experimental methods that may give both local structural and dynamic information. Depending on the available magnetic field, the isotope, the temperature, and type of experiment, NMR methods can probe a wide range of dynamic rates, reveal atomic and molecular details, as well as provide activation energies of the processes. While slower dynamics is visible through line shape perturbations, dynamic rates at the order of the Larmor frequency for the given nuclei at the applied field, ω_0 ($\approx 10^{-9}$ s^{-1}), are best probed by spin−lattice relaxometry (SLR).[5] The

Received: March 15, 2023
Revised: April 24, 2023
Accepted: April 24, 2023

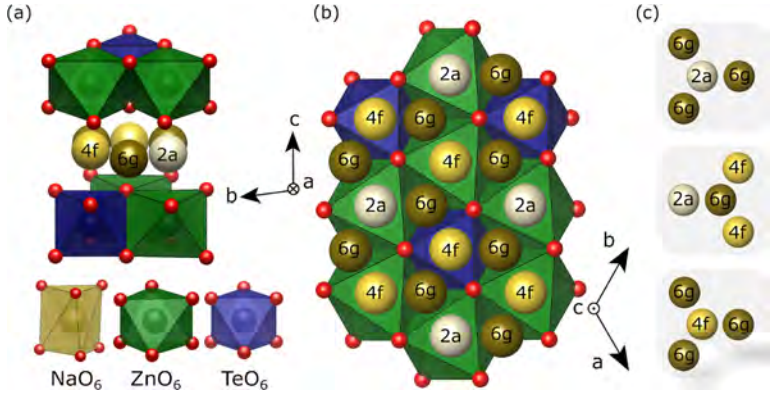

Figure 1. (a) Side view of the $Na_2Zn_2TeO_6$ (NZTO) structure (P2 type; space group $P6_322$). (b) Coordination polyhedra of Na, Zn, and Te. The different sites in the Na layer are highlighted in color. Note that two out of six Na positions per unit cells are filled. (c) The three different Na-sites with closest neighbors. Note that the 2a and 4f positions have only 6g as the closest neighbor.

relaxation time in the laboratory frame, characterized by the time constant T_1, measures the fastest dynamic processes, but slower processes can be measured by SLR in the rotating frame (T_{1_ρ})[6] and by spin−spin relaxation (T_2).[7] The slowest dynamic rates are studied with 2D chemical exchange experiments or other methods like, e.g., spin alignment echo NMR.[8] By measuring relaxation rates over a wide temperature range, the activation energy E_a and jump rates, τ^{-1}, of the underlying dynamic process can be extracted.

The jump rate is assumed following an Arrhenius relationship like

$$\tau_c^{-1} = \tau_0^{-1} \exp\left(\frac{-E_a}{k_B T}\right) \tag{1}$$

with a pre-exponential factor in the order of phonon frequencies[9] or the minimum correlation time at infinite temperature.[10] The relaxation rate T_1^{-1} is related to the correlation time, τ_c, as in the following equation

$$T_1^{-1} \propto \frac{\tau_c}{1 + (\omega_0 \tau_c)^2} \tag{2}$$

ω_0 is the Larmor frequency of the nuclei in question and τ_c is from eq 1. Depending on the actual relaxation mechanism, there will be numerical constants multiplied with one or more expressions as in eq 2. The constants and numeric values will depend on the actual relaxation mechanisms and their contribution. A plot of $\log(1/T_1)$ vs T(K) will, for uncorrelated 3D dynamics, with the so-called BPP behavior,[11] be symmetrical, with the activation energy E_a for the dynamic process determined directly from the slopes. This is, however, rarely true for a real solid material, especially in the low-temperature region ($\omega_0\, \tau_c \gg 1$), where dynamics is hindered, and a smaller slope is typically observed. Such correlated motion can be caused by vacancy diffusion mechanisms, structural disorder, and Coulombic interactions.[5] The high-temperature region ($\omega_0\, \tau_c \gg 1$) is frequency-independent for a 3D conductor, but systems with a reduced dimensionality for the conduction will show a reduced slope.[12,13] Provided that the dimensionality is known, E_a can still be determined on the high-temperature slope. In order to describe in more detail ion diffusion in two-dimensional conductors, the following empirical equation has been put forward[14,15]

$$T_1^{-1} \propto \tau_c \ln\left(1 + \frac{1}{(\omega_0 \tau_c)^\beta}\right) \tag{3}$$

β expresses the frequency dependencies of the relaxation rates and is expected to be 2 for a random noncorrelated diffusion process. A lower value of β indicates correlated diffusion processes. A fit of this equation, coupled with eq 1, yields activation energies and information on ion correlations.

Before we briefly describe some relevant NMR relaxation studies for Li/Na layered materials, some word on notation is in place. Layered oxides with Na as the mobile cation can be denoted as Na_xMO_2 with $0 < x \leq 1$, with either one or more metal or metalloid elements M. These are classified using an *AX*-notation created by Delmas et al. based on the stacking of layers of edge-sharing MO_6 octahedra.[16] *X* denotes the number of distinct MO_x-blocks, while *A* denotes the coordination type for the Na^+ cations, prismatic (P) or octahedral (O). The most common types are P2 and O3. Previous studies of Na dynamics in layered materials are mainly focused on cathode materials, as this has widespread use for these layered oxides. The layered $Na_{0.8}CoO_2$ (cathode) material undergoes an abrupt phase transition between 292 and 291 K, as seen by ^{23}Na NMR relaxometry.[17] There is no change in the narrow central transition peak but a reappearance of satellite peaks. The observation indicates a "melting" of the Na layer into a 2D-liquid state, similar to that for Na^+-dynamics in β-alumina.[18] The strength of the methodology is evident from studies of peak coalescence in P2- and P3-type phases of Na_xCoO_2.[19] At high temperatures, the P2-phase peak coalesces into a single second-order quadrupolar line shape due to ion exchange. For the P3 phase, changes occur toward a Gaussian shape, as the exchange is between sites symmetric in the *ab*-plane but antisymmetric in the *c*-direction, which leads to a cancellation of the V_{zz} contribution and suppresses the quadrupolar line shape. ^{23}Na NMR of $Na_{2/3}Ni_{1/3}Ti_{2/3}O_2$ shows a relatively symmetrical peak shape at room temperature, suggesting fast Na^+ dynamics.[20] There is no quadrupolar line shape at lower temperature, which is suggested to be due to a dominance of magnetic anisotropy and paramagnetism

https://doi.org/10.1021/acsphyschemau.3c00012
ACS Phys. Chem Au XXXX, XXX, XXX−XXX

over the quadrupolar interaction. In the O3-type $Na_{0.8}Ni_{0.6}Sb_{1.2}O_2$, ^{23}Na NMR demonstrates off-centering of the Na-site as a response to the surrounding Na-vacancies.[21]

The currently investigated layered tellurates have been explored as battery materials,[22,23] with $Na_2Zn_2TeO_6$ (NZTO) being a candidate as an SSE.[24] NZTO takes a P2-type structure (Figure 1; space group $P6_322$), with six face-sharing prisms allocating two Na-ions per formula unit. There are three nonequivalent Na-sites (2a, 4f, 6g), differentiated by the surrounding cations in the dense layers above and below. The 6g-based prisms share edges with six-framework octahedra, whereas the 2a- and 4f-based prisms are sharing faces with the octahedra. The 4f-sites are located between Te and Zn-octahedra, whereas the 2a-sites are between Zn-octahedra. Experiments show that the latter site is least favorable for Na.[22,25] Note that we below distinguish between the ideal crystallographic sites (i.e., the 2a, 4f, or 6g-*site*) and the three different types of prismatic coordination polyhedra that are connected with these sites (2a-, 4f-, or 6g-prisms). The latter ones are typically being accompanied by a distribution of deformations. "Site" will therefore be used for crystallographic symmetry, while "prism" will be used when the chemical environment is the important aspect.

For NZTO, the Na ionic conductivity increases on substitution of Zn^{2+} with Ga^{3+}, as the concomitant reduction in the Na^+ content decreases the Na^+−Na^+ repulsion and increases the vacancy concentration.[26] Introduction of Ga is suggested to decrease grain boundary resistance.[27] Enhanced conductivity is also further reported for Ca-substitutions in the Na layer.[28] Ca insertion increases the layer distance, which tentatively makes all Na-sites equally favorable. *Ab initio* molecular dynamics (MD) simulations of NZTO suggest a disordered Na-distribution, revealing that the honeycomb arrangement of the Zn/Te layer does not translate into Na ordering.[25] The very similar cathode material $Na_2Ni_2TeO_6$ (NNTO) has been investigated in a series of MD simulations, showing that disorder and ion−ion correlations influence ionic conductivity.[29] From MD data, Sau and Kumar found that a 20% reduction of Na^+ concentration in the interlayers significantly changed the energy landscape and Na-conductivity,[30] mainly due to a decreased ion−ion repulsion.[31]

In this article, we present variable-temperature (100−500 K) ^{23}Na solid-state (static and MAS) NMR spectroscopy data, supported by DFT modeling, to reveal the Na dynamics in NZTO and Ga-substituted derivatives. NMR experiments (at a magnetic field of 18.8 T) from 100 to 293 K were used for line shape analyses, while NMR experiments (at a field of 11.7 T) were carried out to study line shape variations and to measure T_1 relaxation time constants up to about 500 K. The line shape analyses were used to reveal the onset of Na dynamics at very low temperatures (close to 100 K), and our simulations suggest a complex situation of a three-site exchange system and averaging of interactions. Simulation of the T_1 measurements provided activation energies for the dynamic Na processes and revealed trends in stochastic processes influenced by Ga doping. Substitution of Ga resulted in a lower activation energy and correlated Na dynamics. The DFT modeling gave results consistent with experimental activation energies.

2. EXPERIMENTAL SECTION

2.1. Materials

Samples of $Na_{2-x}Zn_{2-x}Ga_xTeO_6$ with x = 0.00, 0.05, 0.10, 0.15, and 0.20 were synthesized using a conventional sol−gel synthesis, as described earlier.[32] The procedure is reported in S1 for completeness of this work.

2.2. Powder X-ray diffraction (XRD)

Powder X-ray diffraction (XRD) data were measured on a Bruker D8-A25 diffractometer, using $CuK_{\alpha 1}$ radiation, a Ge (111) Johansson monochromator, and a Lynxeye detector, for the 2θ range of 10−128°, with a step size of 0.005°. Rietveld refinements against the collected data were performed using Topas v6.[33]

2.3. Nuclear Magnetic Resonance (NMR)

^{23}Na (I = 3/2) magic angle spinning (MAS) NMR single transient spectra were acquired at 11.7 T using a Bruker Avance AV III WB spectrometer equipped with a 4 mm double channel probe head at a MAS frequency of 10 kHz. The applied ^{23}Na resonance frequency was 132.29 MHz, and 400 free induction decays (FIDs) were accumulated for each spectrum. Each pulse was 1.5 μs long, and we applied a recycle delay of 0.5 s. The magnetic field was adjusted by setting the high-frequency peak of adamantane to 38.48 ppm. For referencing the ^{23}Na spectra, we used 1 M NaCl(aq). The chemical shift of ^{23}Na(aq) was set to 0 ppm. T_1 rates of ^{23}Na were recorded using a saturation recovery sequence at a MAS rate of 10 kHz.

The samples are stored in Ar or in a desiccator, however, being exposed to air during handling and rotor packing. The number of adsorbed water molecules per Na atom was therefore estimated by a method described in S2. The x = 0.20 showed the largest water content, with one water molecule per 119 Na-ions. For x = 0.15, 0.10, 0.05, and 0.00, the ratios are 197, 214, 249, and 315, respectively. The estimated level of hydroxyl groups is similar to the water levels. Based on this, we assume that the ^{23}Na NMR results should not be significantly influenced by the presence of water/OH-groups. Even with significant uncertainties, it is clear that the number of water molecules increases with the Ga content.

^{23}Na low-temperature (LT) MAS and static NMR spectra were recorded on an 18.8 T Avance III WB using an LT-MAS 3.2 mm probe in the temperature range of RT to 100 K. The temperature was calibrated using KBr.[34] ^{23}Na NMR spectra are referenced to 1 M $NaNO_3$(aq) at room temperature. In static conditions, a single-pulse ^{23}Na spectrum was recorded. Under MAS conditions (12.5 kHz), single-pulse spectra were recorded. The pulse duration was 2.25 μs, with a recycle delay of 0.5 s and 256 FIDs accumulated per spectrum. T_1 rates were recorded using a saturation recovery sequence at a MAS of 12.5 kHz. All our relaxation measurements appeared to be described very well with one exponential function. We could not distinguish any multicomponent relaxation in the spectra; hence, all data are based on the total areas of the whole multicomponent peak.

Before Fourier transform of the averaged FIDs, zero filling and apodization were applied to improve line shape definitions and signal to noise. The apodization was done by multiplying the FIDs with a decaying exponential window function with a processing line broadening (LB) factor of 250 Hz (^{23}Na) and 50 Hz (^{125}Te). All NMR spectra were adjusted by signal phasing and baseline corrections. Curve fitting was performed using DMfit.[35]

2.4. DFT Calculations

DFT simulations were performed using the Vienna Ab initio Simulation package (VASP, version 5.4.4)[36−39] and expands our previous works,[32,40] where configurations were used for *ab initio* molecular dynamics simulations (AIMD) to compute ionic mobility in Ga-doped NZTO. Structural optimization calculations were conducted to obtain reliable starting configurations. All computations make use of the conjugate gradient algorithm.

The Ga-doped NZTO is modeled using a 3 × 2 × 1 supercell (24 formula units, 264 atoms; 16.03 × 18.48 × 11.37 Å^3) of the optimized configuration from our previous work,[32] large enough to make

https://doi.org/10.1021/acsphyschemau.3c00012
ACS Phys. Chem Au XXXX, XXX, XXX−XXX

interactions between point defects and their periodic images negligible and to perform molecular dynamics simulation.

AIMD calculations were performed for the supercell model of NZTO and for the two most stable Ga-doped configurations. Their stoichiometries are $Na_{48}Zn_{48}Te_{24}O_{144}$, $Na_{46}Zn_{46}Ga_2Te_{24}O_{144}$, and $Na_{44}Zn_{44}Ga_4Te_{24}O_{144}$. For brevity, the Ga-doped systems are labeled as 2Ga and 4Ga. The simulations were performed within both the canonical (NVT) and the microcanonical (NVE) ensembles: the former for thermalization of the system and the latter for production. In both cases, we use the same parameters as described in the Supporting Information (SI). Calculations within the canonical ensemble are modeled using the Nosé thermostat for controlling temperature oscillations.[41−43] The Nosé mass parameter is set so that the period associated with these fluctuations is 40 fs. A time step of 1 fs was found to be sufficiently small to avoid sudden jumps in the total energy of the system during the simulation.

Production calculations, performed in the microcanonical ensemble, compute 50 ps of dynamics at four distinct temperatures: 750, 1000, 1250, and 1500 K. Diffusion was not observed in the trajectory at 500 K, and these data were therefore not relevant. The analysis of the trajectories relies on three packages: MDANSE,[44] the atomic simulation environment (ASE),[45,46] and QUIPPY, the python interface of QUIP.[47] Vesta is used for rendering ball-and-stick and coordination polyhedra.[48]

3. RESULTS AND DISCUSSION

3.1. Structure

The materials were synthesized and characterized in detail in our previous work, but the main features will be presented here for completeness.[32] Additional information is described in the S1. All materials crystallized in the P2-type phase with the space group $P6_322$, in accordance with previous reports, with the x = 0.00 and 0.05 with a minor ZnO impurity. With increasing substitution of Ga, the c-axis expands and the ab-plane contracts. The exception here is x = 0.15, which was thought to be connected to Na ordering or inhomogeneous filling of the layers, which was indicated in DFT simulations. The inserted Ga-atoms were shown to be placed next to Te-atoms in stoichiometric amounts as shown by ^{125}Te NMR, confirming that the materials have fully substituted Zn with Ga without secondary Ga-containing phases. We also show that the Na content surrounding Te was reduced. This confirms the Ga substitution mechanism.

3.2. Low-Temperature ^{23}Na NMR

Line shape analyses of NZTO and its derived Ga variants were carried out from 100 K up to about 500 K to investigate Na dynamics. First, the NZTO material will be described in detail and later the Ga-doped materials will be described. T_1 relaxation measurements were carried out between 293 and 500 K and will be described and analyzed after all line shape analyses. NMR spectroscopy of nonrotating samples (termed static NMR) shows all line broadening effects in a sample such as dipole−dipole interactions, quadrupole interactions, chemical shift anisotropies, and susceptibility broadenings. However, even with these seemingly complicating interactions, static NMR spectra may provide valuable information of possible dynamic processes with rates comparable to the spectrum widths as temperature is varied. At a low enough temperature, ion dynamics driven by heat will be drastically reduced and the movement of Na will "freeze out" and ^{23}Na NMR spectra without time-averaged peaks can be obtained. The "freeze-out" temperature is difficult to predict; therefore, we carried out our series of ^{23}Na MAS and static NMR experiments down to the lowest possible temperature that could be reached with our apparatus (100 K at 18.8 T). In Figure 2, we show a sequence of static ^{23}Na spectra ranging from 100 K up to 293 K for our NZTO material.

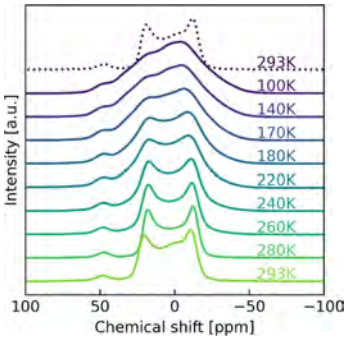

Figure 2. Static NMR (18.8 T) from 100 K up to 293 K. The dotted line is the 293 K peak after cooling and heating, showing the reversible change and facilitating comparison of the sample at the two end point temperatures. The feature around 50 ppm will be discussed in Section 3.4.

The overall observed trend is a gradual narrowing of the spectra going from 100 K up to 293 K. Note that the peak at about 50 ppm is not changing significantly. Initially, at 100 K, the spectrum is almost a featureless shape, but with increasing temperature, a more and more distinct shape emerges. However, only a minor change between 100 and 140 K was observed; hence, it appears that for our NZTO sample, and measurement conditions (field strength, NMR method), Na dynamics is not observed. We therefore take the 100 K spectrum as our nondynamic reference state. We also note the absence of a typical quadrupolar peak shape(s) at these low temperatures. As the temperature is increased, the line shape narrows as expected if Na dynamic is present. The point of coalescence is hard to estimate but could be somewhere between 200 and 240 K. This gives a lower limit of the frequency for the dynamic process. The peak is approximately 25,000 Hz wide at 100 K, and therefore the frequency of the dynamic process at the temperature of coalescence must be at least half of this, which is 12,500 Hz. The static spectra also change between 280 and 293 K, with a shift to the left and the appearance of a central peak. At 280 K, the shape is best described as two maxima with a small component at 45 ppm. At 293 K, an extra component is visible at approximately 0 ppm. This peak is not distinguishable at lower temperatures but is visible both before and after cooling. This could suggest that the peak is a result of a dynamic process. It is safe to assume some additional broadening due to magnetic susceptibility, so the extracted values for dynamic processes from the spectra are overestimated. Due to the complicating line broadening factors and the somewhat unclear situation observed in the static experiments, we carried out a set of similar experiments as those shown in Figure 2, except with MAS, to obtain spectra with more resolved peaks. These are reported in Figure 3a. Figure 3b shows a magnified 100 K spectrum including a curve fitting into three components, their integrated areas, and assigned Na-site. Note that for peaks from dynamic systems, as in Figure 3, the chemical shifts and shapes will be a function of the relative amount and exchange

https://doi.org/10.1021/acsphyschemau.3c00012
ACS Phys. Chem Au XXXX, XXX, XXX−XXX

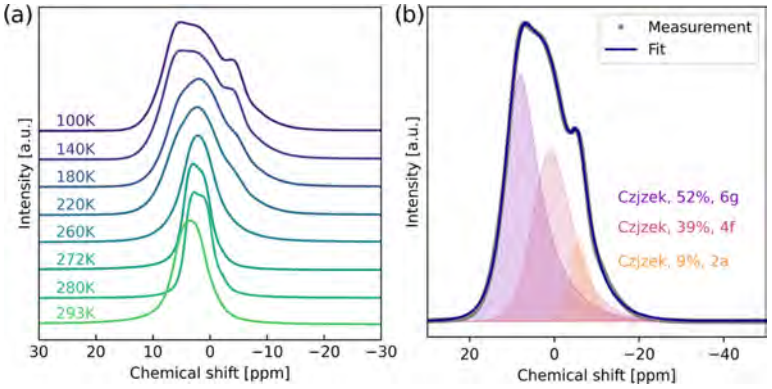

Figure 3. (a) ^{23}Na MAS NMR spectra (18.8 T) of sample NZTO from 100 to 293 K. A plot with a larger spectral width is provided in S3. (b) The spectrum at 100 K with a decomposition shown by the filled-in distributions. All peaks are modeled using the Czjzek model as implemented in DMFit (a table is provided in S4 with details), shown with integrated intensity and the assigned Na-site, which is further discussed below.

rates relative to the spectral (peak region) width. Eventually, the chemical shift of a common high-temperature peak will be determined by the weighted average of the resonances when the exchange rate is much larger than the chemical shift difference (in Hz) between the peaks. Na-ions are dynamic at most of the conditions we have studied; hence, our use of the term "site" is not intended to exclude variations in positions and configurations that may be possible.

Before going further in the analysis of the temperature series for our materials, we will discuss the 100 K ^{23}Na MAS NMR spectrum of the NZTO at 18.8 T in some detail (Figure 3b). At 100 K, the ^{23}Na MAS NMR spectrum does not show any distinct sign of any second-order quadrupolar peak shapes but may be decomposed into three components using a Czjzek distribution,[49] which is a model describing peak shapes originating from a distribution of quadrupolar couplings. Another possibility is a distribution of chemical shifts, with the Na not being localized to a single position. This last situation has previously been described for a similar material in the O3-form,[21] and it is not unlikely that there should be some variance in Na positions for the P2 type. We note that the chemical shift variations between the three peaks are relatively small, which is quite reasonable considering that the difference between the three sites is only in the second coordination sphere. There are three crystallographic Na-sites (6g, 4f, 2a) with a 3:2:1 site multiplicity in NZTO, respectively. However, previously reported refinements of the Na-distribution on these sites are varied, with the 6g-site reported between 43 and 71%, the 4f-site between 22 and 55%, and the 2a-site between 2 and 12%.[22,32,40] Na in the 2a-site is also reported to be less energetically favorable relative to Na in the 4f- and 6g-sites, both from simulations and from measurements,[22,32,40] and is therefore likely to have the lowest occupancy. Based on this, we assign the smallest peak (9%, at ∼ −4 ppm) to Na in the 2a-site. To assign peaks to Na in 4f- and 6g- sites, we note that both the polyhedra around the 2a- and 4f-sites are face-sharing with two-framework layer-octahedra, while the 6g-polyhedron is edge-sharing with six-framework layer-octahedra. Therefore, we expect Na chemical shifts in 4f- and 2a-sites to be relatively similar and different from 6g. We therefore assign the middle peak (39% at ∼1 ppm) as Na in the 4f-sites and the largest peak (52% at ∼7 ppm) from Na in the 6g-sites. This is also in line with the general trend of the relative Na occupancy in these sites. We will use the term 2a-, 4f-, or 6g-peak for Na in these sites/polyhedra.

With the assignment of the peaks in the 100 K ^{23}Na NMR spectrum, we are in a position to discuss the dynamic behavior of Na^+ when the sample is heated. While there are some minor changes in the ^{23}Na MAS spectra (Figure 3a) from 100 to 140 K, we observe that at 180 K the overall peak shape has become narrower, with a shift of the highest point to the middle peak. This change is evidence of Na dynamics between sites at these conditions. Further heating to 260 K shows an expected narrowing of the peak shape and a coalescence into practically one peak at a chemical shift of 35 ppm with an FWHM of 7 ppm. One could then expect that further heating resulted in a narrowing of this peak, but at 272 and 280 K, there are some new peak features emerging. A peak splitting appears with the highest point on the left side. At 293 K, the peak is without these features but is placed further to the left. A qualitative description of the dynamical features observed in Figure 3 may be given by considering several factors. At about 100 K, Na-ions are immobile, but from the onset of Na dynamics, the observed peak positions will be from a weighted average and the total peak shape will change significantly. Furthermore, with increasing Na dynamics dipole−dipole and quadrupolar interactions will be reduced and relaxation rates will change as well, *vide infra*. Reduction of interactions due to dynamics will lead to peak narrowing, and in addition, a reduction in the quadrupolar couplings will impose a change in the position of the peaks toward the left in the spectra. This last effect is, to some extent, already reduced at the high magnetic field strength (18.8 T) applied during these experiments compared to those at 11.7 T. The spectral features during heating from 100 K are therefore a result of changing strengths of interactions between ions experiencing three-site exchange dynamics, with some initial limitations. Our qualitative description of the observed temperature development in Figure 3 is supported by calculations of a three-site exchange model implemented in an in-house written Matlab script (see SI S5). At 100 K, Na is basically nondynamic but will, with increasing temperature, become more and more mobile. We assume that Na will eventually jump between all of the three sites 6g, 4f, and 2a. These are termed 1, 2, and 3, respectively,

https://doi.org/10.1021/acsphyschemau.3c00012
ACS Phys. Chem Au XXXX, XXX, XXX−XXX

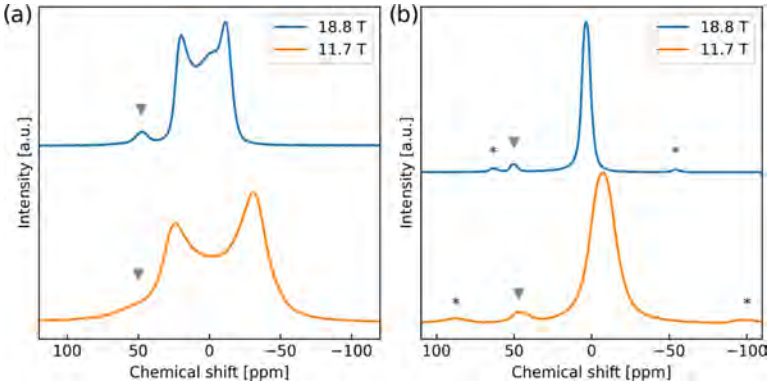

Figure 4. (a) Comparison of ^{23}Na NMR spectra of static NZTO at magnetic fields of 18.8 and 11.74 T. (b) ^{23}Na MAS NMR of NZTO at 18.8 T (MAS rate 12.5 kHz) and at 11.75 T (MAS rate 10 kHz). The feature at 50/45 ppm is denoted with a gray triangle, with spinning sidebands with an asterisk*.

in the figures in S5. However, just after Na dynamics have started, but still at a low temperature, Na jump between sites should preferably go either *from* or *to* a 6g-prism[25] and not directly between 2a and 4f. However, at higher temperatures, the rate of Na jumps may become so fast that several steps take place during acquisition; hence, for modeling purposes, jumps between all three sites must be considered. The simulations show that the observed spectral trend when going up from 100 K is better represented if there is an exchange between sites 6g and 2a in contrast to 6g and 4f, or 4f and 2a (see S5 panel 1, 2, 2X, and 2Z) and is in accordance with the above-mentioned jump order. Furthermore, to mimic the general observed peak shapes, we must include jumps between sites 6g and 2a (panel 3 in S5). To approach the trend toward the 260 K spectrum, jumps between sites 4f and 2a are included as shown in panels 4 and 5. With a further increase in jump rates for all three paths, only a peak narrowing is observed, which contrasts with what is observed at 272 K where a ″peak splitting″ with the highest intensity on the left part of the total peak shape is observed. Such an observation may originate from a significantly reduced quadrupolar coupling of one or two components relative to the other(s), and to represent this, we adjusted slightly the peak positions toward the left when going from panel 5 to 6. However, to mimic the observed trend, we also had to narrow the peak from the 6g position and adjust positions (see panels 7 and 8). Panels 7−9 are all somewhat similar as the observations around 272−280 K. Finally, by increasing all three jump rates to an equally high number and with a slight and equally reduced line broadening of all of the peaks, we were able to progress to a total peak shape that looks like the one observed at 295 K via the split peak (280 K, panel 9). In conclusion, the observed spectra are all a result of a complex interplay and influence by coupling interactions, relaxation times, relative amounts of Na at sites and to available jump-pathways (primarily at low temperature).

As a last comment on the spectra shown in Figures 2 and 3, one may note that the total peak width ratios of the static over MAS spectra are for 100 K about 4 and at 293 K almost 6. This indicates that the dynamic situation at 293 K helps to reduce the peak width in contrast to the dynamic situation at 100 K. For quadrupolar nuclei, MAS can reduce the line width by about a factor of 4.

3.3. Room-Temperature ^{23}Na NMR on NZTO

Our low- (100 K) to high-temperature (500 K) ^{23}Na NMR experiments have been carried out using two different magnetic fields, 18.8 and 11.7 T, respectively, with the room-temperature (∼293 K) measurement being the point of overlap. Figure 4 shows the four NZTO spectra at room temperature to be compared, two at static conditions (left) and two during MAS (right) conditions.

Overall, peaks in the spectra acquired at a higher field are narrower and slightly shifted to the left. In the MAS spectra, the main peak changes from −7 ppm at 11.7 T to 3 ppm at 18.8 T. This implies that there are quadrupolar couplings that must be described by the second-order term in the perturbative development of the Hamiltonian, as this term is inversely proportional to the magnetic field and contains a term giving rise to a shift in peak position. We know that there are Na dynamics at room temperature; hence, the effects we observe in Figure 4 are not purely due to the magnetic field variations. However, the fact that we see the effect of field variation indicates that the dynamic situation at 293 K does not have rates high enough to completely average the quadrupolar couplings at 11.7 T. One could loosely claim we have residual quadrupolar couplings at 293 K for the lowest field strength. Furthermore, the MAS spectrum recorded at 11.7 T is not fully symmetric, but at 18.8 T, the main peak is basically symmetric as seen by curve fitting with a Gaussian and/or a Lorentzian function (S6, Figure S2). The symmetry is indeed high, but the fact that two different types of functions must be used is also a sign that the situation is still somewhat complicated by various interactions. The small components at 45/5 ppm do also shift somewhat when going to the higher field. The left component does barely shift (2.5 ppm), but the right component has a somewhat larger shift (6 ppm).

3.4. High-Temperature ^{23}Na NMR on NZTO

The NZTO and variants (*vide infra*) were studied up to about 500 K at a magnetic field of 11.7 T to unravel Na dynamics through line shape analyses and via T_1 relaxation constant measurements. Note that for NZTO, no phase transition has been reported until between 573 and 673 K where a gradual, reversible change has been observed in the Na-distribution, going from an orthorhombic superstructure to a hexagonal.[22,40]

https://doi.org/10.1021/acsphyschemau.3c00012
ACS Phys. Chem Au XXXX, XXX, XXX−XXX

The line shape variations of NZTO will be described first. Figure 5 shows a stacked plot of ^{23}Na MAS spectra from 293 K up to 508 K.

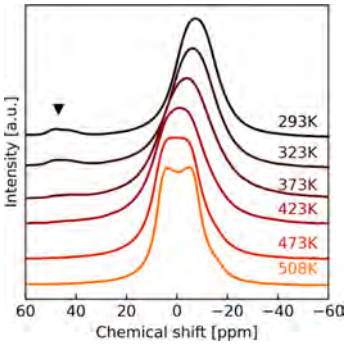

Figure 5. ^{23}Na MAS NMR (11.7 T) of NZTO heated up from 293 K (RT) to 508 K. The triangle marks the small components that reversibly merge with the main peaks at an elevated temperature.

Up to 423 K, the main peak keeps its shape but moves slightly to the left and the small peaks at 45/50 ppm appear to vanish. Upon cooling to 293 K after heating to 508 K, the spectrum regains its original peaks and shapes proving the reversibility of the temperature effects. Na-ions are in structural parts linked with each other and with the interlayer regions. The shift to the left (i.e., higher frequencies) may be explained by a quadrupolar interaction that is weakened by Na dynamics. NMR spectra at 473 and 508 K reveal that the peak has diverged into something that looks like two components with some intensity at the right foot of the peak at 508 K. From the line shape discussion above, the spectral features seen here must be due to variations of rates for the three-site exchange coupled with reduced interaction strengths. The exchange rates are high; hence, the peak splits must mainly be due to reduced quadrupolar and dipole−dipole interactions. Another issue that also may take place is that previous simulations indicate that the Na-distribution in one layer influences the allowed positions in adjacent layers, suggesting that the layers are not as independent as previously assumed and a more complex situation may be expected.[32]

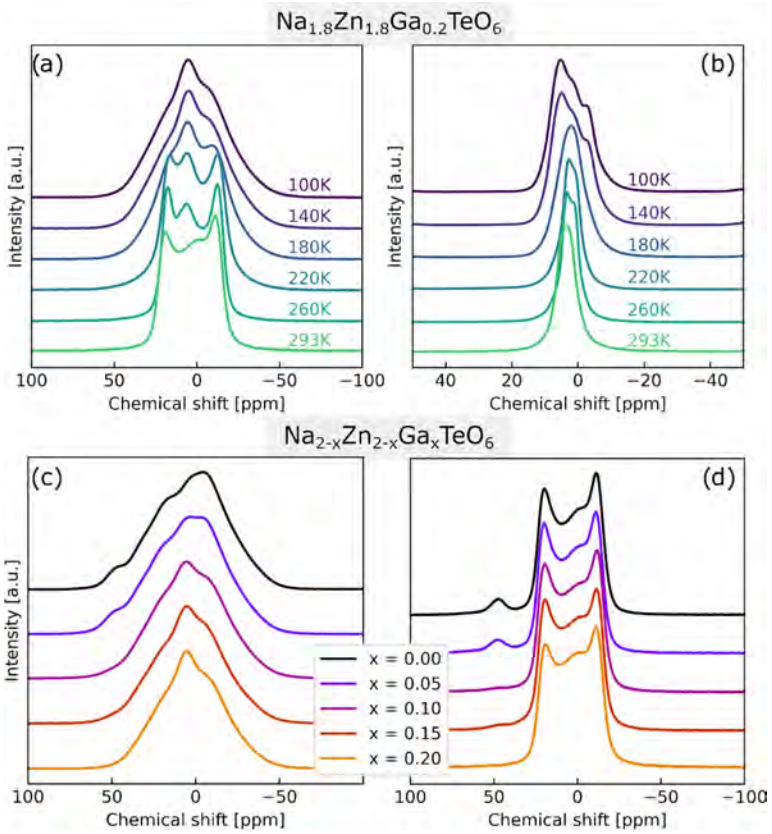

Figure 6. (a) Static and (b) MAS at a rate of 12.5 kHz, and ^{23}Na NMR spectra of $Na_{2-x}Zn_{2-x}Ga_xTeO_6$ (x = 0.20) in the temperature range of 100−293 K (18.8 T). Static ^{23}Na NMR spectra (18.8 T) of $Na_{2-x}Zn_{2-x}Ga_xTeO_6$ (x = 0.00, 0.05, 0.10, 0.15, 0.20): (c) 100 K and (d) 293 K.

https://doi.org/10.1021/acsphyschemau.3c00012
ACS Phys. Chem Au XXXX, XXX, XXX−XXX

3.5. NMR on Ga-Substituted NZTO from 100 to 293 K

With a basic description and understanding of the NZTO material from 100 K up to 508 K, we continue with NMR data analyses for the Ga-doped samples, presenting figures describing the most characteristic trends. Figure 6 shows a panel of selected static and MAS ^{23}Na NMR spectra, between 100 and 293 K, all at 18.8 T, of $Na_{2-x}Zn_{2-x}Ga_xTeO_6$ (x = 0.00, 0.05, 0.10, 0.15, 0.20). Additional static and MAS spectra of Ga-substituted samples are reported in S7 Figures S3 and S4.

In the top row, ^{23}Na NMR data of the sample with the highest Ga doping (x = 0.20) from 100 K up to 293 K is shown: (a) static and (b) MAS experiments. The bottom row shows static ^{23}Na NMR spectra (18.8 T) of $Na_{2-x}Zn_{2-x}Ga_xTeO_6$ (x = 0.00, 0.05, 0.10, 0.15, 0.20): (c) 100 K and (d) 293 K. The spectra in Figure 6a show a clear coalescence of peaks with increasing temperature. A similar coalescence is also shown for intermediate compositions. At 220 K, the peak width in Figure 6b appears to have reached its minimum, in contrast to NZTO where it can be estimated that the minimum peak width was reached at 260 K. This is proof of higher Na dynamic rates in the Ga x = 0.20 sample compared to NZTO. A feature in Figure 6a is the "middle" peak that is present between the two outermost peaks. The NZTO sample did not show any "middle" peak until the spectrum acquired at 293 K. This middle peak is for most of the spectra in Figure 6a at the same position as the highest peak at 100 K until 293 K where it has changed to the right and appears broader. These observations are again indications of higher Na dynamic rates in the Ga x = 0.20 sample and that some exchange effects that broadens the peak are seen at 293 K.

Static spectra of the various Ga-doped samples show significant changes with increasing Ga content. The small component at around 50 ppm becomes smaller with increasing Ga content and appears to vanish for the x = 0.20 sample. The widths of the peak shapes are, however, very similar throughout the series. The MAS spectra of the same set at 100 K, Figure S3a, show a gradual change between components with increasing Ga content, while the 293 K spectra of the same set, Figure S3b, are more similar.

3.6. High-Temperature NMR on Ga-Substituted Samples

The high-temperature (RT up to about 500 K) spectral trends of all of the five samples are relatively similar, and only spectra collected at the highest temperature are shown here in Figure 7. All samples display a splitting behavior at higher temperatures, which is probably due to the above-mentioned complex three-site exchange situation of the Na-ions and reduced quadrupolar and dipole−dipole interactions.

3.7. Spin−Lattice (T_1) Relaxation Measurements

Measurements of T_1 relaxation constants were carried out to investigate dynamic trends in NZTO and how these change with the introduction of Ga in the temperature interval from 293 K up to about 500 K. These measurements probe dynamics faster than observed during peak shape variations at low temperatures, as discussed above. Deviations from a symmetric plot of $\log(1/T_1)$ vs inverse temperature, as seen in fast stochastic 3-dimensional diffusion with only a simple exponential dependency of the correlation time, should be expected since Na is confined between oxide layers. Our relaxation data are plotted as $\log(1/T_1[s])$ vs inverse temperature $(1000/T[K])$ and shown in Figure 8. More details are provided in S8 where Table S2 lists all of the actual

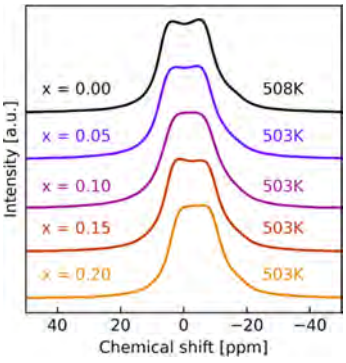

Figure 7. High-temperature measurement of all samples. x = 0.00 is measured at 508 K, while all others are measured at 503 K.

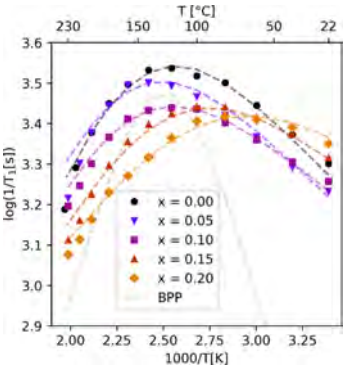

Figure 8. Temperature dependence for ^{23}Na spin−lattice rates ($1/T_1[s]$) for $Na_{2-x}Zn_{2-x}Ga_xTeO_6$ (x = 0.00, 0.05, 0.10, 0.15, 0.20) samples. The reduced slopes on the high-temperature side (left of maxima) are connected to a 2D dimensional process for Na-ions between layers, while the slope reduction on the low-temperature side (right of maxima) is connected to the correlated movement of ions. The dotted lines are results from modeling using eqs 1−3. The dotted, gray, symmetric curve is the expected shape of a random 3D isotropic process with an E_a of 0.32 eV, with a so-called BPP behavior.

measured averaged T_1 values used for Figure 8, and Figure S5 shows a plot of T_1 relaxation data from 100 K up to 293 K, all measured at 18.8 T. Included in Figure 8 are also results (shown as dotted lines) from modeling using eqs 1 and 3 (termed as a 2D model) and a symmetric BPP curve.

All of the curves go through a maximum where the correlation time τ_c is equal to the inverse Larmor frequency. Hence, for each material, there is a different temperature where Na-ions have the same rates for the dynamic processes. Except for sample x = 0.05, the Ga-doped samples have their peak maxima shifted to lower temperatures compared to NZTO. This also indicates that Ga substitution leads to higher ion mobility and a lower activation energy for the dynamic process compared to NZTO, which is also a conclusion from the line shape analyses at low temperatures described above. Furthermore, for NZTO, it appears that a rather steady slope is obtained at the highest temperatures and that the x = 0.05, 0.10, and 0.15 samples seem to converge toward this

https://doi.org/10.1021/acsphyschemau.3c00012
ACS Phys. Chem Au XXXX, XXX, XXX−XXX

approximate slope. The x = 0.20 sample shows a clear shift in its slopes. In the simplest model for T_1 variation with temperature, the peak shape would be symmetrical, with the slope of each side determined by the activation energy, E_a. However, any correlated movement will reduce the slope of the low-temperature region, and any dimensionality in the dynamic process (ion diffusion) will reduce the slope of the high-temperature region.[7] At sufficiently high temperatures, the activation energy for the process may be estimated using an Arrhenius relation based on data points from the highest temperatures or estimated more precisely using a suited 2D model. For a set of samples with a systematic variation, as in our case where the Ga content is adjusted, it is possible to extract trends from relaxation data even if the absolute values contain uncertainties. In Table 1, we report calculated E_a values based on a simple Arrhenius relation and from a more detailed modeling (using the 2D model mentioned above). The temperature where the correlation time is the inverse of the Larmor frequency of ^{23}Na at 11.7 T (τ_c = 1/132.29 MHz) is reported in the last column.

Table 1. E_a for $Na_{2-x}Zn_{2-x}Ga_xTeO_6$ (x = 0.00, 0.05, 0.10, 0.15, 0.20) Samples Calculated from the Leftmost Points in the Graphs (Two Values Are Given for x = 0.00 and 0.05) and the 2D Model and the Temperature for Curve Maxima[a]

x	E_a (eV) Arrhenius relation (points used)	E_a (eV) 2D model (β value in eq 3)	temperature for curve maxima, K
0.00	0.34/0.25 (2/3)	0.32 (1.30)	393
0.05	0.28/0.25 (2/3)	0.32 (1.29)	413
0.10	0.17 (3)	0.30 (1.25)	393
0.15	0.17 (4)	0.26 (1.28)	373
0.20	0.14 (4)	0.20 (1.35)	353

[a]The uncertainty in the 2D model E_a's is approximately ± 0.01 eV.

Both models give similar values for E_a for NZTO, which are similar to results from ion conductivity[26] and calculations (0.33 eV, *vide infra*). With increasing Ga content, both models give reduced E_a, but significantly less reduction is seen for the 2D model. The β values indicate that Na dynamics are strongly correlated. A simple model for correlated motion is when one ion blocks the jump of another, but it appears that the correlations are rather similar even with a reduced Na content. Altogether, the measured decrease in activation energy is likely to be a real effect and will be discussed more in relation to the DFT results in Section 3.8.

3.8. *Ab Initio* MD Simulations for Ionic Conductivity

Three compositions of $Na_{2-x}Zn_{2-x}Ga_xTeO_6$ type with x = 0 (NZTO), 0.083 (2Ga), and 0.167 (4Ga) were explored with the ab initio MD simulation, the latter two, respectively, with 2 and 4 Ga^{3+} ions in a supercell with 24 formula units. The construction of the model and structural insights are reported in our previous work.[32] For each composition x, we consider four simulation temperatures: 750, 1000, 1250, and 1500 K. From the AIMD trajectories, it is also possible to compute the mean square displacement and, thus, the ionic mobility, as described in S9. The diffusion coefficients (D) increase slightly with higher temperatures, but the three cases exhibit very similar values at different temperatures. One thing to note is that the 4Ga structure shows clear indications of inhomogeneous Na-distribution across layers, which is distinctly more favorable than the homogeneous. The 4Ga is calculated twice for better statistics, with the two layers being reported separately. Figure 9 shows the relationship of ln(D) vs 1000/K.

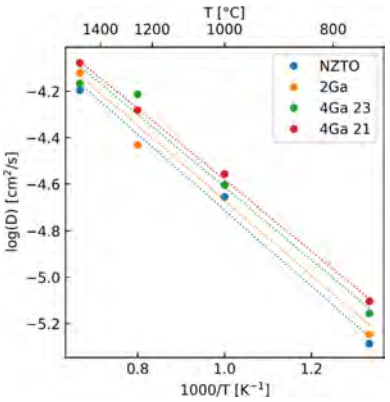

Figure 9. Arrhenius plot for all simulations, with the two individual 4Ga split into two distinct layers.

The calculated activation energy for NZTO is 0.33 eV, in line with the measured range of 0.25−0.34 eV as presented above from the SLR analysis. This suggests that, even with some uncertainty, the approximate correct slope of NZTO reported above is reached. As this translates to an ionic mobility of 1.8 10^{-4} S/cm, it confirms the reported experimental range for NZTO of $\sim 10^{-4} - 10^{-3}$ S/cm.[24,26,27] The simulations of the Ga-substituted materials have a very small decrease in activation energy, with 0.32, 0.31, and 0.30 eV for 2Ga and the two 4Ga layers, respectively, which is quite close to the values given from the 2D model for the most similar materials, i.e., those with x = 0.05 and 0.15. The calculated difference between the structures is within the margin of error and should therefore be considered carefully, but they do suggest a decrease in activation energy with increased Ga content, as expected. Table 2 summarizes the findings from the DFT AIMD calculations.

A discussion of the estimation of E_a, ion conductivity, and the amount of Na is in place at this stage. Previous simulations have shown that in a similar material the $Na_2Ni_2TeO_6$ ionic conductivity can be increased either by underloading the Na layer by 20%[30] or by decreasing the Na−Na repulsion in the simulations.[31] Both of these situations were generated by altering the physical properties or breaking electroneutrality. For a real material, the suggested route for achieving this was a reduction of the Na content, as we have done when making our Ga-substituted materials. The DFT AIMD-calculated activation energies correspond quite well with estimates from impedance spectroscopy, which shows that samples with Ga substitution x = 0.05−0.15 have activation energies in the range of 0.30−0.27 eV.[26] Since our DFT-calculated activation energy is based on the mean square displacement, both of these methods provide values related to long-range movement, whereas SLR relaxation rates probe Na-ion dynamics on a shorter range. It is interesting that nudged elastic band (NEB) calculations of Na jumps in an empty Na-lattice between the

https://doi.org/10.1021/acsphyschemau.3c00012
ACS Phys. Chem Au XXXX, XXX, XXX−XXX

Table 2. AIMD Calculation of Na Diffusion in an Average Lattice[a]

system	act. energy [eV]	diff coeff. 10^{-9} [cm^2/s]	mobility 10^{-4} [S/cm]
NZTO	0.33 ± 0.03	2.0	1.8
2GA	0.33 ± 0.04	3.7	3.3
4GA (23 Na)	0.31 ± 0.03	5.5	4.8
4GA (21 Na)	0.30 ± 0.03	6.9	5.6

[a]Diffusion coefficient and mobility are calculated at room temperature.

framework layers in NZTO gave an activation energy of 0.09 eV[24] and could suggest that increasing the Ga content leads to a situation where more and more Na behaves like Na in an empty lattice. It appears that the decrease in activation energy for Na jumps in the Ga samples cannot be exploited fully for increased ionic conductivity since the previously measured ionic conductivity of x = 0.0 and 0.2 is rather similar. Furthermore, our analysis points to a situation where an optimum composition for ion conductivity for a certain class of layered materials exists, which is what Li et al. observed.[24] If layered material's structure−dynamic relationships can be controlled through preparation, an important step toward creating better solid-state electrolytes can be taken.

4. CONCLUSIONS

We have characterized Na-coordination and dynamics in NZTO and its Ga-substituted derivatives ($Na_{2-x}Zn_{2-x}Ga_xTeO_6$ with x = 0.00, 0.05, 0.10, 0.15, 0.20) by variable-temperature ^{23}Na NMR methods and DFT AIMD simulations. At 100 K, the Na-ions were frozen on the NMR time scale, and a structural characterization was performed. Three spectral components were assigned to the three 2a, 4f, and 6g Na-prisms, as the integrated intensities correspond well with the expected site multiplicity. Variable-temperature measurements from 100 K and upwards on NZTO showed a complex peak shape coalescence. These measurements also show that the Na spectrum acquired at 293 K had some averaging in it due to Na-ion dynamics. A three-site exchange model coupled with reduced quadrupolar and dipole−dipole couplings due to dynamics seem to explain the peak shape observations. A further temperature increase to 500 K did not reveal any new peak shape variations until the highest level, where an apparent peak splitting was observed again. Measurements of T_1 relaxation time constants gave insight into Na dynamics and activation energies. Ga substitution decreased the temperatures for peak coalescence and lead to reduced activation energies for the dynamic processes of Na. The estimated activation energy for Na dynamics in NZTO from relaxation measurements corresponds well with results from DFT AIMD simulations. On Ga substitution, measured activation energies are reduced and are supported by DFT calculations. We suggest that addressing the correlated motion of Na is important for creating a better Na conductor for SSE, as the decrease in activation energy from Ga substitution can be exploited.

■ ASSOCIATED CONTENT

Supporting Information

The Supporting Information is available free of charge at https://pubs.acs.org/doi/10.1021/acsphyschemau.3c00012.

A file containing details on synthesis, water estimation by NMR, enlarged NMR spectra NZTO, simulation parameters for the Czjzek distribution, simulations of a three-site exchange system, line fitting of MAS spectrum at 18.8 T, stacked plots of Ga-doped materials, details on relaxation measurements, and details on DFT calculation of Na mobility (PDF)

■ AUTHOR INFORMATION

Corresponding Author

Bjørnar Arstad − *SINTEF Industry, 0373 Oslo, Norway;* orcid.org/0000-0003-0398-786X; Email: bjornar.arstad@sintef.no

Authors

Frida Sveen Hempel − *SINTEF Industry, 0373 Oslo, Norway; Department of Chemistry and Center for Materials Science and Nanotechnology, University of Oslo, Oslo 0371, Norway;* Present Address: Morrow Technologies AS, c/o Institute for Energy Technology, Instituttveien 18, 2007 Kjeller, Norway

Charlotte Martineau-Corcos − *CortecNet, 91940 Les Ulis, France*

Federico Bianchini − *Department of Chemistry and Center for Materials Science and Nanotechnology, University of Oslo, Oslo 0371, Norway;* Present Address: Center for Bioinformatics, University of Oslo, Gaustadalléen 30, N-0373 Oslo, Norway.

Helmer Fjellvåg − *Department of Chemistry and Center for Materials Science and Nanotechnology, University of Oslo, Oslo 0371, Norway*

Complete contact information is available at: https://pubs.acs.org/10.1021/acsphyschemau.3c00012

Author Contributions

The manuscript was written through contributions of all authors. All authors have given approval to the final version of the manuscript. CRediT: **Frida Sveen Hempel** conceptualization (equal), data curation (equal), formal analysis (equal), investigation (equal), methodology (equal), visualization (equal), writing-original draft (equal), writing-review & editing (equal); **Charlotte Martineau-Corcos** data curation (equal), investigation (equal), methodology (equal), resources (equal), visualization (equal), writing-original draft (equal), writing-review & editing (equal); **Federico Bianchini** formal analysis (equal), investigation (equal), methodology (equal), software (equal), validation (equal), writing-original draft (equal), writing-review & editing (equal); **Helmer Fjellvåg** conceptualization (equal), methodology (equal), resources (equal), supervision (equal), writing-original draft (equal), writing-review & editing (equal); **Bjørnar Arstad** conceptualization (equal), data curation (equal), formal analysis (equal), funding acquisition (equal), investigation (equal), methodology (equal), project administration (equal), resources (equal), software (equal), supervision (equal), validation (equal),

visualization (equal), writing-original draft (equal), writing-review & editing (equal).

Notes

The authors declare no competing financial interest.

■ ACKNOWLEDGMENTS

The authors acknowledge the Research Council of Norway for providing financial support (under project numbers P#272402 and P#255441) and for the computing time (under project numbers NN2875k and NS2875k) at the Norwegian Supercomputer Facility. DFT calculations were performed between June 2019 and August 2020. CMC thanks Dr. Ribal Jabbour and Dr. Anne Lesage (CRMN Lyon) for assistance with the Lt-MAS NMR measurements.

■ REFERENCES

(1) Goodenough, J. B.; Mizushima, K.; Takeda, T. Solid-Solution Oxides for Storage-Battery Electrodes. *Jpn. J. Appl. Phys.* **1980**, *19*, 305−313.

(2) Eshetu, G. G.; Grugeon, S.; Laruelle, S.; Boyanov, S.; Lecocq, A.; Bertrand, J. P.; Marlair, G. In-Depth Safety-Focused Analysis of Solvents Used in Electrolytes for Large Scale Lithium Ion Batteries. *Phys. Chem. Chem. Phys.* **2013**, *15*, 9145−9155.

(3) Sun, P.; Bisschop, R.; Niu, H.; Huang, X. A Review of Battery Fires in Electric Vehicles. *Fire Technol.* **2020**, *56*, 1361−1410.

(4) Goikolea, E.; Palomares, V.; Wang, S.; de Larramendi, I. R.; Guo, X.; Wang, G.; Rojo, T. Na-ion batteries—approaching old and new challenges. *Adv. Energy Mater.* **2020**, *10*, No. 2002055.

(5) Kuhn, A.; Kunze, M.; Sreeraj, P.; Wiemhöfer, H. D.; Thangadurai, V.; Wilkening, M.; Heitjans, P. NMR Relaxometry as a Versatile Tool to Study Li Ion Dynamics in Potential Battery Materials. *Solid State Nucl. Magn. Reson.* **2012**, *42*, 2−8.

(6) Epp, V.; Nakhal, S.; Lerch, M.; Wilkening, M. Two-Dimensional Diffusion in Li0.7NbS2 as Directly Probed by Frequency-Dependent 7Li NMR. *J. Phys. Condens. Matter* **2013**, *25*, No. 195402.

(7) Wilkening, M.; Heitjans, P. From Micro to Macro: Acess to Long Range Li+ Diffusion Parameters in Solids via Microscopic 6,7Li Spin Alignment Echo Nmr Spectroscopy. *Phys. Chem. Chem. Phys.* **2012**, *13*, 53−65.

(8) Kuhn, A.; Epp, V.; Schmidt, G.; Narayanan, S.; Thangadurai, V.; Wilkening, M. Spin-Alignment Echo NMR: Probing Li + Hopping Motion in the Solid Electrolyte Li 7La 3Zr 2O 12 with Garnet-Type Tetragonal Structure. *J. Phys. Condens. Matter* **2012**, *24*, No. 035901.

(9) Heitjans, P.; Schirmer, A.; Indris, S. NMR and β-NMR Studies of Diffusion in Interface-Dominated and Disordered Solids. *Diffus. Condens. Matter* **2005**, 367−415.

(10) Müller, K.; Geppi, M. *Solid State NMR: Principles, Methods, and Applications*; John Wiley & Sons, 2021.

(11) Bloembergen, N.; Purcell, E. M.; Pound, R. V. Relaxation Effects in Nuclear Magnetic Resonance Absorption. *Phys. Rev.* **1948**, *73*, 679−712.

(12) Richards, P. M. Effect of Low Dimensionality on Prefactor Anomalies in Superionic Conductors. *Solid State Commun.* **1978**, *25*, 1019−1021.

(13) Epp, V.; Wilkening, M. Fast Li Diffusion in Crystalline LiBH4 Due to Reduced Dimensionality: Frequency-Dependent NMR Spectroscopy. *Phys. Rev. B* **2010**, *82*, No. 020301.

(14) Wilkening, M.; Heitjans, P. Li Jump Process in H- Li0.7 Ti S2 Studied by Two-Time Li7 Spin-Alignment Echo NMR and Comparison with Results on Two-Dimensional Diffusion from Nuclear Magnetic Relaxation. *Phys. Rev. B: Condens. Matter Mater. Phys.* **2008**, *77*, 1−13.

(15) Gombotz, M.; Lunghammer, S.; Breuer, S.; Hanzu, I.; Preishuber-Pflügl, F.; Wilkening, H. M. R. Spatial Confinement-Rapid 2D F- Diffusion in Micro- and Nanocrystalline RbSn2F5. *Phys. Chem. Chem. Phys.* **2019**, *21*, 1872−1883.

(16) Delmas, C.; Fouassier, C.; Hagenmuller, P. Structural Classification and Properties of Layered Oxides. *Phys. B+C* **1980**, *99*, 81−85.

(17) Weller, M.; Sacchetti, A.; Ott, H. R.; Mattenberger, K.; Batlogg, B. Melting of the Na Layers in Solid Na0.8CoO2. *Phys. Rev. Lett.* **2009**, *102*, 6−9.

(18) Villa, M.; Bjorkstam, J. L. Na23 and Al27 in β-Alumina Solid Electrolytes. *Phys. Rev. B* **1980**, *22*, 5033−5042.

(19) Carlier, D.; Blangero, M.; Ménétrier, M.; Pollet, M.; Doumerc, J. P.; Delmas, C. Sodium Ion Mobility in NaxCoO2 (0.6 <× <0.75) Cobaltites Studied by 23Na MAS NMR. *Inorg. Chem.* **2009**, *48*, 7018−7025.

(20) Han, O. H.; Jung, J. K.; Yi, M. Y.; Kwak, J. H.; Shin, Y. J. Sodium Ion Dynamics in the Nonstoichiometric Layer-Type Oxide Na0.67Ni0.33Ti0.67O2 Studied by 23Na NMR. *Solid State Commun.* **2000**, *117*, 65−68.

(21) Smirnova, O. A.; Rocha, J.; Nalbandyan, V. B.; Kharton, V. V.; Marques, F. M. B. Crystal Structure, Local Sodium Environments and Ion Dynamics in Na0.8Ni0.6Sb0.4O2, a New Mixed Antimonate. *Solid State Ionics* **2007**, *178*, 1360−1365.

(22) Evstigneeva, M. A.; Nalbandyan, V. B.; Petrenko, A. A.; Medvedev, B. S.; Kataev, A. A. A New Family of Fast Sodium Ion Conductors: Na2M 2TeO6 (M = Ni, Co, Zn, Mg). *Chem. Mater.* **2011**, *23*, 1174−1181.

(23) Schmidt, W.; Berthelot, R.; Sleight, A. W.; Subramanian, M. A. Solid Solution Studies of Layered Honeycomb-Ordered Phases O 3 − Na 3 M 2 SbO 6 (M 1/4 Cu, Mg, Ni, Zn). *J. Solid State Chem.* **2013**, *201*, 178−185.

(24) Li, X.; Bianchini, F.; Wind, J.; Pettersen, C.; Wragg, D. S.; Vajeeston, P.; Fjellvåg, H. Insights into Crystal Structure and Diffusion of Biphasic Na 2 Zn 2 TeO 6. *ACS Appl. Mater. Interfaces* **2020**, *12*, 28188−28198.

(25) Bianchini, F.; Fjellvåg, H.; Vajeeston, P. Nonhexagonal Na Sublattice Reconstruction in the Super-Ionic Conductor Na 2 Zn 2 TeO 6: Insights from Ab Initio Molecular Dynamics. *J. Phys. Chem. C* **2019**, *123*, 4654−4663.

(26) Li, Y.; Deng, Z.; Peng, J.; Chen, E.; Yu, Y.; Li, X.; Luo, J.; Huang, Y.; Zhu, J.; Fang, C.; Li, Q.; Han, J.; Huang, Y. A P2-Type Layered Superionic Conductor Ga-Doped Na2Zn2TeO6for All-Solid-State Sodium-Ion Batteries. *Chem. - Eur. J.* **2018**, *24*, 1057−1061.

(27) Wu, J. F.; Wang, Q.; Guo, X. Sodium-Ion Conduction in Na2Zn2TeO6 Solid Electrolytes. *J. Power Sources* **2018**, *402*, 513−518.

(28) Deng, Z.; Gu, J.; Li, Y.; Li, S.; Peng, J.; Li, X.; Luo, J.; Huang, Y.; Fang, C.; Li, Q.; Han, J.; Huang, Y.; Zhao, Y. Ca-Doped Na 2 Zn 2 TeO 6 Layered Sodium Conductor for All-Solid-State Sodium-Ion Batteries. *Electrochim. Acta* **2019**, *298*, 121−126.

(29) Sau, K.; Kumar, P. P. Ion Transport in Na2M2TeO6: Insights from Molecular Dynamics Simulation. *J. Phys. Chem. C* **2015**, *119*, 1651−1658.

(30) Sau, K.; Kumar, P. P. Role of Ion-Ion Correlations on Fast Ion Transport: Molecular Dynamics Simulation of Na2Ni2TeO6. *J. Phys. Chem. C* **2015**, *119*, 18030−18037.

(31) Sau, K. Influence of Ion−Ion Correlation on Na+ Transport in Na2Ni2TeO6: Molecular Dynamics Study. *Ionics* **2016**, *22*, 2379−2385.

(32) Hempel, F. S.; Bianchini, F.; Arstad, B.; Fjellvåg, H. Effects of Ga Substitution on the Local Structure of Na2Zn2TeO6. *Inorg. Chem.* **2022**, *61*, 13067−13076.

(33) Coelho, A. A. TOPAS and TOPAS-Academic: An Optimization Program Integrating Computer Algebra and Crystallographic Objects Written in C++: An. *J. Appl. Crystallogr.* **2018**, *51*, 210−218.

(34) Thurber, K. R.; Tycko, R. Measurement of Sample Temperatures under Magic-Angle Spinning from the Chemical Shift and Spin-Lattice Relaxation Rate of 79Br in KBr Powder. *J. Magn. Reson.* **2009**, *196*, 84−87.

(35) Massiot, D.; Fayon, F.; Capron, M.; King, I.; Le Calvé, S.; Alonso, B.; Durand, J. O.; Bujoli, B.; Gan, Z.; Hoatson, G. Modelling

https://doi.org/10.1021/acsphyschemau.3c00012
ACS Phys. Chem Au XXXX, XXX, XXX−XXX

One- and Two-Dimensional Solid-State NMR Spectra. *Magn. Reson. Chem.* **2002**, *40*, 70−76.
(36) Kresse, G.; Hafner, J. Ab Initio Molecular Dynamics for Liquid Metals. *Phys. Rev. B* **1993**, *47*, 558−561.
(37) Kresse, G.; Furthmüller, J. Efficiency of Ab-Initio Total Energy Calculations for Metals and Semiconductors Using a Plane-Wave Basis Set. *Comput. Mater. Sci.* **1996**, *6*, 15−50.
(38) Kresse, G.; Furthmüller, J. Efficient Iterative Schemes for Ab Initio Total-Energy Calculations Using a Plane-Wave Basis Set. *Phys. Rev. B* **1996**, *54*, 11169−11186.
(39) Kresse, G.; Joubert, D. From Ultrasoft Pseudopotentials to the Projector Augmented-Wave Method. *Phys. Rev. B* **1999**, *59*, 1758−1775.
(40) Li, X.; Bianchini, F.; Wind, J.; Vajeeston, P.; Wragg, D.; Fjellvåg, H. P2 Type Layered Solid-State Electrolyte Na 2 Zn 2 TeO 6: Crystal Structure and Stacking Faults. *J. Electrochem. Soc.* **2019**, *166*, A3830−A3837.
(41) Nosé, S. Constant Temperature Molecular Dynamics Methods Limitations in Simulations in the Microcanonical Ensemble. *Prog. Theor. Phys. Suppl.* **1991**, *103*, 1−46.
(42) Nosé, S. A Unified Formulation of the Constant Temperature Molecular Dynamics Methods. *J. Chem. Phys.* **1984**, *81*, 511−519.
(43) Bylander, D. M.; Kleinman, L. Energy Fluctuations Induced by the Nose Thermostat. *Phys. Rev. B* **1992**, *46*, 13756.
(44) Goret, G.; Aoun, B.; Pellegrini, E. MDANSE: An Interactive Analysis Environment for Molecular Dynamics Simulations. *J. Chem. Inf. Model.* **2017**, *57*, 1−5.
(45) Larsen, A. H.; Mortensen, J. J.; Blomqvist, J.; Castelli, I. E.; Christensen, R.; Dułak, M.; Friis, J.; Groves, M. N.; Hammer, B.; Hargus, C.; Hermes, E. D.; Jennings, P. C.; Jensen, P. B.; Kermode, J.; Kitchin, J. R.; Kolsbjerg, E. L.; Kubal, J.; Kaasbjerg, K.; Lysgaard, S.; Maronsson, J. B.; Maxson, T.; Olsen, T.; Pastewka, L.; Peterson, A.; Rostgaard, C.; Schiøtz, J.; Schütt, O.; Strange, M.; Thygesen, K. S.; Vegge, T.; Vilhelmsen, L.; Walter, M.; Zeng, Z.; Jacobsen, K. W. The Atomic Simulation Environment-a Python Library for Working with Atoms. *J. Phys. Condens. Matter* **2017**, *29*, No. 273002.
(46) Bahn, S. R.; Jacobsen, K. W. An Object-Oriented Scripting Interface to a Legacy Electronic Structure Code. *Comput. Sci. Eng.* **2002**, *4*, 56−66.
(47) QUIP. https://libatoms.github.io/QUIP/ (accessed April 18, 2023).
(48) Momma, K.; Izumi, F. VESTA: A Three-Dimensional Visualization System for Electronic and Structural Analysis. *J. Appl. Crystallogr.* **2008**, *41*, 653−658.
(49) d'Espinose de Lacaillerie, J. B.; Fretigny, C.; Massiot, D. MAS NMR Spectra of Quadrupolar Nuclei in Disordered Solids: The Czjzek Model. *J. Magn. Reson.* **2008**, *192*, 244−251.

https://doi.org/10.1021/acsphyschemau.3c00012
ACS Phys. Chem Au XXXX, XXX, XXX−XXX

Supplementary information

Dynamics of Interlayer Na-ions in Ga-substituted $Na_2Zn_2TeO_6$ (NZTO) studied by variable temperature solid state ^{23}Na NMR spectroscopy and DFT modeling.

Frida Sveen Hempel [1,2,#], Charlotte Martineau-Corcos [3], Federico Bianchini [2,†], Helmer Fjellvåg [2] and Bjørnar Arstad [1,]*

[1] SINTEF Industry, Forskningsveien 1, 0373 Oslo, Norway

[2] Department of Chemistry and Center for Materials Science and Nanotechnology, University of Oslo, Oslo 0371, Norway

[3] CortecNet, 7 avenue du Hoggar, 91940 Les Ulis, France

Present address:

Morrow Technologies AS, c/o Institute for Energy Technology, Instituttveien 18, 2007 Kjeller, Norway

† Center for Bioinformatics, University of Oslo Gaustadalléen 30 N-0373 Oslo, Norway

* Corresponding author: Bjørnar Arstad

S1 Synthesis of materials

The materials in this work are the same as we have previously published.[1] The synthesis procedure and XRD plots are reported here for completeness.

Precursors ZnO (Sigma Aldrich, 99.99%), TeO_2 (Sigma Aldrich, 99.995%) and $Ga(NO_3)_3 * xH_2O$ (Sigma Aldrich, 99.9%) were added in stoichiometric ratio, and Na_2CO_3 (Sigma Aldrich, >99.5%) with a 10% excess to account for evaporation. The ZnO, Na_2CO_3 and TeO_2 is dissolved in nitric acid (Sigma Aldrich, 65%) in a magnetic stirrer on a hot plate at 50°C until solution becomes transparent. Subsequently, $Ga(NO_3)_3 * xH_2O$ is dissolved in water and added. When everything is mixed, citric acid (Sigma Aldrich, 99.5%) compound is added in a ratio of 5:1 to the cations in the precursors, before the solution is heated to 180°C. After the NO_x gas to evaporated and a gel is formed, it was left overnight at 180°C. The powder was then heated to 450°C for 12h, before ball milling at 600 rpm for 20 min. It was then sintered at at 900°C for samples $x = 0.00$-0.10 and 800°C for $x = 0.15$-0.20 for 3h, with a heating/cooling rate of 5°C. The compound is pressed into pellets and covered at the top and bottom the mother powder, to limit evaporation and reduce diffusion length.

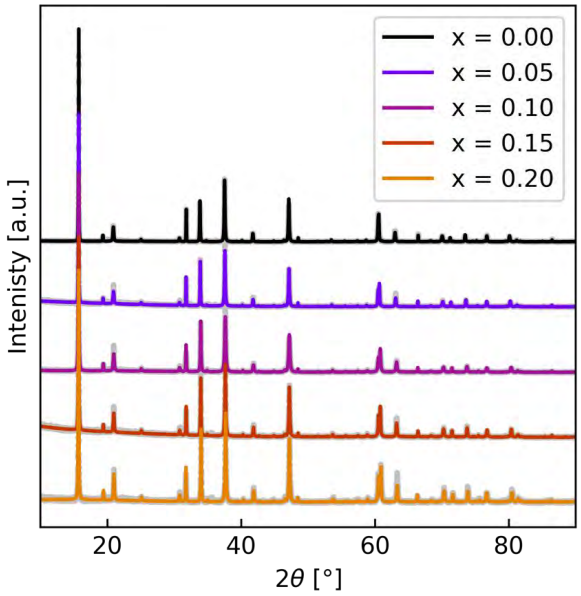

S2 Water estimation

The amount water in the materials was estimated by the following method and is based on carefully executed NMR experiments to obtain quantitative data. We further assume that we can compare absolute integral values from sample to sample (from one NMR experiment to another NMR experiment) when the following protocol is applied. A 50 µl volume (HR-MAS) rotor was carefully washed in acetone and dried before use. Several potential compounds were tried for use as reference for quantitative measurements of levels of H atoms, but most had strong H couplings and integrations that were ambiguous. However, one compound that suited our work was HNa_2PO_4 (Sigma-Aldrich 99.99%, water free). Before use some of the powder was dispersed on a glass plate and dried overnight at 150 C ° to remove water contamination. A carefully weighted amount of HNa_2PO_4 (0.0155 g) was then packed in the HR-MAS rotor and inserted into the NMR probe. Sample handling/packing in an Ar-glove box and rapid packing in air were carried out and compared and it was not found any significant differences, however, a minor component of water was left in the reference that could not be removed at moderate treatment. 0.0155 g is large enough to give reasonable low integration error and we do not need to subtract the background but is also small enough to ensure that all the powder is well within the volume of the coil in the stator. We compared with an external coil + stator to ensure this. Powder outside the coil could give contributions but at non reproducible ways as the pulse angle is smaller for powders outside the coil volume. The amount water in the reference was about 0.4% of the main H peak. For all experiments the exact same experimental setup was used, included the same X-channel tuning, receiver gain and others. A pre-run was carried out before each experiment before a second tune and match was carried out. Acquisition times were tested, and we are quite sure we have used a suited time for signal/FID acquisition, neither too short not too long. The NMR parameter setup was optimized ahead in similar experiments to find suited acquisitions parameters, that later were not changed. The number of scans in all experiments was 40. The recycle delay was for all samples was optimized and checked by doing a series of experiment with increasing recycle delay. For all NZTO based samples reported in this article it was enough to use a 10 s recycle delay, but all averaged numbers are based on experiments with recycle delays from 5 s to 30 s. For the reference HNa_2PO_4 we had several runs to find a suited recycle delay. In the end we used 6000 seconds (2 days and ~18-hour total instrument time) between each scan. It was possible to observe that a recycle delay of 10000 seconds might give a slightly larger area, but we judged it small enough that the underestimation of the area of H in HNa_2PO_4 should be marginally and insignificant compared to errors in the integration of the total areas in the NZTO based

samples. Areas of spinning sidebands were included in the final integrated values. Zero filling and baseline corrections were carried out before integration. However, the baseline corrections were not trivial and several attempts of baseline correction + integrations for each sample were carried out. Since we used five different experiments, each with different recycle delay, for each estimated number we could average five different baseline corrections + integrations from five different NMR experiments on the same sample. By comparing the area from the H atom in the reference sample and through some Excel sheet calculation an equivalent water amount could be estimated for the reference, and this could then be compared to the integrated level of water in the NZTO based samples.

S3 Additional information on ^{23}Na 100-293K NMR

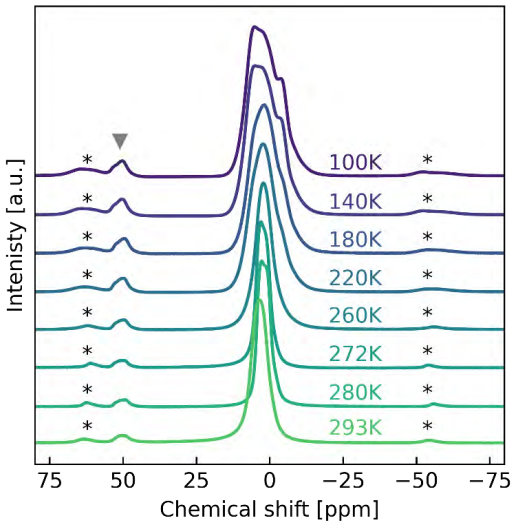

Figure S1: Wider spectral range of the ^{23}Na NMR spectra for NZTO from 100 K to 293 K at 18.8T. Spinning sidebands marked with * and 45ppm feature denoted with a grey triangle.

S4 Simulation parameters for Czjzek distribution

Table S1: Simulation parameters for Czjzek distribution shown in figure 3.

Peak	Position [Hz]	Amplitude [10^8]	FWHM CS	CQ [kHz]	Integrated intensity [%]	Assigned prism
Left	6.6	9.17	2.85	1789	52	*6g*
Middle	1.4	8.38	5.23	1608	39	*4f*
Right	-4.1	3.16	1.41	1265	9	*2a*

S5 Simulations of a three-site exchange system

There are many assumptions to consider in the application of the calculated spectra below, and they will be discussed in some detail here. The calculations are not intended to be a curve fitting giving a "correct" model of the materials in study, but to provide some background for discussing the complex situation, and for providing some visual examples. A standard matrix representation of a three-site exchange system is used, and final signals are generated by multiplication with a decaying exponential function before Fourier transforming the total sum of signals (3) for the spectra shown below.

The first spectrum is designed to be qualitative like the one observed during MAS at 100 K. The peak shapes are Lorentzian and at 100 K this is not the best approximation but at higher temperatures with more Na dynamics this assumption is not that bad as shown by the RT MAS 18.8 T ^{23}Na spectrum in Figure S2 , section S6, further below. Peak shape narrowing due to reduced quadrupolar-, and dipole-dipole - interactions may be simulated by adjusting a line broadening factor (T1#'s) in the calculations. Changes in peak positions due to a reduction of the magnitude of the 2nd order quadrupolar Hamiltonian which is again due to ion dynamics may be simulated by a small shift of the peak's center of gravity towards left, possibly also together with a narrower peak through an adjusted line broadening factor. The following panels of simulated spectra, and with explanation texts, are intended to provide indications the general processes that might take place during heating the samples. The model frequencies are relative to 0 in the spectra. K's are jump rates, and T1's are model parameters for linebroadening.

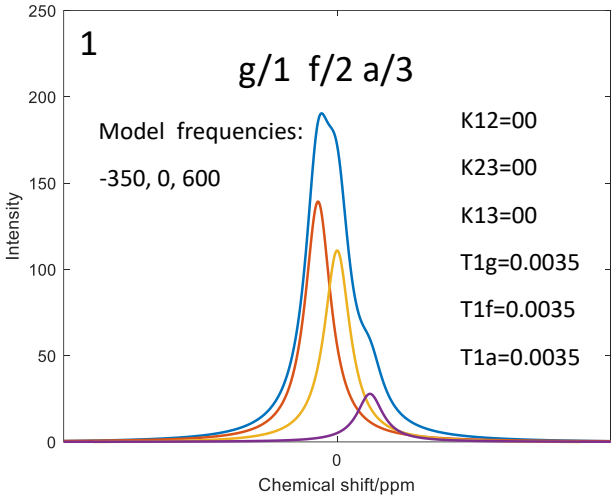

Panel 1: Starting configuration. g/1 f/2 a/3 indicates positions and id (both letter and number). K's and T1's are model parameters simulating jump rates between positions (e.g., K12 is jump rate between 1 and 2) and linebroadening, respectively. The peaks become narrower with an increase in the T1 values. Simulated positions of peaks 1, 2, and 3 are at relative model frequencies of -350, 0, and 600 Hz, respectively. These frequencies are model parameters and not the measured distance between peaks in the data acquired at 18.8 T.

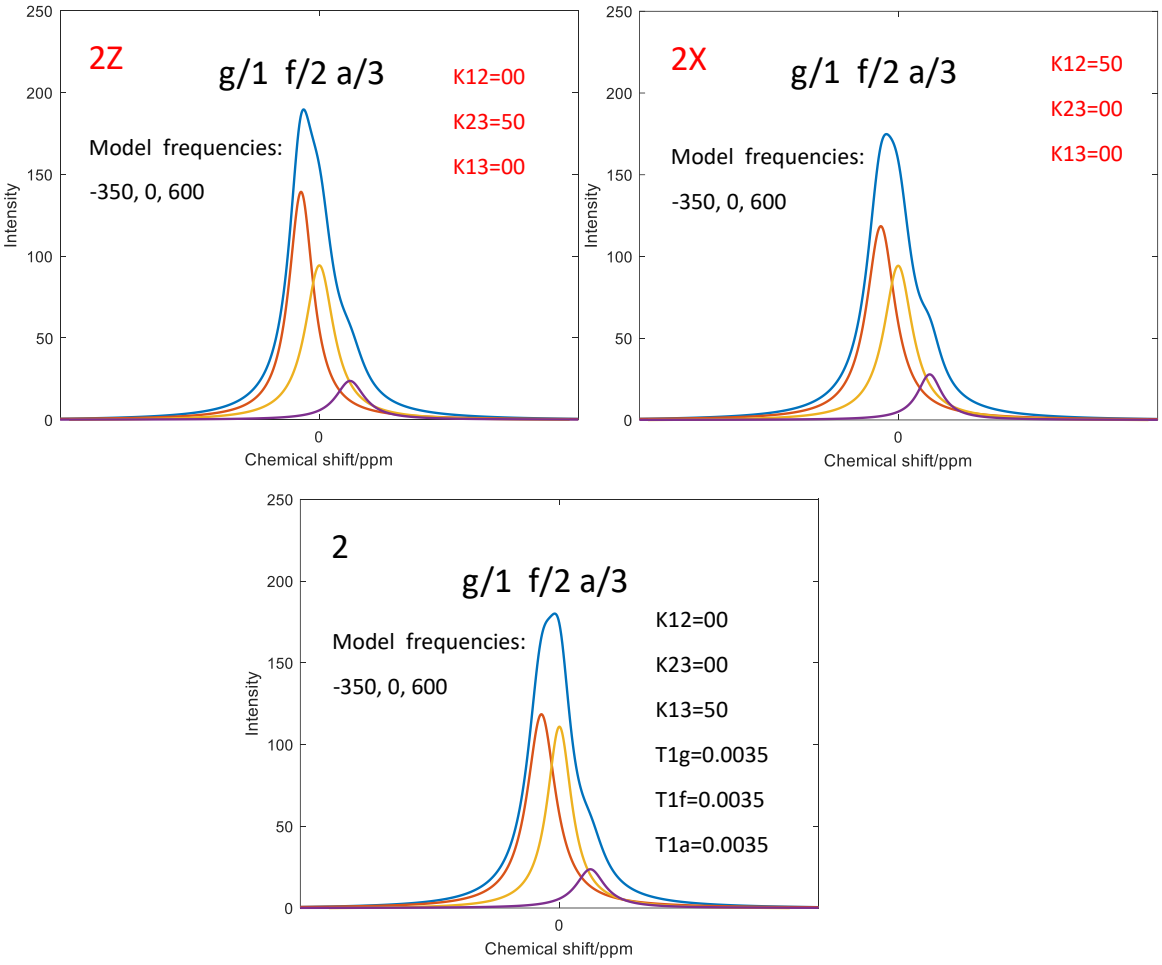

Panel 2, 2X, 2Z. We see that an increase in K13 instead of K12 or K23 give a spectrum that resembles measured data much better, which is also in line with previous reports. The tendency of the spectra in Figure 3 in the manuscript is to have the highest intensity in the middle of the total peak shape. This controls what sites the initial exchange is going between.

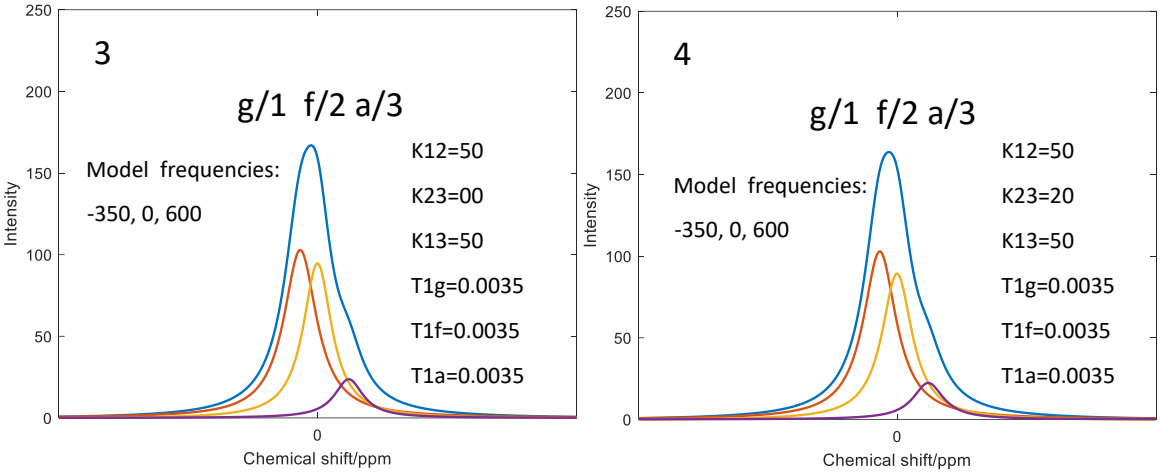

Panel 3 and 4 are spectra from a further increase in jump rates between the positions. In 4 all three sites are experiencing intermixing of ions. Panel 4 is looking somewhat like the 260 K spectrum in Figure 3. However, to resemble the 272 and 280 K spectra we had to adjust differently than just increasing jump rates.

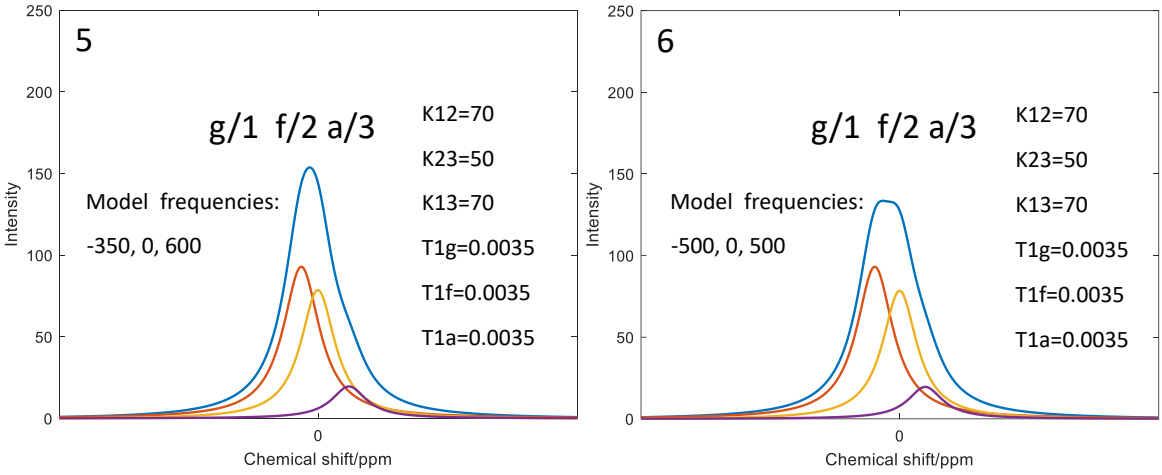

Panel 5 shows a further increase in jump rates relative to panel 4. Panel 6 has the same jump rates as shown in panel 5, but a small change in the positions of peak 1 and 3 to the left to simulate reduced quadrupolar couplings. Simulated positions of peaks 1, 2, and 3 in panel 6 are at relative model frequencies -500, 0, and 500 Hz respectively, in contrast to -350, 0, and 600 Hz for the panel 1-5 simulations.

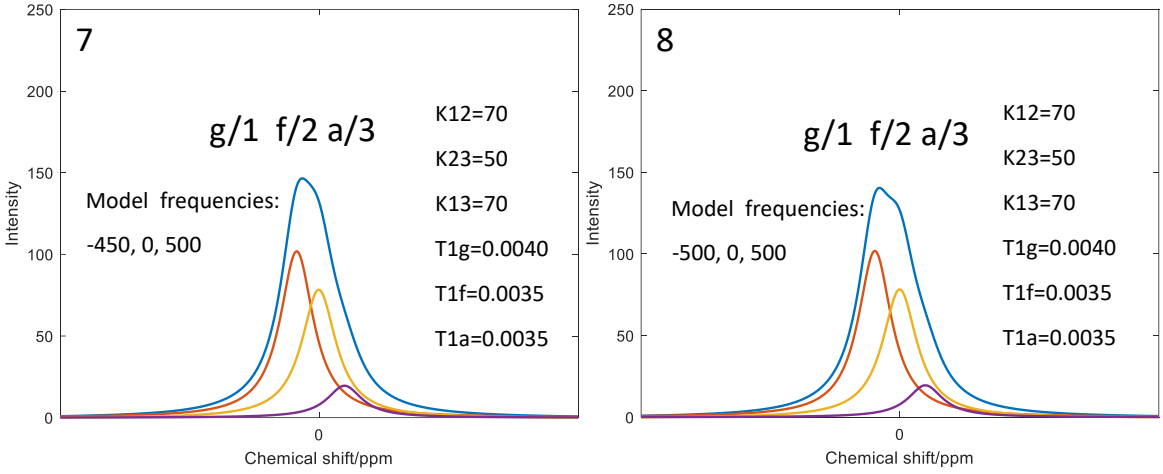

Panel 7 is similar to panel 6 except a slightly narrowing of peak 1 simulated by a higher peak broadening value but with lesser shift in peak positions as the simulated positions of peaks 1, 2, and 3 in panel 7 are at relative model frequencies of -450, 0, and 500 Hz respectively. Panel 8 is the same as 7 except that the peak positions are back to where the peaks in panel 6 were, i.e., the simulated positions of peaks 1, 2, and 3 in panel 8 are at relative model frequencies of -500, 0, and 500 Hz respectively. Panel 8's peak 1 is narrower compared to in panel 6. Panel 8 gives a better similarity with the 272 and 280 K experimental data compared to panel 5, 6, and 7. To approach the 293 K spectrum with a rather symmetric peak we did the simulations shown in panel 9 and 10.

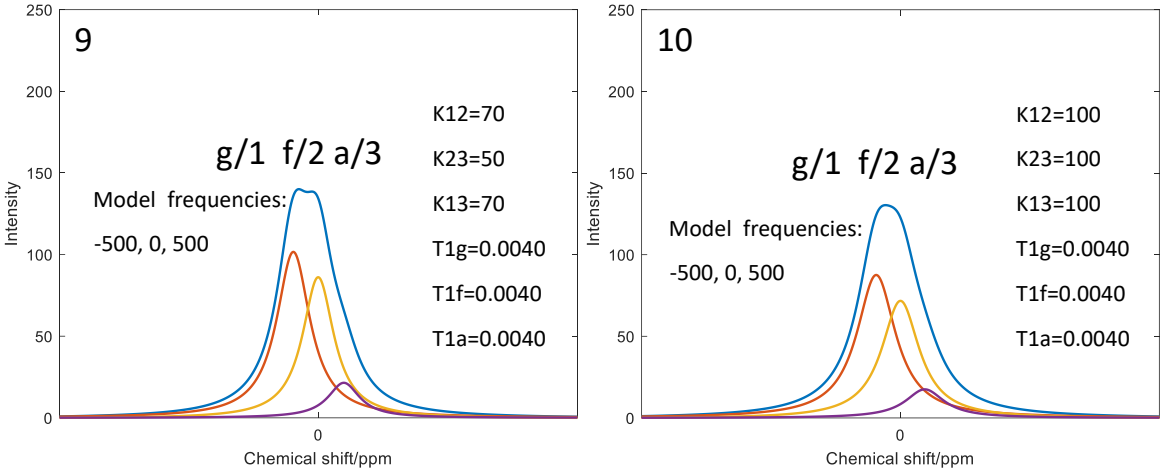

Panel 9 have the same peak positions and jump rates as 8 (model frequencies of -500, 0, and 500 Hz) but peak 2 and 3 are now narrower, and now equal to peak 1. An even further increase in jump rates lead to the spectrum shown in panel 10 and is the spectrum that most resembles the 293 K spectrum.

The overall sequence describing best the measured spectra is then 1 > 2 > 4 > 6 > 8 >9 > 10.

S6 Line fitting of the MAS spectrum acquired at 18.8 T

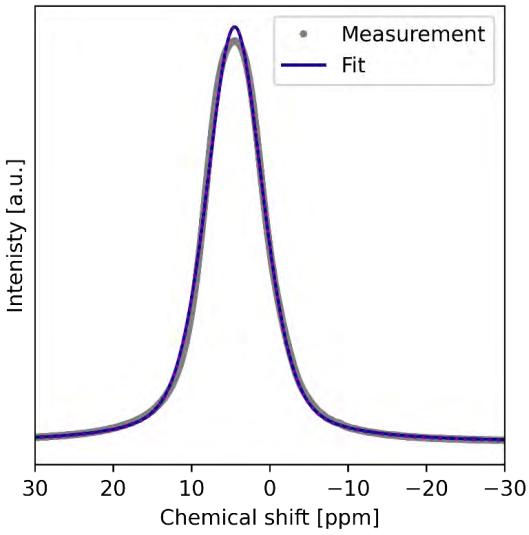

Figure S2: Curve fitting of the ^{23}Na spectrum at 293 K at 18.8 T. the main peak is basically symmetric as seen by curve fitting with a Gaussian and/or a Lorentzian function. A single component is clearly not sufficient for a perfect description, but the high symmetry of the peak demonstrates that the field is strong enough to reduce the quadropolar coupling to a very low value, which would otherwise give a peak with a tailing to the right or some sort of unsymmetric shape.

S7 Stacked plot of Ga-doped materials $Na_{2-x}Zn_{2-x}Ga_xTeO_6$ (x = 0.05, 0.10, 0.15, 0.20) from 100 K up to 293 K at 18.8 T.

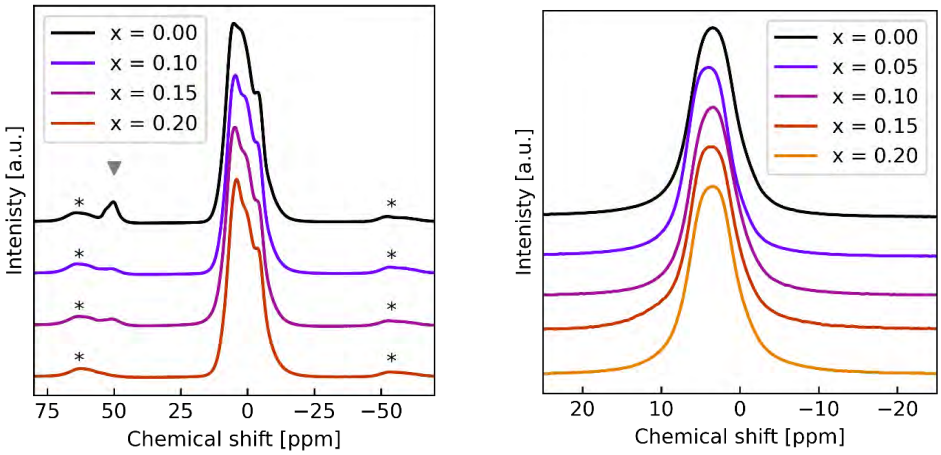

Figure S3: ^{23}Na MAS NMR at 18.8T with MAS rate 12.5 kHz for Ga-substituted samples at (a) 100K for all samples except x = 0.05 and (b) room temperature for all samples.

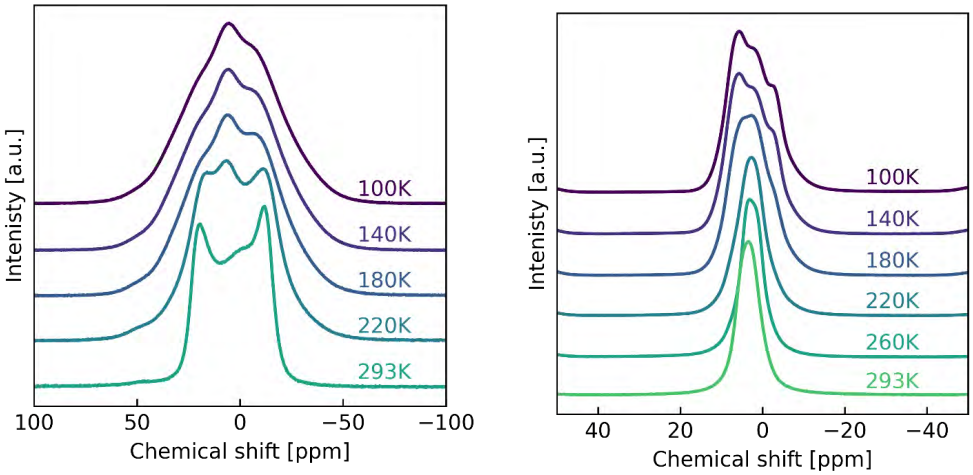

Figure S4: NMR spectra of x = 0.10 from 100 K to 293 K in a 18.8 T field. (a) static and (b) MAS with rate 12.5 kHz.

S8 Relaxation measurements

Topspin 3.6.2 was used to analyse the relaxation data, and the T_1 curve fit for values found from the "Saturation Recovery" method is principally described by the satrec (Bruker defined name) function:

$$Mz = Mz_0 - Mz_0 * \exp\left(\left(\tau/T_1\right)^{\gamma}\right)$$

Mz is the magnetization along the magnetic field and Mz_0 is the equilibrium magnetization after fully recovery along the magnetic field. γ is a stretching factor. However, the uxnmrt1 (Bruker defined name) function is often employed instead, as this allows for experimental errors like imperfect saturation and background variations giving a remnant ^{23}Na signal at t=0. This unction is given by:

$$Mz = Mz_0 + P \exp\left(\left(\tau/T_1\right)^{\gamma}\right)$$

P is a factor correcting residual peak intensities and other systematic variations/imperfections. Repeated measurements at a decided temperature gave variations in T1 up to about 10 μs, which is well within the difference between most points. Upon remeasuring on different days, some of the difference in T_1 could be up to 40 μs in a single measurement, but an average difference between 5 and 20 μs were typically observed. One reason may be that even with apparent stable temperatures during measurement there might be some variations due to variable temperatures within the sample powder. We therefore decided to reduce the uncertainty in T_1 values at each temperature by using an average value from several measurements and find that the trends in measured T_1 values could be trusted.

Table S2: Average measured T_1 values (μs) for all samples x = 0.00, 0.05, 0.10, 0.15 and 0.20 measured at 11.7 T.

T [C]	T [K]	1000/T	NZTO	NZGTO 0.05	NZGTO 0.1	NZGTO 0.15	NZGTO 0.2
22	295	3.39	500	586	553	484	446
40	313	3.19	424	511	496	423	407
60	333	3.00	359	430	437	385	390
80	353	2.83	316	380	396	363	382
100	373	2.68	304	342	367	362	393
120	393	2.54	291	321	364	377	432
140	413	2.42	294	316	369	400	483
160	433	2.31	319	320	388	441	537
180	453	2.21	355	359	431	506	590
200	473	2.11	419	419	500	596	687
215	488	2.05	-	499	567	691	769
220	493	2.03	512	-	-	-	-

230	503	1.99	-	609	637	772	839
235	508	1.97	648	-	-	-	-

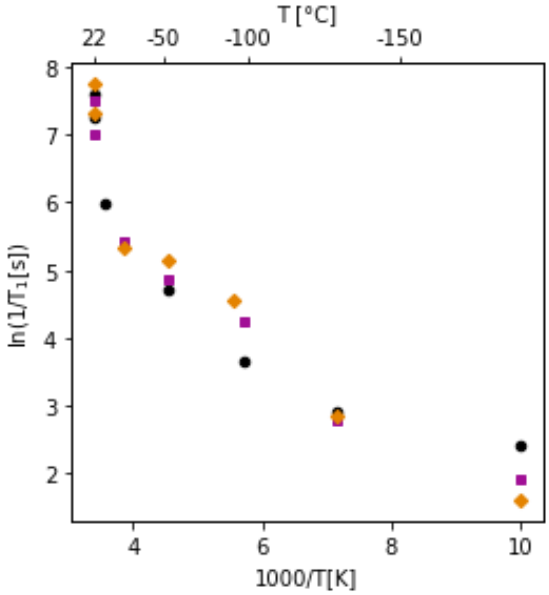

Figure S5. T_1 relaxation constants from 100 K up to 293 K measured at 18.8 T. Note the much larger T_1 value at 100 K compared to at 293 K.

S9 DFT calculation of Na mobility

The mean square displacement of Na atoms is computed as:

$$MSD = \langle | \mathbf{x}(t) - \mathbf{x}_0|^2 \rangle = \frac{1}{N}\sum_{i=1}^{N} \left| \mathbf{x}^{(i)}(t) - \mathbf{x}^{(i)}(0) \right|^2$$

where $x^{(i)}(t)$ is the position of the i^{th} Na atom at time *t*, *N* the total number of Na atoms.

The MSD is related to the diffusion coefficient by the MSD(*t*)= 2nDt + C relation, where *n* is the dimensionality of the diffusion channels, *D* the diffusion coefficient and *C* a constant representing the vibrational contribution to the MDS. After verifying the absence of diffusion along *z*, *n* has been fixed to 2. When the diffusion coefficient is obtained as a function of temperature, the Arrhenius law is used to compute the activation energy and to evaluate the diffusion coefficient at room temperature. Finally, the mobility is obtained from the diffusion coefficient using the Nernst-Einstein relation.

$$\sigma = \frac{DNq^2}{k_B T}$$

III

IV